UNIVERSITÄT DUISBURG-ESSEN

FAKULTÄT FÜR PHYSIK

Implementation and Application of Density Functional Theory Methods for Electron and Nuclear Dynamics

---

DISSERTATION

zur Erlangung des Grades

Doktor der Naturwissenschaften (Dr. rer. nat.)

vorgelegt von

JOSCHA HEKELE

aus Essen

Erstgutachter: Prof. Dr. Peter Kratzer
Zweitgutachter: Prof. Dr. Fabio Caruso

Tag der Disputation: 05.11.2021

Diese Arbeit wurde im Rahmen des DFG-Sonderforschungsbereichs 1242 "Nichtgleichgewichtsdynamik kondensierter Materie in der Zeitdomäne" an der Universität Duisburg-Essen in der Fakultät für Physik unter Anleitung von Prof. Dr. Peter Kratzer angefertigt.

Zusammenfassung

Dynamische Prozesse auf atomarer Skala sind von fundamentaler Bedeutung für unser Verständnis der Natur und der sich daraus ergebenden Anwendungen. Wir nehmen hier primär die Perspektive der Materialwissenschaft ein, deren Erkenntnisse mittels physikalischer und chemischer Methoden häufig in konkrete Anwendungsbereiche fließen.
Diese Arbeit wurde im Rahmen des DFG-Sonderforschungsbereichs 1242 "Nichtgleichgewichtsdynamik kondensierter Materie in der Zeitdomäne" an der Universität Duisburg-Essen erstellt. Im Verlauf dieser Dissertation wurden computergestütze Simulationsmethoden entwickelt und angewandt, um das benötigte theoretische Instrumentarium und den Kenntnisstand in diesem Kontext zu erweitern.
Eine sehr effiziente und oft hinreichend genaue approximative quantenmechanische Methode ist die Dichtefunktionaltheorie (DFT). Wir beschreiben hier die Implementierung der explizit zeitabhängigen Erweiterung der DFT (RT-TDDFT) in die bestehende DFT-Software FHI-aims, deren Validierung, und präsentieren Ergebnisse, welche wir durch Anwendung unserer und bestehender Methoden gewonnen haben.
Wir geben anfänglich einen Überblick über die theoretischen Grundlagen. Im darauffolgenden Teil eruieren wir technische und mathematische Aspekte der Software-Implementierung, welche einen großen Teil dieser Arbeit implizierten.
Der darauf folgende Anwendungs- und Validierungsteil enthält mehrere einzelne Arbeiten. Wir präsentieren hier Absorptionsspektrum-Simulationen für Valenz- und kernnahe Anregungen, sowohl für Moleküle als auch periodische Festkörper. Dies schließt auch eine Benchmark-Studie ein, in der wir systematische Vergleiche mit Linear-Response-TDDFT durchführen. Für den periodischen Fall zeigen wir Simulationsergebnisse für die Erzeugung hoher Harmonischer – ein wichtiger Testfall für stark nichtlineare Dynamik. Weiter wenden wir die Methode an, um Zirkulardichroismus in Molekülen zu untersuchen und präsentieren Ergebnisse einer Modellstudie für den Chiralitätstransfer in einem van der Waals-Molekülkomplex. Der Teil enthält weiter zwei Studien zur Ehrenfest-Molekulardynamik: wir untersuchen hier erstens die nichtadiabatische Dynamik in einem deformierten Molekül und zweitens den Beschuss einer Graphenlage mit einem hochenergetischen Cl-Atom unter Ausnutzung periodischer Randbedingungen. Den letzten Part bildet eine Diskussion der imaginären Zeitentwicklungsmethode, welche zur Berechnung von Grundzuständen verwendet werden kann.
Im folgenden Abschnitt nehmen wir formal eine perturbative, zeitunabhängige Perspektive ein und präsentieren eine kollaborative Studie, in der detailliert das Adsorptionsverhalten von Thiophenolen auf Goldoberflächen untersucht wurde.
Letztlich stellen wir noch eine Analyse der technisch-numerischen Eigenschaften unserer RT-TDDFT-Implementierung vor, in der wir auch das Skalierungsverhalten für große Systeme illustrieren.

Abstract

Dynamical processes on the atomic scale are of fundamental importance for our understanding of nature and for resulting applications. We here primarily take the perspective of materials science, whose insights obtained by physical and chemical methods often yield tangible applications.
This work was conducted within the DFG collaborative research center 1242 'Non-equilibrium Dynamics of Condensed Matter in the Time Domain' at the University of Duisburg-Essen. Within this thesis, we developed and applied computer-aided simulation methods in order to extend the theoretical apparatus and knowledge base in this context.
An efficient and often sufficiently accurate approximative quantum-mechanical method is density functional theory (DFT). We here describe the implementation of the explicitly time-dependent extension of DFT (RT-TDDFT) into the existing DFT software FHI-aims. For this, we present a detailed validation and further results which were obtained by this and other methods' utilizations.
First, we provide an overview of the theoretical basis. In the second part, we discuss technical and mathematical aspects of the software implementation, which implicated a major part of this work.
The following validation and applications chapter contains multiple results. We here present absorption spectra simulations for valence and core-level excitations, both for molecules and periodic solids. This includes a benchmark study, embodying systematic comparison with linear-response TDDFT. For the periodic case, we show simulation results for high-harmonic generation – an important testcase for strongly non-linear dynamics. We further apply our method to analyze circular dichroism in molecules and present results of a model study for the chiral transfer in a van der Waals molecular complex. This part also contains two studies for Ehrenfest molecular dynamics: first, we investigate the non-adiabatic dynamics in a deformed molecule, while the second example is the bombardment of a graphene layer with a high-energy Cl atom, utilizing periodic boundary conditions. The last part contains a discussion of the imaginary-time propagation method which can be used for the calculation of ground state solutions.
In the following chapter, we formally take a perturbative, time-independent perspective and present a collaborative study where we analyzed the adsorption characteristics of thiophenols on gold surfaces in detail.
Finally, we present an analysis of the technical and numerical features of our RT-TDDFT implementation, also shedding light onto its scaling characteristics for larger systems.

Contents

1 Introduction **1**
- 1.1 Overview . . . 1
- 1.2 Goals . . . 6

2 Theoretical Foundation **7**
- 2.1 Density Functional Theory . . . 7
  - 2.1.1 Motivation . . . 7
  - 2.1.2 Hohenberg-Kohn Theorem . . . 10
  - 2.1.3 Kohn-Sham Approach . . . 12
  - 2.1.4 Exchange-Correlation Functionals . . . 14
  - 2.1.5 Basis Sets . . . 16
  - 2.1.6 Self-Consistent Field Solution . . . 19
  - 2.1.7 Forces, Geometry Relaxation and Molecular Dynamics . . . 20
- 2.2 Real-Time Time-Dependent Density Functional Theory . . . 22
  - 2.2.1 Introduction . . . 22
  - 2.2.2 The Runge-Gross Theorem . . . 22
  - 2.2.3 The Time-Dependent Kohn-Sham Equation . . . 23
  - 2.2.4 Coupling to External Optical Fields and Periodic Boundary Conditions . . . 25
  - 2.2.5 Gauge Choice . . . 27
  - 2.2.6 Observables . . . 28
  - 2.2.7 Solving the Time-Dependent Kohn-Sham Equation . . . 29
- 2.3 Coupled Nuclear-Electronic Dynamics . . . 31
  - 2.3.1 Fundamentals . . . 31
  - 2.3.2 Ehrenfest Dynamics . . . 32
- 2.4 Linear-Response Time-Dependent Density Functional Theory . . . 34
  - 2.4.1 Introduction . . . 34
  - 2.4.2 Formulation as Matrix Equation . . . 36

3 Details on the Real-Time TDDFT Implementation **39**
- 3.1 Overview . . . 39
- 3.2 The FHI-aims Code Package . . . 39
- 3.3 RT-TDDFT Functionality Integration . . . 44
  - 3.3.1 Approach . . . 44
  - 3.3.2 Code Structure and Workflow . . . 45

3.3.3 Modes of Operation, Parallel Infrastructure and Optimization . 46
3.4 Numerical Time Propagation . . . 49
3.4.1 The Time-Dependent Kohn-Sham Equation in a Localized Basis 50
3.4.2 Numerical Considerations . . . 51
3.5 Exponential-Based Propagators . . . 53
3.5.1 General Considerations . . . 53
3.5.2 Magnus Expansion . . . 54
3.5.3 Exponential Midpoint Scheme . . . 56
3.5.4 Commutator-Free Magnus Expansion 4 Scheme . . . 57
3.5.5 Matrix Exponentials . . . 58
3.6 Crank-Nicolson Scheme . . . 63
3.7 Predictor-Corrector Scheme . . . 64
3.8 Ehrenfest Dynamics . . . 65
3.8.1 Equations of Motion . . . 66
3.8.2 Numerical Integration . . . 69

4 Real-Time TDDFT Validation and Applications 71
4.1 Overview . . . 71
4.2 Absorption Spectra of Molecules . . . 71
4.2.1 Introduction . . . 71
4.2.2 Theory . . . 72
4.2.3 Simulation of Benzene Linear-Response Excitations . . . 75
4.2.4 Oxygen K-Edge Core-Level Absorption Spectrum for Water . . 80
4.2.5 Benchmarking Real-Time TDDFT for Molecular Optical Absorption . . . 84
4.2.6 Discussion . . . 95
4.3 Response of Periodic Systems . . . 96
4.3.1 Introduction . . . 96
4.3.2 Theory . . . 97
4.3.3 Dielectric Response of Bulk Silicon . . . 99
4.3.4 Core-Level and Valence Absorption of 2H-SiC . . . 101
4.3.5 High-Harmonic Spectrum of Bulk Silicon . . . 104
4.3.6 Discussion . . . 107
4.4 Circular Dichroism . . . 109
4.4.1 Introduction . . . 109
4.4.2 Theory . . . 109
4.4.3 Rotatory Strength of (R)-Methyloxirane . . . 111
4.4.4 Modeling Chiral Transfer in Molecules . . . 112
4.4.5 Discussion . . . 116
4.5 Ehrenfest Dynamics . . . 118
4.5.1 Introduction . . . 118
4.5.2 Forced Rotation of $H_2C{=}N^+H_2$ . . . 120

4.5.3 Collision of a Cl Atom with Graphene . . . 123
4.5.4 Discussion . . . 126
4.6 Imaginary Time Propagation . . . 127
4.6.1 Introduction . . . 127
4.6.2 Theory . . . 127
4.6.3 Benchmarks for IT-TDDFT . . . 129
4.6.4 Discussion . . . 130

5 Time-Independent Methods for Vibrational Spectroscopy 133
5.1 Overview and Motivation . . . 133
5.2 Theory . . . 133
5.2.1 Vibrational Spectra and Harmonic Approximation . . . 133
5.2.2 Density Functional Perturbation Theory . . . 135
5.3 Vibrational Analysis of Nitrothiophenyls on Au(111) Surfaces . . . 136
5.3.1 Introduction . . . 137
5.3.2 Simulation Setup . . . 138
5.3.3 Equilibrium Geometries and Energetics . . . 139
5.3.4 Vibrational Characteristics . . . 145
5.3.5 Discussion . . . 149

6 Analysis of Real-Time TDDFT Implementation and Methods 151
6.1 Overview and Motivation . . . 151
6.2 Evaluation of Propagation Schemes . . . 151
6.2.1 Measures of Numerical Stability . . . 151
6.2.2 Extrapolation and Predictor-Corrector Order . . . 152
6.2.3 Evaluation of Propagation Schemes . . . 155
6.3 General Scaling Characteristic . . . 159
6.4 Discussion . . . 161

7 Conclusion and Outlook 163

A Manual 167
A.1 Core Settings . . . 167
A.2 Ehrenfest Dynamics Settings . . . 178
A.3 Output Settings . . . 179
A.4 Restart Settings . . . 186
A.5 Geometry Settings . . . 187
A.6 Important Remark . . . 187

B Examples 189
B.1 Benzene: Absorption Spectrum . . . 189
B.2 Silicon: High-Harmonic Spectrum . . . 190
B.3 $CH_2{=}NH_2^+$: Ehrenfest Dynamics . . . 191

C Code Structure and Installation **193**
C.1 Installation 193
C.2 Compatibility Remarks 193
C.3 Code Structure 194

D Postprocessing Tools **199**
D.1 Evaluation of Spectral Quantities: eval_tddft.py 199
D.2 DSF Fitting for Spectra Acceleration: ifit_abs.py 201

Publications **203**

Bibliography **205**

Acknowledgements **227**

Declaration **229**

List of Figures

2.1 Illustration of Jacob's Ladder . . . 15
2.2 Illustration for the self-consistent field procedure . . . 20

3.1 Plot of radial basis functions in FHI-aims . . . 41
3.2 Illustration of the RT-TDDFT implementation workflow . . . 46
3.3 Illustration of the 2D block-cyclic distribution . . . 48
3.4 Illustration of the predictor-corrector scheme . . . 65
3.5 Illustration of ion and grid movement . . . 69
3.6 Illustration of the Ehrenfest propagation scheme . . . 70

4.1 Plot of dynamics for weakly perturbed benzene . . . 77
4.2 Plot of the f-sum rule consistency check for benzene . . . 78
4.3 Plot of experimental and calculated benzene valence absorption spectra 79
4.4 Plot of experimental and calculated benzene core absorption spectra . 80
4.5 Plot of RT-TDDFT and experimental water K-edge absorption spectra . 83
4.6 Illustration of molecules in Thiel's set . . . 84
4.7 Plot of Padé and fitting methods for the DSF . . . 88
4.8 Plot of singlet energy differences for basis sets and LR/RT-TDDFT . . 91
4.9 Plot of triplet energy differences for basis sets and LR/RT-TDDFT . . . 91
4.10 Plot of unrefined DSF triplet spectra of ethene . . . 92
4.11 Plot of oscillator strengths and excitation energies in LR/RT-TDDFT . 93
4.12 Plot of distributions of singlet excitations for LR/RT-TDDFT . . . 94
4.13 Plot of distributions of triplet excitations for LR/RT-TDDFT . . . 94
4.14 Plot of method to remove artificial peaks in dielectric function . . . 100
4.15 Plot of dielectric function of silicon from RT-TDDFT and Lindhard theory . . . 101
4.16 Plot of dielectric function of silicon from RT-TDDFT and reference . . . 102
4.17 Plot of zz-dielectric tensor of 2H-SiC from RT-TDDFT and Lindhard theory . . . 103
4.18 Plot of zz-dielectric tensor of 2H-SiC from RT-TDDFT and reference . . 103
4.19 Plot of zz-dielectric tensor of 2H-SiC from RT-TDDFT for different basis sets . . . 103
4.20 Plot of zz-dielectric tensor of 2H-SiC from RT-TDDFT and Lindhard theory for different basis sets . . . 104
4.21 Plot of vector potential and energy for field pulse in silicon . . . 105

4.22 Plot of HHG spectrum of silicon from RT-TDDFT and reference 106
4.23 Plot of rotatory strength function of R-methyloxirane from RT-TDDFT and reference 112
4.24 Illustration of R-MBA and pyrene 113
4.25 Illustration of MBA+pyrene molecular complex 114
4.26 Plots of DSF and RSF for pyrene and MBA 115
4.27 Plots of DSF and RSF for MBA+pyrene molecular complex 116
4.28 Illustration of Ehrenfest/BOMD PES dynamics 119
4.29 Illustration of the rotation of the $H_2C{=}N^+H_2$ molecule 120
4.30 Plot of the $H_2C{=}N^+H_2$ dihedral angle and energy dynamics for low initial kinetic energy 121
4.31 Plot of the $H_2C{=}N^+H_2$ dipole and energy dynamics for high initial kinetic energy 122
4.32 Plot of the $H_2C{=}N^+H_2$ dihedral angle and energy dynamics for high initial kinetic energy 123
4.33 Illustration of supercell used for the simulation of Cl impact on graphene 124
4.34 Plot of the energetics in the Cl collision on graphene 125
4.35 Plot of the kinetic energy distribution in the Cl collision on graphene . 126
4.36 Plot of IT-TDDFT energy convergence for silicon and benzene 129
4.37 Plot of IT-TDDFT energy convergence for fluoromethane and NaCl . . 130
4.38 Plot of IT-TDDFT energy convergence for hex-BN for different vacancies 131

5.1 Illustration of 4-NTP/NBPT/NTPT chemical structures and adsorption geometry descriptors 139
5.2 Illustration of relaxed geometries for 4-NTP on Au(111) 1 140
5.3 Illustration of relaxed geometries for 4-NTP on Au(111) 2 141
5.4 Plot of adsorption energy characteristics of 4-NTP/NTPT/NBPT . . . 143
5.5 Illustration of 4-NTP on Au_7/Au_{19} clusters and selected eigenmodes . 145
5.6 Plot of experimental Raman spectra of 4-NTP on Au(111) and in solution 147
5.7 Plot of experimental/theoretical calibration curve for vSFS intensity ratios 149

6.1 Plot of energy conservation in benzene and Au_2 for PC and extrapolation schemes 153
6.2 Plot of DSF spectra of benzene for weak and strong excitations 154
6.3 Plot of energy conservation characteristics for different propagators . . 156
6.4 Plots of cubic fit functions for computation time of different propagators 157
6.5 Illustration of oligoacenes 159
6.6 Plot of RT-TDDFT computation time per integration step for oligoacenes 160
6.7 Plot of relative computation timings for two oligoacenes 161

D.1 Graphical output produced by the `eval_tddft.py` script 200
D.2 Graphical output for first step of fitting procedure 201

D.3 Graphical output for second step of fitting procedure 202

List of Tables

4.1 Basis set specification for H, C, N and O 89

5.1 Values of 4-NTP/Au(111) adsorption geometry descriptors 140
5.2 Values for the Mulliken analysis of 4-NTP on Au(111) structures 144
5.3 Selected vibrational modes of 4-NTP on Au(111) calculations 146
5.4 Calculated molecular Raman tensor components 149

6.1 Prefactors of numerical effort functions for propagators 158
6.2 Key values for oligoacenes in our benchmark test set 160

List of Abbreviations

DFT	**D**ensity **F**unctional **T**heory
TDDFT	**T**ime-**D**ependent **DFT**
RT-TDDFT	**R**eal-**T**ime-**TDDFT**
LR-TDDFT	**L**inear-**R**esponse-**TDDFT**
IT-TDDFT	**I**maginary-**T**ime-**TDDFT**
DFPT	**D**ensity **F**unctional **P**erturbation **T**heory
XC	E**x**change **C**orrelation
KS	**K**ohn-**S**ham
TDKS	**T**ime-**D**ependent **K**ohn-**S**ham
HK	**H**ohenberg-**K**ohn
HF	**H**artree-**F**ock
HOMO	**H**ighest **O**ccupied **M**olecular **O**rbital
LUMO	**L**owest **U**noccupied **M**olecular **O**rbital
LDA	**L**ocal **D**ensity **A**pproximation
GGA	**G**eneralized **G**radient **A**pproximation
SCF	**S**elf-**C**onsistent **F**ield
ZORA	**Z**eroth-**O**rder **R**egular **A**pproximation
vdW	**v**an **d**er **W**aals
PBC	**P**eriodic **B**oundary **C**onditions
EOM	**E**quations **o**f **M**otion
ED	**E**hrenfest **D**ynamics
BOMD	**B**orn-**O**ppenheimer **M**olecular **D**ynamics
NAO	**N**umerical **A**tom-Centered **O**rbitals
GTO	**G**aussian-**T**ype **O**rbitals
(L)APW	(**L**inearized) **A**ugmented **P**lane **W**ave
PAW	**P**rojector-**A**ugmented **W**ave
MPI	**M**essage-**P**assing **I**nterface
IVP	**I**nitial **V**alue **P**roblem
PC	**P**redictor-**C**orrector
EM	**E**xponential **M**idpoint
CN	**C**rank-**N**icolson
CFM4	**C**ommutator-**F**ree **M**agnus Expansion **4**
ETRS	**E**nforced **T**ime-**R**eversal **S**ymmetry
XANES	**X**-ray **A**bsorption **N**ear-**E**dge **S**pectroscopy
vSFS	**V**ibrational **S**um-**F**requency **S**pectroscopy

To my loved ones

Chapter 1

Introduction

1.1 Overview

Formulated in a most general sense, this work covers technical and quantitative aspects of electron and nuclear dynamics simulations. Before coming to the details of our project and results, we want to provide a short overview of physical phenomena and recent advances that are relevant in this context, providing motivational aspects of research activity in the given scope.

The term *dynamics* explicitly takes into account the temporal evolution of some system and by referring to electron and nuclear dynamics, a vast range of phenomena over a wide span of timescales is included. In the language of quantum mechanics, a system is dynamical when its observables, e.g., energy or electric dipole moment, change when followed in time. For example, an electron in an atom may be promoted to a higher energy state by absorption of an incident photon's kinetic energy, and shortly after de-excite back to its originating level via some relaxation process, as observed step-by-step. While we mostly speak about dynamical *processes* here, the explicit time evolution of a quantum system is not necessarily the subject of study. Often, only the somehow defined *result* of some dynamical process is what one is interested in. For example, perceiving the world that surrounds us with our own eyes, seeing colors and shapes, can be thought of as the *result* of light absorption and emission – *processes* that take place on specific timescales. We may thus discuss the dynamical process itself, or the measured result of such a process happening.

This leads us to the term of *spectroscopy* which generally denotes the analysis of some form of radiation with respect to its frequency or wavelength. Within this context, this only means electromagnetic or photoelectron radiation. Historically, spectroscopic experiments substantially – but not exclusively – motivated the development of quantum mechanics as the nowadays central microscopic theory, as, e.g., via Einsteins fundamental work on the photoelectric effect or Niels Bohr's model for the atomic structure. In this context and within the scope of this thesis, the spectroscopically analyzed processes of absorption and emission of electromagnetic radiation by a quantum system, were of central interest (among others). At the present day, there

exists a vast amount of spectroscopic methods that play important roles in physics, chemistry, biology or medicine (and more fields). Some very interesting and important techniques and applications are:

- The design of efficient organic or inorganic solar cells that allow energy harvesting from the sunlight. The determination of the semiconducting material's electronic structure can be performed by absorption spectroscopy. It provides some key insights needed to make progress in this field.
- The structural clarification of large biomolecules like DNA or proteins is of great importance in biochemistry, e.g., for drug development. A rather uncomplicated method for this purpose is circular dichroism spectroscopy, measuring if and how differently circularly polarized light is absorbed by analytes.
- Characterization of chemical bonding and orientation of adsorbates on surfaces is of fundamental importance in the field of surface science, e.g., for catalysis used in chemical processing. Here, X-ray absorption spectroscopy is an important tool, allowing to characterize unoccupied electronic states which are populated by core electrons due to the X-ray excitation.
  Another technique popular for such applications is Raman spectroscopy which makes use of inelastic photon scattering. The scattered light's energy can be used to characterize certain excitations, often vibrational modes, being specific for molecular bonding or orientation.
- Identification of specific elements in a sample can be achieved by using photoemission spectroscopy. Here, the sample is ionized and the kinetic energy of ejected photoelectrons is specific for their origin electronic state. In its angle-resolved variant, photoemission spectroscopy can also be used to reconstruct the electronic band structure of solids.

Note that the aforementioned methods are generally used in very different fields for many different purposes, and that several more specific variants exist.

In contrast to most traditional spectroscopic techniques that do not explicitly incorporate a time-dependent perspective, spectroscopic methods were developed in the recent past that take into account this degree of freedom. Typically, the analyzed phenomena take place on very short timescales. In order to sufficiently resolve such dynamics, it is necessary to probe them with high temporal resolution, i.e., with ultrashort laser pulses. The relevant timescales are here within femto- (10^{-15}) or attoseconds (10^{-18}). Already the construction of lasers that provide such short pulses is a challenging task that requires the understanding of processes like high-harmonic generation, where a sample emits radiation at higher integer multiple frequencies of an incident generating beam.

Typical applications of ultrashort laser pulses are:

- In organic solar cells, the lifespan of photoexcited electron states is crucial in order to harvest charges in often heterogeneous materials. Here, transient absorption spectroscopy is employed, which uses two (or more) time-delayed short laser pulses to characterize temporal *changes* in the sample's absorption. The first pulse populates excited states, whereas the second pulse possibly probes the absorption of higher excited states. Variations of the pulse delay yield a time-resolved picture.

- The time-resolved formation or break of chemical bonds is important, e.g., when studying the reaction of DNA to ultraviolet radiation exposure. Time-resolved photoelectron spectroscopy is an often used tool for such cases, as it is also sensitive to nuclear vibrational states and obeys no selection rules. One may also employ a pump-probe scheme, where initially excited states are probed by the kinetic energy of photoemitted electrons.

Again, many different methods exist in this context, often complementing each other, and being used for different purposes.

At this point, it makes sense to discuss whether a system exhibits a *linear* or *non-linear* response with respect to an external stimulation, e.g., a laser pulse. Consider a situation where an electron system in an atom, a molecule, or a crystal, is excited by an electromagnetic field. The electric dipole moment is an observable describing the field-induced charge distortion, which serves as response function in this discussion. For sufficiently weak fields, the dynamical change of this observable is predominantly directly proportional to the external perturbation, i.e., the electric field amplitude. This is the regime of standard absorption and emission spectroscopy. In contrast, the regime of non-linear response is usually characterized by strong external fields or multi-photon processes, driving the system far away from equilibrium. For example, the dipolar response is here only correctly described when taking into account its full non-linear character, as quadratic, cubic, and higher-order terms of the electric field enter the description. The aforementioned high-harmonic process is a typical example for this regime. For theoretical treatment, the distinction between linear and non-linear response can make a significant difference, as, e.g., approximations that are valid for weak excitations cannot be employed anymore when describing strong excitations.

So far, in our former discussions, we laid our focus mainly on the dynamics of electrons. The explicit inclusion of nuclear dynamical degrees of freedom cannot be neglected for the correct description of many physical phenomena and applications. In the following list, we provide some examples where the nuclear dynamics are of central importance:

- Vibrational states of molecules or collective lattice oscillations in solids (phonons) can be probed by Raman or infrared (IR) spectroscopy, providing information about specific chemical bonds, elements, heat conductivity, and more. In the case of Raman scattering, incident photons lose some of their energy upon scattering, exciting specific nuclear oscillatory states. Such states can also be excited by complete absorption of photonic energy, which is the basis for infrared spectroscopy. IR and Raman spectroscopy can be used complementary and the respective modes are even mutually exclusive in centrosymmetric molecules.
- A very fundamental chemical process is the structural change of molecules due to optical excitation, e.g., dissociation. The non-dissociative light-induced structural change is commonly denoted as photo-switching, which can for example be employed in electronics to design photo-transistors.
- The collision of ions with solid matter is a process that can be of technological interest, e.g., to inject doping atoms into semiconductors or to create corrosion-resistant surface layers. A key quantity is here the so-called stopping power which measures energy transfer along an ion trajectory. It is often conceptually divided into nuclear and electronic stopping power, where the latter may be connected to strong electronic excitation by ion impact.

While a complete formal description involves the full quantum-mechanical treatment of both electrons and nuclei, often a classical treatment of the latter is employed, substantially simplifying the mathematical description. Another common approach is the use the Born-Oppenheimer or *adiabatic* approximation, leading to the electrons being in the ground state at every instant of nuclear movement. While this approximation can be of great use, it fails when excited electronic states are present, which is for example the case in high-energy ion collision experiments.

This work and the corresponding position was embedded in the collaborative research center 1242 (CRC 1242) 'Non-Equilibrium Dynamics of Condensed Matter in the Time Domain' at the University of Duisburg-Essen[1]. As the title suggests, the focus of this collaborative experimental and theoretical effort is the study of non-equilibrium dynamics, formally grouped into three project areas, namely 'Isolated Excitations' (area A), 'Extended and Propagating Excitations' (area B), and 'Structural and Cooperative Dynamics' (area C). Several of the aforementioned methods are employed within the context of the CRC 1242. The project this work was allocated to is part of area B, titled 'B02 – Ab-initio Simulation of Electronic Excitation and Relaxation'. It was the pre-defined goal to implement, test and apply ab-initio simulation software capable to describe electronic excitations in real-time on the level of density functional theory (DFT), in order to provide a sophisticated tool for the theoretical perspective and to deliver new insights. The corresponding approach

[1] https://www.uni-due.de/sfb1242/

is called real-time time-dependent density functional theory (RT-TDDFT), which can be used for the quantum-mechanical simulation of linear and non-linear response with a favorable trade-off between efficiency and accuracy. We further made use of the possibility of this method to describe non-adiabatic electron-nuclear dynamics based on the Ehrenfest approach. The developed software can thus be employed within different contexts of the CRC 1242.

Density functional theory is nowadays a very well-known and successful approximate approach to treat ground state quantum-mechanical problems. For larger systems composed of hundreds or thousands of atoms, the method offers an unrivaled compromise between efficiency and accuracy. Its extension to the time-dependent case is substantiated formally, but most applications are carried out in the linear-response variant (LR-TDDFT), mostly being used to compute absorption spectra. The real-time variant is a lesser-known approach that gained more and more popularity over the past years, at it can be used to simulate real time-evolution both for linear and non-linear response situations.

We here describe our implementation of the RT-TDDFT functionality into the existing DFT software package FHI-aims and present several applications. Of special importance is here the basis set used to represent the Kohn-Sham wave functions. Over the last years, several RT-TDDFT implementations emerged for different types of basis sets. The specialty in our case is that we employ so-called numerical atom-centered basis sets together with an all-electron description. As we will elucidate over the course of this work, this approach provides an especially effective and accurate framework for several relevant physical cases.
We start by introducing the theoretical basis of DFT, real-time- and linear-response TDDFT, and RT-TDDFT-based Ehrenfest dynamics within Chapter 2. Thereafter, we describe the technical and mathematical specifics of the implementation in Chapter 3. In Chapter 4, we show several validations and applications of our RT-TDDFT code: linear-response valence and core absorption spectroscopy simulations both for molecules and solids, including a basis-set benchmark study, high-harmonic generation in extended systems, circular dichroism spectroscopy in molecules, Ehrenfest dynamics both for finite and extended systems, and finally imaginary-time propagation for finite and extended systems. While the former chapter provides a sophisticated study of real-time TDDFT capabilities, we take a different perspective in Chapter 5 in order to construct a more general picture of DFT-based theoretical spectroscopy. Here, we employ perturbative methods that are applicable for infrared and Raman spectroscopy, but do not require explicit time-dependent treatment, and present a detailed study for a specific case of molecular surface adsorption. Subsequently, we provide a technical analysis of the RT-TDDFT implementation in Chapter 6. We here shed light onto some implications specific to our approach and offer suggestions for optimal usage, based on our results. Additionally, we analyze the

scaling of the method, having in mind possible large-scale simulations in the future. A conclusion is presented in Chapter 7, summarizing our results and giving some outlook for future research. The appendix contains further information relevant for any user or developer: a manual (Chapter A), several examples for RT-TDDFT simulations (Chapter B), remarks about installation and code structure (Chapter C), and finally short manuals for our postprocessing tools (Chapter D).

1.2 Goals

In the same way experimental physicists build complex measurement setups, theoretical physicists not only build mathematical models, but also numerical software in order to generate insightful physical data. Therefore, it is an intrinsically important task of applied theoretical physics to build accurate and efficient simulation software.

Probably one of the most impactful interplays between theory and numerical simulation in physics and chemistry is given by the successes of modern density functional theory. Not only the formal basis by works of Walter Kohn and others, but also practical aspects of the theory's computer code implementation by John Pople and others were honored with the Nobel price in chemistry. Publications in this field are cited 100000s of times in the literature and many very useful insights could be obtained.

It was a defined goal within this work to deliver an implementation that is not only as complete as possible and readily usable, but also being structured and encapsulated enough such that it is no too difficult to understand for a possible contributor, motivating additional future extensions. We therefore try to provide a transparent systematic overview of the implementation, its capabilities and applications.

As a framework with numerous capabilities was developed in the course of this thesis, we aim to provide an analysis of most of these features within this document. This is not only of interest for physical applications, but it is also a necessity in our opinion to prove the validity of our work.

In view of possibly future extensions or applications, the author makes clear that he is willing to assist in such endeavors (under the constraints of what the future brings).

Chapter 2

Theoretical Foundation

2.1 Density Functional Theory

In this chapter, we will cover the most important aspects of ground state density functional theory in order to provide the required formal basis needed to establish the extension of the theory to the time-dependent case.

2.1.1 Motivation

The most successful theory for the description of microscopic systems consisting of electrons and nuclei is quantum mechanics, essentially founded in the 1920s by Erwin Schrödinger, Paul Dirac, Werner Heisenberg, Max Born and more [1, 2, 3, 4]. Its success can hardly be captured by any defined metric but it is clear that many technological advances of our modern society would not have been possible without our understanding of microscopic systems based on quantum mechanics.
A stationary system, i.e., a system whose observables are not following temporal change, consisting of interacting N electrons and M nuclei can be described by the time-independent Schrödinger equation [5]

$$\mathcal{H}_{\text{tot}}\Phi = E_{\text{tot}}\Phi \tag{2.1}$$

where Φ is called the (generally complex-valued) many-body wave function of the system and $\mathcal{H}_{\text{tot}}$ the Hamiltonian operator corresponding to the total energy E_{tot}. The abstract wave function Φ is an object collectively describing all of the system's components – electrons and nuclei – and thus depends on all these degrees of freedom, making it an extremely complex quantity.
At this point, we introduce the Born-Oppenheimer approximation [6] which assumes spatially fixed nuclei, as viewed from the electronic perspective. This is justified since the nuclei are heavier than electrons by more than 3 orders of magnitude, thus moving much slower. For any nuclear configuration, it is assumed that the electron system is instantly in its ground state. Mathematically, the many-body wave function can be factorized, yielding two decoupled Schrödinger equations: one for the nuclei and one for the electrons, the latter one in parametric dependence of the

nuclear coordinates via the nuclear potential. The Born-Oppenheimer approximation thus reduces the complexity of the problem significantly, as one is most often only interested in the electronic wave function, also assuming classical point-like nuclei. Later in this thesis, we will also introduce the more general Ehrenfest approach, being able to describe non-adiabatic electron-nuclei coupling in an averaged way, allowing for excited-state molecular dynamics.
We will conduct the following discussion only for the electronic degrees of freedom, i.e., the electronic wave function Ψ, the electronic Hamiltonian $\mathcal{H}$ and the electronic energy E, corresponding to the stationary electronic Schrödinger equation

$$\mathcal{H}\Psi = E\Psi. \tag{2.2}$$

If not stated otherwise, we do not take the electron's spin quantum number explicitly into account for upcoming discussions. The N-electron wave function is a quantity incorporating all

$$\{(\mathbf{r}_i)\} \equiv (\mathbf{r}_1, ..., \mathbf{r}_\mathrm{N}) \tag{2.3}$$

degrees of freedom, where $\mathbf{r}_i$ describes the position of an electron in a fixed coordinate space. Ψ is a vector in a Hilbert space and $\mathcal{H}$ is a Hermitian operator in this space, given by

$$\begin{aligned}\mathcal{H} &= \mathcal{T} + \mathcal{V} + \mathcal{W} \\ &= \sum_{i=1}^{\mathrm{N}} \hat{t}_i + \sum_{i=1}^{\mathrm{N}} \hat{v}(\mathbf{r}_i) + \frac{1}{2}\sum_{i\neq j}^{\mathrm{N}} \hat{w}(\mathbf{r}_i, \mathbf{r}_j)\end{aligned} \tag{2.4}$$

with the *kinetic energy* operator $\mathcal{T}$, the *potential energy* operator $\mathcal{V}$ and the *interaction energy* operator $\mathcal{W}$. We will use atomic units, $\hbar = m_e = e = 4\pi\epsilon_0 = 1$, for all upcoming discussions and for the rest of this thesis. The one-electron operator

$$\hat{t}_i = -\frac{1}{2}\nabla_i^2 \tag{2.5}$$

corresponds to the kinetic energy of an electron with index i and thus, the expectation value of $\mathcal{T}$ yields the kinetic energy of the whole electron system:

$$\begin{aligned}T &= \langle\Psi|\mathcal{T}|\Psi\rangle \\ &= \int ... \int d^3\mathbf{r}_1 ... d^3\mathbf{r}_\mathrm{N}\, \Psi^*(\mathbf{r}_1, ..., \mathbf{r}_\mathrm{N})\, \mathcal{T}\, \Psi(\mathbf{r}_1, ..., \mathbf{r}_\mathrm{N}).\end{aligned} \tag{2.6}$$

We here introduced the inner product of the Hilbert space by the bra-ket notation $\langle\cdot|\cdot\rangle$. Further, the one-electron operator $\hat{v}(\mathbf{r}_i)$ describes the potential energy of a single electron in an external potential, e.g., the nuclear Coulomb potential introduced

by the nuclei's protons

$$\hat{v}(\mathbf{r}_i) = -\sum_{I=1}^{\mathrm{M}} \frac{\mathrm{Z}_I}{|\mathbf{r}_i - \mathbf{R}_I|}, \tag{2.7}$$

(for M nuclei in the system, each with a given atomic number Z_I) or any other static interaction potential. The Coulomb repulsion between a pair of electrons is given by the two-electron interaction operator

$$\hat{w}(\mathbf{r}_i, \mathbf{r}_j) = \frac{1}{|\mathbf{r}_i - \mathbf{r}_j|}. \tag{2.8}$$

The temporal evolution is described by the time-dependent Schrödinger equation

$$i\frac{\partial}{\partial t}\Psi = \mathcal{H}\Psi \tag{2.9}$$

with essentially the same Hamiltonian operator as defined above, only incorporating the possible dependence of the external potential on time, i.e., $\hat{v}(\mathbf{r}) \rightarrow \hat{v}(\mathbf{r}, t)$, which could for example correspond to an oscillating electric field.
For the description of a stationary electron system, one has to solve Equation 2.1 for the ground state wave function Ψ, and for the description of a time-dependent electron system, one has to solve Equation 2.9 for the time-dependent wave function $\Psi(t)$, taking into account that the wave functions depend on the coordinates $\{(\mathbf{r}_i)\}$ of *all* electrons. Considering that even any single element with higher atomic number than helium imposes a $N > 2$ body problem, that molecules can consist of dozens to hundreds to thousands etc. of atoms and that a cm^3 of a bulk material has approximately 10^{28} particles, the analytical and numerical solutions of these equations for most systems are effectively impossible and will possibly be over the whole human existence [7].
This intimidating hindrance motivated scientists to think about approximate solutions making practical applications even possible. One of the earliest and most important approaches in this sense is the theory by Hartree and Fock [8, 9] which approximates the actual wave function by a single Slater determinant (a multi-electron wave function composed of single-electron wave functions, satisfying the Pauli principle, i.e., being antisymmetric by particle exchange) and describing electronic interaction in an averaged way. This theory builds the basis for methods that employ some form of a multi-electron wave function as central object. A different approach was taken by Thomas and Fermi [10, 11] who used the electron density as central object – while this approach is very limited, it can be seen as predecessor of modern density functional theory (DFT).

Given the electron density operator

$$\hat{\rho}(\mathbf{r}) = \sum_{i=1}^{\mathrm{N}} \delta(\mathbf{r} - \mathbf{r}_i), \tag{2.10}$$

the electron density at a given point in space $\mathbf{r}$ can be obtained by the expectation value of $\hat{\rho}$:

$$\begin{aligned}\rho(\mathbf{r}) &= \langle\Psi|\hat{\rho}(\mathbf{r})|\Psi\rangle \\ &= \mathrm{N}\int ... \int d^3\mathbf{r}_2 ... d^3\mathbf{r}_\mathrm{N}\, |\Psi(\mathbf{r}, ..., \mathbf{r}_\mathrm{N})|^2.\end{aligned} \tag{2.11}$$

This object depends only on 3 variables (the coordinates x, y, z) instead of 3N for the full electron wave function. The key idea of DFT is now to obtain physical observables, most prominently the total energy E, as functionals of the electron density alone, i.e.,

$$E \rightarrow E[\rho], \tag{2.12}$$

instead of explicitly using the electronic wave function.

2.1.2 Hohenberg-Kohn Theorem

While by mere assumption, there is no strict logic enabling the use of the electron density as key variable, luckily a proof enabling this strategy was found by Hohenberg and Kohn [12]. The first part of the argumentation is commonly referred to as the *existence theorem* and states that the electron density of a non-degenerate ground state *uniquely* corresponds to an external potential (modulo an arbitrary constant) acting on the electronic system. With this, the Hamiltonian and thus all electronic properties of the ground state are determined. The proof of this statement can easily be performed by reductio ad absurdum in the sense of disproving its complement. For this, we consider two inherently different (meaning that they differ not only by a constant) external potentials v_1 and v_2, corresponding to wave functions Ψ_1 and Ψ_2. We further assume that both wave functions correspond to the same ground state density $\rho_0(\mathbf{r})$. The energies corresponding to the two Hamiltonians $\mathcal{H}_1$ and $\mathcal{H}_2$ are – analogously to Eq. 2.4 – given as

$$\begin{aligned}E_n &= \langle\Psi_n|\mathcal{H}_n|\Psi_n\rangle = \langle\Psi_n|\mathcal{T}+\mathcal{V}+\mathcal{W}|\Psi_n\rangle \\ &= \langle\Psi_n|\int \mathrm{d}^3\mathbf{r}\,\hat{\rho}(\mathbf{r})v_n(\mathbf{r})\,|\Psi_n\rangle + \langle\Psi_n|\mathcal{T}+\mathcal{W}|\Psi_n\rangle \\ &= \int \mathrm{d}^3\mathbf{r}\,\rho_0(\mathbf{r})v_n(\mathbf{r}) + \langle\Psi_n|\mathcal{T}+\mathcal{W}|\Psi_n\rangle.\end{aligned} \tag{2.13}$$

At this point, we consider the Rayleigh-Ritz variational principle [13]

$$E = \langle\Psi|\mathcal{H}|\Psi\rangle < \langle\Psi'|\mathcal{H}|\Psi'\rangle\,,\ \ \Psi \neq \Psi', \tag{2.14}$$

where Ψ is a normalized eigenfunction of $\mathcal{H}$ and Ψ' is a normalized trial wave function. This lets one obtain the corresponding inequalities

$$\begin{aligned} E_1 < \langle \Psi_2 | \mathcal{H}_1 | \Psi_2 \rangle &= \int \mathrm{d}^3\mathbf{r}\, \rho_0(\mathbf{r}) v_1(\mathbf{r}) + \langle \Psi_2 | \mathcal{T} + \mathcal{W} | \Psi_2 \rangle \\ &= \int \mathrm{d}^3\mathbf{r}\, \rho_0(\mathbf{r}) \Big(v_1(\mathbf{r}) - v_2(\mathbf{r}) \Big) \\ &\quad + \int \mathrm{d}^3\mathbf{r}\, \rho_0(\mathbf{r}) v_2(\mathbf{r}) + \langle \Psi | \mathcal{T} + \mathcal{W} | \Psi \rangle \\ &= \int \mathrm{d}^3\mathbf{r}\, \rho_0(\mathbf{r}) \Big(v_1(\mathbf{r}) - v_2(\mathbf{r}) \Big) + E_2. \end{aligned} \tag{2.15}$$

Evaluating above expression with switched indices and adding both results leads to the contradiction

$$E_1 + E_2 < E_1 + E_2 \tag{2.16}$$

which implies that the assumption of two different external potentials v_1 and v_2 corresponding to the same ground state density $\rho_0(\mathbf{r})$ cannot be true, ultimately stating that there exists a one-to-one mapping $v(\mathbf{r}) \leftrightarrow \rho_0(\mathbf{r}) \leftrightarrow \Psi[\rho_0]$. This allows the definition of the total energy of a many-electron system under the influence of a static external potential as a unique functional of the ground state electron density:

$$\begin{aligned} E_0 = E[\rho_0] = \langle \Psi[\rho_0] | \mathcal{H} | \Psi[\rho_0] \rangle &= \int \mathrm{d}^3\mathbf{r}\, \rho_0(\mathbf{r}) v(\mathbf{r}) + \mathcal{F}[\rho_0], \\ \mathcal{F}[\rho_0] &= \langle \Psi[\rho_0] | \mathcal{T} + \mathcal{W} | \Psi[\rho_0] \rangle. \end{aligned} \tag{2.17}$$

A key insight from this equality is that the functional $\mathcal{F}[\rho_0]$ is independent of the external potential $v(\mathbf{r})$ and can be regarded as universal functional of the density $\rho_0(\mathbf{r})$, meaning that it applies to any system, provided its form is known.

The second part of the Hohenberg-Kohn theorem states that the energy functional $E[\rho_0]$ becomes minimal for the exact ground state electron density $\rho_0(\mathbf{r})$ of a system subject to a given external potential $v(\mathbf{r})$, i.e., meaning that one can systematically obtain the exact ground state energy E_0 and density ρ_0 by varying the electron density ρ and locating the minimum of the expression

$$E_0 = \min_{\rho(\mathbf{r})} \left\{ \int \mathrm{d}^3\mathbf{r}\, \rho(\mathbf{r}) v(\mathbf{r}) + \mathcal{F}[\rho] \right\}. \tag{2.18}$$

This can easily be seen by comparing to Eq. 2.15, i.e., by the variational principle: any trial density will always yield a lower energy when approaching the exact ground state density. The minimum for the total energy by means of the electron density corresponds to the Euler-Lagrange equation

$$0 = \frac{\delta}{\delta \rho(\mathbf{r})} \left\{ \int \mathrm{d}^3\mathbf{r}\, \rho(\mathbf{r}) v(\mathbf{r}) - \mu_\mathrm{N} \left(\mathrm{N} - \int \mathrm{d}^3\mathbf{r}\, \rho(\mathbf{r}) \right) + \mathcal{F}[\rho] \right\} \tag{2.19}$$

where μ_N is a Lagrange multiplier imposing the constraint that the overall density integral yields the total number of electrons N in the system. At this point, the mathematical framework on how to use the electron density instead of the total electronic wave function to describe the ground state has been defined and an abstract procedure on how to approach the actual minimum could set the basis for numerical simulations. It should be noted that several extensions of the Hohenberg-Kohn theorem exist, e.g., for degenerate ground states [14], open-shell systems [15] or magnetism [16]. However, the shape of the universal functional $\mathcal{F}[\rho]$ is at this point still unknown, which leads to the next chapter.

2.1.3 Kohn-Sham Approach

The problem of the unknown universal functional $\mathcal{F}[\rho]$ renders the Hohenberg-Kohn formalism mostly useless, but the solution proposed by Kohn and Sham [17] ultimately gave rise to the powerful DFT framework as it is known today. The key idea in their approach was to construct a fictitious system of non-interacting electrons that has exactly the same ground state electron density as the real system with interacting electrons, using the Hohenberg-Kohn theorem in the sense that both densities correspond to the same physical ground state. It is thus the first step to define the universal functional as

$$\begin{aligned}\mathcal{F}[\rho] &= \mathcal{T}[\rho] + \mathcal{W}[\rho] \\ &\equiv \mathcal{T}[\rho] + E_H[\rho] + E_{xc}[\rho]\end{aligned} \tag{2.20}$$

where $\mathcal{T}[\rho]$ is the electronic kinetic energy functional, $E_H[\rho]$ is the classical mean-field Hartree electron-electron interaction energy functional and $E_{xc}[\rho]$ is the so-called exchange-correlation (XC) energy functional which formally describes all non-classical electron-electron interactions. In principle, one now has a system of non-interacting electrons and the total wave function Ψ_s can be expressed as a single Slater determinant

$$\Psi_s = \frac{1}{\sqrt{N!}} \begin{vmatrix} \psi_1(\mathbf{r}_1) & \dots & \psi_N(\mathbf{r}_1) \\ \dots & \dots & \dots \\ \psi_1(\mathbf{r}_N) & \dots & \psi_N(\mathbf{r}_N) \end{vmatrix}. \tag{2.21}$$

The single-particle electronic wave functions $\{\psi_n\}$ are commonly referred to as Kohn-Sham (KS) orbitals and the corresponding density matrix and electron density read

$$\bar{\rho}_{nm}(\mathbf{r}) = \psi_n^*(\mathbf{r})\psi_m(\mathbf{r}), \tag{2.22}$$

$$\rho(\mathbf{r}) = \mathrm{tr}\{\bar{\rho}\} = \sum_{n=1}^{N_{occ}} f_n \psi_n^*(\mathbf{r})\psi_n(\mathbf{r}), \tag{2.23}$$

where N_{occ} is the number of occupied single-particle orbitals and $f_n \in [0,2]$ is the occupation number, providing the number of electrons in the respective orbitals. It must be noted here that the kinetic energy operator is in practice actually not given

as density functional, unlike defined for the general case in Eq. 2.20. The reason for this is that this general form is unknown, and therefore, the single-particle kinetic energy functional is a purely orbital-dependent function, intrinsically missing some part of the many-particle kinetic contributions. The single-particle kinetic energy and the Hartree energy in Eq. 2.20 are in terms of the KS orbitals given as

$$\mathcal{T}_s = \sum_{n=1}^{\mathrm{N_{occ}}} f_n \langle \psi_n | \hat{t}_\mathrm{s} | \psi_n \rangle = -\frac{1}{2} \sum_{n=1}^{\mathrm{N_{occ}}} f_n \langle \psi_n | \nabla^2 | \psi_n \rangle \tag{2.24}$$

$$E_\mathrm{H}[\rho] = \sum_{n=1}^{\mathrm{N_{occ}}} f_n \langle \psi_n | \hat{v}_\mathrm{H}[\rho](\mathbf{r}) | \psi_n \rangle = \frac{1}{2} \sum_{n=1}^{\mathrm{N_{occ}}} f_n \langle \psi_n | \int \mathrm{d}^3\mathbf{r}' \, \frac{\rho(\mathbf{r}')}{|\mathbf{r}_n - \mathbf{r}'|} \, | \psi_n \rangle \tag{2.25}$$

where we introduced the single-particle kinetic energy operator $\hat{t}_\mathrm{s}$ and the Coulomb operator $\hat{v}_\mathrm{H}[\rho](\mathbf{r})$. The remaining many-particle energy contributions are formally incorporated in the exchange-correlation energy functional as

$$E_\mathrm{xc}[\rho] = \mathcal{F}[\rho] - \mathcal{T}_\mathrm{s} - E_\mathrm{H}[\rho]. \tag{2.26}$$

The functional derivative of this functional yields the exchange-correlation potential

$$v_\mathrm{xc}[\rho](\mathbf{r}) = \frac{\delta E_\mathrm{xc}[\rho]}{\delta \rho(\mathbf{r})}, \tag{2.27}$$

analogously the Hartree potential is explicitly given via

$$v_\mathrm{H}[\rho](\mathbf{r}) = \frac{\delta E_\mathrm{H}[\rho]}{\delta \rho(\mathbf{r})} = \int \mathrm{d}^3\mathbf{r}' \, \frac{\rho(\mathbf{r}')}{|\mathbf{r} - \mathbf{r}'|}. \tag{2.28}$$

With this, we can define the single-particle electronic Kohn-Sham Hamiltonian

$$\mathcal{H}_\mathrm{KS} = \hat{t}_\mathrm{s} + \hat{v}_\mathrm{H}[\rho](\mathbf{r}) + v_\mathrm{ext}(\mathbf{r}) + v_\mathrm{xc}[\rho](\mathbf{r}). \tag{2.29}$$

for some external potential $v_\mathrm{ext}(\mathbf{r})$. The following eigenvalue equation is denoted as the *Kohn-Sham equation*:

$$\mathcal{H}_\mathrm{KS} \psi_n(\mathbf{r}) = \epsilon_n \psi_n(\mathbf{r}). \tag{2.30}$$

Its solutions, the single-particle electronic orbitals $\{\psi_n\}$, have to be determined self-consistently due to the dependence of the Hamiltonian on the electronic density, itself being determined by the KS orbitals. The eigenvalues $\{\epsilon_n\}$ have the dimension of energy but no direct physical meaning due to the underlying single-particle approximation. However, it could be shown [18, 19] that the eigenvalue of the highest occupied orbital, ϵ_HO, is equal to the negative first ionization energy IP of an interacting N-electron system:

$$\epsilon_\mathrm{HO}(\mathrm{N}) = -\mathrm{IP}(\mathrm{N}) = -\Big(E_0(\mathrm{N}-1) - E_0(\mathrm{N}) \Big). \tag{2.31}$$

In addition, the highest occupied orbital eigenvalue of an N+1 electron system is equal to the negative electron affinity EA of the interacting N-electron system,

$$\epsilon_{\mathrm{HO}}(\mathrm{N}+1) = -\mathrm{EA}(\mathrm{N}) = -\Big(E_0(\mathrm{N}) - E_0(\mathrm{N}+1)\Big), \tag{2.32}$$

provided the exchange-correlation functional is exact (i.e., making above quantities dependent onto the quality of the approximate XC description). However, many situations are found where the single-particle eigenvalues give reasonable approximations to the true electron energy levels, which is for example often employed in band structure calculations in periodic solids [18]. Concluding, the major approximations of DFT are incorporated via the exchange-correlation functional and the quality of simulated results depends heavily on the chosen approximation.
Finally, we note that the total energy can be expressed as

$$E[\rho] = \sum_{n=1}^{\mathrm{N_{occ}}} f_n \epsilon_n - E_{\mathrm{H}}[\rho] - \int \mathrm{d}^3\mathbf{r}\, \rho(\mathbf{r}) v_{\mathrm{xc}}(\mathbf{r}) + E_{\mathrm{xc}}[\rho]. \tag{2.33}$$

In this sense, the total energy is built from the sum of single-particle orbital energies plus some many-particle corrections.

2.1.4 Exchange-Correlation Functionals

As already mentioned, the whole Kohn-Sham formalism shifts any electronic properties above the single-particle approximation into the exchange-correlation functional, making it a quantity of fundamental importance. Unfortunately, the exact form of the XC functional is not known and may never be. Thus, one has to employ intelligent approximations, and huge effort was – and still is – made to find best possible models. These are often adapted to certain physical situations, being a result of the insight that different established XC approximations may have specific regimes where they perform better or worse.
One can define a hierarchical order for XC functionals, beginning from the so-called local density approximation (LDA) [20] and going towards more complexity by considering density derivatives, exact exchange and so on (i.e., going from low to high complexity). Figure 2.1 depicts this scheme which is also commonly referred to as 'Jacob's Ladder' [21, 22]. Historically and conceptually, the first approximation for the exchange-correlation energy was given by

$$E_{\mathrm{xc}}[\rho] = \int \mathrm{d}^3\mathbf{r}\, \epsilon_{\mathrm{xc}}[\rho](\mathbf{r})\, \rho(\mathbf{r}), \tag{2.34}$$

where ϵ_{xc} is the exchange-correlation energy density functional, being a function of the coordinate $\mathbf{r}$, i.e., depending locally on the position. The simplification of neglection of this explicit dependence on $\mathbf{r}$ yields the class of local density approximation

Empirical type	Level of theory	Non-empirical type
	Exact exchange & partially exact correlation	
B3LYP, X3LYP, ...	Hybrid- & hybrid-meta-GGA	PBE0
MPWB95, ...	Meta-GGA	TPSS
BLYP, BP86	GGA	PBE, PB91, ...
	LDA	PW-LDA, PZ-LDA, ...

FIGURE 2.1: Hierarchical scheme of exchange-correlation functionals, also known als 'Jacob's Ladder' [21, 22].

(LDA) functionals of the general form

$$E_{\mathrm{xc}}^{\mathrm{LDA}}[\rho] = \int \mathrm{d}^3\mathbf{r}\, \epsilon_{\mathrm{xc}}^{\mathrm{hom}}[\rho]\, \rho(\mathbf{r}). \tag{2.35}$$

Here, $\epsilon_{\mathrm{xc}}^{\mathrm{hom}}$ is the XC energy density of a homogeneous interacting electron gas with density $\rho(\mathbf{r})$. For this system, the analytical form of the exchange energy is known exactly,

$$E_{\mathrm{x}}^{\mathrm{LDA}}[\rho] = -\frac{3}{4}\left(\frac{3}{\pi}\right)^{\frac{1}{3}} \int \mathrm{d}^3\mathbf{r}\, \rho^{\frac{4}{3}}(\mathbf{r}), \tag{2.36}$$

indicating that the XC energy can be decomposed into the exchange and correlation parts separately as $E_{\mathrm{xc}}^{\mathrm{LDA}}[\rho] = E_{\mathrm{x}}^{\mathrm{LDA}}[\rho] + E_{\mathrm{c}}^{\mathrm{LDA}}[\rho]$. The correlation term for the LDA is a more complicated object and is usually obtained by numerical techniques, e.g., Monte Carlo. These different forms of the correlation term define specific LDA functionals, often named after their authors, e.g., PZ-LDA (Perdew-Zunger) [20], PW-LDA (Perdew-Wang) [23] and so on. LDA functionals often show good results for situations where the electron density is more or less homogeneous, as in metals, but less good in molecules. However, this depends on the situation and generally, LDA functionals can also perform satisfactory in inhomogeneous systems [24].

The next level of theoretical sophistication is reached by inclusion of the density's gradient in the XC energy functional, defining the generalized gradient approximation (GGA) class of functionals of the form

$$E_{\mathrm{xc}}^{\mathrm{GGA}}[\rho] = \int \mathrm{d}^3\mathbf{r}\, \epsilon_{\mathrm{xc}}[\rho, \nabla\rho]\, \rho(\mathbf{r}). \tag{2.37}$$

The first obvious advantage of this approach is that spatial rates of change of the possibly rapidly varying electron density are included explicitly in the XC energy density – this fact is the reason why this class of functionals are sometimes called

semi-local [25]. GGA functionals often yield better results for ground state energies and geometries than LDA functionals and are clearly superior in the description of covalent bonds or weakly-bonded systems. Generally, a density gradient based factor is defined which affects the exchange and correlation energies. Based on this, the different GGA functionals are named after their respective authors, e.g., PBE (Perdew-Burke-Ernzernhof) [26], PW91 (Perdew-Wang) [27] or LYP (Lee-Yang-Parr) [28]. The class of so-called meta-GGA functionals like TPSS (Tao-Perdew-Staroverov-Scuseria) [29] additionally employs the Laplacian of the density and/or the kinetic density and were shown to improve GGA performance.

A major problem of (semi-) local functionals is the so-called *self-interaction error* [30] which describes spurious interactions of electrons with themselves, as incorporated in the Hartree potential. This can lead to problems in the description of charge-transfer states and processes, as single electrons may be artificially repelled by their own charge density [30, 31].
This leads us to another class of XC functionals, namely the hybrid functionals which are constructed by using the exact exchange energy as occurring in the Hartree-Fock method [22, 32]:

$$E_{\mathrm{x}}^{\mathrm{HF}} = -\frac{1}{2}\sum_{mn}^{\mathrm{N}} f_n f_m \int\int \mathrm{d}^3\mathbf{r}_1 \mathrm{d}^3\mathbf{r}_2\, \psi_m^*(\mathbf{r}_1)\psi_n^*(\mathbf{r}_2)\frac{1}{|\mathbf{r}_1-\mathbf{r}_2|}\psi_n(\mathbf{r}_1)\psi_m(\mathbf{r}_2) \tag{2.38}$$

(where ψ_n are the KS orbitals). The expression for the non-local HF exchange can be used to reduce the effects of the self-interaction problem. This is in practice handled by the construction of functionals that mix exact HF exchange with other contributions for the electron exchange and correlation. Different functionals in this class are constructed from linear combinations of LDA and/or GGA functionals in combination with HF exchange, introducing a specific set of weight parameters. The probably most widely used hybrid functional is the B3LYP [33] functional using three parameters $\{a_1, a_2, a_3\}$ which are obtained by fitting to experimental data:

$$E_{\mathrm{xc}}^{\mathrm{B3LYP}} = E_{\mathrm{x}}^{\mathrm{LDA}} + a_1(E_{\mathrm{x}}^{\mathrm{HF}} - E_{\mathrm{x}}^{\mathrm{LDA}}) + a_2(E_{\mathrm{x}}^{\mathrm{GGA}} - E_{\mathrm{x}}^{\mathrm{LDA}}) + a_3(E_{\mathrm{c}}^{\mathrm{GGA}} - E_{\mathrm{c}}^{\mathrm{LDA}}). \tag{2.39}$$

Another popular hybrid functional is the GGA-based PBE0 [34] functional which has 25% HF exchange without empirical mixing parameters. The hybrid functionals are known to perform better particularly for molecular systems, especially with aromatic character [22].

2.1.5 Basis Sets

Many density functional theory or wave function-based approaches (like Hartree-Fock as the most simple example) represent the electronic wave functions by a linear combination of basis functions, enabling the numerical treatment of algebraic equations instead of partial differential equations. A different approach is, e.g., to

employ real-space grids using finite-element, finite-difference or wavelet methods. We do not further discuss these strategies here and refer to the literature, e.g., Refs. [35, 36, 37]

We will restrict the further discussion to the DFT case and denote *molecular orbitals* as solutions of the Kohn-Sham equation. Mathematically, a molecular orbital $\psi_n(\mathbf{r})$ is thus a linear combination of a given set of N_b smooth, continuous and sufficiently differentiable basis functions $\phi_i(\mathbf{r})$:

$$\psi_n(\mathbf{r}) = \sum_{i=1}^{N_b} c_{in}\, \phi_i(\mathbf{r}). \tag{2.40}$$

An exact representation of $\psi_n(\mathbf{r})$ would be achieved for a given basis set when $N_b \to \infty$, commonly denoted as *complete basis set limit*. For any actual computer simulation, a finite basis set is employed, with N_b ranging over several magnitudes of order, depending on the basis ansatz. We will provide a short discussion about this rather technical topic, as it plays an important role in several discussions over this thesis.

One can generally find three classes of basis function types: localized, extended and mixed functions. In principle one can choose any of those for a given problem, but it makes sense to choose a basis set according to the physical situation.

- **Localized basis functions:** one of the earliest approaches for radially exponentially decaying analytic atomic basis functions goes back to Slater (Slater-type orbitals / STOs) [38]. However, these sets are nowadays barely used due to undesired properties for multi-center integrals (which cannot be expressed analytically for certain orders, imposing high numerical overhead) [18].
  The most used localized basis sets nowadays are probably the Gaussian-type orbital (GTO) based sets of the form

  $$\phi_i(\mathbf{r}) = N f_k(x) g_l(y) h_m(z) e^{-\alpha_i(\mathbf{r}-\mathbf{R}_i)^2} \tag{2.41}$$

  with some scalar functions f_l, g_l, h_m possibly defining angular momentum, α_i controlling the radial extent, N as normalization constant and $\mathbf{R}_i$ being the corresponding atomic center of the basis function. The most important advantage of such basis sets is the fact that the corresponding real-space integrations can be carried out via analytical expressions and that they are very flexible. There exist numerous variants of GTO basis sets [39], with several being constructed to optimally capture specific phenomena like electronic correlation (e.g., the cc-pVXZ basis sets by Dunning et al. [40]). A disadvantage is that Gaussians are not really physical in the sense that they do not correspond to solutions of the (atomic) Schrödinger equation, imposing a higher number of basis functions needed to accurately describe physical phenomena, in turn raising the computational demand.
  Numerical atomic orbitals (NAOs) [41] denote orbitals that are not analytically

defined like STOs or GTOs, but are numerically tabulated solutions of a free-atom or -ion Schrödinger-like equation (SE). As these functions have a direct physical meaning, the sizes of these basis sets are rather small, as less basis functions are needed (as, e.g., compared to GTOs). More advantages are given by their intrinsic property of describing core wave functions nearly exact [42] and that they can be systematically localized by applying constraining potentials in their calculation, yielding the famous order-N scaling for large systems [42, 43]. Also, more complete basis sets can be systematically generated by calculating ionic or less constrained solutions of the SE. Drawbacks are the more complicated real-space integration techniques, as no analytical expressions are available and inhomogeneous integration grids may be needed in the all-electron case (due to highly oscillatory core basis functions). However, NAO methods belong to the most accurate and efficient methods especially for molecular systems, rewarding the additional technical effort [42, 43, 44].
A drawback of all non-orthogonal basis functions like NAOs or GTOs is that they introduce non-vanishing overlap matrix elements between each other. This corresponds to the possibility of a so-called basis set superposition error (BSSE) which may need additional corrective measures [45]. In general, NAO basis sets are much less prone to BSSE than GTO sets [42].
Due to the atom-centered localization, additional force and stress terms have to be considered, making the framework somewhat more complex [42, 46, 47].

- **Extended basis functions:** in this case, the electron orbitals are expanded in analogy to a Fourier series, defining the basis functions as the plane-wave Fourier basis

$$\phi_{\mathbf{kG}}(\mathbf{r}) = e^{i(\mathbf{k}+\mathbf{G})\cdot\mathbf{r}}. \tag{2.42}$$

The number of basis functions is controlled by the wave vector grid $\{\mathbf{G}\}$ which can be systematically increased. Since periodicity is intrinsic in this case, a periodic unit cell is always required to host the physical system. For solids, this is the natural choice, making plane-wave basis sets very suited for such systems. Other advantages are the intrinsic orthonormality and the comparably simple evaluation of forces and stresses. Disadvantages are that core states need prohibitively many plane waves in order to describe the highly oscillatory shape, imposing the need of so-called pseudopotentials which *artificially* describe core states in order to reduce the plane-wave basis size [43, 48]. As many basis functions (in the order of ten-thousands to millions) may be needed, high memory demand must be handled. When simulating unit cells with vacuum (i.e., molecules or slabs), the plane wave basis also fills the empty space, yielding unnecessary computational demand (but on the other hand being flexible to describe excited states). Also, the use of hybrid functionals imposes very high numerical demand due to the form of the exchange operator [49].

- **Mixed basis sets:** these basis sets are based on the so-called muffin-tin approximation by Slater [50]. The core idea is here to construct two differently treated types of volume in a crystal: spherical volumes around individual atoms and the remaining space, called interstitial space. The latter is filled with plane wave basis functions which only see a constant potential. Inside the spheres, a radially symmetric potential is assumed and here, basis functions that are products of spherical harmonics and radial solutions of a radial Schrödinger equation are used. The total wave function is thus constructed by the two different basis sets, matching each other in value at the sphere boundaries. This is known as the augmented plane wave (APW) method. However, this approach has the disadvantage that the basis functions inside the spheres depend on the solution of the electronic energy. Modern approaches like the linearized APW (LAPW) approach [51] circumvent this problem by modified boundary conditions.
  Especially noteworthy is another extension of this approach (actually a generalization), given by the projector-augmented wave (PAW) method: it combines the idea of pseudopotential treatment originating in the plane-wave approach with the APW approach in the sense that auxiliary interstitial wave functions are constructed that are numerically favorable, i.e., spatially smooth, but incorporate the presence of core orbitals (which are usually given as frozen-core states within the augmentation spheres) [52, 53]. Both LAPW, PAW basis sets and modifications thereof have been proven as very accurate [54]. Similar to standard plane wave approaches, the mixed basis set methods are more natural to periodic systems and are computationally less efficient in isolated systems.

2.1.6 Self-Consistent Field Solution

As mentioned before, the core task in ground state DFT is the solution of the Kohn-Sham equation, yielding the single-particle KS orbitals $\{\psi_n\}$. However, since the KS Hamiltonian is a functional of the density, which itself is constructed from the KS orbitals, the solution of the KS equation depends on itself:

$$\mathcal{H}_{\mathrm{KS}}[\rho] \leftrightarrow \rho(\mathbf{r}) \leftrightarrow \psi_n(\mathbf{r}). \tag{2.43}$$

A solution to this problem is found in the so-called *self-consistent field* method. This is an iterative procedure, beginning with some trial input, that seeks to find a converged solution of the problem, as – but not only – measured by the change in the total energy. An illustration is provided in Fig. 2.2. Converging the SCF iteration is often a heavily optimized task in DFT frameworks, as this procedure can in principle require much computation time. Usually, one employs *mixing* methods like, e.g., the popular scheme by Pulay [55], which perform some kind of 'smart' mixing between

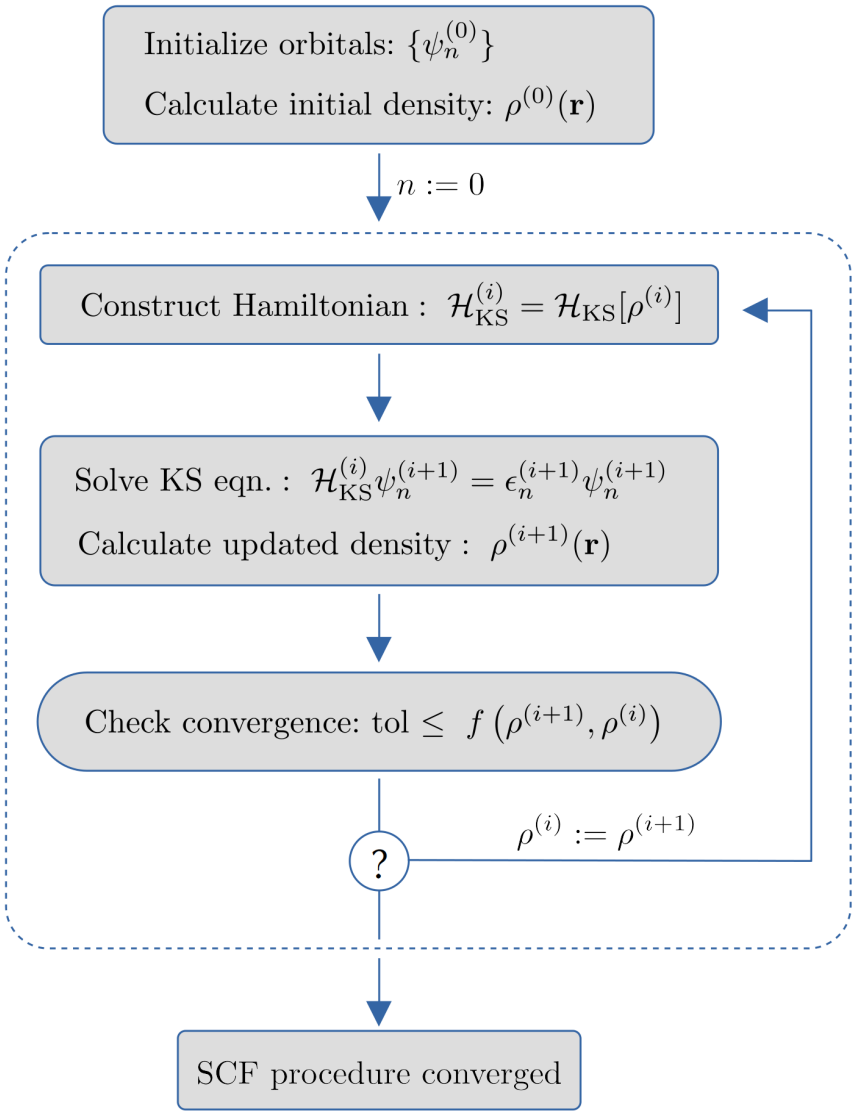

FIGURE 2.2: Illustration for the self-consistent field procedure for the solution of the Kohn-Sham equation. We denote f as some function serving as a convergence metric - this could for example be the difference in total energies computed from the last and current density.

densities of previous steps in order to obtain a good guess for the next SCF step. Formally, such methods belong to the class of fixed-point solving algorithms like, e.g., the Newton-Raphson method. Often, converging the SCF solution is not a problem, with many systems being converged in $\mathcal{O}(10)$ iterations. Anyway, exceptions exist which are possibly much more difficult to converge.

2.1.7 Forces, Geometry Relaxation and Molecular Dynamics

Given the total energy of the electronic and ionic system,

$$E_{\mathrm{tot}} = E[\rho] + \frac{1}{2}\sum_{I\neq J}^{\mathrm{N_{at}}} \frac{Z_I Z_J}{|\mathbf{R}_I - \mathbf{R}_J|}, \tag{2.44}$$

with the first term being the Kohn-Sham electronic energy as defined in Eq. 2.33 and the second term being the Coulomb repulsion of the N_{at} nuclei with atomic numbers Z_I, one can obtain nuclear forces via

$$\mathbf{F}_I = -\nabla_{\mathbf{R}_I} E_{\text{tot}}. \tag{2.45}$$

Thus, the nuclei are subject to a potential based on the Kohn-Sham energy functional plus the interatomic Coulomb repulsion. Note that this expression does therefore also depend on the choice of the given exchange-correlation functional, imposing the need to derive the corresponding force terms of these potentials.
The nuclear forces can be used to explore the ground state potential energy surface which the nuclei are subject to, most importantly to find the structure which corresponds to minimal total energy, i.e., the equilibrium structure. This is one of the core tasks of typical density functional theory applications.
In practice, one starts at a given geometry $\{\mathbf{R}_I\}$ (in the most optimal case being close to the final structure), calculates a converged SCF solution, the associated forces, and updates the structure, and so on until the optimization converges by some metric (residual forces for example). For example, the popular BFGS algorithm [56] seeks to converge the sequence

$$\mathbf{R}_I^{(n+1)} = \mathbf{R}_I^{(n)} + \Delta^{(n)} \mathbf{S}_I^{(n)} \tag{2.46}$$

where $\Delta^{(n)}$ is a step size and $\mathbf{S}_I^{(n)}$ is the search direction, and both expressions are evaluated via the forces and the Hessian of the total energy.
Another important application are so-called Born-Oppenheimer molecular dynamics [57, 58]. Here, the forces are used to integrate the classical Newtonian equations of motion

$$M_I \ddot{\mathbf{R}}_I(t) = \mathbf{F}_I(t) \tag{2.47}$$

in order to dynamically simulate molecular motion, given a thermodynamic ensemble (e.g., NVT for constant temperature or NVE for constant energy). A typical algorithm for this is the velocity Verlet algorithm [58] given by

$$\mathbf{R}_I(t + \Delta t) = \mathbf{R}_I(t) + \mathbf{V}_I(t)\Delta t + \frac{1}{2}\mathbf{F}_I(t)\Delta t^2, \tag{2.48}$$

$$\mathbf{V}_I(t + \Delta t) = \mathbf{V}_I(t) + \frac{1}{2}\Big(\mathbf{F}_I(t) + \mathbf{F}_I(t + \Delta t)\Big)\Delta t. \tag{2.49}$$

As the corresponding potential is still always dictated by the respective electronic ground state, no non-adiabatic excited-state trajectories can be obtained. This and related methods have been very successfully employed especially in the study of large and chemically rather complex systems [57].

2.2 Real-Time Time-Dependent Density Functional Theory

Having established the basis of ground state DFT, we now consider the case of explicitly time-dependent potentials. We start with the time-dependent Schrödinger equation and successively introduce the formalism of time-dependent density functional theory.

2.2.1 Introduction

We consider the time-dependent electronic Schrödinger equation, given as

$$i\frac{\partial}{\partial t}\Psi(t) = \mathcal{H}(t)\Psi(t) \tag{2.50}$$

with an explicitly time-dependent Hamiltonian operator, defined by

$$\mathcal{H}(t) = \mathcal{T} + \mathcal{V}(t) + \mathcal{W}. \tag{2.51}$$

Equation 2.50 represents an initial-value problem, i.e., the solution also depends on the initial state $\Psi(t_0)$ which is not necessarily the ground state [59]. The kinetic energy operator $\mathcal{T}$ and the interaction energy operator $\mathcal{W}$ are independent of time and remain as given before. The time-dependence of the electrons is imposed by the time-dependent potential energy operator

$$\mathcal{V}(t) = \sum_{i=1}^{N} \hat{v}(\mathbf{r}_i, t), \tag{2.52}$$

which could for example incorporate an electromagnetic field and/or a dynamical ionic potential. Based on the success of ground state Kohn-Sham density functional theory, its extension to the time-dependent case was a logical step. As for the case of KS-DFT, the application of density-functionalization has to be rigorously proven to work for the dynamical case, too.

2.2.2 The Runge-Gross Theorem

The analogue of the Hohenberg-Kohn theorem for the time-dependent case is the proof found by Runge and Gross in 1984 [60]. This proof could not be built on the variational principle as in static DFT and needs to consider the time-dependent Schrödinger equation being an initial-value problem; it is thus less simple. Here, the central result is that two time-dependent scalar potentials $v_1(\mathbf{r}, t)$ and $v_2(\mathbf{r}, t)$ differing by not just a time-dependent function, acting on the same initial state $\Psi(t = t_0) \equiv \Psi_0$, will always yield two different time-dependent densities $\rho_1(\mathbf{r}, t)$ and $\rho_2(\mathbf{r}, t)$.
Key quantities for the proof's discussion are the time-dependent electron density

$$\rho(\mathbf{r}, t) = \langle \Psi(t) | \hat{\rho}(\mathbf{r}) | \Psi(t) \rangle, \tag{2.53}$$

and the time-dependent electronic current density

$$\mathbf{j}(\mathbf{r},t) = \langle \Psi(t)|\hat{\mathbf{j}}(\mathbf{r},t)|\Psi(t)\rangle, \tag{2.54}$$

$$\hat{\mathbf{j}}(\mathbf{r},t) = -\frac{i}{2}\sum_{i=1}^{N}\Big(\nabla_i\delta(\mathbf{r}-\mathbf{r}_i) + \delta(\mathbf{r}-\mathbf{r}_i)\nabla_i\Big), \tag{2.55}$$

where $\hat{\rho}(\mathbf{r})$ is the electron density operator as given before and $\Psi(t)$ is the time-dependent Kohn-Sham wave function. Both quantities are related to each other by the continuity equation

$$i\frac{\partial}{\partial t}\rho(\mathbf{r},t) = -\nabla\cdot\mathbf{j}(\mathbf{r},t). \tag{2.56}$$

Since the whole proof is rather complicated, we here focus on the essential outline, following the argumentation by Ullrich [59]:

1. An initial restriction is that only potentials $v(\mathbf{r},t)$ that can be expanded in a Taylor series around t_0 are considered.

2. For such potentials, it is proven that different potentials will always result in different current densities when evolving in time.

3. Due to the continuity equation, different current densities are intrinsically connected to different charge densities, too.

4. Closing the argumentation circle, it is proven that a unique 1:1 correspondence between current density and potential is established for an initial condition Ψ_0 for the time-dependent case, i.e.,

$$v(\mathbf{r},t) \quad\leftrightarrow\quad \rho(\mathbf{r},t). \tag{2.57}$$

Ultimately, this allows one to establish the potential as functional of the electron density, as in ground state DFT:

$$v(\mathbf{r},t) = v[\rho,\Psi_0](\mathbf{r},t), \tag{2.58}$$

incorporating the dependence onto the initial state.

2.2.3 The Time-Dependent Kohn-Sham Equation

Having established the foundation of extending the DFT approach to the dynamical case via the Runge-Gross theorem, the time-dependent Kohn-Sham equation is defined as

$$i\frac{\partial}{\partial t}\psi_n(\mathbf{r},t) = \mathcal{H}_{\mathrm{KS}}(t)\psi_n(\mathbf{r},t), \tag{2.59}$$

$$\mathcal{H}_{\mathrm{KS}}(t) = \hat{t}_s + v_{\mathrm{H}}[\rho](\mathbf{r},t) + v_{\mathrm{ext}}(\mathbf{r},t) + v_{\mathrm{xc}}\left[\rho,\Psi_0^{(\mathrm{I})},\Psi_0^{(\mathrm{KS})}\right](\mathbf{r},t), \tag{2.60}$$

where the single-particle kinetic energy operator is the same as before. The Hartree potential is of same form, but evaluated for the time-dependent density $\rho(\mathbf{r}, t)$, i.e.,

$$v_{\mathrm{H}}[\rho](\mathbf{r}, t) = \int \mathrm{d}^3\mathbf{r}' \frac{\rho(\mathbf{r}', t)}{|\mathbf{r} - \mathbf{r}'|}. \tag{2.61}$$

The external potential $v_{\mathrm{ext}}(\mathbf{r}, t)$ is explicitly time-dependent and needs to be specified. An intrinsic problem of this most general definition is the dependence of the exchange-correlation potential on not only the density $\rho(\mathbf{r}, t)$, but also on the initial many-body wave function of the exact interacting system, $\Psi_0^{(\mathrm{I})}$, and on the initial non-interacting Kohn-Sham wave function $\Psi_0^{(\mathrm{KS})}$ [59]. While this implication is potentially problematic, it is usually not important in practice where simulations evolve from a given ground state. In this case, due to the one-to-one correspondence from the Hohenberg-Kohn theorem, the initial wave functions are functionals of the initial ground state density, meaning that the XC potential can be defined as a pure density functional:

$$\Psi_0^{(\mathrm{I})} \leftrightarrow \rho(\mathbf{r}, t = t_0) \leftrightarrow \Psi_0^{(\mathrm{KS})} : \; v_{\mathrm{xc}}\left[\rho, \Psi_0^{(\mathrm{I})}, \Psi_0^{(\mathrm{KS})}\right](\mathbf{r}, t) \;\leftrightarrow\; v_{\mathrm{xc}}[\rho](\mathbf{r}, t). \tag{2.62}$$

Another intricacy stems from the XC potential with its complicated dependence on the density, being non-local both in space and time:

$$v_{\mathrm{xc}}[\rho](\mathbf{r}, t) \;\leftrightarrow\; \rho(\mathbf{r}', t') \;\; \forall t' \leq t \,, \;\; \forall \mathbf{r}' \neq \mathbf{r} \in V. \tag{2.63}$$

This means that the density for all other points in space and all former times is formally incorporated in the XC functional. The dependence on the density's history is commonly referred to as the memory dependency of the time-dependent XC functional and in principle vastly complicates the theory. While there have been works trying to consider the memory dependence [59, 61], the practical approach is to employ the so-called *adiabatic approximation*

$$v_{\mathrm{xc}}^{\mathrm{ad}}[\rho](\mathbf{r}, t) \;\leftrightarrow\; \rho(\mathbf{r}', t) \;\; \forall \mathbf{r}' \neq \mathbf{r} \in V, \tag{2.64}$$

i.e., only the instantaneous density $\rho(\mathbf{r}, t)$ is evaluated in the XC functional, completely omitting its memory dependence. While the breakdown of the adiabatic approximation is commonly expected for situations with highly varying temporal behaviour, several studies could show that it often still works quite well [59]. The vast majority of real-time TDDFT studies does in fact employ the adiabatic approximation, nevertheless one should keep in mind that its use can be problematic for certain systems.

For completeness, we note that there are some subtle, but intrinsic problems remaining in the formal basis established by the Runge-Gross theorem. Ullrich et al. [59, 62] gave are more in-detail discussion and we will only shortly cover most of these

aspects. The first aspect is about the v-representability problem: in ground state DFT, the usual logic is to obtain the ground state density $\rho_0(\mathbf{r})$, given a potential $v(\mathbf{r})$. Considering the other way around, i.e., obtaining a potential $v(\mathbf{r})$ from a given ground state density $\rho_0(\mathbf{r})$, imposes the question whether this is generally possible, i.e., if this potential always exists (the Hohenberg-Kohn theorem only states that there exists a 1:1 correspondence *if* it exists). If not, one could have problems to define functional derivatives at all [59]. The question of v-representability transfers to TDDFT and is in the most general sense unanswered. However, van Leeuwen [63] found a partial proof showing that v-representability is given in the time-dependent Kohn-Sham approach for functionals that can be Taylor-expanded around t_0 (denoted as TE0).
The second aspect is linked to the first since the requirement TE0 also applies for the time-dependent densities. Thus, the van Leeuwen theorem fails for densities that are non-TE0 - such densities naturally appear near the nucleus due to the Coulomb singularity.
These points are in practice often ignored but remain important to establish the formal basis of TDDFT. More details about above-mentioned problems can be found in Refs. [62, 64]. Another formally delicate point of TDDFT was not discussed here: the presence of external electromagnetic fields. Since this situation is intrinsic within our work, we provide some more details in the next chapter.

2.2.4 Coupling to External Optical Fields and Periodic Boundary Conditions

As the Runge-Gross theorem is only valid for time-dependent scalar potentials, introducing the interaction of a Kohn-Sham system with electromagnetic radiation is non-trivial, but fortunately there exists a proof, commonly denoted as the Ghosh-Dhara theorem [65], which allows one to do so. This theorem is in principle an extension of the Runge-Gross theorem for the case of electromagnetic coupling and the resulting theory is commonly denoted as time-dependent *current* DFT (TDCDFT). It is thus a more general form of TDDFT that not only incorporates the time-dependent electron density $\rho(\mathbf{r},t)$ as key quantity, but also the time-dependent electronic current density $\mathbf{j}(\mathbf{r},t)$, as we will illustrate in the following. Ghosh and Dhara could show that $\rho(\mathbf{r},t)$ and $\mathbf{j}(\mathbf{r},t)$ uniquely determine the time-dependent scalar and vector potentials $v(\mathbf{r},t)$ and $\mathbf{A}(\mathbf{r},t)$, respectively, and that there exists a universal exchange-correlation functional $E_{\mathrm{xc}}[\rho,\mathbf{j}]$ that does not depend on the external potentials. The exact single-particle current and charge densities are determined by time-dependent Kohn-Sham equations of the form

$$i\frac{\partial}{\partial t}\psi_n(\mathbf{r},t) = \left(\frac{1}{2}\Big(-i\nabla + \mathbf{A}(\mathbf{r},t)\Big)^2 + v(\mathbf{r},t)\right)\psi_n(\mathbf{r},t). \tag{2.65}$$

In the Coulomb gauge $\nabla \cdot \mathbf{A} = 0$, the potentials are given by

$$\mathbf{A}(\mathbf{r},t) = \mathbf{A}_{\text{ext}}(\mathbf{r},t) + \int \mathrm{d}^3\mathbf{r}' \frac{\mathbf{j}(\mathbf{r}',t)}{|\mathbf{r}-\mathbf{r}'|} + \frac{\delta E_{\text{xc}}[\rho,\mathbf{j}](t)}{\delta \mathbf{j}(\mathbf{r},t)}, \tag{2.66}$$

and

$$v(\mathbf{r},t) = v_{\text{ext}}(\mathbf{r},t) + v_{\text{H}}[\rho](\mathbf{r},t) + \frac{\delta E_{\text{xc}}[\rho,\mathbf{j}](t)}{\delta \rho(\mathbf{r},t)}. \tag{2.67}$$

This formalism poses the major difficulty of having to find a reasonable approximation to $E_{\text{xc}}[\rho,\mathbf{j}](t)$, as the exact form is unknown [66]. The approach we employ in this work, which is also common practice in the vast majority of real-time TDDFT applications, is again denoted as the *adiabatic approximation*. In this case, the functional dependence on the current density is completely neglected and the XC functional used is the ground state functional, evaluated for the instantaneous electron density:

$$E_{\text{xc}}[\rho,\mathbf{j}](t) \to E_{\text{xc}}[\rho]\Big|_{\rho=\rho(\mathbf{r},t)} := E_{\text{xc}}^{\text{ad}}[\rho](t). \tag{2.68}$$

By doing so, the effective potentials reduce to

$$\mathbf{A}(\mathbf{r},t) = \mathbf{A}_{\text{ext}}(\mathbf{r},t), \tag{2.69}$$

$$v(\mathbf{r},t) = v_{\text{ext}}(\mathbf{r},t) + v_{\text{H}}[\rho](\mathbf{r},t) + \frac{\delta E_{\text{xc}}^{\text{ad}}[\rho](t)}{\delta \rho(\mathbf{r},t)}. \tag{2.70}$$

The time-dependent Kohn-Sham equation with electromagnetic coupling within the adiabatic approximation is thus given by

$$\begin{aligned} i\frac{\partial}{\partial t}\psi_n(\mathbf{r},t) = \Bigg(&\frac{1}{2}\Big(-i\nabla + \mathbf{A}_{\text{ext}}(\mathbf{r},t)\Big)^2 + v_{\text{ext}}(\mathbf{r},t) \\ &+ v_{\text{H}}[\rho](\mathbf{r},t) + v_{\text{xc}}^{\text{ad}}[\rho](\mathbf{r},t)\Bigg)\psi_n(\mathbf{r},t) \end{aligned} \tag{2.71}$$

It should be noted that there are cases where the full TDCDFT description is necessary, e.g., for time-varying magnetic fields or for more convenient inclusion of dynamical [59, 67] and long-range XC effects [68]. Another case is formally the class of systems with periodic boundary conditions: in this case, the Runge-Gross theorem does not apply, as it is formulated for densities of finite extent. This means that the 1:1 correspondence between external field and density cannot be established [69]. TDCDFT on the other hand solves this problem, as both density and current density establish the connection [70]. We note that most applications of RT-TDDFT in periodics are conducted without current-functionalization, i.e., ignoring the above-mentioned problem. This admittedly lacks strict formal justification but often yields correct results [71, 72, 73, 74, 75, 76, 77].

We will now introduce the so-called *dipole approximation*, also known as *long-wavelength approximation* [78], which also reflects common practice in most RT-TDDFT applications [59]: here, the spatial dependence of the electric field (and thus also of the

vector potential) is neglected, i.e.,

$$\mathbf{E}(\mathbf{r},t) \to \mathbf{E}(t), \tag{2.72}$$

$$\mathbf{A}(\mathbf{r},t) \to \mathbf{A}(t). \tag{2.73}$$

The justification for this originates in the fact that the spatial variation of the electromagnetic field is much smaller than the size of the quantum system for typical wavelengths in laser-matter experiments (in the range of 100s of nanometers for the visible spectrum). This treatment significantly simplifies the mathematical apparatus but one has to keep in mind that the dipole approximation breaks down at some point both for the field wavelength and its amplitude [78].

2.2.5 Gauge Choice

From a formal point, the time-dependent Kohn-Sham equations are gauge invariant under transformations of the form

$$\mathbf{A}'_{\text{ext}}(\mathbf{r},t) = \mathbf{A}_{\text{ext}}(\mathbf{r},t) + \nabla\chi(\mathbf{r},t), \tag{2.74}$$

$$v'_{\text{ext}}(\mathbf{r},t) = v_{\text{ext}}(\mathbf{r},t) - \frac{\partial}{\partial t}\chi(\mathbf{r},t), \tag{2.75}$$

with an arbitrary differentiable real function $\chi(\mathbf{r},t)$ [66]. One can thus switch between gauges by the unitary transformation

$$\psi'_n(\mathbf{r},t) = e^{-i\chi(\mathbf{r},t)}\psi_n(\mathbf{r},t). \tag{2.76}$$

We will from now on employ the dipole approximation, as introduced above; the vector potential and electric field are thus spatially homogeneous. Regarding the specific gauge choice for the description of the external field, the two most common choices used are the *length* gauge (LG), defined as

$$\mathbf{A}_{\text{ext}}(t) \equiv \mathbf{0}, \tag{2.77}$$

$$v_{\text{ext}}(\mathbf{r},t) \equiv -\mathbf{r}\cdot\mathbf{E}(t), \tag{2.78}$$

and the *velocity* gauge (VG)

$$\mathbf{A}_{\text{ext}}(t) \equiv -\int_{t_0}^{t} \mathrm{d}t'\, \mathbf{E}(t'), \tag{2.79}$$

$$v_{\text{ext}}(\mathbf{r},t) \equiv 0, \tag{2.80}$$

being related to each other by the function [66]

$$\chi(\mathbf{r},t) = -\mathbf{r}\cdot\int_{t_0}^{t} \mathrm{d}t'\, \mathbf{E}(t'). \tag{2.81}$$

By definition, both gauges yield the same observables – formally. In any actual simulation, numerical approximations (most prominently the basis set used to expand the wave functions) break the gauge invariance to some extent [66, 78, 79, 80]. Problem-specific numerical differences for these gauges can be reason alone to make a specific choice, but we mainly discuss the topic because for the following reason: when attempting to describe coupling to an external field via the LG in case of *periodic* systems, i.e., with periodic boundary conditions (PBC), the position operator is ill-defined [81, 82]. This problem can however be solved and the solution is intrinsically linked to the modern theory for the bulk polarization by King-Smith and Vanderbilt [83] and its generalization to the case with external time-dependent fields by Souza et al. [84]. The polarization $\mathbf{P}$ with the unit of charge dipole per volume formally requires to evaluate an expression including the position operator and is thus also ill-defined with periodic boundary conditions. King-Smith and Vanderbilt showed that the polarization of an extended system can be calculated via the Berry phase of the $\mathbf{k}$-vector,

$$\mathbf{P}_\mu = \frac{2i}{(2\pi)^3} \int_{\mathrm{BZ}} \mathrm{d}^3\mathbf{k} \sum_{n=1}^{\mathrm{N_v}} \langle u_{n\mathbf{k}} | \partial_{\mathbf{k}_\mu} | u_{n\mathbf{k}} \rangle, \tag{2.82}$$

where $\mathrm{N_v}$ is the number of valence bands and $\{u_{n\mathbf{k}}\}$ are the periodic parts of the Bloch functions . In this sense, the position operator and a spatial integral is replaced by the expression $i\partial_{\mathbf{k}_\mu}$ and an integral over the Brillouin zone. The same ansatz can be employed to define the correct form of the LG coupling for PBC [81, 82]. However, from a computational point of view, this requires the evaluation of derivatives with respect to $\mathbf{k}$-vectors, which itself can be numerically challenging [80] and may introduce considerable numerical overhead, depending on the implementation.
The velocity gauge on the other hand requires no additional considerations in case of PBC and can be implemented without further treatment [74, 81, 85] . Our implementation thus only employs the velocity gauge for the simulation of light-matter interaction in extended systems. For completeness, we note that the LG may be advantageous when non-local pseudopotentials or dephasing operators are present [86]; however, both of these cases are not considered in our work.

2.2.6 Observables

As by the Runge-Gross theorem, the time-dependent KS wave function $\Psi(t)$ becomes a functional of the density $\rho(\mathbf{r}, t)$ and the initial wave function Ψ_0 – i.e., $\Psi[\rho, \Psi_0](t)$ – due to the density-functionalization of the potential and consequently the time-dependent Hamiltonian. Therefore all observables $O(t)$ related to operators $\hat{O}$ are functionals of the time-dependent density, too:

$$O(t) = \langle \Psi[\rho, \Psi_0](t) | \hat{O} | \Psi[\rho, \Psi_0](t) \rangle. \tag{2.83}$$

Formally, the initial-state dependency vanishes when the time-propagation evolves from the ground state wave function since by the Hohenberg-Kohn theorem, the ground state wave function is a functional of the density alone [59].

The time-dependent total energy of the Kohn-Sham system within the adiabatic approximation is given by

$$E_{\text{tot}}(t) = \sum_{n=1}^{N_{\text{occ}}} f_n \langle \psi_n(t) | \mathcal{H}_{\text{KS}}(t) | \psi_n(t) \rangle - \int \mathrm{d}^3\mathbf{r}\, \rho(\mathbf{r},t) v_{\text{xc}}^{\text{ad}}(\mathbf{r}) + E_{\text{xc}}^{\text{ad}}[\rho](t) - \frac{1}{2}\int \mathrm{d}^3\mathbf{r}\, \rho(\mathbf{r},t) v_{\text{H}}(\mathbf{r},t) + E_{\text{nuc}}(t). \tag{2.84}$$

This is basically the conventional definition of the total energy in DFT with the difference that the time-dependent electron density is evaluated and that the eigenvalues from the solution of the time-independent KS eigenvalue equation are replaced by the time-dependent expectation values of the time-dependent KS Hamiltonian (i.e., the single-particle energies of the time-dependent KS states). With the existence of external electromagnetic fields, another energy term depending on the chosen gauge would have to be added in order to include this contribution to the total energy; however, as this contribution is not really of interest since we usually only care for energy differences within the time-evolution, we omit it here.

2.2.7 Solving the Time-Dependent Kohn-Sham Equation

Formally, the solution of the TDKS equation can in principle equivalently be formulated analogous to the time-dependent Schrödinger equation. Equivalently, analogous practical considerations arise due to the self-dependence of the TDKS equation's solutions, the time-dependent single-particle KS orbitals, on the electronic density. We will come back to these considerations in Section 3.4 and now consider the formal solution of Eq. 2.59 via the operator $\mathcal{U}(t,t_0)$:

$$\psi_n(\mathbf{r},t) = \mathcal{U}(t,t_0)\psi_n(\mathbf{r},t_0). \tag{2.85}$$

Above relation connects the solution of the TDKS equation for some arbitrary time t to an initial solution at some time t_0 via the so-called time-evolution operator $\mathcal{U}(t,t_0)$ (usually called *propagator*), advancing the initial solution to the current time [87]. This result arises from an equivalent way to write down the TDKS equation via the propagator:

$$i\frac{\mathrm{d}}{\mathrm{d}t}\mathcal{U}(t,t_0) = \mathcal{H}_{\text{KS}}(t)\mathcal{U}(t,t_0). \tag{2.86}$$

Above equation can also be formulated as an integral equation for the propagator $\mathcal{U}(t,t_0)$:

$$\mathcal{U}(t,t_0) = \hat{1} - i\int_{t_0}^{t} \mathrm{d}t'\, \mathcal{H}_{\text{KS}}(t')\mathcal{U}(t',t_0). \tag{2.87}$$

Obviously, the solution depends on all points in time between t_0 and t. A formal solution can be given by a Dyson series as

$$\mathcal{U}(t,t_0) = \hat{1} + \sum_{m=1}^{\infty} (-i)^m \int_{t_0}^{t} \mathrm{d}t_1 \int_{t_0}^{t_1} \mathrm{d}t_2 \ldots \int_{t_0}^{t_{m-1}} \mathrm{d}t_m \, \mathcal{H}_{\mathrm{KS}}(t_1) \ldots \mathcal{H}_{\mathrm{KS}}(t_m). \tag{2.88}$$

This form is rather complicated due to the integration limits being integration variables, too. One can find a more simple version by using the *time-ordering operator* $\mathcal{T}_o$ defined by

$$\mathcal{T}_o\Big\{\mathcal{H}_{\mathrm{KS}}(t_1)\mathcal{H}_{\mathrm{KS}}(t_2)\Big\} = \begin{cases} \mathcal{H}_{\mathrm{KS}}(t_1)\mathcal{H}_{\mathrm{KS}}(t_2) & , \quad t_1 > t_2 \\ \mathcal{H}_{\mathrm{KS}}(t_2)\mathcal{H}_{\mathrm{KS}}(t_1) & , \quad t_1 < t_2 \end{cases} \tag{2.89}$$

which takes into account that time-dependent Hamiltonians do generally not commute, as follows:

$$\mathcal{U}(t,t_0) = \hat{1} + \sum_{m=1}^{\infty} \frac{(-i)^m}{m!} \int_{t_0}^{t} \mathrm{d}t_1 \int_{t_0}^{t} \mathrm{d}t_2 \ldots \int_{t_0}^{t} \mathrm{d}t_m \, \mathcal{T}_o\Big\{\mathcal{H}_{\mathrm{KS}}(t_1) \ldots \mathcal{H}_{\mathrm{KS}}(t_m)\Big\}. \tag{2.90}$$

The factorial stems from the implicit reduction of the inflated integration hypervolume by the time-ordering operator. The given form is reminiscent of the series definition of the exponential and allows to write down an even simpler form as

$$\mathcal{U}(t,t_0) = \mathcal{T}_o \exp\left(-i \int_{t_0}^{t} \mathrm{d}t' \, \mathcal{H}_{\mathrm{KS}}(t')\right). \tag{2.91}$$

However, one should note that this is not a true exponential function, but rather a conventional way to write down the complicated Dyson series. Aside from a formal motivation, the (exact) propagator $\mathcal{U}(t,t_0)$ has important and insightful properties, each being critical for actual numerical implementations of a RT-TDDFT (or Schrödinger dynamics) scheme [87].

- Unitarity: the property

  $$\mathcal{U}^{\dagger}(t,t_0) = \mathcal{U}^{-1}(t,t_0) \tag{2.92}$$

  is directly connected to the wave function's probability conservation, i.e.,

  $$\begin{aligned} \int \mathrm{d}^3\mathbf{r} \, |\psi_n(\mathbf{r},t)|^2 &= \int \mathrm{d}^3\mathbf{r} \, \psi_n^*(\mathbf{r},t)\psi_n(\mathbf{r},t) \\ &= \int \mathrm{d}^3\mathbf{r} \, \psi_n^*(\mathbf{r},t_0)\mathcal{U}^{\dagger}(t,t_0)\mathcal{U}(t,t_0)\psi_n(\mathbf{r},t_0) \\ &= \int \mathrm{d}^3\mathbf{r} \, \psi_n^*(\mathbf{r},t_0)\psi_n(\mathbf{r},t_0) = \int \mathrm{d}^3\mathbf{r} \, |\psi_n(\mathbf{r},t_0)|^2, \end{aligned} \tag{2.93}$$

  for a Hermitian Hamiltonian which is always the case here.

- Time-reversal symmetry: this can be expressed as

  $$\mathcal{U}(t,t_0) = \mathcal{U}^{-1}(t_0,t) \tag{2.94}$$

and simply implies the effect of time-reversion to be symmetric (in the absence of magnetic fields):

$$\psi_n(t_0) = \mathcal{U}(t_0,t)\psi_n(t) = \mathcal{U}(t_0,t)\mathcal{U}(t,t_0)\psi_n(t_0). \tag{2.95}$$

- Composition: any propagation interval can be split into smaller intervals due to the property

$$\mathcal{U}(t,t_0) = \prod_{m=0}^{\mathrm{M}_t} \mathcal{U}(t_m + \Delta t_m, t_m) \tag{2.96}$$

(with $t_0 = 0,\ t_{m+1} = t_m + \Delta t_m,\ t_{\mathrm{M}_t} = t$) which is obviously of major practical importance when discretizing time evolution for a computer algorithm with finite accuracy.

Any numerical representation of a propagator should retain unitarity as good as possible, and equally for the time-reversal invariance.

2.3 Coupled Nuclear-Electronic Dynamics

In this section, we will extend the presented formalisms for the description of time-dependent electron degrees of freedom by taking into account the time-dependence of classically treated nuclei. This leads to coupled nuclear-electronic dynamics within the frame of Ehrenfest dynamics.

2.3.1 Fundamentals

Extending the electron-only Schrödinger (or Kohn-Sham) dynamics to include nuclear degrees of freedom by explicitly taking into account atomic coordinates $\{\mathbf{R}_I\}$ yields the following Schrödinger equation:

$$i\frac{\partial}{\partial t}\Psi\Big(\{\mathbf{r}_i\},\{\mathbf{R}_I\},t\Big) = \mathcal{H}'\Psi\Big(\{\mathbf{r}_i\},\{\mathbf{R}_I\},t\Big). \tag{2.97}$$

The total wave function is thus depending on all electron coordinates, all atomic coordinates and on time. The Hamiltonian operator is now given by

$$\mathcal{H}' = \mathcal{T}_{\mathrm{nuc}} + \mathcal{H} \tag{2.98}$$

where $\mathcal{H}$ is the electronic Hamiltonian as defined before in Eq. 2.51 and

$$\mathcal{T}_{\mathrm{nuc}} = -\frac{1}{2}\sum_{I=1}^{\mathrm{N}_{\mathrm{at}}} \frac{1}{M_I}\nabla_I^2 \tag{2.99}$$

is the nuclear kinetic energy operator (with the atomic masses $\{M_I\}$). We additionally note here that the potential energy operator also includes internuclear Coulomb

repulsion via

$$\mathcal{V} = \sum_{i=1}^{N_{el}} \hat{v}(\mathbf{r}_i, t) + \sum_{I<J}^{N_{at}} \frac{Z_I Z_J}{|\mathbf{R}_I - \mathbf{R}_J|} \tag{2.100}$$

with the atomic numbers $\{Z_I\}$ and the usual single-electron potential energy operator $\hat{v}(\mathbf{r}, t)$ describing electron-nuclear Coulomb attraction and possible external time-dependent fields.
The simplest strategy to obtain individual (but coupled) dynamical equations for electrons and nuclei is applying a single product ansatz for the total wave function, i.e.,

$$\Psi\Big(\{\mathbf{r}_i\}, \{\mathbf{R}_I\}, t\Big) \approx \Phi\Big(\{\mathbf{r}_i\}, t\Big)\Theta\Big(\{\mathbf{R}_I\}, t\Big) \exp\left(i \int_{t_0}^{t} \mathrm{d}t' \, \epsilon(t')\right), \tag{2.101}$$

with Φ being the purely electronic und Θ being the purely nuclear wave function, each being normalized at any time. The phase factor

$$\epsilon(t) = \int \mathrm{d}^3\mathbf{r} \, \mathrm{d}^3\mathbf{R} \, \Phi^*\Big(\{\mathbf{r}_i\}, t\Big)\Theta^*\Big(\{\mathbf{R}_I\}, t\Big)\mathcal{H}'\Phi\Big(\{\mathbf{r}_i\}, t\Big)\Theta\Big(\{\mathbf{R}_I\}, t\Big) \tag{2.102}$$

is introduced for convenience; the integrals run over all individual coordinates as indicated by the expressions for the wave functions. This ansatz is referred to as a single-configuration approach that will lead to a mean-field character of the dynamics described here [57]. Employing this product ansatz for the coupled Schrödinger equation yields the two differential equations [57]

$$\begin{aligned} i\frac{\partial}{\partial t}\Phi\Big(\{\mathbf{r}_i\}, t\Big) = &-\frac{1}{2}\sum_{i=1}^{N_{el}} \nabla_i^2 \Phi\Big(\{\mathbf{r}_i\}, t\Big) \\ &+ \left\{\int \mathrm{d}^3\mathbf{R} \, \Theta^*\Big(\{\mathbf{R}_I\}, t\Big) \, \mathcal{V} \, \Theta\Big(\{\mathbf{R}_I\}, t\Big)\right\} \Phi\Big(\{\mathbf{r}_i\}, t\Big), \end{aligned} \tag{2.103}$$

$$\begin{aligned} i\frac{\partial}{\partial t}\Theta\Big(\{\mathbf{R}_I\}, t\Big) = &-\frac{1}{2}\sum_{I=1}^{N_{at}} \frac{1}{M_I} \nabla_I^2 \Theta\Big(\{\mathbf{R}_I\}, t\Big) \\ &+ \left\{\int \mathrm{d}^3\mathbf{r} \, \Phi^*\Big(\{\mathbf{r}_i\}, t\Big) \, \mathcal{H}' \, \Phi\Big(\{\mathbf{r}_i\}, t\Big)\right\} \Theta\Big(\{\mathbf{R}_I\}, t\Big). \end{aligned} \tag{2.104}$$

One can directly see the mean-field character in the respective potential energy contributions in both equations: the motion of the electronic wave function Φ includes the nuclear wave function-averaged potential energy contribution and vice versa.

2.3.2 Ehrenfest Dynamics

Since it was the goal here to describe quantum-mechanical electron motion coupled with semi-classical nuclear dynamics, the classical limit for the nuclei needs to be taken – in this case for the formerly presented mean-field approach. The strategy is in detail described in Refs. [57, 88] and we provide some more general remarks about this method in Section 4.5. First, we formulate the nuclear wave function as a

product

$$\Theta\Big(\{\mathbf{R}_I\},t\Big) \equiv A\Big(\{\mathbf{R}_I\},t\Big)\exp\left(iS\Big(\{\mathbf{R}_I\},t\Big)\right) \tag{2.105}$$

where $A \in \mathbb{R}^+$ and $S \in \mathbb{R}$. Inserting this ansatz into above nuclear mean-field equations yields the amplitude and phase equations

$$\frac{\partial S}{\partial t} + \frac{1}{2}\sum_{I=1}^{\mathrm{N_{at}}}\frac{1}{M_I}(\nabla_I S)^2 + \int \mathrm{d}^3\mathbf{r}\,\Phi^*\,\mathcal{H}\,\Phi = \frac{1}{2}\sum_{I=1}^{\mathrm{N_{at}}}\frac{1}{M_I}\frac{1}{A}\nabla_I^2 A, \tag{2.106}$$

$$\frac{\partial A}{\partial t} + \sum_{I=1}^{\mathrm{N_{at}}}\frac{1}{M_I}(\nabla_I A)(\nabla_I S) + \frac{1}{2}\sum_{I=1}^{\mathrm{N_{at}}}\frac{1}{M_I}A(\nabla_I^2 S) = 0. \tag{2.107}$$

The equation for A can be formulated as a continuity equation for the nuclear particle probability when identifying $A^2 = |\Theta|^2$. The equation for S directly serves the purpose of constructing semi-classical nuclear dynamics when taking the classical limit $\hbar \to 0$ which results in the RHS of Eq. 2.106 becoming zero (due to the use of atomic units, $\hbar$ is not occurring, but in fact is a prefactor of the sum). The transformation $\mathcal{P}_I = \nabla_I S$ with the nuclear momentum operator $\mathcal{P}_I$ leads to the following form of Equation 2.106 when also performing the classical limit:

$$\frac{\partial S}{\partial t} + \sum_{I=1}^{\mathrm{N_{at}}}\frac{1}{2M_I}\mathcal{P}_I^2 + \int d^3\mathbf{r}\,\Phi^*\mathcal{H}\Phi = 0 \tag{2.108}$$

$$\Leftrightarrow \quad \frac{\partial S}{\partial t} + \bar{\mathcal{H}}\Big(\{\mathbf{R}_I\},\{\mathcal{P}_I\}\Big) = 0 \tag{2.109}$$

The last equation with the Hamiltonian $\bar{\mathcal{H}}$ has an isomorphic equation of motion in the Hamilton-Jacobi formalism, enabling to define the Newtonian equation of motion

$$\dot{\mathcal{P}}_I = M_I\ddot{\mathbf{R}}_I = -\nabla_I\langle\Phi|\mathcal{H}'|\Phi\rangle \tag{2.110}$$

where we can see by defining $V_E \equiv \langle\Phi|\mathcal{H}|\Phi\rangle$ that the nuclear motion is given by the effective potential V_E, actually being the expectation value of the electronic Hamiltonian, i.e., incorporating an averaging character, for a fixed configuration of nuclear positions $\{\mathbf{R}_I\}$.

The last step is to define the nuclei as classical particles which is done by setting the nuclear charge density to a product of delta distributions and evaluating the potential part of Eq. 2.103 on this basis:

$$\begin{aligned}\int \mathrm{d}^3\mathbf{R}\,\Theta\Big(\{\mathbf{R}_I\},t\Big)\,\mathcal{V}\,\Theta\Big(\{\mathbf{R}_I\},t\Big) &= \int \mathrm{d}^3\mathbf{R}\,\Big|\Theta\Big(\{\mathbf{R}_I\},t\Big)\Big|^2\,\mathcal{V}\\ &\equiv \prod_I\int \mathrm{d}^3\mathbf{R}\,\delta(\mathbf{R}-\mathbf{R}_I(t))\,\mathcal{V}\\ &\equiv V_{\mathrm{ne}}\Big(\{\mathbf{r}_i\},\{\mathbf{R}_I(t)\}\Big).\end{aligned} \tag{2.111}$$

This finally yields the dynamical equation for the electrons where the Hamiltonian and the wave functions parametrically depend on a fixed configuration $\{\mathbf{R}_I\}$ of nuclear positions:

$$i\frac{\partial}{\partial t}\Phi\Big(\{\mathbf{r}_i\},\{\mathbf{R}_I\},t\Big) = -\sum_i \frac{1}{2}\nabla_i^2\Phi\Big(\{\mathbf{r}_i\},\{\mathbf{R}_I\},t\Big) + V_{\mathrm{ne}}\Big(\{\mathbf{r}_i\},\{\mathbf{R}_I(t)\}\Big)\,\Phi\Big(\{\mathbf{r}_i\},\{\mathbf{R}_I\},t\Big). \tag{2.112}$$

In the TDDFT framework, this equation is the single-particle Kohn-Sham equation for the KS orbitals $\{\psi_n\}$. The simultaneous solution of Equations 2.110 and 2.112 constitutes the Ehrenfest dynamics approach. We will discuss applications and practical considerations further in Chapter 4.5.

2.4 Linear-Response Time-Dependent Density Functional Theory

Having established before the framework given by the general time-dependent Kohn-Sham equation, we will now consider the special case of weak perturbations. This leads to the linear-response formulation of TDDFT, which is of significant practical relevance.

2.4.1 Introduction

The most popular formulation of the time-dependent variant of DFT (TDDFT) is found in its linear-response formulation (LR-TDDFT) which enables a quite economic way to calculate excitation energies of an electronic system in the perturbative regime [64]. This approach does not involve actual time propagation and one effectively only needs to efficiently solve a (possibly large) eigenvalue problem. The key idea is to write the time-dependent external potential as

$$v(\mathbf{r},t) \equiv v_0(\mathbf{r}) + \delta v(\mathbf{r},t), \tag{2.113}$$

i.e., by a time-independent potential and a weak time-dependent potential, acting as a perturbation on the system. From the Taylor expansion of the response of the electronic density,

$$\rho(\mathbf{r},t) = \rho_0(\mathbf{r}) + \delta\rho(\mathbf{r},t) + \text{h.o.t.}, \tag{2.114}$$

where ρ_0 is the ground state density, one can write the first order density response as

$$\delta\rho(\mathbf{r},t) = \int \mathrm{d}t' \int \mathrm{d}^3\mathbf{r}'\, \chi(\mathbf{r},t,\mathbf{r}',t')\,\delta v(\mathbf{r}',t'). \tag{2.115}$$

The quantity $\chi(\mathbf{r}, t, \mathbf{r}', t')$ is the susceptibility, also often named the density-density response function. The *single-particle* density-density response function can be defined as

$$\chi_{\mathrm{KS}}(\mathbf{r}, t, \mathbf{r}', t') = \left.\frac{\delta\rho(\mathbf{r}, t)}{\delta v_{\mathrm{KS}}(\mathbf{r}', t')}\right|_{v_{\mathrm{KS}}[\rho_0]}. \tag{2.116}$$

Its poles are the *single-particle* Kohn-Sham orbital excitations and not those of the true fully interacting system (same for the oscillator strengths which are related to optical absorption intensities). We proceed by defining the so-called linear response kernel as the functional derivative of the exchange-correlation potential,

$$f_{\mathrm{xc}}[\rho_0](\mathbf{r}, t, \mathbf{r}', t') = \left.\frac{\delta v_{\mathrm{xc}}[\rho](\mathbf{r}, t)}{\delta\rho(\mathbf{r}', t')}\right|_{\rho=\rho_0}. \tag{2.117}$$

For example, a very popular exchange-correlation kernel is based on the LDA XC functional, yielding the often used notation 'TDLDA' for LR-TDDFT based calculations using the so-called adiabatic LDA (ALDA) XC kernel [59, 64]. Formally, Equation 2.115 can equivalently be written via a non-interacting Kohn-Sham system as

$$\delta\rho(\mathbf{r}, t) = \int \mathrm{d}t' \int \mathrm{d}^3\mathbf{r}'\, \chi_{\mathrm{KS}}(\mathbf{r}, t, \mathbf{r}', t')\, \delta v_{\mathrm{KS}}(\mathbf{r}', t'), \tag{2.118}$$

assuming that the Kohn-Sham potential v_{KS} includes the true exchange-correlation description. The first-order change in the KS potential is given as

$$\begin{aligned}\delta v_{\mathrm{KS}}(\mathbf{r}, t) = \delta v(\mathbf{r}, t) &+ \int \mathrm{d}^3\mathbf{r}' \frac{\delta\rho(\mathbf{r}', t)}{|\mathbf{r} - \mathbf{r}'|} \\ &+ \int \mathrm{d}t' \int \mathrm{d}^3\mathbf{r}'\, f_{\mathrm{xc}}[\rho_0](\mathbf{r}, t, \mathbf{r}', t')\, \delta\rho(\mathbf{r}', t').\end{aligned} \tag{2.119}$$

Equating the expressions 2.115 and 2.118 yields a Dyson equation of the form

$$\begin{aligned}\chi[\rho_0](\mathbf{r}, t, \mathbf{r}', t') = \chi_{\mathrm{KS}}[\rho_0](\mathbf{r}, t, \mathbf{r}', t') \\ + \int \mathrm{d}t'' \int \mathrm{d}^3\mathbf{r}'' \int \mathrm{d}t''' \int \mathrm{d}^3\mathbf{r}'''\, \chi_{\mathrm{KS}}[\rho_0](\mathbf{r}, t, \mathbf{r}'', t'') \\ \times \left(\frac{\delta(t'' - t''')}{|\mathbf{r}'' - \mathbf{r}'''|} + f_{\mathrm{xc}}[\rho_0](\mathbf{r}'', t'', \mathbf{r}''', t''')\right) \chi[\rho_0](\mathbf{r}''', t''', \mathbf{r}', t').\end{aligned} \tag{2.120}$$

The next step is to express above equation in frequency space via canonical Fourier transformation. It is important here to note that the exchange-correlation kernel only depends on time differences due to time translation invariance of the unperturbed ground state system, resulting in only one frequency variable: $\mathcal{F}[f_{\mathrm{xc}}(\mathbf{r}, \mathbf{r}', t - t')] = f_{\mathrm{xc}}[\rho_0](\mathbf{r}, \mathbf{r}', \omega)$. We omit the explicit Fourier transform of Eq. 2.120 but rather give the formal solution as the key result:

$$\chi^{-1}(\mathbf{r}, \mathbf{r}', \omega) = \chi_{\mathrm{KS}}^{-1}(\mathbf{r}, \mathbf{r}', \omega) - f_{\mathrm{H,xc}}[\rho_0](\mathbf{r}, \mathbf{r}', \omega) \tag{2.121}$$

(note that the inverse function is given, providing a rather simple expression). Here, we introduced the Hartree-exchange-correlation kernel

$$f_{\mathrm{H,xc}}[\rho_0](\mathbf{r},\mathbf{r}',\omega) = \frac{1}{|\mathbf{r}-\mathbf{r}'|} + f_{\mathrm{xc}}[\rho_0](\mathbf{r},\mathbf{r}',\omega). \tag{2.122}$$

The solution $\chi(\mathbf{r},\mathbf{r}',\omega)$ contains the sought information, namely the true excitation energies of the system, as its poles. In analogy to a system of weakly perturbed coupled oscillators in classical mechanics with specific eigenmodes (and -vectors), the excitation energies are the eigenmodes of the interacting electronic system [59].

2.4.2 Formulation as Matrix Equation

For practical calculations, i.e., to solve the equation for the fully interacting density-density response function, the corresponding quantities are expressed in the basis of the Kohn-Sham orbitals $\{\psi_n\}$, each of which are associated with a certain spin, energy eigenvalue and occupation $\{(\sigma_n, \epsilon_{n\sigma}, f_n)\}$. These representations are

$$\chi(\mathbf{r},\mathbf{r}',\omega) = \sum_{nm\sigma}\sum_{kl\sigma'}\Big(\psi_n(\mathbf{r}\sigma)\psi_m^*(\mathbf{r}\sigma)\psi_k(\mathbf{r}'\sigma')\psi_l^*(\mathbf{r}'\sigma')\Big)X_{nm\sigma,kl\sigma'}(\omega), \tag{2.123}$$

$$\delta v(\mathbf{r},\omega) = \sum_{nm\sigma}\psi_n(\mathbf{r}\sigma)\psi_m^*(\mathbf{r}\sigma)V_{nm}(\omega), \tag{2.124}$$

$$f_{\mathrm{H,xc}}(\mathbf{r},\mathbf{r}',\omega) = \sum_{nm\sigma}\sum_{kl\sigma'}\Big(\psi_n(\mathbf{r}\sigma)\psi_m^*(\mathbf{r}\sigma)\psi_k(\mathbf{r}'\sigma')\psi_l^*(\mathbf{r}'\sigma')\Big)F_{nm\sigma,kl\sigma'}(\omega). \tag{2.125}$$

We will see later that only the Hartree-exchange-correlation kernel matrix elements

$$F_{nm\sigma,kl\sigma'}(\omega) = \langle\psi_{k\sigma'}|\langle\psi_{n\sigma}|f_{\mathrm{H,xc}}[\rho_0](\omega)|\psi_{m\sigma}\rangle|\psi_{l\sigma'}\rangle \tag{2.126}$$

have to be calculated explicitly. Further, the single-particle susceptibility is simply given via the Kohn-Sham orbital occupations and eigenvalues, as the latter build its poles by definition:

$$\chi^{\mathrm{KS}}_{nm\sigma,kl\sigma'}(\omega) = \delta_{\sigma\sigma'}\delta_{nk}\delta_{ml}\frac{f_{k\sigma}-f_{n\sigma}}{\omega-(\epsilon_{n\sigma}-\epsilon_{k\sigma})}. \tag{2.127}$$

In this basis, the Fourier transform of Eq. 2.115 now reads

$$\delta\rho_{nm\sigma}(\omega) = \sum_{nm\sigma}\delta v_{nm\sigma}(\omega)\,\chi_{nm\sigma,kl\sigma'}(\omega) \tag{2.128}$$

and by inserting Eq. 2.121 into above equation and rearranging, we obtain the following linear-response equation:

$$\sum_{kl\sigma'}\Big(\big(\chi^{\mathrm{KS}}_{nm\sigma,kl\sigma'}(\omega)\big)^{-1} - F_{nm\sigma,kl\sigma'}(\omega)\Big)\delta\rho_{nm\sigma}(\omega) = \delta V_{nm\sigma}(\omega), \tag{2.129}$$

where the inverse single-particle susceptibility $\left(\chi^{\mathrm{KS}}_{nm\sigma,kl\sigma'}(\omega)\right)^{-1}$ is obtained by simply inverting Eq. 2.127. Note that the matrix elements have to be evaluated for all possible combinations of occupied and unoccupied Kohn-Sham orbitals. Since this is an infinite set, the number of states is in practice truncated. Expressing above equation in matrix form yields the equation

$$\chi^{-1}\begin{bmatrix}\mathbf{X}\\ \mathbf{Y}\end{bmatrix} = \left(\omega\begin{bmatrix}\mathbb{1} & 0\\ 0 & -\mathbb{1}\end{bmatrix} - \begin{bmatrix}\mathbf{A} & \mathbf{B}\\ \mathbf{B}^* & \mathbf{A}^*\end{bmatrix}\right)\begin{bmatrix}\mathbf{X}\\ \mathbf{Y}\end{bmatrix} = \begin{bmatrix}\delta\mathbf{V}\\ \delta\mathbf{V}^*\end{bmatrix} \tag{2.130}$$

where $X_{nm\sigma} = \delta\rho_{nm\sigma}$ and $Y_{nm\sigma} = \delta\rho_{mn\sigma}$. The matrices $\mathbf{A}$ and $\mathbf{B}$ are given by

$$A_{nm\sigma,kl\sigma'} = \delta_{\sigma\sigma'}\delta_{nk}\delta_{ml}(\epsilon_{n\sigma} - \epsilon_{m\sigma}) + F_{nm\sigma,kl\sigma'}, \tag{2.131}$$

$$B_{nm\sigma,kl\sigma'} = F_{nm\sigma,lk\sigma'}. \tag{2.132}$$

We used the notation χ^{-1} on the left hand side of Equation 2.130 to illustrate that this matrix corresponds to the inverse fully interacting response function. Its poles are by definition the exact excitation energies $\{\omega_i\}$ and thus, those can be obtained by solving the generalized eigenvalue problem

$$\begin{bmatrix}\mathbf{A} & \mathbf{B}\\ \mathbf{B}^* & \mathbf{A}^*\end{bmatrix}\begin{bmatrix}\mathbf{X}_i\\ \mathbf{Y}_i\end{bmatrix} = \omega_i\begin{bmatrix}\mathbb{1} & 0\\ 0 & -\mathbb{1}\end{bmatrix}\begin{bmatrix}\mathbf{X}_i\\ \mathbf{Y}_i\end{bmatrix}. \tag{2.133}$$

The eigenvalues correspond to occupied-unoccupied transitions $\omega_i > 0 \leftrightarrow (n \rightarrow k)$ (excitations) and unoccupied-occupied transitions $\omega_i < 0 \leftrightarrow (n \leftarrow k)$ (de - excitations). The neglect of de-excitations is mediated by setting $\mathbf{B} = \mathbf{0}$ which is called the Tamm-Dancoff approximation [89]. Equation 2.133 can under certain requirements be reformulated as the ordinary eigenvalue problem usually denoted as Casida's equation [90]

$$\mathbf{\Omega}\mathbf{F}_i = \omega_i^2\mathbf{F}_i \tag{2.134}$$

with $\mathbf{F}_i = (\mathbf{A}-\mathbf{B})^{-1}(\mathbf{X}_i - \mathbf{Y}_i)$ and the so-called Casida matrix $\mathbf{\Omega} = (\mathbf{A}-\mathbf{B})^{1/2}(\mathbf{A}+\mathbf{B})(\mathbf{A}-\mathbf{B})^{-1/2}$. The latter quantity can be directly given by

$$\Omega_{nm\sigma,kl\sigma'} = \delta_{\sigma\sigma'}\delta_{nk}\delta_{ml}(\epsilon_{n\sigma'} - \epsilon_{m\sigma})^2 + \sqrt{\Delta f_{nm\sigma'}\Delta\epsilon_{nm\sigma}\Delta f_{kl\sigma'}\Delta\epsilon_{lk\sigma'}}F_{nm\sigma,kl\sigma'} \tag{2.135}$$

with $\Delta\epsilon_{nm\sigma} = \epsilon_{m\sigma} - \epsilon_{n\sigma}$ and $\Delta f_{nm\sigma'} = f_{n\sigma'} - f_{m\sigma'}$. Practically, the solution is thus obtained by solving the Casida eigenvalue problem.

Chapter 3

Details on the Real-Time TDDFT Implementation

3.1 Overview

We will in this section provide an overview about the mostly technical implications of our computer code implementation of real-time TDDFT. For this, we will shortly introduce the FHI-aims DFT software, which is the basis of our framework. After that, we provide several key concepts and paradigms which we employed in the software development. The formalism of RT-TDDFT for atom-centered basis functions will be introduced in succession. After that, we will cover important mathematical aspects of the numerical integration of the time-dependent Kohn-Sham equation, also introducing various time-propagation schemes.

3.2 The FHI-aims Code Package

The FHI-aims software package is one of the younger density functional theory computer codes. The first official publication from Blum et al. [42] describing the implementation is from the year 2009. Since then, the paper has been cited well over 1500 times[1], indicating the success of the all-electron numerical atom-centered basis function approach. Noteworthy is here also that the software has been benchmarked as one of the most accurate in the field [54]. It was shown that FHI-aims is an order-N code, meaning that is offers a favorable $\mathcal{O}(\mathrm{N})$ scaling of the computational cost for large systems [42, 91]. Besides the robust basic DFT functionality, many additional techniques were introduced by now: van der Waals description based on the Tkatchenko-Scheffler [92] oder many-body-dispersion approaches [93, 94, 95, 96], many-body perturbation methods like MP2, RPA, G_0W_0 [97] or self-consistent GW [98], an implementation of the Bethe-Salpeter equation approach [99], density functional perturbation theory [100], or quasi-four-component relativistic description [101].
The combination of the all-electron description in a highly efficient and accurate framework that can treat both finite and extended systems forms a very interesting

[1] https://www.sciencedirect.com/science/article/pii/S0010465509002033, 18.06.2021

basis for RT-TDDFT applications. In order to illustrate the specifics of the underlying implementation, we will here provide a discussion of the most important aspects.

The Kohn-Sham single-particle orbitals

$$\psi_n(\mathbf{r}) = \sum_{j=1}^{\mathrm{N_b}} c_{jn}\phi_j(\mathbf{r}) \tag{3.1}$$

(with $\mathrm{N_b}$ being the number of basis functions) are represented in the FHI-aims code package via numeric atom-centered orbital (NAO) basis functions, i.e.,

$$\phi_j(\mathbf{r}) = \frac{u_j(r)}{r} Y_{l_j m_j}(\theta, \phi), \tag{3.2}$$

where $u_j(r)$ is a purely radial function, $Y_{l_j m_j}(\theta, \phi)$ a spherical harmonic and it should be noted that the angular indices are implicit functions of the basis function index j, thus (l_j, m_j) [42]. We note here that the functions $Y_{l_j m_j}(\theta, \phi)$ are either the real *or* the imaginary parts of generally complex spherical harmonics, effectively making the basis functions $\phi_j(\mathbf{r})$ purely real-valued. The radial functions $u_j(r)$ are numerically tabulated and originate from free-atom or -ion calculations, i.e., from the solution of the following Schrödinger-like radial equation

$$\left(-\frac{1}{2}\frac{\mathrm{d}^2}{\mathrm{d}r^2} + \frac{l(l+1)}{r^2} + v_j(r) + v_{\mathrm{cut}}(r)\right) u_j(r) = \epsilon_j u_j(r), \tag{3.3}$$

where $v_j(r)$ is the atom-specific potential (defining the specific shape of the solution function by a major impact) and $v_{\mathrm{cut}}(r)$ is the confining potential which effectively limits the radial function's spatial extent and yields smooth decay. This makes the basis functions very flexible due to the tunability of the integration grid and the choice of specific boundary conditions to localize them. A *minimal* basis is obtained by using the self-consistent free-atom radial potential for $v_j(r)$ and solving above equation corresponding to the occupied states of the free atom; this serves as a basis to construct more complete basis sets (which always include all smaller basis sets used to construct them). A specific advantage of the all-electron description here is that (the highly localized) core states are already described very well in the minimal basis. A systematic scheme is presented in Ref. [42] and the code package includes optimized, tiered basis sets for nearly all elements which begin at the 'light' basis set, followed by 'tight' and 'very tight' basis sets (among other more customized basis sets, e.g., with augmented Gaussians), converging to the basis set limit. Figure 3.1 illustrates the radial functions $u_j(r)$ for the 'tight+aug2' basis set of carbon. This basis set additionally includes two diffuse Gaussian functions that enlarge the relevant radial extent significantly. Real-space integrations are performed via a partitioning scheme introduced by Becke, Delley and others [102, 103, 104]: here, the overall volume spanned by the overlapping atom-centered grids is partitioned into localized

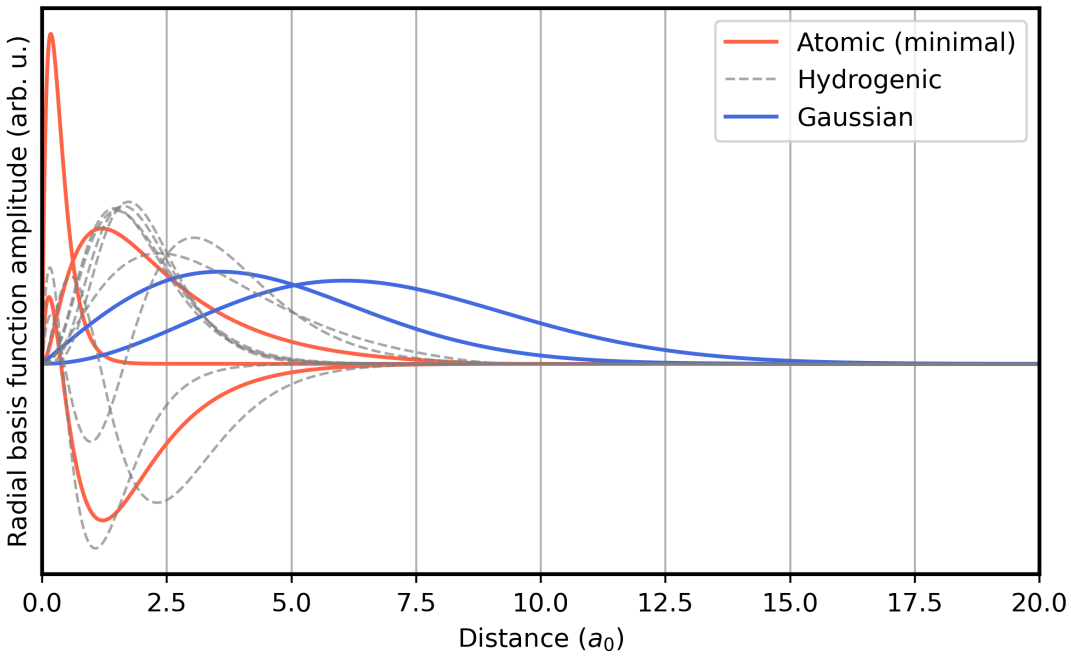

FIGURE 3.1: Carbon radial basis functions from the 'tight+aug2' basis set. The atomic minimal basis, i.e., the basis functions used to construct the 1s, 2s and 2p$_i$ orbitals is colored in red. Additional hydrogenic basis functions are indicated by the dashed grey lines, while the two diffuse Gaussian functions are colored in blue.

atom-centered subvolumes (which are then distributed to computational tasks), i.e.,

$$\int_V \mathrm{d}^3\mathbf{r}\, h(\mathbf{r}) = \sum_{I=1}^{\mathrm{N_{at}}} \int_V \mathrm{d}^3\mathbf{r}\, p_I(\mathbf{r})\, h(\mathbf{r}). \tag{3.4}$$

The integrand $h(\mathbf{r})$ can be any real-valued function on the grid, most often it is a matrix element of an operator $\hat{\mathcal{O}}$, $h(\mathbf{r}) := \phi_i(\mathbf{r})\hat{\mathcal{O}}\phi_j(\mathbf{r})$. The atom-centered partition functions have the form

$$p_I(\mathbf{r}) = \frac{g_I(\mathbf{r})}{\sum_{J=1}^{\mathrm{N_{at}}} g_J(\mathbf{r})}, \tag{3.5}$$

where $g_I(\mathbf{r})$ is a strongly peaked function on atom I, and one can directly see that this corresponds to a *partition of unity*, as the sum of the partition functions equals one everywhere. The functions $p_I(\mathbf{r})$ are centered on their corresponding atom I and their choice has important implications on accuracy and efficiency. In FHI-aims, an efficient scheme by Stratmann et al. [103] is employed.

Each of the single-atom integration grids is spanned by a spherical grid that is comprised of N_r radial shells $r(s)$ $(s = 1, .., \mathrm{N}_r)$ that each contain a specific number of angular integration points and weights, the latter obtained by a scheme of Delley [105]. The radial shells are defined via

$$r(s) = r_{\mathrm{outer}} \frac{\log(1 - (s/(\mathrm{N}_r + 1)^2)}{\log(1 - (\mathrm{N}_r/(\mathrm{N}_r + 1)^2))} \tag{3.6}$$

with r_{outer} being the radius of the outmost shell, as suggested by Baker et al. [106]. The spatial extent (and of course the employed grid density) of the radial basis functions is thus critical for performance but also for the correct description of valence electrons, especially when dealing with excitations.

Due to the all-electron description, relativistic treatment is required and here implemented on an approximate scalar-relativistic level, avoiding the four-component Dirac equation. The scaled zeroth order regular approximation (ZORA) by van Lenthe [107] is used in this context and of most practical significance is the so called *atomic ZORA* treatment [42]. In this approach, the scalar-relativistic free-atom kinetic operator is defined as

$$\hat{t}_{\text{at.ZORA}}(i) = \hat{\mathbf{p}} \cdot \frac{c^2}{2c^2 - v^{\text{free}}_{I(i)}} \hat{\mathbf{p}} \tag{3.7}$$

(c is the speed of light). Here, $\hat{\mathbf{p}} = -i\nabla$ is the momentum operator and $v^{\text{free}}_{I(i)}$ is the free-atom potential of the atom I which the basis function i is attached to, and which is subject to the action of the kinetic operator.

In the case of periodic systems, i.e., slabs or bulk solids, the periodic boundary conditions are implemented by the definition of generalized basis functions of the form

$$\chi_{i\mathbf{k}}(\mathbf{r}) = \sum_{\mathbf{M}} e^{i\mathbf{k}\cdot\mathbf{T_M}} \phi_i \left(\mathbf{r} - \mathbf{R}_{I(i)} - \mathbf{T_M}\right) \equiv \sum_{\mathbf{M}} e^{i\mathbf{k}\cdot\mathbf{T_M}} \phi_{i\mathbf{M}}. \tag{3.8}$$

Here, ϕ_i is an atomic basis function centered on atom I, including its location in a unit cell indicated by the translation vector $\mathbf{T_M}$. The latter specifically refers to a unit cell location $\mathbf{T_M} = M_1\mathbf{a}_1 + M_2\mathbf{a}_2 + M_3\mathbf{a}_3$ with $\{\mathbf{a}_i\}$ being the lattice vectors of the unit cell. These generalized basis functions lead to KS orbitals satisfying the Bloch condition, as

$$\begin{aligned}
\psi_{n\mathbf{k}}(\mathbf{r}+\mathbf{T_N}) &= \sum_{i=1}^{\text{N}_{\text{occ}}} c_{in\mathbf{k}} \chi_{i\mathbf{k}}\left(\mathbf{r}+\mathbf{T_N}\right) \\
&= \sum_{i=1}^{\text{N}_{\text{occ}}} c_{in\mathbf{k}} \sum_{\mathbf{M}} e^{i\mathbf{k}\cdot\mathbf{T_M}} \phi_i \left(\mathbf{r} - \mathbf{R}_{I(i)} - \mathbf{T_M} + \mathbf{T_N}\right) \\
&= e^{i\mathbf{k}\cdot\mathbf{T_N}} \sum_{i=1}^{\text{N}_{\text{occ}}} c_{in\mathbf{k}} \sum_{\mathbf{M}} e^{i\mathbf{k}\cdot(\mathbf{T_M}-\mathbf{T_N})} \phi_i \left(\mathbf{r} - \mathbf{R}_{I(i)} - (\mathbf{T_M} - \mathbf{T_N})\right) \\
&= e^{i\mathbf{k}\cdot\mathbf{T_N}} \sum_{i=1}^{\text{N}_{\text{occ}}} c_{in\mathbf{k}} \sum_{\mathbf{M}'} e^{i\mathbf{k}\cdot\mathbf{T_{M'}}} \phi_i \left(\mathbf{r} - \mathbf{R}_{I(i)} - \mathbf{T_{M'}}\right) \\
&= e^{i\mathbf{k}\cdot\mathbf{T_N}} \psi_{n\mathbf{k}}(\mathbf{r}).
\end{aligned} \tag{3.9}$$

Real-space, $\mathbf{k}$-dependent matrix elements of an operator $\hat{O}$ (e.g., the Hamiltonian operator) now have the form

$$O_{ij\mathbf{k}} \equiv \langle \chi_{i\mathbf{k}} | \hat{O} | \chi_{j\mathbf{k}} \rangle = \sum_{\mathbf{M},\mathbf{N}}{}' e^{i\mathbf{k}\cdot(\mathbf{T_N}-\mathbf{T_M})} \langle \phi_{i\mathbf{N}} | \hat{O} | \phi_{j\mathbf{M}} \rangle_{\text{uc}}. \tag{3.10}$$

The primed sum symbol indicates the fact that only basis functions that actually

have spatial overlap in the central unit cell add contributions. The corresponding real-space integrations are only carried out in the central unit cell by mapping back any outer contributions of periodic basis function images:

$$\langle \phi_{i\mathbf{N}} | \hat{O} | \phi_{j\mathbf{M}} \rangle_{\mathrm{uc}} = \int_{V_{\mathrm{uc}}} \mathrm{d}^3\mathbf{r}\, \phi_{i\mathbf{N}}\, \hat{O}\, \phi_{j\mathbf{M}}. \tag{3.11}$$

This simply means that non-zero spatial integration contributions outside the central unit cell are actually integrated in the central unit cell by exploiting the lattice symmetry. Any expectation value of an operator $\hat{O}$ is in the periodic case also carried out over **k**-space, as the Kohn-Sham orbitals depend on the **k**-vector:

$$O \equiv \langle \hat{O} \rangle = \frac{1}{V_{\mathrm{BZ}}} \int_{V_{\mathrm{BZ}}} \mathrm{d}^3\mathbf{k} \sum_{n=1}^{\mathrm{N_{occ}}} f_n \langle \psi_{n\mathbf{k}} | \hat{O} | \psi_{n\mathbf{k}} \rangle. \tag{3.12}$$

Here, V_{BZ} is the volume of the Brillouin zone which is effectively sampled with a discrete **k**-point mesh. This mesh (i.e., the density of the **k**-points or their alignment with respect to high-symmetry points) has to be chosen carefully, as e.g., metallic systems need a higher **k**-space resolution in order to handle the Fermi discontinuity [108].

Two different methods to compute the electron density $\rho(\mathbf{r})$ from input Kohn-Sham eigenvectors $\psi_n(\mathbf{r})$ are implemented in FHI-aims. The standard method is the simple evaluation of the expression

$$\rho(\mathbf{r}) = \sum_{n=1}^{\mathrm{N_{occ}}} f_n \psi_n^*(\mathbf{r}) \psi_n(\mathbf{r}) \tag{3.13}$$

(with the occupation numbers f_n), where a summand $\psi_n^*(\mathbf{r})\psi_n(\mathbf{r})$ must be built by a matrix product over $\mathrm{N_b} \times \mathrm{N_b}$ entries at *each* grid point **r** (see Eq. 3.1), making this an expensive operation in general, scaling as $\mathcal{O}(\mathrm{N_{at}^2})$ with a large prefactor. When the system size increases, a point will be reached where the number of occupied states $\mathrm{N_{occ}}$ becomes larger than the number of non-zero basis functions at this integration coordinate (due to the local character of the basis functions). At this point, it is numerically more favorable to update the electron density with the density matrix

$$\rho_{ij} = \sum_{n=1}^{\mathrm{N_{occ}}} f_n c_{in}^* c_{jn}, \tag{3.14}$$

$$\rho(\mathbf{r}) = \sum_{ij}^{\mathrm{N_b^{nz}}} \phi_i(\mathbf{r})\, \rho_{ij}\, \phi_j(\mathbf{r}), \tag{3.15}$$

where $\mathrm{N_b^{nz}}$ is the number of non-zero basis functions at this coordinate. This shrinks the scaling of the density update to $\mathcal{O}(\mathrm{N_{at}})$, greatly reducing the computational overhead. It is thus a very important property of the FHI-aims code to scale linearly with system size in this sense, allowing the efficient computation of large systems.

3.3 RT-TDDFT Functionality Integration

Within this section, we first present the code design and the paradigms which we followed in our implementation. We then outline the actual code structure and the workflow of a RT-TDDFT simulation. Thereafter, we discuss the important topic of parallelization and the different modes of operation. In this frame, we further discuss our strategies for optimization.

3.3.1 Approach

Before going into technical details of our implementation, we want to illustrate our general approach and the key concepts we followed throughout this work. The following points can be regarded as our implementation paradigms.

- **Modularization**: the RT-TDDFT functionality is provided as isolated module and itself is strictly modularized, allowing for future extensions. This incorporates two key ideas: first, the code itself is well-separated and organized inside the parent package in order to ease understanding by another programmer, possibly simplifying further code additions in the future or for maintenance. Currently, the RT-TDDFT module consists of 18 modules encapsulated in a corresponding subdirectory. Second, the existing codebase is only modified if absolutely necessary. This reduces the risk of incompatibilities and bugs. Most necessary modifications are related to real-space operations like density update and matrix integrations, e.g., to consider complex-valued eigenvectors.

- **Efficiency**: we used as much highly optimized numerical infrastructure as possible to make our own implementation maximally efficient for related operations. This also denotes the use of subroutines from optimized electronic structure libraries like the ELSI library [109] (e.g., for diagonalization or matrix inversion).

- **Parallel infrastructure**: as FHI-aims is a fully MPI-parallelized code package that has been tested for 1000s of atoms [42], our implementation was also built for full parallel support. This has several implications which we will demonstrate later. Overall, we parallelized all relevant operations according to the parent infrastructure. This mostly affects numerical linear algebra operations based on (Sca-)LAPACK [110, 111] or custom libraries.

- **Usability and readability**: the over 35000 lines of our commented Fortran90 code are kept very clean and conform to a strict coding format in order to ease future modifications. We integrated regression tests into the standardized test-suite which also serve educational purpose. Application control is interfaced

to the existing codebase in a separated and structured way. The existing manual was extended to describe the functionalities introduced by us and we tried to make the keywording transparent.

3.3.2 Code Structure and Workflow

In this chapter, we will provide a condensed picture of the general code structure and the workflow for real-time propagation simulations. The FHI-aims `main()` subroutine encapsulates any operation that is done with the software and incorporates, e.g., preprocessing, self-consistent field (SCF) calculation and post-processing. The RT-TDDFT functionality is called after any SCF operation and is thus integrated in the workflow in this manner.
The subroutine `rt_tddft()` is called from `main()` and will then call the subroutines

- `rt_tddft_initialization()`,
- `rt_tddft_run_propagation()`,
- `rt_tddft_finalize()`,

in this order. The corresponding RT-TDDFT workflow is depicted in Fig. 3.2 in a simplified general picture, including remarks about the specific operations.
With *module-global*, we denote arrays that RT-TDDFT modules/subroutines have access to via their defined scope of the parent module. Such arrays are not only needed for the storage of physical entities like the Hamiltonian, overlap matrix, eigenvectors, etc., but also for (Sca-)LAPACK work arrays. There is always a minimum number of such (`real` or `complex` type) arrays that are needed for numerical tasks and we pre-allocate these in order to reduce dynamical memory allocation within the sub-infrastructure. We further note that any (relevant) memory allocation is tracked by the recently introduced `aims_memory_tracking` infrastructure which allows real-time tracking and evaluation of memory consumption. It should be noted that we aimed to encapsulate most work arrays or other variables within the corresponding subroutine in order to avoid global access/tight coupling (which is prone to introducing bugs in the code), but on the other hand allowed global access to some numerical operation work arrays, logical flags or other variables that are related to the parent infrastructure.
The core modules (cf. Figure 3.2) `rt_tddft_initialization`, `rt_tddft_main` and `rt_tddft_finalization` contour the backbone of a RT-TDDFT simulation and each possibly utilizes some other core modules, e.g., `rt_tddft_observables_and_output` or `rt_tddft_time_propagation`. Since especially the latter is connected to several numerical and parallelization implications, we will present and discuss these characteristics in upcoming section and at later points. Regarding in- and output, we refer to the manual in Section A in the appendix. For a more detailed description and list of all incorporated modules, we refer to Section C in the appendix.

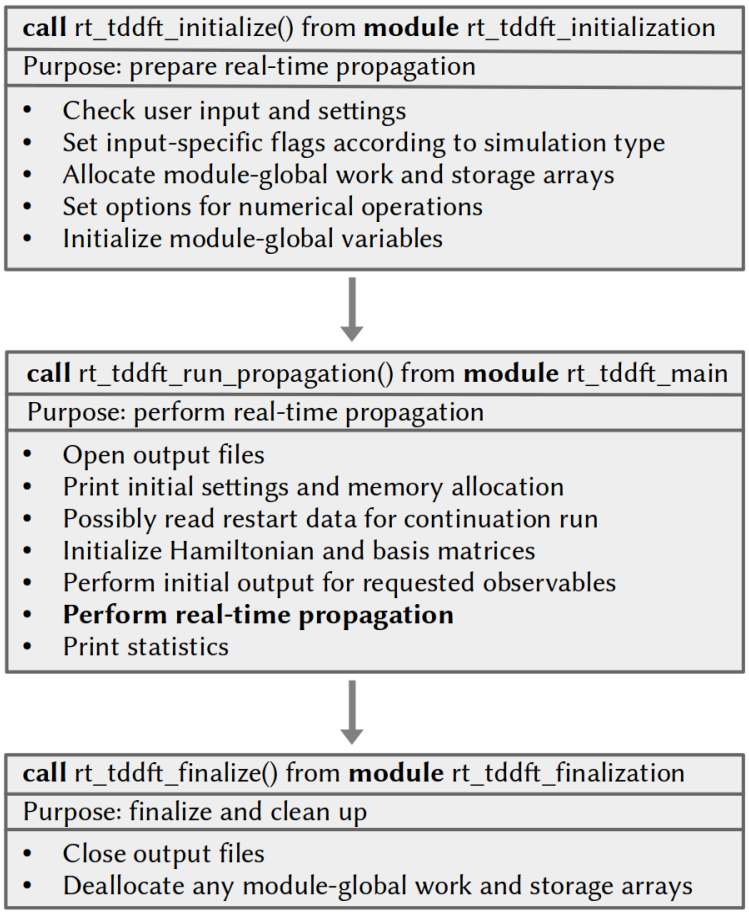

FIGURE 3.2: General workflow conducted when a real-time propagation is requested, as executed by the `rt_tddft()` subroutine within the FHI-aims `main()` subroutine.

3.3.3 Modes of Operation, Parallel Infrastructure and Optimization

Aside serial operation mode, i.e., code execution on a single process without MPI-parallelism, FHI-aims incorporates essentially two structurally different modes of operation, also depending on the type of calculation, e.g., whether one employs periodic boundary conditions or not. Also, in connection to the type of the calculation, the number of parallel tasks may impact the mode of operation employed (as explained further below). As our code is able to adapt to these different modes, we here elucidate these, as several numerical or memory-related implications arise.
The numerically most expensive parts can roughly be divided into two categories with specific parallel operability characteristics, namely

- **Real-space grid operations**: this denotes functionalities where operations are conducted over a large number of points in real space. Important examples here include the computation of the electronic density $\rho(\mathbf{r})$ or integration of real-space matrix elements like $\langle\phi_i|\mathcal{H}_{\mathrm{KS}}|\phi_j\rangle$ or $\langle\phi_i|\phi_j\rangle$ (and others). Typically, atom-centered integration grids are of order $\mathcal{O}(10^4)$ [42] with respect to the integration points. The parallel treatment is here to divide and distribute the

complete real-space grid in *batches* of $\mathcal{O}(100)$ grid points that are distributed onto processes (such that one process only has neighboring subvolumes) which then handle the required computation on relatively small data structures individually, also known as domain decomposition.

- **Matrix algebra**: despite the fact that most numerical operations in this context are conducted via some form of matrix operations, we here specifically refer only to operations that are performed with matrices of size $N_b \times N_b$ or $N_b \times N_{occ}$ (N_b is the number of basis functions and N_{occ} the number of occupied orbitals). The most prominent example in the ground-state case is the diagonalization of the Hamiltonian matrix $\mathbf{H} \in \mathbb{K}^{N_b \times N_b}$. In this case, the parallel treatment of numerical linear algebra operations depends on the system setup (periodic boundary conditions and number of **k**-points), which we will elucidate further.

Since we adapt the basic machinery for real-space grid operations in our implementation (with several modifications to serve our purpose), the parallelization and performance characteristics of FHI-aims in this sense directly transfer to the RT-TDDFT case. In contrast to this, the RT-TDDFT functionality incorporates a large amount of matrix algebra operations as defined above. FHI-aims includes numerical linear algebra support via the libraries (Sca)LAPACK [110, 111] or ELSI [109], also building the foundation of our implementation.
Before going into detail with the different modes, we will provide a short overview about the parallel data and numerical linear algebra infrastructure. For large dense matrices, the so-called block-cyclic distribution approach may be applied, as illustrated in Fig. 3.3. Typically, the global matrices being subject to the distribution have the dimension $N_b \times N_b$ or $N_b \times N_{occ}$. Large values for N_b in a still realistic context are of $\mathcal{O}(1000)$, i.e., the corresponding storage is in the range of several hundreds of MB for complex 16 Byte datatypes per process (without any additional multiplicators like spin, **k**-points, etc.).
Given a block-cyclic distribution of matrices, numerical linear algebra operations on the distributed process-local matrices can be performed without any inter-process communication and usually without any additional memory demand except preallocated required workspace. For the computation of global quantities, in this context, e.g., expectation values of operators, MPI-communication is required (like MPI_reduce or MPI_allreduce, see, e.g., Ref. [112] for details). Such operations cost additional simulation time and should only be applied when necessary.
We set up the given infrastructure for our purpose in order to profit from the highly efficient numerical linear algebra functionality. In case that parallel treatment or block-cyclic distribution based functionality cannot be used, our code operates in the standard serial LAPACK mode (as denoted by now). Else, we strictly employ use of local block-cyclically distributed matrices, also in order to reduce unnecessary memory demand; any real-space grid-related results are directly distributed.

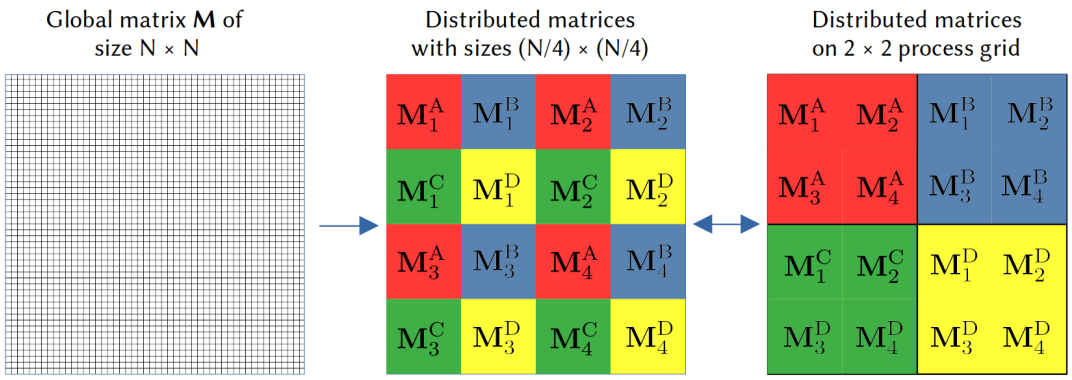

FIGURE 3.3: Illustration of 2D block-cyclic distribution of an N×N matrix into 16 local representations on a 2x2 process grid. For simplicity N is an even number here. Submatrices $\mathbf{M}_i^K$ with sub-index i and process index K. The process grid and block sizes are chosen for an optimal workload distribution.

Reduce operations are only conducted on few, unavoidable situations: update of electron density and potentials, geometry update and force calculations, calculation of observables. The pre-allocated workspace, i.e., work arrays, for numerical operations is minimized and depends on the mode of operation. Nevertheless, additional memory workspace may be allocated in the time evolution process, but can always be tracked (which applies to any allocation) and is predictable.
Concluding this topic, the following modes of operation are implemented (N_{proc} is the number of parallel processes and N_k is the number of **k**-points):

- **Non-periodic calculation with MPI:** ScaLAPACK mode with block-cyclic distribution and operation over all processes
- **Non-periodic calculation without MPI:** LAPACK (serial) mode with full storage and operations
- **Periodic calculation with MPI and** $N_{proc} > N_k$: ScaLAPACK mode with block-cyclic distribution and operation over **k**-points
- **Periodic calculation with MPI and** $N_{proc} \leq N_k$: LAPACK mode with full storage and operations with each process incorporating multiple **k**-points
- **Periodic calculation without MPI:** LAPACK mode with full storage and operation

Thus, for any type of calculation and any parallelization mode that is incorporated in the FHI-aims package, we offer the corresponding functionality for real-time TDDFT.

Regarding specific optimizations, the corresponding numerical operations are conducted appropriate to possible symmetries of the given objects (e.g., for Hermitian/symmetric/triangular/orthogonal/etc. matrices) and strictly within possible subspaces (e.g., only for occupied orbitals, and local dimensions of distributed matrices). If possible, only real (8 Byte) datatype arrays are used for basis matrices like,

e.g., the overlap matrix, the dipole matrix, and so on. Products between complex (16 Byte) and real matrices are strictly carried out as

$$\mathbf{A}_\mathrm{R}\mathbf{B}_\mathrm{C} = \mathbf{A}_\mathrm{R}\mathrm{Re}\{\mathbf{B}_\mathrm{C}\} + \mathbf{A}_\mathrm{R}\mathrm{Im}\{\mathbf{B}_\mathrm{C}\} \tag{3.16}$$

$$\mathbf{B}_\mathrm{C}\mathbf{A}_\mathrm{R} = \mathrm{Re}\{\mathbf{B}_\mathrm{C}\}\mathbf{A}_\mathrm{R} + \mathrm{Im}\{\mathbf{B}_\mathrm{C}\}\mathbf{A}_\mathrm{R}, \tag{3.17}$$

with $\mathbf{A}_\mathrm{R}$ being a real and $\mathbf{B}_\mathrm{C}$ being a complex matrix, i.e., avoiding unnecessary multiplications of zero-value imaginary parts. This strategy also improved the computation time for the density update significantly, as only the eigenvectors enter as complex quantities here (which is always the case in RT-TDDFT).
Further, we included several options that let the user control symmetry-specific and IO-specific optimizations. The selectable options are the following:

- The computation of observables (and required matrix elements) that have more than one dimension in the sense of Cartesian components, spin, etc., can be set such that only the desired dimension is computed and sent to output. For example, if only the z-component of the electronic dipole moment is of interest, only the corresponding components will be computed to save computational resources.
- Observables can be set to be only computed for their own time stepping, e.g., the total energy is only computed every N real-time simulation steps.
- Numerical stability indicators like the unitarity of the time-evolution operator are only computed on request.
- Different output levels can be set, meaning that a variable amount of console output is produced.
- Geometry constraints can be applied for all or individual directions, resulting in forces being only computed for active coordinates (in the case of Ehrenfest dynamics). This can yield large gains in efficiency, as force computations are comparably expensive.

For a complete description of the user-specified options and modes of operation, we refer to the manual in Section A of the appendix.

3.4 Numerical Time Propagation

This section introduces the formulation of the time-dependent Kohn-Sham equation in the given basis set, such that it can be solved by numerical linear algebra methods. We discuss some numerical implications arising from this approach and how external fields and non-local exchange operators are treated within the algorithms.

3.4.1 The Time-Dependent Kohn-Sham Equation in a Localized Basis

We reconcile here first the form of the initial value problem to solve, i.e., the time-dependent Kohn-Sham equation

$$i\frac{\partial}{\partial t}\psi_n(\mathbf{r},t) = \mathcal{H}_{\mathrm{KS}}[\rho(t),t]\psi_n(\mathbf{r},t) \quad \forall n \in \mathrm{N_{occ}}, \tag{3.18}$$

$$\psi_n(\mathbf{r},t=0) = \psi_n^{\mathrm{SCF}}(\mathbf{r}), \tag{3.19}$$

which – as indicated – has to be solved for all occupied states $\mathrm{N_{occ}}$ resulting from a former SCF ground-state calculation or another suitable initial preparation for the Kohn-Sham wave functions $\psi_n(\mathbf{r},t=0)$. We changed the notation of the time-dependent Kohn-Sham Hamiltonian from $\mathcal{H}_{\mathrm{KS}}(t)$ to $\mathcal{H}[\rho(t),t]$ in order to clarify the implicit time-dependence via the electron density and the explicit time - dependence via an external potential. The KS orbitals are expanded in a finite basis of non-orthogonal localized, atom-centered basis functions $\{\phi_j(\mathbf{r}-\mathbf{R}_{I(j)}) \equiv \phi_j(\mathbf{r})\}$,

$$\psi_n(\mathbf{r},t) = \sum_{j=1}^{\mathrm{N_b}} c_{in}(t)\phi_j(\mathbf{r}). \tag{3.20}$$

Given this expansion, Equation 3.18 has the form

$$i\sum_{j=1}^{\mathrm{N_b}}\left(\frac{\partial}{\partial t}c_{jn}(t)\right)\phi_j(\mathbf{r}) = \sum_{j=1}^{\mathrm{N_b}} c_{jn}(t)\mathcal{H}[\rho(t),t]\phi_j(\mathbf{r}). \tag{3.21}$$

Via multiplying both sides by $\phi_i(\mathbf{r})$ (which are real here) and integration over the whole relevant volume V, above equation is written as

$$i\sum_{j=1}^{\mathrm{N_b}}\left(\frac{\partial}{\partial t}c_{jn}(t)\right)\int_V \mathrm{d}^3\mathbf{r}\,\phi_i(\mathbf{r})\phi_j(\mathbf{r}) = \sum_{j=1}^{\mathrm{N_b}} c_{jn}(t)\int_V \mathrm{d}^3\mathbf{r}\,\phi_i(\mathbf{r})\mathcal{H}[\rho(t),t]\phi_j(\mathbf{r}). \tag{3.22}$$

For simplicity, we will from now on employ matrix notation,

$$\mathrm{S}_{ij} = \int_V \mathrm{d}^3\mathbf{r}\,\phi_i(\mathbf{r})\phi_j(\mathbf{r}), \tag{3.23}$$

$$\mathrm{H}_{ij}[\rho(t),t] = \int_V \mathrm{d}^3\mathbf{r}\,\phi_i(\mathbf{r})\mathcal{H}_{\mathrm{KS}}[\rho(t),t]\phi_j(\mathbf{r}), \tag{3.24}$$

$$\mathrm{C}_{in}(t) = c_{in}(t), \tag{3.25}$$

resulting in the following system of (non-linear) differential equations for the time-dependent KS expansion coefficients,

$$i\mathbf{S}\frac{\partial}{\partial t}\mathbf{C}(t) = \mathbf{H}[\rho(t),t]\mathbf{C}(t), \tag{3.26}$$

with the overlap matrix $\mathbf{S} \in \mathbb{K}^{\mathrm{N_b}\times\mathrm{N_b}}$, the Hamiltonian matrix $\mathbf{H} \in \mathbb{K}^{\mathrm{N_b}\times\mathrm{N_b}}$ and the eigencoefficient matrix $\mathbf{C} \in \mathbb{C}^{\mathrm{N_b}\times\mathrm{N_{occ}}}$. This representation is in this case actually

used when solving the TDKS equation numerically, i.e., by numerical linear algebra methodology.

3.4.2 Numerical Considerations

The properties of $\mathbf{S}$ and $\mathbf{H}$ have substantial implications for the numerical implementation and treatment. The solution of Eq. 3.26 can be very sensitive to certain properties, as we will explain now. When writing Eq. 3.26 as

$$\frac{\partial}{\partial t}\mathbf{C}(t) = -i\mathbf{S}^{-1}\mathbf{H}[\rho(t), t]\mathbf{C}(t), \tag{3.27}$$

one can easily see that the inverse overlap matrix $\mathbf{S}^{-1}$ may be a problematic object. Considering the eigendecomposition of $\mathbf{S}$,

$$\mathbf{S} = \mathbf{\Sigma}_\mathbf{S}\mathbf{\Lambda}_\mathbf{S}\mathbf{\Sigma}_\mathbf{S}^T \tag{3.28}$$

where $\Lambda_{S,ij} = \sigma_i\delta_{ij}$ is the diagonal matrix containing the eigenvalues of $\mathbf{S}$ and $\mathbf{\Sigma}_\mathbf{S} = (\sigma_1, ..., \sigma_{\mathrm{N_b}})$ holds the orthogonal eigenvectors, i.e., $\mathbf{\Sigma}^{-1} = \mathbf{\Sigma}^T$. Given this, $\mathbf{S}^{-1}$ can be written as

$$\mathbf{S}^{-1} = \mathbf{\Sigma}_\mathbf{S}\mathbf{\Lambda}_\mathbf{S}^{-1}\mathbf{\Sigma}_\mathbf{S}^T. \tag{3.29}$$

When the basis set size crosses the over-completeness limit by adding too many or very diffuse basis functions, the overlap matrix $\mathbf{S}$ contains linearly dependent axes and very small eigenvalues σ_i occur, leading to numerical problems, i.e., $\mathbf{S}$ is singular or, equivalently, ill-conditioned [109, 113]. We introduce the condition number of a (symmetric) matrix $\mathbf{M}$ for later use,

$$\kappa(\mathbf{M}) = ||\mathbf{M}||\,||\mathbf{M}^{-1}||, \tag{3.30}$$

which is a large number in the case of ill-conditioning (note that κ depends on the chosen norm). Ill-conditioning of $\mathbf{S}$ is often defined by the lowest eigenvalue $\sigma_{i,\mathrm{min}} \leq 10^{-5}$ [113] and we will discuss ways to handle this problem at a later point.

Other important considerations become clear when writing the general solution of Eq. 3.27 similar to Eq. 2.91 in the theory part as

$$\mathbf{C}(t) = \hat{\mathcal{T}}\exp\left(-i\mathbf{S}^{-1}\int_0^t \mathbf{H}[\rho(t'), t']\mathrm{d}t'\right)\mathbf{C}(0). \tag{3.31}$$

First of all, one can see that the exponential of a matrix has to be computed (which we will also cover in more detail later). Second, since the solution is essentially given by a complex exponential function, it becomes clear that this is in general an oscillatory problem which is characterized by the eigenvalues of the Hamiltonian matrix. In this framework we even have to consider the all-electron character, which increases

the eigenvalue spectrum of **H** to very negative values. For numerical considerations, it plays an important role whether deep eigenvalues are "active" in a sense of corresponding to external excitation: the deepest time-dependent eigenvalue will in this case set a limit to the numerical time step that yields correct results for the active modes – we will consider this further in Chapter 6 (numerical details).

As noted in Section 2.2.4, the Hamiltonian can be coupled to the external field via the length or the velocity gauge. In our implementation, this is handled in the following ways:

- **Length gauge**: the potential term $V_{\text{ext}}(\mathbf{r}, t) = -\mathbf{r} \cdot \mathbf{E}(t)$ is directly added to the remaining potential terms within the real-space integration loop. This is not associated with any significant computational or memory cost.
- **Velocity gauge**: since the real-space integration of the Hamiltonian matrix elements is conducted on real-valued datatype arrays only (before possible **k**-dependence is obtained in a periodic calculation), the strategy to include the complex-valued velocity gauge matrix elements is different. We store the matrix elements $G_{\mu,ij} = \langle \phi_i | \partial_\mu | \phi_j \rangle$ (which are often needed for other operations, too) in order to add the VG matrix to the whole $\mathrm{N}_b \times \mathrm{N}_b$ Hamiltonian matrix, i.e.,
$$H_{ij}[\rho(t), t] = H_{ij}[\rho(t)] - i\mathbf{A}(t) \cdot \mathbf{G}_{ij} + \frac{1}{2}\mathbf{A}^2(t) S_{ij} \tag{3.32}$$
where **S** is the overlap matrix that is always available. In case of periodic boundary conditions, the respective matrices are naturally **k**-dependent.

We also included support for hybrid exchange-correlation functionals and thus need to discuss some implications of this circumstance. As elaborated in Section 2.1.4, this means that exact Hartree-Fock exchange is incorporated in the XC functional. This translates into the Hamiltonian incorporating a corresponding non-local exchange potential operator. Its time-dependent matrix elements in the given basis set are given by
$$\Sigma^x_{ij}(t) = \sum_{kl}^{\mathrm{N_b}} \rho_{kl}(t)(ik|lj) \tag{3.33}$$
which is also called the exchange matrix [97]. Here, the time-dependent density matrix
$$\rho_{kl}(t) = \sum_{n=1}^{\mathrm{N_{occ}}} f_n c^*_{kn}(t) c_{ln}(t) \tag{3.34}$$
is incorporated and the four-center two-electron integral is given by
$$(ik|lj) = \int\int \mathrm{d}^3\mathbf{r}\, \mathrm{d}^3\mathbf{r}'\, \phi_i(\mathbf{r})\phi_k(\mathbf{r}) \frac{1}{|\mathbf{r} - \mathbf{r}'|} \phi_l(\mathbf{r}')\phi_j(\mathbf{r}'). \tag{3.35}$$

In FHI-aims, the matrix elements $(ik|lj)$ are computed by the so-called Resolution-of-Identity (RI) approach [97] where one exploits that large amounts of pairs $\phi_i(\mathbf{r})\phi_j(\mathbf{r})$ are linearly dependent. This makes the computation of these matrix elements, which is in principle a memory- and computation-expensive operation, more efficient. Some versions of this approach are incorporated in FHI-aims and we refer the reader to the manual [114] and the relevant literature [97].
An important point when considering explicit time-propagation is that the imaginary part of the density matrix in Eq. 3.33 cannot be neglected, in contrast to the time-independent case (using purely real basis functions) [115]. This makes the exchange matrix an intrinsically complex (Hermitian) matrix and the time-dependent Hamiltonian matrix with exact exchange reads

$$H_{ij}[\rho(t),t] = H_{ij}^{\text{base}}[\rho(t),t] + \alpha\Sigma_{ij}^{x}(t), \tag{3.36}$$

where the part denoted by 'base' includes the kinetic, Hartree, external potential and remaining exchange-correlation matrix elements, and α is a mixing parameter (cf. Section 2.1.3). The mixing parameter and the remaining XC matrix elements depend on the type of hybrid functional. Thus, in this case, we always have a full complex Hamiltonian matrix, which the algorithm adapts to. Note that major computational effort here is the computation of $(ik|lj)$ – however, for fixed nuclei, this is only performed once. Thus, only the exchange matrix needs to be evaluated via the density matrix and is then added to the Hamiltonian matrix at every time step.

3.5 Exponential-Based Propagators

In this chapter, we introduce exponential-based propagators used for the solution of the time-dependent Kohn-Sham equation, discuss the formal basis given by the Magnus expansion, and introduce some approximations used in practice. We further discuss numerical techniques needed for the computation of matrix exponentials.

3.5.1 General Considerations

As demonstrated in the last chapter, the time-dependent Kohn-Sham equation can be reduced to the initial value problem (IVP)

$$\frac{\partial}{\partial t}\mathbf{C}(t) = \mathbf{M}(t)\mathbf{C}(t) \tag{3.37}$$

with $\mathbf{M}(t) = -i\mathbf{S}^{-1}\mathbf{H}(t)$. A simple approach to solve this IVP numerically could, e.g., be to formulate it via the explicit Euler scheme

$$\mathbf{C}(t+\Delta t) = \mathbf{C}(t) + \Delta t\mathbf{M}\left(t\right)\mathbf{C}\left(t\right) \tag{3.38}$$

or via an explicit Runge-Kutta method, see Ref. [56]. However, this will certainly only work for extremely small time steps Δt, as the matrix $\mathbf{M}$ has very high, purely imaginary eigenvalues (by the structure of the Hamiltonian), making the solution extremely fast oscillating – in other words, this IVP corresponds to a *stiff* problem [116]. One could argue that implicit Euler, Runge-Kutta, or other such schemes would resolve the stiffness issue, as they possess much better stability. But also these methods require an excessively small time step in order to handle the high accuracy requirement imposed by the strong oscillatory character of the solution [116, 117, 118].
This leads to the class of exponential-based propagators, founded on the idea to define an integrator that is structurally equivalent and thus has the same stiffness properties as the underlying equation's solution. In a very general sense, this would here correspond to a solution

$$\mathbf{C}(t) = \exp(\bar{\mathbf{M}})\mathbf{C}(t_0) \tag{3.39}$$

(with some unknown exact form of $\bar{\mathbf{M}}$) which contains the full oscillatory character and preserves this information. For such integrators, it could be shown that the error of the problem's numerical solution is actually not necessarily bound by the highest frequencies (i.e., eigenvalues of $\mathbf{H}$) of the system [116]. Many of the vivid developments of numerical integration schemes for the Schrödinger or the KS equation were achieved for this class of propagators [117, 119, 120, 121].
For these reasons, we focused on exponential propagation schemes in our implementation and set up a framework that can also easily be expanded for additional schemes belonging to this class. In the following, we will give an overview about this functionality. For completeness, we note some exponential integrators that we do not cover here explicitly, but that are relevant in the community: split-operator propagation, integrating factor method and exponential time-differencing – a good review of these methods is given by Kidd et al. [120].

3.5.2 Magnus Expansion

The general approach is, when considering the linear differential equation

$$\dot{\mathbf{X}}(t) = \mathbf{M}(t)\mathbf{X}(t) \ , \quad \mathbf{X}(t=0) = \mathbf{X}_0, \tag{3.40}$$

where $\mathbf{X} \in \mathbb{K}^{N\times M}$ and $\mathbf{M} \in \mathbb{K}^{N\times N}$, to write the general solution as

$$\mathbf{X}(t) = \exp\big(\mathbf{\Omega}(t)\big)\mathbf{X}_0, \tag{3.41}$$

where $\mathbf{\Omega}(t) \in \mathbb{K}^{N\times N}$ is a matrix that has to be determined. Magnus [122] derived an explicit differential equation for $\mathbf{\Omega}(t)$ that involves an infinite series of nested

commutators:

$$\dot{\mathbf{\Omega}}(t) = \mathbf{M}(t) - \frac{1}{2}\big[\mathbf{\Omega}(t), \mathbf{M}(t)\big] + \frac{1}{12}\Big[\mathbf{\Omega}(t), \big[\mathbf{\Omega}(t), \mathbf{M}(t)\big]\Big] + \dots . \tag{3.42}$$

By Picard iteration, the solution can be written down as infinite sum of integrals of commutators only involving the matrix $\mathbf{M}(t)$. This is commonly denoted as the *Magnus Expansion* [123] and is given by

$$\begin{aligned}\mathbf{\Omega}(t) &= \int_0^t \mathrm{d}\tau_1\, \mathbf{M}(\tau_1) - \frac{1}{2}\int_0^t \mathrm{d}\tau_2 \left[\int_0^{\tau_1} \mathrm{d}\tau_2\, \mathbf{M}(\tau_2), \mathbf{M}(\tau_1)\right] \\ &\quad + \frac{1}{6}\int_0^t \mathrm{d}\tau_1 \left[\int_0^{\tau_1} \mathrm{d}\tau_2 \left[\int_0^{\tau_2} \mathrm{d}\tau_3\, \mathbf{M}(\tau_3), \mathbf{M}(\tau_2)\right] \mathbf{M}(\tau_1)\right] + \dots \\ &= \sum_{l=1}^{\infty} \mathbf{\Omega}_l(t). \end{aligned} \tag{3.43}$$

Each element $\mathbf{\Omega}_l(t)$ in this series contains an l-fold integral and l-1 nested commutators of $\mathbf{M}$. Based on a truncated expansion of order N,

$$\mathbf{\Omega}^{(\mathrm{N})}(t) = \sum_{l=1}^{\mathrm{N}} \mathbf{\Omega}_l(t), \tag{3.44}$$

numerical schemes to solve Eq. 3.40 can be obtained by first discretizing in time and then evolving the solution from the discrete timestep t_k to the next timestep $t_k + \Delta t$, Δt denoting a constant stepsize. The most general discretized-time solution of Eq. 3.40 now reads

$$\mathbf{X}(t_k + \Delta t) = \exp\left(\mathbf{\Omega}^{(\mathrm{N})}(t_k + \Delta t)\right)\mathbf{X}(t_k) \equiv \mathbf{U}^{(\mathrm{N})}_{\mathrm{Mag}}(t_k + \Delta t, t_k)\mathbf{X}(t_k) \tag{3.45}$$

and it can be shown [118] that the truncated Magnus expansion based propagator $\mathbf{U}^{(\mathrm{N})}_{\mathrm{Mag}}(t_k + \Delta t, t_k)$ coincides with the exact Magnus expansion propagator up to $\mathrm{N}+1$ th order, i.e., the error is [118]

$$\epsilon = \left|\left| \exp\left(\mathbf{\Omega}(t_k + \Delta t)\right) - \mathbf{U}^{(\mathrm{N})}_{\mathrm{Mag}}(t_k + \Delta t, t_k)\right|\right| \in \mathcal{O}\left(\Delta t^{\mathrm{N}+1}\right). \tag{3.46}$$

The l-fold integrals in the summands $\mathbf{\Omega}_l(t_k + \Delta t)$ can be simplified by a Legendre expansion of $\mathbf{M}(t_k + \Delta t)$ [124], yielding expansion coefficients

$$\tilde{\mathbf{M}}_m = (2m-1)\Delta t \int_0^1 \mathrm{d}\sigma\, \mathbf{M}(\sigma\Delta t) P_{m-1}(\sigma) \tag{3.47}$$

for each $m = 1, \dots, l$ and $P_i(x)$ being Legendre polynomials, resulting in all multi-dimensional integrals in every $\mathbf{\Omega}_l$ being replaced by one-dimensional integrals, possibly including commutators of $\tilde{\mathbf{M}}_m$.
This finally yields numerical methods to solve Eq. 3.40. In this frame, the actual

differential equation will be solved for the expansion coefficients $\mathbf{C}_n(t)$ with

$$\mathbf{M}(t) = -i\mathbf{S}^{-1}\mathbf{H}(t), \tag{3.48}$$

which means that for $\mathbf{\Omega}_{\mathrm{KS}}(t)$, the time-dependent Kohn-Sham Hamiltonian matrix has to be evaluated at possibly different points on the time axis. This notation somehow hides the fact that $\mathbf{H}(t)$ is not a simple expression that can be straightfowardly evaluated for a given time t, as the time-dependent Kohn-Sham Hamiltonian implicitly depends on the solution of the TDKS equation via the electron density. This makes it very difficult to construct higher-order Magnus expansions for numerical integrators in an exact (self-consistent) way, as different points in time need to be considered.
Different approaches have produced a variety of Magnus expansion-based exponential propagation schemes, from which several were incorporated in our implementation and of which some will be introduced below.

3.5.3 Exponential Midpoint Scheme

The exponential midpoint (EM) scheme is one of the most widely used exponential propagators for solving time-dependent Schrödinger-like equations, also in the real-time TDDFT community [87, 120, 121, 125].
The EM propagator is obtained from the Magnus expansion in two steps. The first step is to neglect any commutators in the time-discretized expansion, yielding only

$$\mathbf{\Omega}_{\mathrm{KS}}(t) = -i\mathbf{S}^{-1}\int_{t_k}^{t_k+\Delta t} \mathrm{d}\tau\, \mathbf{H}(\tau). \tag{3.49}$$

In the second step, the integral over the Hamiltonian matrix is evaluated via the standard midpoint quadrature rule [125]

$$\int_a^b \mathrm{d}x\, f(x) \approx (b-a) f\left(\frac{b-a}{2}\right), \tag{3.50}$$

eventually defining the EM propagator for the time-dependent Kohn-Sham expansion coefficients via

$$\mathbf{U}^{\mathrm{EM}}(t_k+\Delta t, t_k) \equiv \exp\left(\mathbf{\Omega}^{\mathrm{EM}}_{\mathrm{KS}}(t_k+\Delta t)\right) = \exp\left(-i\Delta t\mathbf{S}^{-1}\mathbf{H}\left(t_k+\frac{\Delta t}{2}\right)\right) \tag{3.51}$$

which results in an implicit numerical integration scheme. This propagator in principle conserves time-reversal symmetry and is unitary (if obtained self-consistently with a sufficiently good method for the matrix exponential) [87]. The error of this method is given by

$$\epsilon = \left|\left| \exp\left(\mathbf{\Omega}(t_k+\Delta t)\right) - \mathbf{U}^{\mathrm{EM}}(t_k+\Delta t, t_k)\right|\right| \in \mathcal{O}\left(\Delta t^2\right). \tag{3.52}$$

Several studies showed that the EM scheme is quite robust with respect to cost vs. accuracy, making it a solid choice [119, 121].

3.5.4 Commutator-Free Magnus Expansion 4 Scheme

The evaluation of (nested) commutators in any Magnus expansion method of higher order than 1 can be considered as comparatively costly operation, especially for large input matrices. While this is not necessarily a problem in every implementation, it has still led to a class of commutator-free Magnus Expansion-based propagators which possess desirable numerical properties beside reduced computational cost [121, 123, 124, 126] .
The general idea to avoid commutator evaluations is to find an approximation of the form

$$\mathbf{X}(t_k + \Delta t) \approx \exp\left(\mathbf{\Omega}_k^{(1)}\right) \exp\left(\mathbf{\Omega}_k^{(2)}\right) ... \exp\left(\mathbf{\Omega}_k^{(N_M)}\right) \mathbf{X}(t_k) \tag{3.53}$$

that does not include any commutators of the matrix $\mathbf{M}$ as in Eq. 3.43 but only sums, including evaluations of it at different points in time, $t_m \in [t_k, t_k + \Delta t]$,

$$\mathbf{\Omega}_k^{(l)} = \Delta t \sum_{m=1}^{\mathrm{M}} \alpha_{lm} \tilde{\mathbf{M}}_m, \tag{3.54}$$

for all $l = 1, ..., \mathrm{N_M}$ where $\mathrm{N_M}$ denotes the product order of the involved exponentials, M denotes the sum order and $\tilde{\mathbf{M}}_m = \mathbf{M}(t_k + c_m \Delta t)$ with some coefficient c_m. In fact, $\mathrm{N_M}$, M and the weight coefficients α_{lm}, c_m are to be determined such that the overall error of this expansion is of a given order $O + 1$, where O denotes the order of the commutator-free Magnus expansion, relative to the former general solution as in Eq. 3.45. Specifically, given the order O commutator-free Magnus expansion propagator,

$$\mathbf{U}^{\mathrm{CFM}(O)}(t_k + \Delta t, t_k) \equiv \exp\left(\mathbf{\Omega}_k^{(1)}\right) \exp\left(\mathbf{\Omega}_k^{(2)}\right) ... \exp\left(\mathbf{\Omega}_k^{(\mathrm{N_M})}\right), \tag{3.55}$$

the relative error introduced will be

$$\epsilon = \left|\left| \exp\left(\mathbf{\Omega}(t_k + \Delta t)\right) - \mathbf{U}^{\mathrm{CFM}(O)}(t_k + \Delta t, t_k) \right|\right| \in \mathcal{O}\left(\Delta t^{O+1}\right) \tag{3.56}$$

which allows the systematic construction of a commutator-free Magnus expansion for a desired order. The 4-th order CFM scheme is given as

$$\mathbf{U}^{\mathrm{CFM}(4)}(t_k + \Delta t, t_k) = \exp\left(\mathbf{\Omega}_k^{(1)}\right) \exp\left(\mathbf{\Omega}_k^{(2)}\right) \tag{3.57}$$

$$\alpha_{11} = \alpha_{12} = \frac{1}{4} - \frac{\sqrt{3}}{6} \tag{3.58}$$

$$\alpha_{12} = \alpha_{21} = \frac{1}{4} + \frac{\sqrt{3}}{6} \tag{3.59}$$

$$c_{1/2} = \frac{1}{2} \mp \frac{\sqrt{6}}{6}. \tag{3.60}$$

3.5.5 Matrix Exponentials

All exponential-based propagators require the computation of the exponential function of a matrix, i.e., formally

$$\exp(\mathbf{M}) = \sum_{l=0}^{\infty} \frac{1}{l!} \mathbf{M}^l \tag{3.61}$$

with $\mathbf{M} \in \mathbb{K}^{\mathrm{N}\times\mathrm{N}}$ always incorporating the Hamiltonian matrix in some form, depending on the actual propagation scheme, i.e., $\mathbf{M} = -i\mathbf{f}(\mathbf{H}_{\mathrm{KS}})$. The computation of a matrix exponential can be done in many different ways [127] and the efficiency and accuracy of this highly depend on the underlying dynamics and on the shape and properties of the matrix $\mathbf{M}$.

Probably the first quantity to consider in the frame of electronic structure theory is the dimension N, here given as the number of basis functions N_b used to expand the Kohn-Sham wave functions. In plane-wave approaches, N_b can be a very large number, e.g., around 10^5 [87], even prohibiting the memory storage of the full Hamiltonian matrix on a single computation node and imposing sparse matrix usage, also restricting the methods for the computation of the matrix exponential. In this case, Krylov subspace projection in combination with the Lanczos procedure is very efficient [87, 127]. When using localized basis functions like Gaussians or numerical basis sets, like in the FHI-aims code, i.e., in this implementation, N_b is typically much smaller compared to the plane-wave approach. For many RT-TDDFT applications, N_b is of $\mathcal{O}(10)$ per atom, enabling the use of quite straightforward methods based on eigendecomposition or series expansions, as described later. Actually, for a wide range of molecular and extended systems, the real-space operations are at *least* one order higher in computational cost relative to most matrix operations like multiplication, inversion or diagonalization.

Other properties of a general matrix $\mathbf{M}$ further affecting the range of applicable methods and their numerical implementations are, e.g., whether it is Hermitian, invertible, positive definite, etc.

Before we elucidate further on methods of the matrix exponential calculation, we first need to go back to the time-dependent Kohn-Sham equation for the expansion coefficients of the chosen atomic basis,

$$\mathbf{S}\dot{\mathbf{C}} = -i\mathbf{H}\mathbf{C} \quad \Leftrightarrow \quad \dot{\mathbf{C}} = -i\mathbf{S}^{-1}\mathbf{H}\mathbf{C} \tag{3.62}$$

with the eigencoefficients $\mathbf{C} \in \mathbb{C}^{\mathrm{N_b}\times\mathrm{N_{occ}}}$, the Hamiltonian matrix $\mathbf{H} \in \mathbb{K}^{\mathrm{N_b}\times\mathrm{N_b}}$ and the overlap matrix $\mathbf{S} \in \mathbb{K}^{\mathrm{N_b}\times\mathrm{N_b}}$. The right hand side equivalence may actually be an undesired representation of this equation because $\mathbf{S}^{-1}\mathbf{H}$ is not Hermitian anymore – which is in practice a very useful property of $\mathbf{H}$.
We will introduce two different representations for Eq. 3.62, both making use of different matrix decompositions of the overlap matrix. Both methods are part of our implementation, with the first one being default and the second one automatically switching on when the overlap matrix is ill-conditioned (i.e., having very small eigenvalues) due to an overcomplete basis set.

Preparation 1: Power Decomposition We rewrite Equation 3.62 as

$$\mathbf{S}^{\frac{1}{2}}\mathbf{S}^{\frac{1}{2}}\dot{\mathbf{C}} = -i\mathbf{H}\mathbf{C} \tag{3.63}$$

$$\Leftrightarrow \quad \mathbf{S}^{\frac{1}{2}}\dot{\mathbf{C}} = -i\mathbf{S}^{-\frac{1}{2}}\mathbf{H}\mathbf{S}^{-\frac{1}{2}}\mathbf{S}^{\frac{1}{2}}\mathbf{C}, \tag{3.64}$$

and by redefining $\mathbf{C}' \equiv \mathbf{S}^{\frac{1}{2}}\mathbf{C}$, $\mathbf{H}' \equiv \mathbf{S}^{-\frac{1}{2}}\mathbf{H}\mathbf{S}^{-\frac{1}{2}}$ we arrive at

$$\dot{\mathbf{C}}' = -i\mathbf{H}'\mathbf{C}' \tag{3.65}$$

where $(\mathbf{H}')^\dagger = \mathbf{H}'$ can be exploited [128]. The matrices $\mathbf{S}^{\pm\frac{1}{2}}$ are obtained from the eigendecomposition of $\mathbf{S}$ (which is always symmetric or Hermitian and thus diagonalizable),

$$\begin{aligned}\mathbf{S}^{\pm\frac{1}{2}} &= \mathbf{\Sigma}_\mathbf{S}\mathbf{\Lambda}_\mathbf{S}^{\pm\frac{1}{2}}\mathbf{\Sigma}_\mathbf{S}^\dagger \\ &= \mathbf{\Sigma}_\mathbf{S}\,\mathrm{diag}(\sigma_1^{\pm\frac{1}{2}},...,\sigma_{\mathrm{N}_b}^{\pm\frac{1}{2}})\mathbf{\Sigma}_\mathbf{S}^\dagger,\end{aligned} \tag{3.66}$$

with $\mathbf{\Sigma}_\mathbf{S} \in \mathbb{K}^{\mathrm{N}_b\times\mathrm{N}_b}$ being the eigenvector matrix of $\mathbf{S}$ and $\mathbf{\Lambda} \in \mathbb{R}^{\mathrm{N}_b\times\mathrm{N}_b}$ with $\Lambda_{ij} = \sigma_i\delta_{ij}$ containing the eigenvalues of $\mathbf{S}$ on the diagonal.
Solving Eq. 3.65 by a Magnus expansion scheme results in

$$\mathbf{C}'(t_k+\Delta t) = \exp\Big(\mathbf{\Omega}(\mathbf{H}')\Big)\mathbf{C}'(t_k) \equiv \mathbf{U}'(t_k+\Delta t, t_k)\mathbf{C}'(t_k), \tag{3.67}$$

i.e., the exponential is calculated for some expression of $\mathbf{\Omega}(\mathbf{H}')$ incorporating the transformed Hamiltonian matrix $\mathbf{H}'$. The actual solution requires backtransformation of $\mathbf{C}'(t)$ to $\mathbf{C}(t)$ and the final result will read

$$\mathbf{C}(t_k+\Delta t) = \mathbf{S}^{-\frac{1}{2}}\,\mathbf{U}'(t_k+\Delta t, t_k)\,\mathbf{S}^{\frac{1}{2}}\,\mathbf{C}(t_k). \tag{3.68}$$

Preparation 2: Eigendecomposition This approach is directly based on the eigendecomposition of the overlap matrix and can be used to actively mitigate effects of an ill-conditioned overlap matrix [109]. Let us consider

$$\mathbf{S} = \mathbf{\Sigma_S}\, \mathbf{\Lambda_S}\, \mathbf{\Sigma_S^\dagger} \equiv \tilde{\mathbf{\Sigma}}_\mathbf{S}\, \tilde{\mathbf{\Sigma}}_\mathbf{S}^\dagger, \tag{3.69}$$

with $\mathbf{S}$, $\mathbf{\Sigma_S} \in \mathbb{K}^{N_b \times N_b}$, and where we used the scaled eigenvectors $\tilde{\Sigma}_{ij} = \sqrt{\sigma_i}\Sigma_{ij}\, \forall i,j \in N_b$ on the right hand side, where $\{\sigma_i\}$ are the eigenvalues. At this point, one can check for problematic eigenvalues $\sigma_i \leq \sigma_{\text{thresh}}$ where σ_{thresh} is a defined threshold, in this case 10^{-5} as per default in the FHI-aims software. One can now exclude the corresponding problematic eigenvectors, i.e., define

$$\bar{\Sigma}_{ij} = \sqrt{\sigma_i}\Sigma_{ij}\, \forall i \in N_b\ ,\ \forall j \in N_{ns} \tag{3.70}$$

where $N_{ns} < N_b$ is the number of non-singular eigenvectors. We now have $\bar{\mathbf{\Sigma}}_\mathbf{S} \in \mathbb{K}^{N_b \times N_{ns}}$ and thus for the TDKS equation

$$\bar{\mathbf{S}}\dot{\mathbf{C}} = -i\mathbf{H}\mathbf{C} \tag{3.71}$$

$$\Leftrightarrow\ \bar{\mathbf{\Sigma}}_\mathbf{S}\, \bar{\mathbf{\Sigma}}_\mathbf{S}^\dagger \dot{\mathbf{C}} = -i\mathbf{H}\mathbf{C} \tag{3.72}$$

$$\Leftrightarrow\ \bar{\mathbf{\Sigma}}_\mathbf{S}^\dagger \dot{\mathbf{C}} = -i\bar{\mathbf{\Sigma}}_\mathbf{S}^{-1}\mathbf{H}\bar{\mathbf{\Sigma}}_\mathbf{S}^{-\dagger}\bar{\mathbf{\Sigma}}_\mathbf{S}^\dagger\mathbf{C}. \tag{3.73}$$

Based on this, we define $\bar{\mathbf{C}} \equiv \bar{\mathbf{\Sigma}}_\mathbf{S}^\dagger$ and $\bar{\mathbf{H}}_{\text{KS}} \equiv \bar{\mathbf{\Sigma}}_\mathbf{S}^{-1}\mathbf{H}\bar{\mathbf{\Sigma}}_\mathbf{S}^{-\dagger}$ and the transformed TDKS equation reads

$$\dot{\bar{\mathbf{C}}} = -i\bar{\mathbf{H}}\bar{\mathbf{C}} \tag{3.74}$$

with $\bar{\mathbf{C}} \in \mathbb{C}^{N_{ns} \times N_{occ}}$ and most notably $\bar{\mathbf{H}} \in \mathbb{K}^{N_{ns} \times N_{ns}}$, i.e., the Hamiltonian matrix is now of reduced dimension because $N_{ns} < N_b$. Nevertheless, the TDKS equation is still valid [109].
Similar to above discussion of the power decomposition, the solution to Eq. 3.74 via the Magnus expansion approach reads

$$\bar{\mathbf{C}}(t_k + \Delta t) = \exp\left(\mathbf{\Omega}(\bar{\mathbf{H}})\right)\bar{\mathbf{C}}(t_k) \equiv \bar{\mathbf{U}}(t_k + \Delta t, t_k)\bar{\mathbf{C}}(t_k) \tag{3.75}$$

with the transformed Hamiltonian matrix. The time-propagated eigenvectors are here given by back-transformation via

$$\mathbf{C}(t_k + \Delta t) = \mathbf{\Sigma_S^{-\dagger}}\, \bar{\mathbf{U}}(t_k + \Delta t, t_k)\, \mathbf{\Sigma_S^\dagger}\mathbf{C}(t_k). \tag{3.76}$$

With above preparation for the formulation of the propagator, we now come back to the discussion of the actual computation of matrix exponentials. Depending on the specific propagation scheme, one (EM) or multiple (CFM4) exponentials have to be calculated in order to construct the propagator $\mathbf{U}(t_k + \Delta t, t_k)$ (see, e.g., Ref. [123] for

some other common Magnus propagators). In principle, this can be a costly computation and should be implemented as efficient – but also as accurate – as possible. The three approaches implemented into our code are presented now formally, while a discussion of their performance is included in Chapter 4.2.5.

Method 1: Eigendecomposition This method is based on the relation

$$\mathbf{M}\boldsymbol{\Sigma}_{\mathbf{M}} = \boldsymbol{\Lambda}_{\mathbf{M}}\boldsymbol{\Sigma}_{\mathbf{M}}\,, \quad \boldsymbol{\Lambda}_{\mathbf{M}} = \mathrm{diag}(m_1, ..., m_N) \tag{3.77}$$

$$\exp(\lambda\mathbf{M}) = \boldsymbol{\Sigma}_{\mathbf{M}}\,\mathrm{diag}\left(e^{\lambda m_1}, ..., e^{\lambda m_N}\right)\,\boldsymbol{\Sigma}_{\mathbf{M}}^{-1}, \tag{3.78}$$

with $\boldsymbol{\Sigma}_{\mathbf{M}}$ containing the eigenvectors of a matrix $\mathbf{M} \in \mathbb{K}^{\mathrm{N}\times\mathrm{N}}$ on its columns and $\{m_i\}$ being the eigenvalues. It should be noted that this appealing method is not guaranteed to work well when $\mathbf{M}$ is defective, i.e., does not have a complete set of linearly independent eigenvectors which makes $\boldsymbol{\Sigma}_{\mathbf{M}}^{-1}$ problematic [127]. Anyway, in our case, we usually do not have this problem because the (transformed) Hamiltonian matrix $\mathbf{H}$ – which is in some way always the subject of exponentiation – is Hermitian and its eigenvectors $\boldsymbol{\Sigma}_{\mathbf{H}}$ are always orthogonal, i.e.,

$$\mathbf{H} = \mathbf{H}^{\dagger} \;\Rightarrow\; \boldsymbol{\Sigma}_{\mathbf{H}}^{-1} = \boldsymbol{\Sigma}_{\mathbf{H}}^{\dagger}, \tag{3.79}$$

$$\exp(\lambda\mathbf{H}) = \boldsymbol{\Sigma}_{\mathbf{H}}\,\mathrm{diag}\left(e^{\lambda\epsilon_1}, ..., e^{\lambda\epsilon_{\mathrm{N_b}}}\right)\,\boldsymbol{\Sigma}_{\mathbf{H}}^{\dagger}, \tag{3.80}$$

where $\lambda = -i\alpha$ with $\alpha = 1$, e.g., for the EM propagator or some scaling factor, e.g., for the CFM4 propagator. Of course, this also applies for a sum of Hamiltonian matrices (as in the commutator-free Magnus propagators). This method is also very favorable in our case due to the high optimization level of the corresponding diagonalization subroutines in FHI-aims [42, 109].

Method 2: Scaling and Squaring The second method is considered as one of the most robust and general methods for matrix exponential computations [127], both for reliability and efficiency. It can also be used for general, non-Hermitian matrices which here occur for an *effective* Hamiltonian matrix in Ehrenfest dynamics with atom-centered orbitals (explained in detail in Section 3.8).
It belongs to the class of series expansion methods. The general idea is based on the exponential property

$$e^{\lambda\mathbf{M}} = \left(e^{\frac{\lambda\mathbf{M}}{m}}\right)^{m}\,, \quad m = 2^n\,, \quad n \in \mathbb{N}, \tag{3.81}$$

where in the first step, n is chosen such that $||\lambda\mathbf{M}||/m \leq 1$ so that $\exp(\lambda\mathbf{M}/m)$ can be computed accurately and efficiently by (q,q)-Padé approximants $\mathbf{R}_{qq}$ in this case:

$$\mathbf{R}_{qq}(\lambda\mathbf{M}) = \mathbf{Q}_{qq}^{-1}(\lambda\mathbf{M})\,\mathbf{P}_{qq}(\lambda\mathbf{M}), \tag{3.82}$$

$$\mathbf{Q}_{qq}(\lambda\mathbf{M}) = \sum_{k}^{q} \frac{(2q-k)!}{(2q)!(q-k)!}(\lambda\mathbf{M})^k, \tag{3.83}$$

$$\mathbf{P}_{qq}(\lambda\mathbf{M}) = \sum_{k}^{q} \frac{(2q-k)!q!}{(2q)!k!(q-k)!}(-\lambda\mathbf{M})^k. \tag{3.84}$$

The overall exponential is then computed by sequential squaring, i.e.,

$$e^{\lambda\mathbf{M}+\mathbf{\Gamma}} = \prod_{i=1}^{n} \mathbf{R}_{qq}\left(\frac{\lambda\mathbf{M}}{2^n}\right)^2, \tag{3.85}$$

where $\mathbf{\Gamma}$ is the introduced error which depends on the choice of n and q. Based on a desired error bound ϵ and on the value of $||\lambda\mathbf{M}||$, optimal pairs (n,q) can be derived. We implemented a modified version of the scaling and squaring method after Higham [129] which is further optimized with respect to the choice of (n,q) and incorporates adaptivity to find an optimal solution. This method is rather lengthy and we omit it here.

Method 3: Taylor Expansion This is probably the most direct approach for the computation of a matrix exponential. The truncated series expansion of the exponential function is used here:

$$\exp(\lambda\mathbf{M}) \approx \sum_{l=0}^{\mathrm{N_T}} \frac{1}{l!}(\lambda\mathbf{M})^l. \tag{3.86}$$

While this approach may be regarded as least sophisticated method, it has the advantage that it can be used for any matrix and that qualitatively better results are obtained systematically by increasing $\mathrm{N_T}$. In practice, depending on the problem given (i.e., the properties of the matrix $\mathbf{M}$ and the factor λ), only a rather small number for $\mathrm{N_T}$ may be sufficient, possibly making this approach a very economic choice, as only matrix products have to be computed. Castro and Marques [87] note that $\mathrm{N_T} = 4$ can be a particularly good choice, while O'Rourke and Bowler found a value of 6 to work very well [130]. Of course, in this context, other factors have to be considered, i.e., that this method always requires the inverse overlap matrix, as $\mathbf{M} = \mathbf{S}^{-1}\mathbf{H}$, and that $\mathbf{H}$ may have very negative eigenvalues, affecting stability and accuracy of this method significantly. In addition, a truncation of this series may break the unitarity of the method rather quickly, which must be taken into account. Nevertheless we found some value in this approach and will present some characteristics later.

3.6 Crank-Nicolson Scheme

The most general form of the Crank-Nicolson (CN) propagator in this context is given by

$$\mathbf{U}(t_k + \Delta t, t_k) = \frac{\sum_{m=1}^{\mathrm{N_{CN}}} \frac{1}{m!} \Big(- i\Delta t \mathbf{S}^{-1} \mathbf{H}(t_k + \Delta t/2) \Big)^m}{\sum_{m=1}^{\mathrm{N_{CN}}} \frac{1}{m!} \Big(i\Delta t \mathbf{S}^{-1} \mathbf{H}(t_k + \Delta t/2) \Big)^m} \equiv \mathbf{M}_+^{-1} \mathbf{M}_- \tag{3.87}$$

which is simply an approximation to the exact matrix exponential of $(-i\Delta t \mathbf{S}^{-1}\mathbf{H})$ via the Padé approximation [131]. In contrast to the former schemes, one does usually not compute the propagator explicitly, but rather formulates the propagation equation as

$$\mathbf{M}_+ \mathbf{C}(t_k + \Delta t) = \mathbf{M}_- \mathbf{C}(t_k), \tag{3.88}$$

which is a scheme equivalent to the method by Crank and Nicolson, originally formulated for heat conduction equations [132]. In dependence of the truncation order $\mathrm{N_{CN}}$, we may denote the corresponding scheme as CN($\mathrm{N_{CN}}$) for the rest of this thesis. Often, the CN scheme is employed in its 1st order form ($\mathrm{N_{CN}}$=1), also making the computation of $\mathbf{S}^{-1}$ unnecessary, which is achieved by multiplication of both sides of the equation with $\mathbf{S}$:

$$\Big(\mathbf{S} + i\Delta t \mathbf{H}(t_k + \Delta t/2) \Big) \mathbf{C}(t_k + \Delta t) = \Big(\mathbf{S} - i\Delta t \mathbf{H}(t_k + \Delta t/2) \Big) \mathbf{C}(t_k). \tag{3.89}$$

In the form as given by Eq. 3.88, the propagation equation has the general shape

$$\mathbf{M}_+ \mathbf{C}(t_k + \Delta t) = \mathbf{B}(t_k) \tag{3.90}$$

with $\mathbf{B}(t_k) = \mathbf{M}_- \mathbf{C}(t_k)$, which is solved via a linear equation solving algorithm. For very large systems, i.e., systems consisting of many basis functions, optimized iterative solvers like GMRES [133] exist. The numerical error in the computation of the exponential is given as

$$\epsilon = \Big|\Big| \exp\left(\mathbf{\Omega}(t_k + \Delta t)\right) - \mathbf{U}^{\mathrm{CN(O)}}(t_k + \Delta t, t_k) \Big|\Big| \in \mathcal{O}(\Delta t^{O+1}). \tag{3.91}$$

An intrinsic advantage of the CN scheme is its numerical simplicity and that it can also be applied out-of-the-box for non-Hermitian Hamiltonians. Also, higher order forms increase the accuracy with little additional effort (one additional matrix multiplication per order). It is also unitary and preserves time-reversal symmetry [87]. A disadvantage is that there is no simple way to handle ill-conditioned overlap matrices. The CN scheme belongs to the class of implicit methods, as the Hamiltonian is evaluated one half step ahead.

3.7 Predictor-Corrector Scheme

When considering any propagator based on the Magnus expansion or the Crank-Nicolson scheme, we find that the time-evolution operator depends on the Hamiltonian of some future time, e.g., for the EM propagator as

$$\mathbf{U}^{\mathrm{EM}}(t_k + \Delta t, t_k) = \exp\left(-i\Delta t \mathbf{S}^{-1}\mathbf{H}\left(t_k + \frac{\Delta t}{2}\right)\right). \tag{3.92}$$

Since this translates into the time-dependence onto the electron density and the external time-dependent potential via

$$\mathbf{H}\left(t_k + \frac{\Delta t}{2}\right) = \mathbf{H}\left[\rho\left(t_k + \frac{\Delta t}{2}\right)\right] + \mathbf{V}_{\mathrm{ext}}\left(t_k + \frac{\Delta t}{2}\right) \tag{3.93}$$

(where we used the matrix representation of the external potential for simplicity), one finds that the resulting time-evolution equation for the eigenstates has implicit character due to $\rho(t_k + \Delta t/2) = \rho(\mathbf{C}(t_k + \Delta t/2))$. One now has several options on how to solve the corresponding implicit scheme. The situation is even more involved when considering Magnus propagators above the first order, as these incorporate dependencies on more than one future solution. The simplest approach is to neglect any dependence on future times and to insert the instantaneous density $\rho(t_k) = \rho(\mathbf{C}(t_k))$ into the scheme, which translates into employing the initial Hamiltonian $\mathbf{H}(t_k)$ to construct the propagator. The resulting schemes are unsurprisingly relatively unstable, i.e., require a small time step, and lack time-inversion symmetry. Improvements are achieved by extrapolation techniques which aim to find an approximation of $\mathbf{H}(t_k + \Delta t/2)$ based on former Hamiltonians. As, e.g., discussed by Pueyo et al. [121], this can be done via Lagrange extrapolation

$$\mathbf{H}^{\mathrm{ex}}(t_k + \alpha\Delta t) = \sum_{l=1}^{\mathrm{N_{ex}}} \mathbf{H}(t_k - l\Delta t) P_l(t + \alpha\Delta t) \tag{3.94}$$

with Lagrange polynomials P_l. Of course, one has to be cautious not to introduce errors when choosing a too large time step or extrapolation order.
Ideally, the implicit scheme is solved self-consistently in order to get an accurate and stable numerical solution to the problem. A popular method in this context is given by the semi-implicit predictor-corrector method [62, 134]. Here, one performs an initial guess to obtain a full-step solution, which is then used to construct a half-step Hamiltonian by interpolation. A subsequent propagation is denoted as corrector step, which itself can be repeated for a fixed number of steps (often 1) or by a convergence criterion. We also employ the (semi-implicit) predictor-corrector method, but in combination with Lagrange extrapolation in order to get a better initial guess for the predictor step (another approach is the so-called railway curve interpolation that explicitly preserves time-reversal symmetry, but requires the computation of time derivatives of the potential, possibly increasing the numerical cost

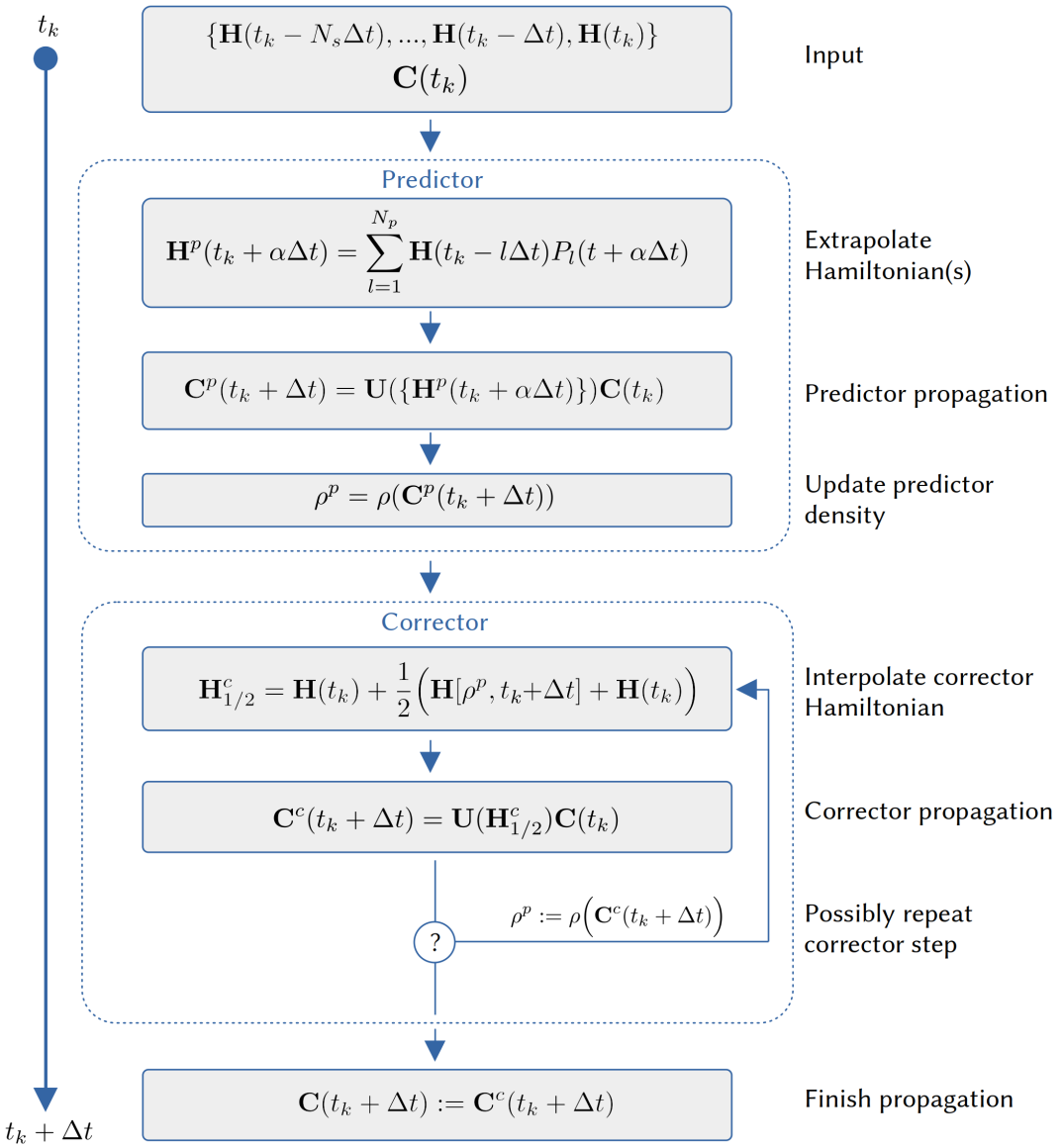

FIGURE 3.4: Illustration for the predictor-corrector scheme. In the predictor step, the Hamiltonian may be extrapolated based on formerly saved instances. The then propagated states build the predictor density, which is used to build the corresponding Hamiltonian. The corrector cycle will be repeated (e.g., until convergence or for a fixed number), the corrector density is used to interpolate to the half-step.

[135]). This does not come at additional computational effort (but requires some additional memory consumption, as former Hamiltonian matrices need to be stored). The scheme is illustrated in Fig. 3.4.

3.8 Ehrenfest Dynamics

In this section, we present the formulation of the Ehrenfest dynamics scheme in the given localized-basis framework. The equations of motion for electrons and nuclei

are introduced and we discuss the numerical integration of the non-adiabatically coupled set of equations.

3.8.1 Equations of Motion

We transfer the fundamentals of Ehrenfest Dynamics (ED) to our specific implementation by first remembering that an atom-centered localized basis is used, i.e.,

$$\psi_n(\mathbf{r},t) = \sum_{j=1}^{\mathrm{N_b}} c_{jn}(t)\,\phi_j\left(\mathbf{r}-\mathbf{R}_{I(j)}(t)\right), \tag{3.95}$$

but now explicitly including time dependence of the atomic positions $\{\mathbf{R}_{I(j)}(t)\}$, each possibly representing the center for multiple basis functions ϕ_j. Since the nuclei are now able to move, above relation has to be considered and implies numerous additional modifications. First, the time derivative in the time-dependent Kohn-Sham equation is now also applied to basis functions and the chain rule yields

$$\begin{aligned}\frac{\partial}{\partial t}\psi_n(\mathbf{r},t) = \sum_{j=1}^{\mathrm{N_b}} \Bigg\{ & \dot{c}_{jn}(t)\,\phi_j\left(\mathbf{r}-\mathbf{R}_{I(j)}(t)\right) \\ & + c_{jn}(t)\sum_{I=1}^{\mathrm{N_{at}}}\frac{\partial \mathbf{R}_{I(j)}(t)}{\partial t}\nabla_{\mathbf{R}_{I(j)}}\phi_j\left(\mathbf{r}-\mathbf{R}_{I(j)}(t)\right)\Bigg\}.\end{aligned} \tag{3.96}$$

We will use the relation

$$\nabla_{\mathbf{R}_{I(j)}}\phi_j\left(\mathbf{r}-\mathbf{R}_{I(j)}(t)\right) = -\nabla_{\mathbf{r}}\phi_j\left(\mathbf{r}-\mathbf{R}_{I(j)}(t)\right) \equiv -\nabla\phi_j\left(\mathbf{r}-\mathbf{R}_{I(j)}(t)\right) \tag{3.97}$$

from now on, leading us to the modified KS equation for time-dependent basis centers:

$$\begin{aligned} i\sum_{j=1}^{\mathrm{N_b}}\dot{c}_{jn}(t)\,\phi_j\left(\mathbf{r}-\mathbf{R}_{I(j)}(t)\right) = \sum_{j=1}^{\mathrm{N_b}}\Bigg\{ & c_{jn}(t)\mathcal{H}_{\mathrm{KS}}\phi_j\left(\mathbf{r}-\mathbf{R}_{I(j)}(t)\right) \\ & + ic_{jn}(t)\sum_{I=1}^{\mathrm{N_{at}}}\dot{\mathbf{R}}_{I(j)}(t)\nabla\phi_j\left(\mathbf{r}-\mathbf{R}_{I(j)}(t)\right)\Bigg\}. \end{aligned} \tag{3.98}$$

Proceeding as usual in this case by multiplying ϕ_i from the left side and integrating over the whole volume, above equation is written in matrix form as

$$i\mathbf{S}\dot{\mathbf{C}} = \mathbf{H}\mathbf{C} + i\sum_{I=1}^{\mathrm{N_{at}}}\mathbf{K}_I\mathbf{C} \tag{3.99}$$

$$\Leftrightarrow\quad \dot{\mathbf{C}} = -i\mathbf{S}^{-1}\left(\mathbf{H} + i\sum_{I=1}^{\mathrm{N_{at}}}\mathbf{K}_I\right)\mathbf{C} \tag{3.100}$$

$$\equiv -i\mathbf{S}^{-1}\tilde{\mathbf{H}}\mathbf{C} \tag{3.101}$$

where we introduced the coupling matrix $\mathbf{K}_I$ using the nuclear velocities $\dot{\mathbf{R}}_I$ and the basis gradient matrix $\mathbf{G}_I$ as

$$\mathrm{K}_{I,ij} = \dot{\mathbf{R}}_{I(j)} \cdot \mathbf{G}_{I,ij}, \tag{3.102}$$

$$\mathbf{G}_{I,ij}\left(\{\mathbf{R}_I\}\right) = \int_V \phi_i\left(\mathbf{r} - \mathbf{R}_{I(i)}\right) \nabla\phi_j\left(\mathbf{r} - \mathbf{R}_{I(j)}\right) \delta_{I,I(j)}, \tag{3.103}$$

and an *effective* Hamiltonian matrix $\tilde{\mathbf{H}} \equiv \mathbf{H} + i\sum_{I=1}^{\mathrm{N_{at}}} \mathbf{K}_I$. We note here that $\mathrm{K}_{I,ij}$ only incorporates the nuclear velocity of the atom for which the column index j, i.e., a basis function, is associated to. One can show that the additional spatial gauge term $i\sum_{I=1}^{\mathrm{N_{at}}} \mathbf{K}_I$ preserves the norm of the KS wave functions for mobile basis centers [136]. However, since $\tilde{\mathrm{H}}^*_{ji} = \mathrm{H}^*_{ji} - i\sum_I \mathrm{K}^*_{I,ji} = \mathrm{H}_{ij} - i\sum_I \mathrm{K}_{I,ji}$, $\mathrm{K}_{I,ij} \neq -\mathrm{K}_{I,ji}$ the *effective* Hamiltonian matrix is not Hermitian, affecting the numerical options to solve the modified KS-ED equation (e.g., for the numerical diagonalization possibly used in exponential schemes).

The atomic forces are obtained from the quantum-mechanical action as described in Section 2.3.2:

$$\mathcal{A}_{\mathrm{QM}} = \int_{t_0}^{t_1} \mathrm{d}t\, \mathcal{L}_{\mathrm{QM}}(t) = \int_{t_0}^{t_1} \mathrm{d}t \left\{ \sum_{n=1}^{\mathrm{N_{occ}}} f_n \langle\psi_n| i\frac{\partial}{\partial t} |\psi_n\rangle - E_{\mathrm{el}} \right\}, \tag{3.104}$$

and we now have to express the functional $\mathcal{L}_{\mathrm{QM}}(t)$ in the given basis, using our former result in Eq. 3.98, resulting in

$$\mathcal{L}_{\mathrm{QM}} = \sum_{n=1}^{\mathrm{N_{occ}}} f_n \mathbf{c}_n^* \left(\mathbf{S}^{-1}\mathbf{H} + i\sum_{I=1}^{\mathrm{N_{at}}} \mathbf{K}_I \right) \mathbf{c}_n - E_{\mathrm{el}}. \tag{3.105}$$

From the Euler-Lagrange equation for $\mathcal{A}_{\mathrm{QM}}$ [137], the forces are then obtained by

$$M_I \ddot{\mathbf{R}}_I = \nabla_{\mathbf{R}_I} \mathcal{L}_{\mathrm{QM}} - \frac{\mathrm{d}}{\mathrm{d}t} \nabla_{\dot{\mathbf{R}}_I} \mathcal{L}_{\mathrm{QM}}. \tag{3.106}$$

Lengthy calculations [136, 137] yield the following expressions:

$$M_I \ddot{\mathbf{R}}_I = -\nabla_{\mathbf{R}_I} E_{\mathrm{el}} + \sum_{n=1}^{\mathrm{N_{occ}}} f_n \mathbf{c}_n^* \left\{ \mathbf{X}_I^{(1)} + \mathbf{X}_I^{(2)} + \mathbf{X}_I^{(3)} + \mathbf{X}_I^{(4)} \right\} \mathbf{c}_n, \tag{3.107}$$

$$\mathbf{X}_I^{(1)} = -\nabla_{\dot{\mathbf{R}}_I} \mathbf{H}, \tag{3.108}$$

$$\mathbf{X}_I^{(2)} = \mathbf{G}_I \mathbf{S}^{-1}\mathbf{H} + \mathbf{H}\mathbf{S}^{-1}\mathbf{G}_I^\dagger, \tag{3.109}$$

$$\mathbf{X}_I^{(3)} = i\left(\mathbf{G}_I \mathbf{S}^{-1}\mathbf{K}_I + \mathbf{K}_I^\dagger \mathbf{S}^{-1}\mathbf{G}_I^\dagger \right), \tag{3.110}$$

$$\mathbf{X}_I^{(4)} = i\left(\mathbf{D}_I - \mathbf{D}_I^\dagger \right). \tag{3.111}$$

We here introduced another quantity, namely the double basis gradient matrix

$$D_{I,ij} = \sum_{I=1}^{\mathrm{N_{at}}} \dot{\mathbf{R}}_I \int_V \left(\nabla\phi_i\left(\mathbf{r} - \mathbf{R}_{I(i)}\right) \right) \cdot \left(\nabla\phi_j\left(\left(\mathbf{r} - \mathbf{R}_{I(j)}\right) \right) \delta_{I,I(i)}. \tag{3.112}$$

Equation 3.107 is the correct full expression for the forces acting on the nuclei. One can show that this complicated relation can be written as the sum of two force components, i.e.,

$$M_I \ddot{\mathbf{R}}_I = \mathbf{F}_I^{\mathrm{EC}} + \sum_{n=1}^{\mathrm{N_{occ}}} f_n \mathbf{c}_n^* \left\{ \mathbf{X}_I^{(3)} + \mathbf{X}_I^{(4)} \right\} \mathbf{c}_n \tag{3.113}$$

with $\mathbf{F}_I^{\mathrm{EC}}$ conserving the total energy in the system and the remaining part being responsible for the total (nuclear and electronic) momentum to be conserved [136, 137]. Others have already discussed that the momentum-conserving term can be neglected in many situations, as nuclear velocities may be relatively small [136]. However, for a complete picture, one must evaluate the whole expression. We implemented this as an optional feature.
For completeness we note that the term $-\nabla_{\mathbf{R}_I} E_{\mathrm{el}}$ in Equation 3.107 not only contains purely electrostatic contributions of the electron-nuclei and nuclei-nuclei interactions, but additional contributions that stem from the numerical approach and the exchange-correlation functional [42]:

- Multipole force corrections arise since the electrostatic potential is calculated via a truncated multipole expansion of the electron density [102]. Atom-centered multipole correction contributions yield a corresponding force term. For periodic systems, an additional force correction term needs to be taken into account, compensating for yet another multipole error.

- For GGA-based exchange-correlation functionals, the density gradient derivative is responsible for an additional force term that includes several density gradient contributions [42].

- When Hartree-Fock exchange is included in hybrid-functional calculations, respective force terms resulting from the gradient of the hybrid functional are introduced. Currently, these contributions can not be included in our implementation, as the existing framework is not general enough for the time-dependent case. However, it is possible that this functionality is added in the near future.

- In case of relativistic atomic ZORA treatment, the dependence of the modified kinetic operator onto atom-centered free-atom potentials yields an additional force term.

- The standard Pulay forces [47] on the other hand are *not* included here. In the static case, they arise from atom-centered basis functions and also include the single-particle eigenvalues. Their time-dependent analogue is incorporated in the $\mathbf{X}_I^{(1)}$ and $\mathbf{X}_I^{(2)}$ terms in Equation 3.107.

Multipole-, XC functional- and relativity-related forces are thus evaluated using the instantaneous single-particle wave functions, yielding their time-dependent representations.

The practical procedure now involves the solution of the time-dependent KS equation and the solution of Equation 3.107 at once, which we will discuss in the next section.

3.8.2 Numerical Integration

In the case of Ehrenfest dynamics, two coupled differential equations must be integrated, while the dynamics of the corresponding two subsystems have different effective timescales, i.e., the electronic motion is much faster than ionic motion due to the fact that the masses of nuclei and electrons differ by three orders of magnitude. An economic algorithm should thus make use of this and it is often sensible to propagate both equations with different time steppings [138].
Additional considerations come into play here with respect to numerical cost, as force computations and geometry updates are expensive operations. Specifically, a geometry update in this context not only refers to ionic locations but also includes updating the atom-centered basis functions and radial grids, i.e., $\phi_i\big(\mathbf{r} - \mathbf{R}_{I(i)}(t)\big)$. As integrations are only carried out on overlapping radial spheres, technically, a geometry update also involves re-computation of many grid-related quantities. The Hamiltonian matrix, overlap matrix and all other basis-dependent matrices thus parametrically depend on the ionic positions and have to be re-integrated, as the geometry changes. For the modified time-dependent Kohn-Sham equation in the

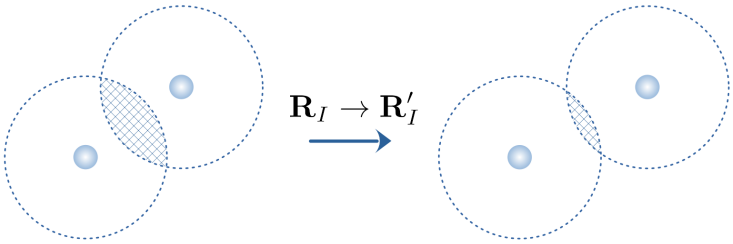

FIGURE 3.5: Illustration of ion dynamics (blue dots) implying movement of atomic basis functions and radial grids.

case of mobile centers, one has a dependency onto the time-dependent velocities $\{\dot{\mathbf{R}}_I(t)\}$ of the ions, which has to be taken into account when discretizing. Several different schemes to integrate the EOM in Ehrenfest dynamics have been proposed before [136, 138, 139, 140, 141], but we defined (to our knowledge) a new scheme that has proven to work well and is quite economic. The integrator for the TDKS equations can be chosen as any appropriate propagator (i.e., it must be able to handle the non-Hermitian effective Hamiltonian matrix), while a modified form of the well-known velocity Verlet scheme [142] is used for the nuclei.
Our scheme requires that the nuclear time step $\Delta T = 2n\Delta t$ with the electronic time step Δt and $n \geq 1$, ideally $n \geq 2$ (we usually used $n = 2 - 10$ in our calculations, but this depends on the dynamics in general) as it is designed such that the nuclear velocity coupling of the Ehrenfest-KS equation, as given by Equations 3.99-3.103, is defined by the intermediate interpolated velocities before and after the full step

update for the nuclear coordinates. See Figure 3.6 for a detailed illustration of the algorithm. We found that this scheme helps to stabilize the propagation, as the velocity coupling of the Ehrenfest-KS equation is crucial to keep the electronic states orthonormal with the moving basis functions.
In addition, it requires only the minimum number of density updates (4), grid integrations (4), geometry reinitializations (1) and force computations (1) per one full step for the nuclei, ΔT. This effective scheme can thus help to reduce the often high computational demand of RT-TDDFT based Ehrenfest dynamics simulations.

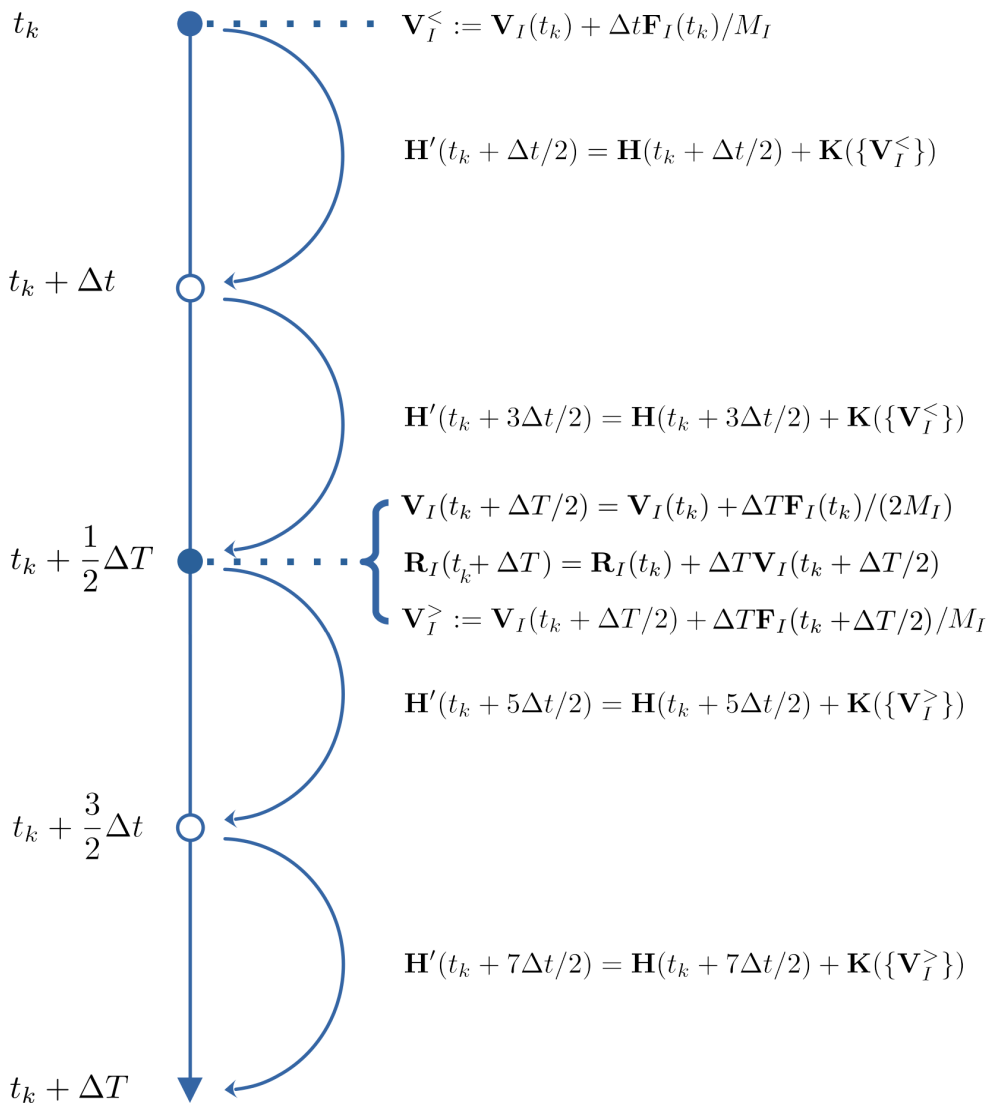

FIGURE 3.6: Ehrenfest propagation scheme for coupled electron-nuclei equations of motion. In this example, the nuclear time step is $\Delta T = 4\Delta t$ with Δt as the electronic time step. The key idea is to use interpolated coupling velocities $\{\mathbf{V}_I^{><}\}$ before and after the geometry half-step in order to stabilize the velocity-coupled electronic EOM. The coupling is mediated by the coupling matrix $\mathbf{K}(\{\mathbf{V}_I^{><}\})$ which is added to the effective propagation Hamiltonian inside the predictor-corrector scheme. The matrix $\mathbf{K}$ symbolizes the second term on the RHS of Eq. 3.99.

Chapter 4

Real-Time TDDFT Validation and Applications

4.1 Overview

This chapter serves three purposes: first, we want to demonstrate the correctness of our implementation. For this aim, we provide internal consistency checks and exemplary comparisons with previously published experimental or theoretical data for most included functionalities of our software.
Second, we provide some new results for selected examples. Some details are meant to also illustrate some specifics of our framework, for example the use of NAO basis sets and the all-electron description. Some of these results were obtained by collaborative work and are published, and we specify these parts explicitly in the publications part after the appendix.
Third, we want to provide insight into the techniques that are incorporated in the code and what can be done with these features to motivate future applications. For this purpose, we also try to give a clear presentation and follow an instructive elaboration style, also providing references to the most important publications for the respective topics. We will make clear that our implementation adds value to the field of electronic structure methods.

4.2 Absorption Spectra of Molecules

Within this chapter, we introduce the methodology for the computation of linear-response absorption spectra via RT-TDDFT simulations and show results for several systems. Within this frame, we first present calculations of core-level and valence spectra of individual molecules. Thereafter, a detailed basis set benchmark study for a molecular test set is presented.

4.2.1 Introduction

Weak optical excitations cause response in systems in linear dependence of the perturbation and the frequency-dependent light absorption is described via an absorption spectrum [143]. These spectra give an imprint of the electronic structure of the

systems and are of fundamental importance in understanding the process of light absorption. Different regimes are commonly defined in dependence of the relevant region within the electromagnetic spectrum, i.e., X-ray, UV, mid-UV, and so on.
For the weak-excitation case, linear-response TDDFT (cf. Section 2.4) is one of the most popular approaches, most often being used to compute optical absorption spectra and oscillator strengths [59, 144, 145]. One of this method's advantages is the high computational efficiency for small- to medium-sized systems. Formally, the computational effort for LR-TDDFT scales as $\mathcal{O}(N_{at}^6)$ with N_{at} being the number of atoms [146]. Thus, for larger systems, the cost rises dramatically (however, several approximative methods exist that have more favorable scaling [147, 148, 149]). Another potential bottleneck is the number of excitations which need to be computed, becoming prohibitive around values of $10^3 - 10^4$ [150]. A further disadvantage of LR-TDDFT is that the exchange-correlation kernel needs to be derived from a given XC functional and that this quantity may introduce numerical problems, as it incorporates a second-order derivative (the functional derivative of the XC potential with respect to the electron density).
In comparison, RT-TDDFT has a much better formal scaling, namely as $\mathcal{O}(N_{at}^2)$ to $\mathcal{O}(N_{at}^3)$ – but with a much larger prefactor, as compared to LR-TDDFT [151]. This difference leads to a crossover where RT-TDDFT becomes much more efficient than standard LR-TDDFT, when considering larger and larger system sizes. Linear-response RT-TDDFT simulations are performed with a $\delta-$like external field which means that a broadband excitation excites the *whole* spectrum (only the time step limits the spectral range, i.e., $\omega_{max} \sim 1/\Delta t$). In addition, most XC functionals can be used for RT-TDDFT straightforwardly by employing the time-dependent electron density (within the adiabatic approximation).
Considering these points, there are valid reasons to make use of RT-TDDFT for linear-response calculations, as already done in recent studies, e.g., Refs. [73, 74, 115, 150, 152, 153, 154, 155, 156].

4.2.2 Theory

The microscopic electronic response to an external optical field $\mathbf{E}(t)$ (i.e., within the dipole approximation) can be characterized via the electronic dipole moment $\boldsymbol{\mu}(t)$. The general response formula is given by the expansion

$$\mu_i(t) = \sum_{j=1}^{3} \int_{-\infty}^{\infty} \mathrm{d}t' \, \tilde{\alpha}_{ij}(t-t') \, E_j(t') + \text{h.o.t.} \tag{4.1}$$

where the remaining terms include the higher-order response functions (often denoted as non-linear susceptibilities). As optical absorption measurements are carried out with external fields that are small compared to the ionic fields inside matter, we can truncate above expansion after the first term which yields the linear-response

connection between electronic dipole moment and external electric field via the polarizability tensor $\tilde{\alpha}(t) \equiv \mathcal{F}^{-1}[\alpha(\omega)](t)$ (indicating the common use of this quantity in the frequency domain). The polarizability characterizes the field-induced dipolar distortion of the electronic charge distribution and is thus of fundamental importance, as it includes electron-electron interactions and electronic correlation [131]. By Fourier transforming and use of the convolution theorem, above truncated expression can be written as

$$\mathcal{F}[\mu_i](\omega) = \sum_{j=1}^{3} \alpha_{ij}(\omega)\mathcal{F}[E_j](\omega). \tag{4.2}$$

The quantity of interest is the complex polarizability tensor $\alpha_{ij}(\omega)$, characterizing the linear response of the system. To resolve all of its components, the weak-field excitation is performed along all three Cartesian axes, i.e., pairwise orthogonal field amplitudes, meaning

$$\alpha_{ij}(\omega) = \frac{\mathcal{F}[\mu_i(t)](\omega)}{\mathcal{F}[E_j(t)](\omega)}. \tag{4.3}$$

Dipole-forbidden transitions can nevertheless not be resolved here and one would have to consider higher-order moments for this task [157]. The electronic dipole moment is calculated from the time-dependent Kohn-Sham single-particle states via

$$\boldsymbol{\mu}(t) = \sum_{n=1}^{\mathrm{N_{occ}}} f_n \langle \psi_n(t)|\hat{\mathbf{r}}|\psi_n(t)\rangle = \sum_{n=1}^{\mathrm{N_{occ}}} f_n \mathbf{c}_n^{\dagger}(t)\mathbf{D}\mathbf{c}_n(t) \tag{4.4}$$

with the dipole basis matrix $\mathbf{D}_{ij} = \langle \phi_i|\hat{\mathbf{r}}|\phi_j\rangle$, incorporating the position operator $\hat{\mathbf{r}}$. The linear response of the system requires a sufficiently weak external field and usually, one wants to excite the whole spectrum, which is achieved by applying a δ-like external field, i.e., $\mathbf{E}(t) \sim \mathbf{E}_0\delta(t - t_0)$ (as the Fourier transform of a δ-function is a constant). The polarizability tensor can in principle be attained by a single calculation, but this carries the risk that several modes are not excited, as the external field has a defined direction which may be orthogonal to specific transition dipoles [158]. For a complete reconstruction, one thereby usually performs three individual calculations, each with a field polarized along one of the three Cartesian axes.
From the polarizability tensor, one can obtain the absorption cross section tensor

$$\sigma(\omega) = \frac{4\pi\omega}{c}\mathrm{Im}\{\alpha(\omega)\} \tag{4.5}$$

(with the speed of light c) and from its trace, the so-called dipole strength function (DSF) can be calculated:

$$S(\omega) = \frac{1}{3}\mathrm{Tr}[\sigma(\omega)]. \tag{4.6}$$

An alternative representation of the DSF is given as

$$S(\omega) = \frac{2}{3}\sum_{l=1}^{\infty}\sum_{k=1}^{3}|\langle\Psi_0|\hat{r}_k|\Psi_l\rangle|^2\omega\delta(\omega-\omega_l) = \sum_{l=1}^{\infty}\tilde{f}_l\frac{\omega}{\omega_l}\delta(\omega-\omega_l), \tag{4.7}$$

where the sum over all transition dipole moments $\boldsymbol{\mu}_{0l} = \langle\Psi_0|\hat{\mathbf{r}}|\Psi_l\rangle$ between the system's ground state Ψ_0 and excited states Ψ_l, the excitation energies ω_l and the corresponding oscillator strengths $\tilde{f}_l$ build the whole excitation spectrum [158]. The peaks in a DSF spectrum are thus proportional to the oscillator strengths and are centered at excitation energies. As a result of the finite propagation time, the line shapes of the DSFs always have a certain broadening. Thus, for real signals and finite external field pulses, the DSF yields a continuous spectrum that can directly be compared to experimental absorption spectra. It should be noted that due to the intrinsic properties of the Fourier transform, the accuracy, i.e., the spectral resolution of DSFs, is directly proportional to the total simulation time, and that the maximum resolved frequency is inversely proportional to the time step. These considerations play a major role when performing real-time simulations in order to get spectral information. We will cover this topic in more detail in Chapter 4.2.5.
Another important property of the DSF is provided by the f-sum rule [159] which builds a connection between the number of electrons that are involved in the absorption process, the DSF, and the oscillator strengths:

$$N_e^{\text{abs}} = \int_0^{\infty} \mathrm{d}\omega\, S(\omega) = \sum_{l=1}^{\infty}\tilde{f}_l. \tag{4.8}$$

In practice, this quantity can be used to verify the consistency of a calculation.
It should further be noted that it is common practice [154] to apply a damping function to the dipole time series before Fourier transforming in order to attain well-defined Lorentzian-like lineshapes [73]. A frequent choice is an exponential damping function

$$f(t) = e^{-\gamma t} \tag{4.9}$$

with the parameter γ controlling the line width. Another possible choice is a polynomial function of the form

$$f(t) = 1 - 3\left(\frac{t}{T}\right)^2 + 2\left(\frac{t}{T}\right)^3 \tag{4.10}$$

with the total simulation time T. This function has the desired properties $f(0) = 1$ and $f(T) = f'(T) = 0$ which ensure smooth decay and also preserve the f-sum rule (while exponential damping does not). The resulting FWHM widths are in this case given as approximately $6.2/T$ [73]. It should be noted that any spectrum generated by RT-TDDFT will converge to a stick spectrum for infinite-time propagation, i.e., the finite line widths are artificial and damping is only an auxiliary way to modify the line shapes. As pointed out by Lopata et al., one could obtain physical lineshapes

via ab-initio coupled electron-nuclear dynamics [156].

To further decompose a linear-response DSF spectrum into contributions of specific excitations, one can employ a projection technique that uses ground state molecular orbitals to resolve the individual occupied-unoccupied contributions [155]. Given a set of (occupied and unoccupied) ground state orbitals via the coefficient matrix $\mathbf{C}_0 \in \mathbb{C}^{N_b \times N_{states}}$ ($N_{states} \leq N_b$ is the total number of states considered in the algorithm), the density matrix of the time-dependent occupied states, $\mathbf{P}(t) = \mathbf{C}(t)\mathbf{C}^\dagger(t) \in \mathbb{C}^{N_b \times N_b}$ and the dipole basis matrix $\mathbf{D} \in \mathbb{R}^{N_b \times N_b}$ as defined before, one can express the latter two quantities in the basis of the ground state orbitals via

$$\mathbf{P}^{GS}(t) = \mathbf{C}_0^{-1}\mathbf{P}(t)\mathbf{C}_0^{-\dagger}, \tag{4.11}$$

$$\mathbf{D}_0^{GS} = \mathbf{C}_0^\dagger \mathbf{D}\mathbf{C}_0. \tag{4.12}$$

We note that for large and/or augmented basis sets, one possibly has to consider a reduced set of ground state molecular orbitals (since linear dependencies occur, as also explained before in Chapter 3.5.5), which then requires the use of left and right pseudoinverses of $\mathbf{C}_0$ to calculate the molecular orbital (MO) density matrix $\mathbf{P}^{GS}(t)$. We implemented this technique but not explain it further here (see Ref. [155] for details).
The MO dipole and density matrices contain the information of all occupied and unoccupied ground state orbitals which is used to express the transition dipole moment as

$$\begin{aligned}\boldsymbol{\mu}_{kl}(t) &= \sum_{n=1}^{N_{occ}} \langle\psi_k(0)|\mathbf{r}|\psi_l(0)\rangle\langle\psi_l(0)|\psi_n(t)\rangle\langle\psi_n(t)|\psi_k(0)\rangle + (k \leftrightarrow l) \\ &= \mathbf{D}_{0,kl}^{GS}\mathbf{P}_{lk}^{GS}(t) + \mathbf{D}_{0,lk}^{GS}\mathbf{P}_{kl}^{GS}(t).\end{aligned} \tag{4.13}$$

These moments describe all possible transitions based on the ground state orbitals. The total electronic dipole moment can be expressed via

$$\boldsymbol{\mu}(t) = \boldsymbol{\mu}(0) + \sum_{o=1}^{N_{occ}} \sum_{u=N_{occ}+1}^{N_b} \boldsymbol{\mu}_{ou}(t), \tag{4.14}$$

which means that the time-dependent part stems from occupied-unoccupied transitions, giving direct physical interpretation (keeping in mind the Kohn-Sham approach). The spectra of individual occupied-unoccupied transition dipole moments thus yield information about specific excitations [155]. We implemented this deconvolution technique as it is a useful tool to characterize linear response spectra.

4.2.3 Simulation of Benzene Linear-Response Excitations

Given the provided methodology, we here provide results both for valence and core-level excitation RT-TDDFT absorption spectra for a prototypical example molecule

and compare our results with experimental data.

Valence Excitation Spectrum

We chose the prototypical conjugated hydrocarbon molecule benzene as a first example here, as it is a well-studied system both experimentally [160, 161] and theoretically [119, 130, 162, 163, 164, 165]. Albeit the extensive theoretical literature, we only want to present comparison with experimental data at this point in order to prove that our method is able to provide accurate physical results.
We carry out our investigation with a moderate amount of theory, employing the well-established PBE XC functional [26] in combination with a 'tight' basis set. The geometry used for further investigations was equilibrated with the mentioned settings, resulting in C-C neighbor bond distances of 1.39 Å (which are all equal due to aromaticity). RT-TDDFT simulations were carried out with a time step of 0.4 a.u. = 0.0096 fs for a total simulation time of 2500 a.u. = 60.5 fs which is in this case enough to obtain well-converged spectra. The time-propagation method was given by the semi-implicit exponential midpoint method in combination with a 2-point extrapolation scheme as presented in Sec. 3.5.3. A weak initial external field kick was realized by applying a constant field with an amplitude of 0.005 a.u. = $2.6 \cdot 10^9$ V/m for the first simulation step - this was done for three individual calculations, each with a field polarization along the x,y,z axes.

Figure 4.1 shows the dynamics of the excitation for the simulation where an initial kick was applied to the x-direction. The upper panel shows the electronic dipole response along the x-axis, $\mu_x(t)$, and one can clearly identify the onset of significant oscillations via the external field (the molecule does not have a permanent dipole moment). We then observe a heterogeneous oscillation pattern including all of the system's modes. The lower panel shows the total energy deviation (relative to the first value after the excitation was applied) on a meV scale and we note that usually a visible shift is seen in the electronic energy when an external resonant field is switched on, corresponding to the absorption of field energy. In this case, the shift is not visible as we intend to show the good energy conservation after the onset of the excited dynamics. Regarding the comparatively large time step, this still shows stable time propagation with total energy being conserved up to a few meV.
From the three individual simulations, we calculated the corresponding DSF spectrum. We first show the f-sum rule consistency check in Figure 4.2, i.e., the integral over the DSF in dependence of the energy:

$$N_e^{\mathrm{abs}}(\omega) = \int_0^{\omega} \mathrm{d}\omega' \, S(\omega'). \tag{4.15}$$

We also provide the partial sums of LR-TDDFT oscillator strengths as internal consistency check, since the total value which the f-sum rule provides depends on numerical accuracy (these calculations were performed for the same basis set and functional

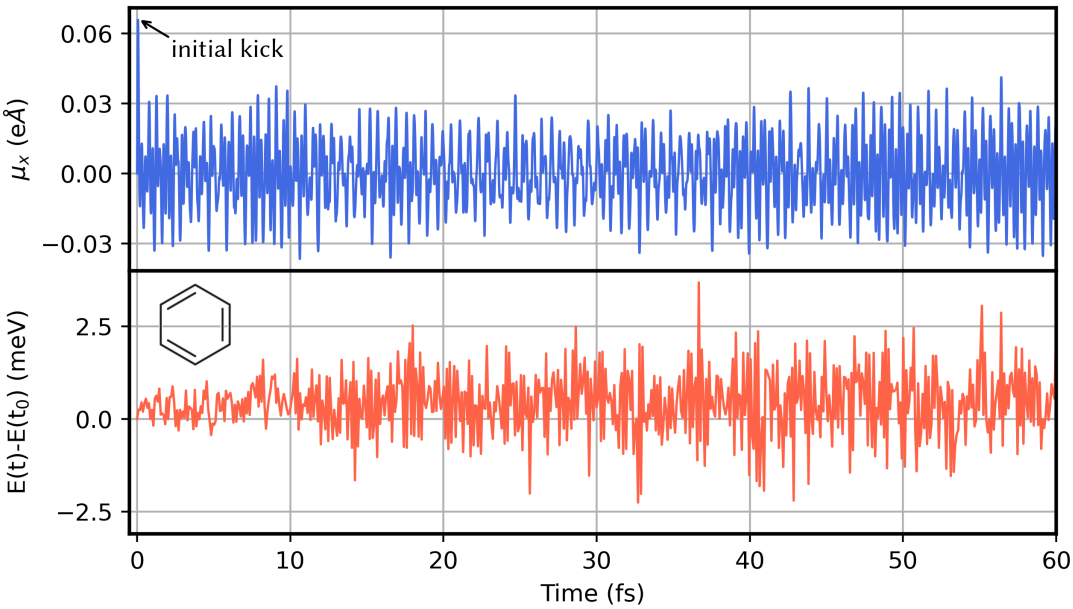

FIGURE 4.1: Dynamics of benzene for an initial weak delta-kick excitation parallel to the x-axis. Upper panel: dynamics of the x-component of the electronic dipole moment. Lower panel: total energy deviation relative to the initial value at excitation.

with FHI-aims). In the figure, we additionally show the RT-TDDFT results obtained from different time steps, namely for $\Delta t = 0.2$ a.u. $= 0.0048$ fs and $\Delta t = 0.05$ a.u. $= 0.0012$ fs. One can clearly observe perfect match below 50 eV. After that, small differences occur. However, for smaller time steps, the RT-TDDFT spectrum converges towards the LR-TDDFT spectrum. This is most likely explained by the fact that smaller time steps better resolve high-energy and core-valence excitations in RT-TDDFT. At 350 eV, a number of 34.4 excited electrons is given by the LR-TDDFT f-sum rule, which is reasonable, but ultimately affected by numerical and physical approximations. Overall, the agreement is very good and shows the expected convergence behavior with respect to time step.

The DSF together with the experimental absorption spectrum [160] is shown in Fig. 4.3. We included the DSFs for the transition dipole moments between occupied-unoccupied pairs $(20 \rightarrow 22)$, $(21 \rightarrow 23)$, $(20 \rightarrow 23)$, $(21 \rightarrow 22)$ (group A) and $(20 \rightarrow 26)$, $(21 \rightarrow 25)$ (group B). The two degenerate HOMOs are the states with index 20 and 21. The inset plot shows only one curve for the first and second group of transition dipole moments, as the spectra are equivalent: this stems from the fact that the respective occupied/unoccupied states are degenerate.

Group A corresponds to the $\pi \rightarrow \pi^*$ ($^1E_{1u} \leftarrow {}^1A_{1g}$) HOMO-LUMO transition experimentally located at 6.96 eV [166]. The sum of the 4 transition dipole moment peaks of this group contribute largely to the major peak of the total DSF that is here located at 6.91 eV which is very close to the experimental value. The peak at 6.84 eV of the group B DSF likely corresponds to a Rydberg transition which has an experimental value of 6.93 eV [161, 166].

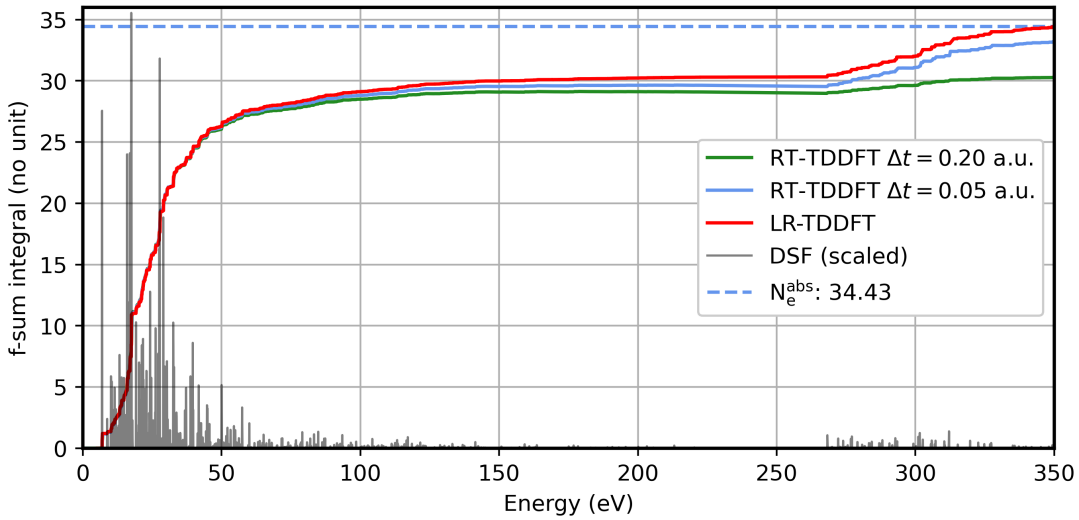

FIGURE 4.2: Illustration for the f-sum rule consistency check: the solid lines denote the integral over the DSF in dependence of energy (for LR-TDDFT and RT-TDDFT with different time steps), the dashed blue line is the LR-TDDFT limit value at 350 eV, $N_c = 34.43$, and the black line shows the scaled DSF (given without units here).

The overall overlap with the experimental spectrum is thus to be considered very good, although higher excitations are rather difficult to compare due to the low structure of the experimental spectrum and the fact that excitations from valence orbitals into higher unoccupied orbitals occurring in this energy range may depend significantly on the basis set. The possibility to extract individual dipole transition moments based on the ground state Kohn-Sham eigenvectors can be regarded as useful tool to further investigate individual transitions.

K-Edge Core-Level Excitation Spectrum

As a sufficiently narrow delta-kick pulse, like performed here, corresponds to a broadband excitation, we are directly able to resolve core-level excitations, i.e., simulate X-ray absorption spectroscopy (XAS), where core electrons are excited into valence or above-valence states. Depending on the specific origin core-level state, the excitations are conventionally labeled as K-edge for 1s, L_1-edge for 2s, etc. TDDFT is well-suited for near-edge XAS (XANES), denoting transitions from core electrons into virtual states (but below ionization), as localized core holes are well-described and electronic effects are included ab-initio, requiring no specific preparation (in contrast to, e.g., the ΔSCF approach for core-level spectra [167]), enabling rather straightforward computations [156, 168].

As the simulation time step limits the total range of the resolvable excitation energies, it has to be set accordingly small. We consider here the carbon K-edge transitions which are experimentally found starting from 285 eV. The simulation settings are the same as for the valence excitations, while the time step was set as 0.1 a.u. = 0.0024 fs. For comparison we took experimental data from Ref. [169]. It is known

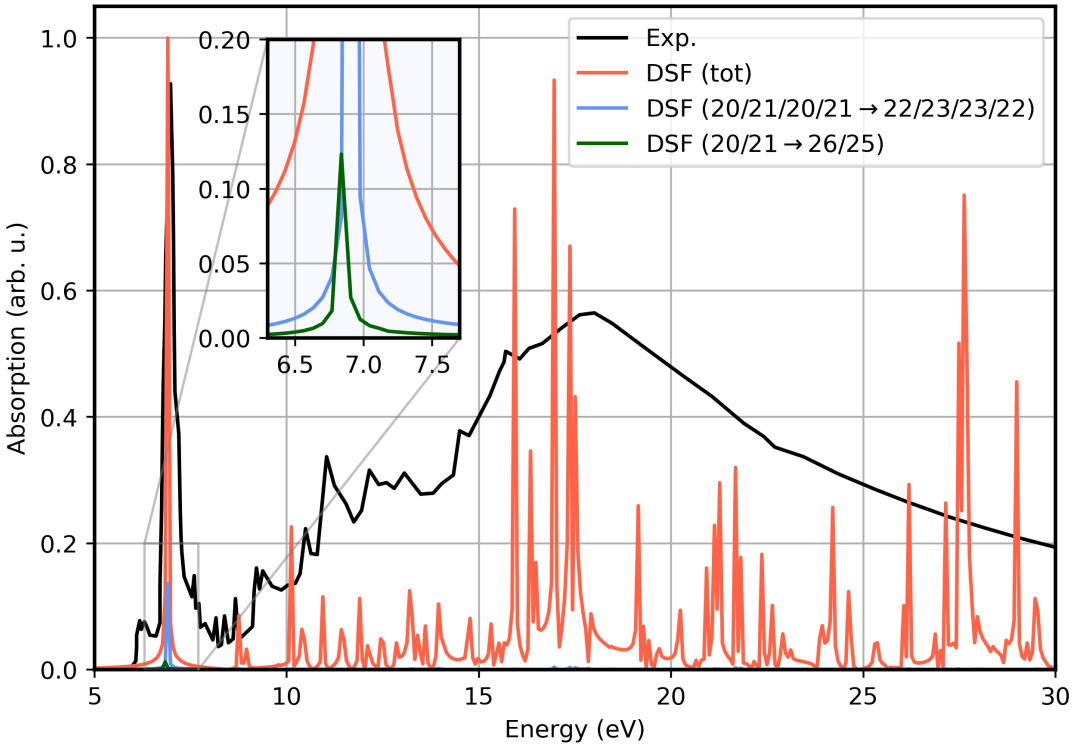

FIGURE 4.3: Comparison of the experimental absorption spectrum [160] (black line) of benzene with the DSF (red line) from the total electronic dipole moments from our RT-TDDFT simulations. Also shown are the DSFs generated from the transition dipole moments of the (20 → 22) and (20 → 26) occupied-unoccupied excitations. The spectra are scaled such that the highest peaks match.

that core-level spectra from RT-TDDFT are very sensitive to the exchange-correlation functional, however this results essentially only in constant shifts of excitations [156]. The most interesting information is on the other hand incorporated in the relative alignment of transitions, i.e., peaks in the absorption spectra. Thus, one usually shifts the core-level spectra in order to match experimental results.

Figure 4.4 shows the DSF within the range of 280-315 eV, where the onset of carbon K-edge transitions takes place (the spectra are scaled to match each other). In this figure, the experimental spectrum has the correct alignment while the DSF was shifted by +16.9 eV such that the lowest excitations match. We note that this value is needed with PBE and is much likely reduced by a functional that captures these transitions better. However, our calculations included atomic ZORA treatment and one can expect larger required shifts without so.
Both spectra agree very well and one can clearly identify corresponding carbon K-edge transitions at around 285, 289, 290, and 293 eV. Above 295 eV, the experimental spectrum likely shows continuum transitions. The small experimental peak at 287.4 eV does not seem to be captured by theory directly, but one can suspect a correspondence to the DSF transition at 286.9 eV. Judged by the rather 'simple' simulation

setup via the 'tight' basis set and the PBE XC functional, a surprisingly good agreement between experimental and theoretical spectra can be obtained for the benzene molecule. We will provide some more details about core-level spectroscopy via RT-TDDFT in the next section.

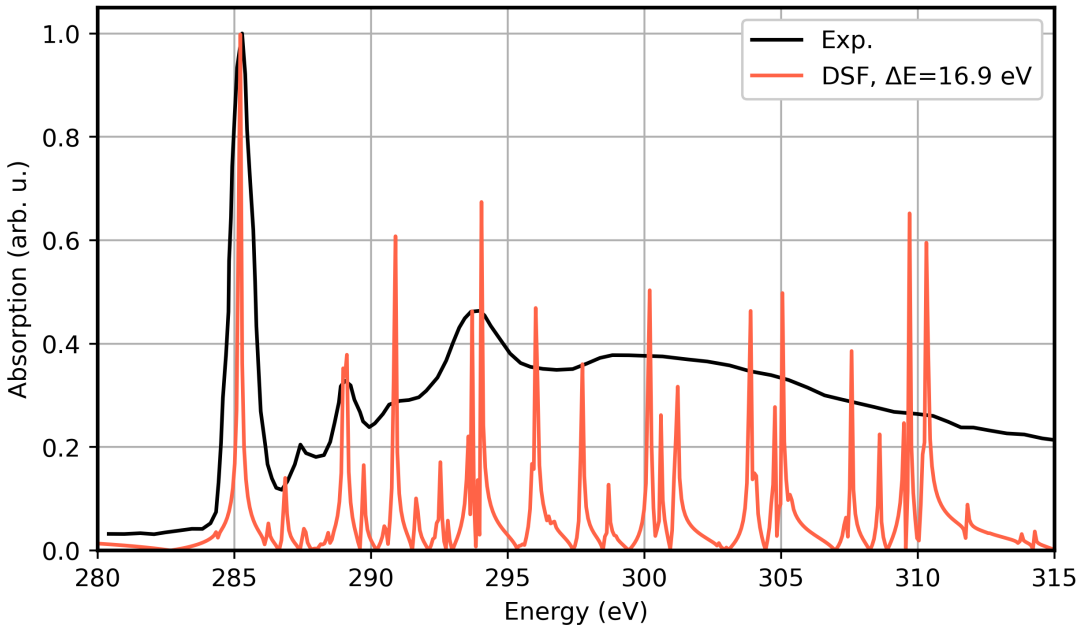

FIGURE 4.4: Comparison of the experimental carbon K-edge core absorption spectrum [169] (black line) of benzene with the DSF (red line) from the electronic dipole moments from our RT-TDDFT simulations. The DSF spectrum was shifted by +16.9 eV such that the lowest excitations match. The spectra are scaled such that the highest peaks match.

4.2.4 Oxygen K-Edge Core-Level Absorption Spectrum for Water

As a second example for XANES simulations, we selected the water molecule. We chose to provide a comparison with not only experimental [170], but also with real-time TDDFT results from another implementation to discuss energy shifts in the spectra and to put our findings into context with an existing framework. The RT-TDDFT XANES simulations by Lopata et al. [156] were done for (gas-phase) water, carbon monoxide and some other systems, but we will only provide comparison for water as a prototypical example. The reference simulations were performed with the GTO-based NWChem software [171]. Here, the Sapporo-QZP basis set including additional diffuse Gaussians [172] and the B3LYP exchange-correlation functional [33] were employed. The Sapporo-type basis sets are constructed to efficiently incorporate core and valence correlations.

We not only aimed to exactly reproduce the reference data with the same basis set and functional, but also evaluated the native numerical basis sets of FHI-aims for this task. In contrast to the reference, we were also able to measure the impact of the atomic ZORA relativistic treatment on the core-level absorption spectra. Equal

to Lopata et al., we used a geometry that was relaxed with the B3LYP XC functional and the aug-cc-PVTZ GTO basis set, which is included in the FHI-aims package for benchmark purposes. The Sapporo-QZP basis set was obtained from Basis Set Exchange [173] ('Sapporo-QZP-diffuse') and we used very dense and extended real-space integration grids in this case. The RT-TDDFT simulations were performed with a time-step of 0.02 a.u. = 0.0004 fs for a total duration of 700 a.u. = 17 fs – in total three calculations with $\{x, y, z\}$-polarized initial field kicks with amplitudes of 0.001 a.u. = $5.14 \cdot 10^8$ V/m.

Figure 4.5 shows the absorption spectra from experiment, the theory reference and both our RT-TDDFT simulations for the 'tight+aug2' and the 'Sapporo-QZP-diffuse' basis sets in the relevant region where oxygen K-edge excitations can be observed. It additionally shows results for different basis sets ('tight', 'tight+aug2' and a custom 'very tight+aug2') in the second row, and results for different XC functionals (B3YLP, PBE0, PBE) in the third row. We will discuss these results one after another. Note that all calculations were performed without relativistic atomic ZORA corrections if not stated otherwise. As discussed in Ref. [156], the simulated spectra have to be shifted by a constant value to match experimental data – a consequence of the sensitive dependency onto the exchange-correlation functional. However, the relative positions of peaks are expected to be in good agreement with experiment. The shift needed to align the lowest oxygen K-edge excitation to experiment in the work of Lopata et al. is +15.4 eV but we added another 0.15 eV in order to align the spectra better to the experimental spectrum.

In the top row, we can see that our calculations with the 'Sapporo-QZP-diffuse' basis set reproduce the results of Lopata et al. nearly perfectly, as measured by the spectral structure. The peaks around 540 eV are less prolonged in our results but show the same features. The spectrum generated by the 'tight+aug2' basis set shows the same features, but with a smaller overall corrective shift of 15.4 eV, and the third and fourth peak being redshifted relative to the reference theory spectra.

In the second row of the plot, one can observe a significant sensitivity of the spectrum with respect to the basis set. Clearly, the diffuse Gaussian augmentation functions in the 'tight+aug2' set yield significant convergence of the spectrum relative to the standard 'tight' set, hinting towards an important contribution of the augmentation functions. Between the 'tight+aug2' and the 'very tight+aug2' set, one can still identify clear differences. The custom 'very tight+aug2' set was set equally to the 'tight+aug2' set but includes additional 2p (ionic), 4f, 4d and 2s (hydrogenic) basis functions from the native 'Tier 3' basis set specification. While the lowest excitation is obviously converged here, higher excitations still alter their relative positions. Interestingly, the fourth peak is shifted less than the second and third one. Comparing with the experimental spectrum, it is possible that the fourth theoretical

peak corresponds to the third peak measured in the experiment. Since the augmentation functions and the grid specifications are the same in the 'very tight+aug2' and the 'tight+aug2' set, we likely observe an improvement due to the additional ionic/hydrogenic basis functions in this case.

Finally, the third row shows spectra for the 'tight+aug2' basis set but for different XC functionals – PBE, PBE0, B3LYP – and *with* relativistic ZORA treatment in one case for B3LYP. The spectra are much less affected from the choice of functional within this selection and only some small shifts are seen for the 2nd and 3rd peaks. The PBE0 spectrum shows the most visible differences relative to the other spectra. However, the shifts are quite different with +23.9 eV for PBE, 13.7 eV for PBE0 and 15.4 eV for B3LYP. In the latter case, relativistic treatment is responsible for a shift of +0.8 eV, but does not otherwise affect the spectrum. In this sense, PBE0 seems to capture the core-level excitation best, as it required the smallest correctional shift.

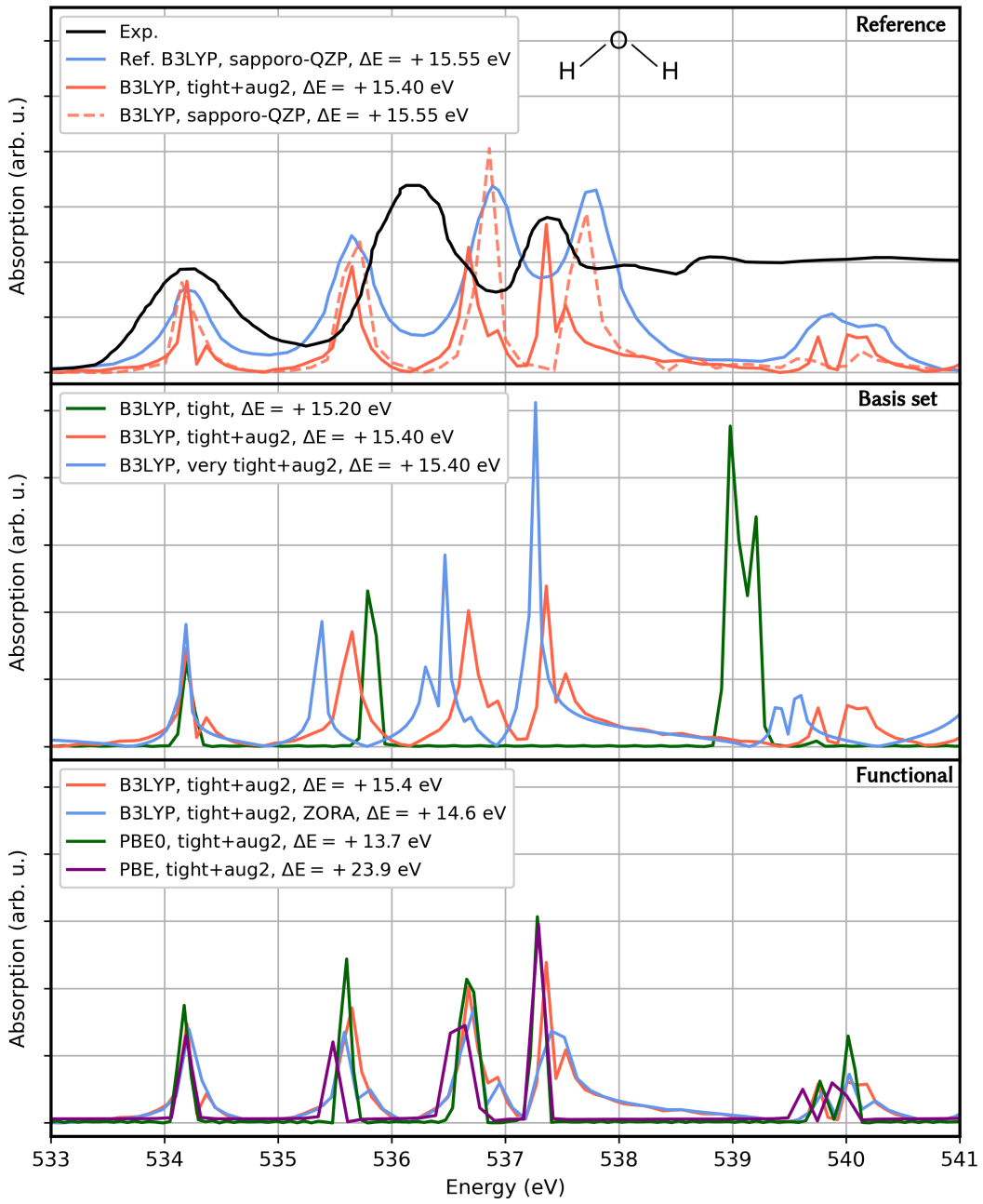

FIGURE 4.5: Top row: comparison of the experimental oxygen K-edge core-level absorption spectrum (black line) [170] of water with B3LYP-RT-TDDFT spectra obtained with our code ('tight+aug2' basis set: red line, 'Sapporo-QZP-diffuse' basis set: dashed red line), and B3LYP-RT-TDDFT spectra by Lopata et al. [156]. The real-time TDDFT spectra are x-shifted for comparison with the experimental data (see legend). The spectra are scaled to match each other, as they were given in arbitrary units in the references. Middle row: B3LYP-RT-TDDFT spectra from our code for the basis sets 'tight', 'tight+aug2' and 'very tight+aug2'. Bottom row: RT-TDDFT spectra from our code with the 'tight+aug2' basis set and B3YLP (with and without atomic ZORA correction), PBE0 and PBE XC functionals.

4.2.5 Benchmarking Real-Time TDDFT for Molecular Optical Absorption

Introduction

As noted and presented before, real-time TDDFT can also be used to describe linear-response electron processes within the DFT picture. We decided to contribute to this knowledge base by employing our RT-TDDFT implementation for an optical absorption molecular benchmark study. This also serves as a detailed linear-response assessment of our implementation described here. It was our aim to assess possible technical differences between LR-TDDFT and RT-TDDFT for this task, given the fact that both methods must in principle yield the same information. Since the method of data extraction plays a role in RT-TDDFT simulations [155, 158], as spectral quantities need to be generated from explicitly time-dependent observables, we also discuss this topic in some more detail. Also, to our knowledge, this is the first study systematically comparing not only singlet, but also triplet excitations between LR- and RT-TDDFT.

We chose a popular electronic excitation ab-initio simulation test set by Schreiber et al. [165], commonly known as 'Thiel's set'. This set consists of 28 small- to medium-sized organic molecules consisting of H, C, N and O elements. In the

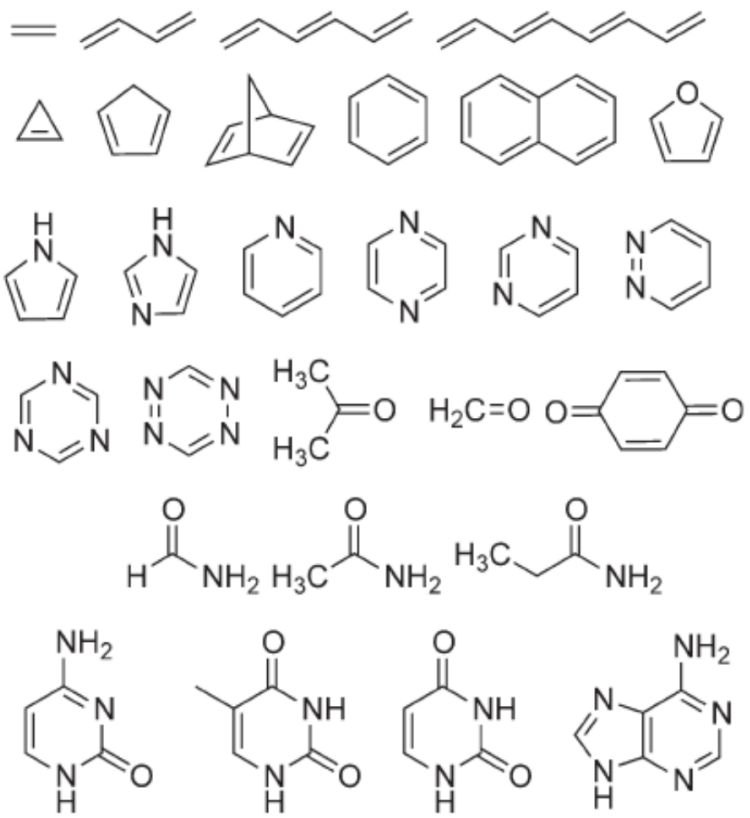

FIGURE 4.6: Molecules in Thiel's set. Picture from Ref. [174], copyright granted by John Wiley and Sons (license number 5097571063931).

mentioned study, several quantum-chemical methods, namely LR-TDDFT, coupled cluster (CC2, CCSD, CC3), multistate complete-active-space second-order perturbation theory (MS-CASPT2) and DFT+multireference configuration interaction (DFT + MRCI), were used to calculate optical absorption spectra and oscillator strengths in order to obtain 'best estimate' values.
In contrast to this goal, we did not put the focus of our study onto the physical accuracy, i.e., absolute excitation energies, but rather on the characteristics with respect to the used basis set, motivated by a study of Liu et al. [99], where implementations of LR-TDDFT and a G_0W_0-based Bethe-Salpeter equation method (G_0W_0 + BSE) into the FHI-aims code were assessed in this regard and for the Thiel set. An important result was that the *augmented* 'tight+aug2' basis set forms a very accurate and economic choice to converge excitation energies for a fixed level of theory. We follow the same route here for a comparison between LR- and RT-TDDFT, given the fact that the results of the mentioned study are directly comparable, as the same codebase is used.

Calculation of Triplet Excitations

The foundation of RT- and LR-TDDFT and the method of linear-response calculations with real-time TDDFT were already given before and we will refer the reader to the corresponding chapters. Anyway, as stated already, this study incorporated the calculation of both singlet and triplet excitation spectra. In the standard approach, linear-response RT-TDDFT simulations only yield information about singlet excitations, as the α and β electron densities have the same dynamics (introducing the α/β notation for up/down spin). Isborn et al. [175] showed that triplet excitations can be modeled in real-time TDDFT by introducing a spin-dependent external perturbing field that breaks the spin symmetry of the time-evolved superposition state. The Hamiltonian and the time-evolution operator thus become spin-dependent, imposing different dynamics on the spin eigenstates which are nevertheless being coupled by the density-functionalization:

$$\mathcal{H}_{\mathrm{KS},\sigma}[\rho(t),t] = \mathcal{H}_{\mathrm{KS}}[\rho_\alpha(t)+\rho_\beta(t)] + V_{\mathrm{ext},\sigma}(t), \tag{4.16}$$

$$\psi_{n\sigma}(t) = \mathcal{U}_\sigma(t,t_0)\psi_{n\sigma}(t_0). \tag{4.17}$$

The external field is then only applied to one selected spin component, i.e., $V_{\mathrm{ext},\sigma}(t) = V_{\mathrm{ext}}(t)\delta_{\sigma\sigma'}$. The superposition state now also contains triplet contributions which we illustrate by a two-electron, two-orbital system, analogous to Ref. [175]: the system has one bonding orbital $\phi^b(\mathbf{r})$ and one non-bonding orbital $\phi^n(\mathbf{r})$, and is initially in the ground state S_0. In RT-TDDFT, the time-dependent wave function is formally a mixture of occupied and virtual molecular orbitals and thus, the spin-perturbed

molecular orbitals are

$$\phi_{\alpha\sigma}(\mathbf{r},t) = \Big(\phi^b(\mathbf{r}) + c_\alpha(t)\phi^n(\mathbf{r})\Big)\alpha(\sigma), \tag{4.18}$$

$$\phi_{\beta\sigma}(\mathbf{r},t) = \Big(\phi^b(\mathbf{r}) + c_\beta(t)\phi^n(\mathbf{r})\Big)\beta(\sigma) \tag{4.19}$$

(σ is the spin variable). The superposition state is given as

$$\begin{aligned}\Psi(t) &= \frac{1}{N(t)}|\phi_{\alpha\sigma_1}(\mathbf{r}_1,t)\phi_{\beta\sigma_2}(\mathbf{r}_2,t)| \\ &= \frac{1}{N(t)}\left(\Psi_{S_0} + \left(\frac{c_\alpha(t)+c_\beta(t)}{\sqrt{2}}\right)\Psi_{S_1}\right. \\ &\qquad \left. + \left(\frac{c_\beta(t)-c_\alpha(t)}{\sqrt{2}}\right)\Psi_{T_0} + c_\alpha(t)c_\beta(t)\Psi_{S_2}\right)\end{aligned} \tag{4.20}$$

with the normalization $N(t) = \sqrt{(1+c_\alpha^2(t))(1+c_\beta^2(t))}$ and $|\cdot|$ denotes a Slater determinant. One can see configurations for the ground state singlet Ψ_{S_0}, the excited state singlet Ψ_{S_1}, the excited state triplet Ψ_{T_0} and a doubly excited singlet state Ψ_{S_2}. Since $c_\alpha \neq c_\beta$ due to the spin-dependent field, one can observe the triplet contributions in the superposition state. The corresponding excitation spectra are generated from individual α/β spin components of the total dipole moment $\boldsymbol{\mu}(t) = \boldsymbol{\mu}_\alpha(t) + \boldsymbol{\mu}_\beta(t)$ – the total dipole moment does in contrast not show triplet contributions.

Simulation Setup and Analysis

In contrast to linear-response TDDFT where excitation energies are computed as discrete eigenvalues of a transition matrix, real-time TDDFT yields dynamical observables, in this case the electronic dipole moment, which need to be Fourier transformed in order to identify excitations as peaks of the resulting spectra. Spectral width and resolution are thus directly determined by the finite simulation time and time step. One thus has to deal with finite-width excitation peaks for a limited resolution in frequency space. While the spectral resolution scales with the simulation time, the latter quantity is always limited and is subject to economic constraints. One thus wants to achieve a best possible spectral resolution for a given, short-as-possible, propagation time.

We employed two recently suggested methods to optimize the accuracy of our simulations, which were always performed with an economic choice of about 60 fs simulation time. Each of these methods belongs to post-processing and aims to optimize spectral information. Schelter et al. [158] derived an analytical expression for the

DSF based on a model where the system is subject to a δ-pulse – this resulting expression corresponds to Equation 4.7 and reads

$$S(\omega) = \sum_{l=1}^{\infty} \bar{f}_l \frac{\omega}{\omega_l} \frac{\sin\Big((\omega - \omega_l)T\Big)}{\pi(\omega - \omega_l)}, \tag{4.21}$$

where $\{\bar{f}_l\}$ are oscillator strengths, $\{\omega_l\}$ are the excitation frequencies of the system, and T denotes the total simulation time. The proposed technique is based on fitting above equation to a zero-padded Fourier transform of the electronic dipole moment with respect to the oscillator strengths and the excitation frequencies – thus, these values have to be provided by the user initially and ultimately are the extracted data of the fit. Zero-padding denotes the addition of zero-value entries to the input signal of the FT in order to artificially increase the frequency resolution. This procedure helps to convergence the fit and thus increases the achieved accuracy.
Another method proposed by Bruner et al. [155] is based on artificially increasing the spectral resolution by calculating the necessary Fourier transforms not via Fast Fourier Transform (FFT) as usually done, but rather by doing so via Padé approximants [176]. The FT of the dipole moment is in this way calculated via a ratio of two power series

$$\begin{aligned} \mathcal{F}[\mu_i(t)](\omega) &= \sum_{k=1}^{\mathrm{M}} \mu_i(t_k) \left(e^{-i\omega\Delta t}\right)^k \equiv \sum_{k=1}^{\mathrm{M}} c_k z^k \\ &= \left(\sum_{k=1}^{\mathrm{M}/2} a_k z^k\right) \left(\sum_{k=1}^{\mathrm{M}/2} b_k z^k\right)^{-1} \end{aligned} \tag{4.22}$$

where we set $c_k := \mu_i(t_k)$ and $z^k := \exp(-i\omega\Delta t)^k$. Here, a diagonal scheme is presented, therefore we have $\mathrm{M}/2$ as sum limits in Expression 4.22 [155]. For the computation, one needs to determine the coefficients appearing in the ratio expansion first and can then calculate the FT for arbitrary frequencies ω. The coefficient vectors $\mathbf{a}$ and $\mathbf{b}$ are successively obtained by first solving the equation

$$\mathbf{C}\mathbf{b} = \mathbf{d} \tag{4.23}$$

for $\mathbf{b}$ with $C_{km} = c_{\mathrm{M}-m+k}$ and $d_k = -c_{\mathrm{M}+k}$. The vector $\mathbf{a}$ is afterwards computed using the relation

$$a_k = \sum_{m=0}^{k} b_m c_{k-m} \ , \ \ k = 1, ..., \mathrm{M}. \tag{4.24}$$

This procedure thus allows to generate very highly resolved spectra with sharp peaks. One can also think of this as frequency-space interpolation, which corresponds to extrapolation on the time axis. In fact, Bruner et al. used this technique together with the decomposition of occupied-unoccupied transition dipole moments $\boldsymbol{\mu}_{ou}(t)$ (as explained in Sec. 4.2.2): since the transition dipole moment spectra are rather sparse, one can accelerate the total spectrum convergence (with respect to

simulation time) by constructing it from the individual, Padé-FT sharpened transition dipole moment spectra. We did not employ this acceleration technique here, as this would mean too much effort with little gain. Instead, as suggested by Schelter et al. [158], we used the Padé-FT technique in combination with the fitting technique in order to generate highly resolved initial guesses for the fitting procedure and to identify peaks in problematically dense regions where the fitting technique fails. In this sense, we found that both methods complement each other: for very weak and/or densely lying excitations, the fitting technique mostly fails in practice, while the Padé method can usually handle them. However, the latter method can introduce artificial peaks for very short simulation times [155], which one has to be aware of (our simulations are although most likely not in this regime).
Figure 4.7 shows an illustration of this procedure for spectra of the s-tetrazine molecule (which is part of the benchmark set): the upper panel shows the log-scaled Padé-FT DSF spectrum and one can clearly identify excitations near 2 eV and between 5.4 eV and 6.3 eV. The corresponding excitation energies are used as input

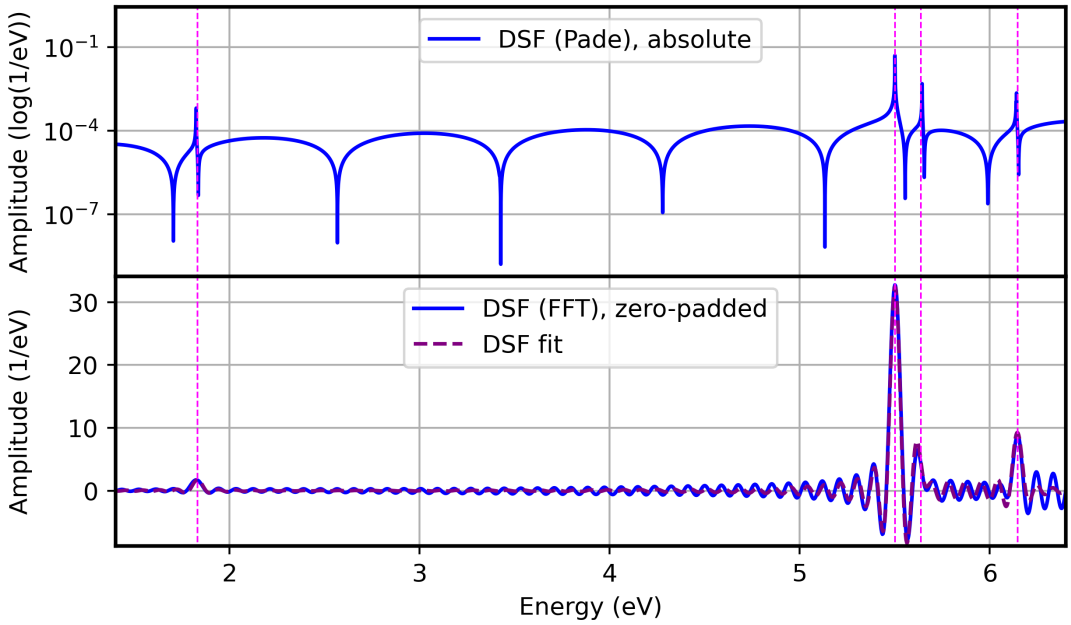

FIGURE 4.7: Illustration of the Padé and fitting methods for the DSF spectrum of the s-tetrazine molecule. The upper panel shows the Padé-DSF (on a logarithmic y-axis) and one can clearly identify excitations which are marked also as pink dashed lines. The lower panel shows the zero-padded DSF (blue) and the corresponding fit (purple dashed) that was initialized using the excitation energies of the Padé method.

for the fitted DSF spectrum shown in the lower panel. The fit will only yield good results for good initial guesses, including excitations with low oscillator strength. For very problematic cases, i.e., when the fit could not be converged (which has to be done by hand), we selected the excitation energies from the Padé DSF only. We used self-written python scripts for this procedure, employing the Numpy [177] and SciPy [178] libraries. These scripts are also contained in the software package and

short manuals can be found in Appendix D.

We carried out our simulations for two basis sets, namely the 'tight' and the doubly augmented 'tight+aug2' basis set, as contained in FHI-aims. While the 'tight' basis set can be considered a solid choice [42], the 'tight+aug2' basis set additionally contains two diffuse Gaussians as augmentation functions, which is known to noticeably improve excitation energies with moderate additional computational cost [99]. See Table 4.1 for the specifications of the used basis sets. It should be noted that, while only 2 additional Gaussians are added per atom, the computational demand is mainly increased due to the significantly denser and more elongated radial integration grids with higher angular momentum multipliers.

TABLE 4.1: Specifications for the 'light', 'tight' and 'tight+aug2' basis sets used in our calculations. All basis functions are of hydrogenic type if not specified otherwise. Radial and angular quantum numbers indicate the shape, in parentheses are given the effective charges in the defining Coulomb potential. Gaussian functions are defined by gauss_{LN} where L specifies angular momentum and N the number of primitive Gaussians; the exponent (in a_0^{-2}) is given in the following parentheses. Each row adds another basis function to the last filled row above in that column.

	Basis functions			
Basis set	Hydrogen	Carbon	Nitrogen	Oxygen
'light'	minimal	minimal	minimal	minimal
	2s (2.10)	2p (1.70)	2p (1.80)	2p (1.80)
	2p (3.50)	3d (6.00)	3d (6.80)	3d (7.60)
		2s (4.90)	3s (5.80)	3s (6.40)
'tight'	1s (0.85)	4f (9.80)	4f (10.80)	4f (11.60)
	2p (3.70)	3p (5.20)	3p (5.80)	3p (6.20)
	2s (1.20)	3s (4.30)	1s (0.80)	3d (5.60)
	3d (7.00)	5g (14.40)	5g (16.00)	5g (17.60)
		3d (6.20)	3d (4.90)	1s (0.75)
'tight+aug2'	gauss_{01} (0.02)	gauss_{01} (0.04)	gauss_{01} (0.05)	gauss_{01} (0.06)
	gauss_{11} (0.07)	gauss_{11} (0.03)	gauss_{11} (0.04)	gauss_{11} (0.04)

The real-time TDDFT simulations were performed with total simulation times of 2500 a.u. $=$ 60.48 fs together with the semi-implicit exponential midpoint propagator. Usually, we set the time step to 0.4 a.u. $=$ 0.0096 fs, which can be considered as relatively large. For some cases, numerical instabilities forced us to reduce the time step to 0.3 a.u. $=$ 0.0072 fs – this happened always when using the 'tight+aug2' basis set. We measure the numerical stability by the degree of energy conservation for a given threshold: a short time after the kick pulse was applied, a reference value E_{ref} of the total electronic energy is kept fixed and at every subsequent step where the total energy $E(t)$ is evaluated, the deviation between the current and the reference value must not exceed a threshold value. We here set $|E(t) - E_{\text{ref}}| \leq 0.001$ eV, where E_{ref} is set at 25 a.u. $=$ 0.60 fs, which is 15 a.u. $=$ 0.24 fs after the center of the

kick pulse with a Gaussian shape of FWHM = 2.8 a.u. = 0.07 fs. The amplitude of the electric field was set to $E_0 = 0.01$ a.u. $= 5.1 \cdot 10^9$ V/m. It should be noted that we employed a rather strict threshold for the deviation in total energy and that it is likely possible that larger time steps could have been used in most cases. We observed that slight linear drifts in the total energy (e.g., below 0.1 eV deviation over the whole simulation time) do not really alter the resulting dynamics. For the given time steps, one can clearly expect converged valence spectra, as we also show in Section 6.2.2.

We used the PBE exchange-correlation functional [26] for the RT-TDDFT simulations, while the LR-TDDFT calculations were performed with the PW-LDA XC kernel [23] (provided by the LibXC library [179]), based on ground state PBE solutions – we denote these settings as 'LR-TDDFT-LDA@PBE', similar to Ref. [99]. For both calculations, the same pre-relaxed geometries were used (for the same basis set and level of theory).

Results

Comparison of Basis Set Dependence We first analyze the sensitivity of excitation energies with respect to basis set type for both methods. In this context, this can only be done in a restricted way, as it is not straightforwardly possible to compare/identify specific excitations between simulations that were conducted with different basis sets or XC functional (for the same physical system). One can nevertheless compare the respective lowest energy excitations; we thus extracted the respective lowest visible excitation energies in order to compare them. We denote the difference of the lowest excitation with respect to basis set as $\Delta E_1 = E_1(\text{tight}) - E_1(\text{tight} + \text{aug2})$, i.e., this value is signed and can usually be expected as positive since a more complete basis set lowers energy, as, e.g., shown in Ref. [99].

The singlet excitation results for all 28 molecules are shown in Fig. 4.8, both for LR-TDDFT and RT-TDDFT. This figure contains a second y-axis on the right side which corresponds to the dashed grey line, showing LUMO energies from PBE calculations with the 'tight+aug2' basis set. The reason for this is that previous studies [99, 180] showed that diffuse augmentation basis functions can be important in order to describe electron affinities (EA) correctly. The density functional theory version of Koopman's Theorem states that the Kohn-Sham EA $= -$ LUMO$_{\text{KS}}$ [18], however, one should not take the corresponding values shown here as accurate since these are usually underestimated with standard functionals [181, 182]. Nevertheless, one can clearly see correlations between ΔE_1 and the LUMO energies, indicating that lower electron affinities are connected to stronger convergence with respect to basis set size, underlining the formerly mentioned observations. This is not surprising, as low excitations that are already close to the ionization level are susceptible to basis set errors, as the corresponding wave functions have extent into the vacuum.

Regarding the characteristics of ΔE_1, a very high agreement between LR- and RT-TDDFT can be seen, on average (for all molecules), $\Delta E_1(\text{RT}) - \Delta E_1(\text{LR}) \approx -0.001$

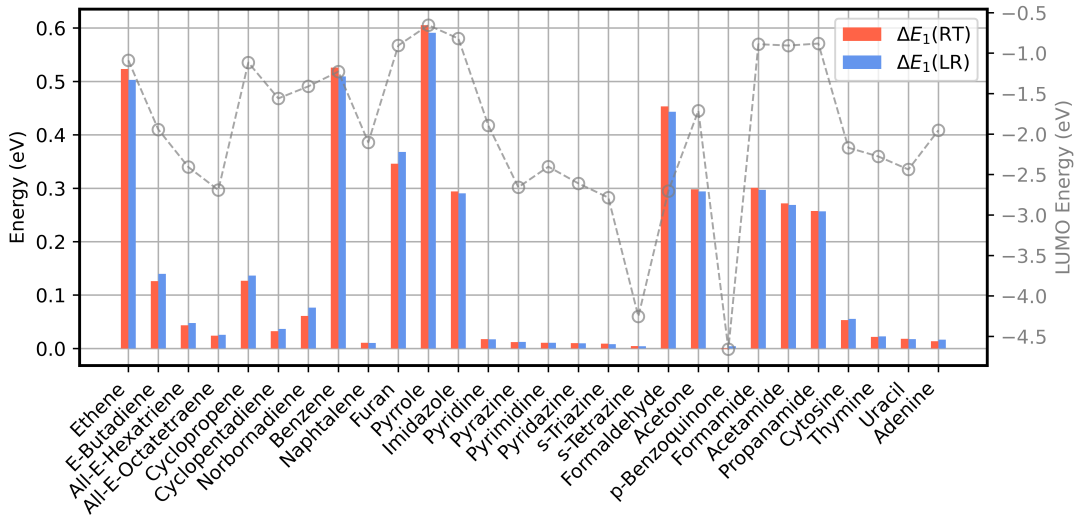

FIGURE 4.8: Singlet energy differences ΔE_1 of the lowest excitations between 'tight' and 'tight+aug2' basis sets for RT-TDDFT (RT) and LR-TDDFT (LR) for all molecules in the benchmark set. The grey dashed line and the corresponding y-axis on the right side show the respective LUMO energies obtained from SCF calculations with the PBE XC functional and the 'tight+aug2' basis set.

eV, with minimum and maximum differences of -0.022 eV and 0.016 eV, respectively. The individual differences are considerable and we group them arbitrarily, based on the absolute scale: small deviations below 0.02 eV are observed for 10 molecules, average deviations between 0.02 eV and 0.15 eV are observed for 8 molecules and large deviations above 0.15 eV are seen for 10 molecules, with a maximum of 0.6 eV for pyrrole.

The lowest triplet excitation energy differences for both methods are shown in Figure 4.9. We did not include LUMO energies as no visible correlation is present in

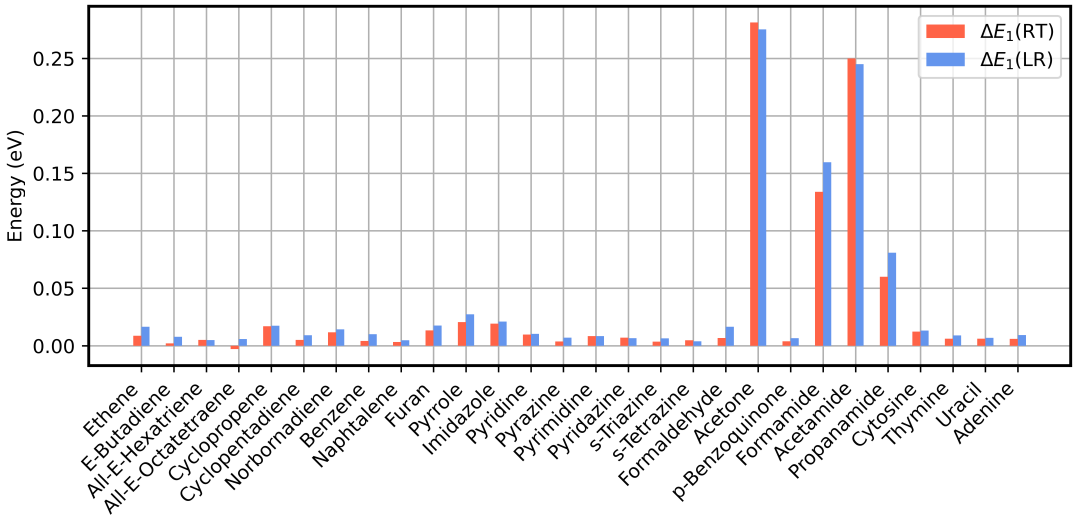

FIGURE 4.9: Triplet energy differences ΔE_1 of the lowest excitations between 'tight' and 'tight+aug2' basis sets for RT-TDDFT (RT) and LR-TDDFT (LR) for all molecules in the benchmark set.

this case, which may originate in the generally lower triplet excitation energies due to the reduced Coulomb repulsion, as by Hund's rule [183]. In contrast to singlet excitations, the relevant energy range is approximately halved (to ~ 0.3 eV) and one can directly see that most excitations display significantly lower convergence with respect to basis set quality – the overall basis effect is thus smaller. However, this does not necessarily apply to all excitations: in Figure 4.10 we exemplary present the triplet DSF of ethene, showing a significant basis effect for higher-lying excitations. Some cases not only show larger values of ΔE_1, but also comparably larger differences between LR- and RT-TDDFT results, namely formamide (0.03 eV) and acetamide (0.07 eV). For all the mentioned cases, the RT-TDDFT excitation energies are less affected by the basis set change, compared to LR-TDDFT excitations. For the remaining molecules, the differences are very small, meaning below 0.03 eV. On average, LR-TDDFT excitation energies are larger than RT-TDDFT excitation energies by 0.004 eV. In summary, both methods have high agreement and show the same sensitivity to the basis set.

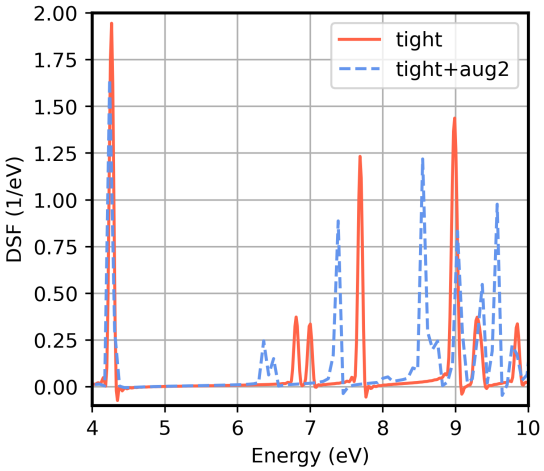

FIGURE 4.10: Unrefined DSF triplet spectra of ethene for both basis sets.

Comparison between LR- and RT-TDDFT Excitations We will here provide an analysis of LR- and RT-TDDFT excitations in direct comparison in order to identify possible distinctions, as in the previous section, only differences of the lowest excitations were compared. Since we aim to capture trends as well as corner cases, we selected the first 8-18 lowest clearly identifiable and comparable excitations. We employed both the fitting and the Padé technique and found that both methods mostly yield exactly the same results, i.e., differences were generally in the meV range, and we thus do not provide further comparison. For very dense spectral regions or weak excitations where the fitting method was problematic, we relied on the Padé method. For all excitations that could be fitted correctly, we obtained the oscillator strengths (OS) by this method. The OS values from LR- and RT-TDDFT are generally close to each other, i.e., deviating by 2.2% for the 'tight' basis set and 9.15% for the 'tight+aug2' basis set. However, one must be cautious for degenerate excitations, e.g., in benzene, as these can not really be resolved via RT-TDDFT. In this case, the peak heights do not correspond so well to the correct oscillator strengths. For smaller peaks, the uncertainty from the fitting has larger impact, which can be seen in Fig. 4.11 (left), showing the signed ratio for LR- and RT-TDDFT in dependence of the absolute OS.

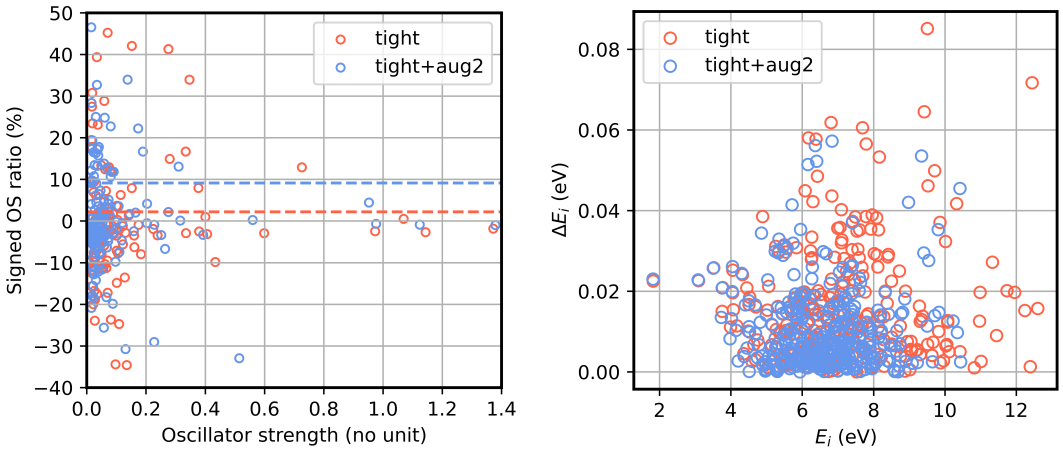

FIGURE 4.11: Left: signed ratio of oscillator strengths betwen LR- and RT-TDDFT, defined via $R_{\mathrm{OS}} = (\bar{f}_l(\mathrm{RT})/\bar{f}_l(\mathrm{LR}) - 1) \cdot 100\%$ as function of the absolute oscillator strength. The dashed lines denote the respective averages and we only show values for OS > 0.01. Right: pairs of $(\Delta E_l, E_l)$ for all molecules and excitations, indicating possible relationships between excitation energy method difference and absolute excitation energy, for both basis sets.

The higher mean deviations in the 'tight+aug2' case clearly stem from the deviations in the small OS region. For these small values, numerical precision plays a more important role, yielding higher deviations. Most tracked excitations have lower OS in the region between 0.005 and 0.2, where the spread is noticeable. For higher OS, both methods are visibly more consistent.

We now turn to the discussion of the excitation energies. Before discussing these in more detail, we shed light on the overall differences between LR- and RT-TDDFT in dependence of the absolute excitation energies: Figure 4.11 (right) shows these pairs for all molecules. It additionally shows the overall range of tracked excitations. It is clear that most excitation energies are located between 4 and 10 eV, as we selected the few lowest peaks. Regarding the differences, we observe that the distributions spread upwards with higher excitation energies. This is more pronounced for the 'tight+aug2' basis set, which also has a higher center of mass on the y-axis. While no strong correlations are evident, the differences appear overall slightly higher with the larger basis set.

Regarding the differences for the individual molecules, i.e., the values $\{E_l(\mathrm{RT}) - E_l(\mathrm{LR})\}$ for excitations l for each molecule, we start by discussing the singlet characteristics via Figure 4.12. It shows the individual distributions via the observed min/max values as whiskers, the averages as red bars and the blue boxes contain 50% of the respective data. The differences are overall small, with the absolute averages being bound by approximately 0.03 eV. Some larger min/max values are observed especially in the 'tight' dataset. Overall, the RT-TDDFT excitations are lower by 0.007 eV as the LR-TDDFT excitations. Anyway, this trend is relatively consistent for all molecules. The more complete basis set yields less spread in nearly all cases and also reduces the overall shift slightly. However, the spreads for both basis

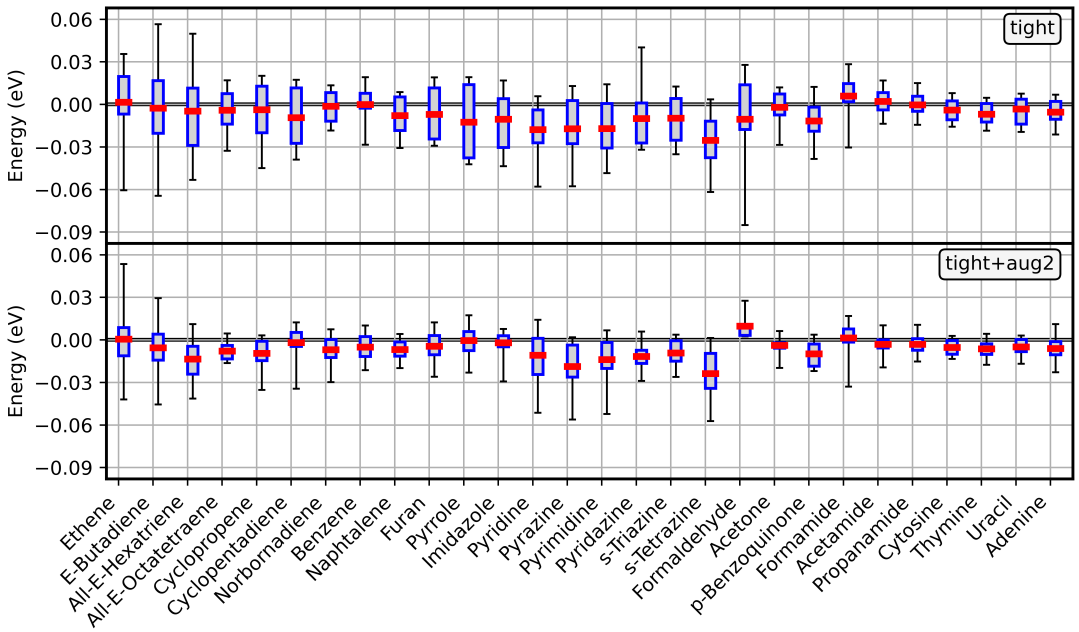

FIGURE 4.12: Singlet excitations: distributions of energy differences between RT-TDDFT and LR-TDDFT, i.e., $E_l^{\mathrm{mol}}(RT) - E_l^{\mathrm{mol}}(LR)$, for 'tight' (upper panel) and 'tight+aug2' (lower panel) basis set. Red bars denote the averages, blue boxes contain 50% of the respective values, and whiskers denote min/max values.

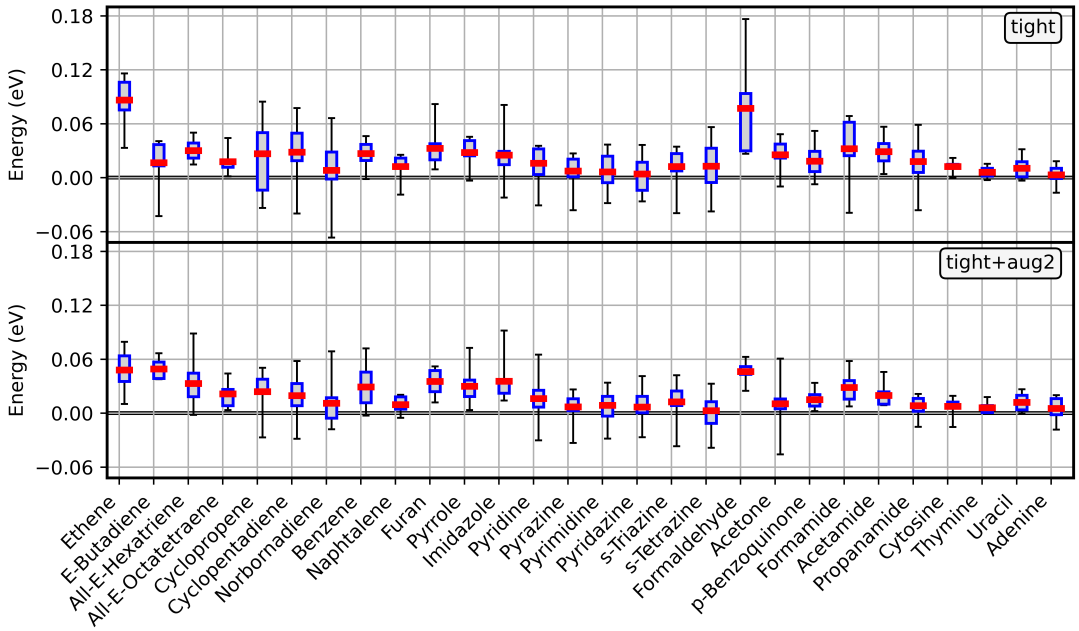

FIGURE 4.13: Triplet excitations: distributions of energy differences between RT-TDDFT and LR-TDDFT, i.e., $E_l^{\mathrm{mol}}(RT) - E_l^{\mathrm{mol}}(LR)$, for 'tight' (upper panel) and 'tight+aug2' (lower panel) basis set. Red bars denote the averages, blue boxes contain 50% of the respective values, and whiskers denote min/max values.

sets have quite similar characteristic which points to methodological differences that are likely not related to the basis set. The analogous data for the triplet excitations is depicted in Figure 4.13. We find that the deviations are on average larger than in the singlet case. Especially ethene and formaldehyde present noticeably larger differences which reduce with the more sophisticated basis set. On average, the RT-TDDFT excitations are 0.022 eV (0.020 eV) lower for the 'tight' ('tight+aug2') basis set, as compared to LR-TDDFT. The overall trend is thus inverse to the singlet case, where RT-TDDFT excitation energy differences are on average lower. As in the singlet case, the spread is more pronounced for the 'tight' basis set. Also, the overall characteristics between the basis sets are very similar, again indicating a methodological cause. Overall the agreement between both methods is very high, but we observe some smaller differences that were also sensitive to the basis set.

4.2.6 Discussion

In this chapter, we have shown real-time TDDFT results for a variety of linear-response calculations for molecules. For the first test case benzene, as presented in Section 4.2.3, an excellent agreement with experimental data could be obtained both for valence and core-level excitations. As this is a prototypical testcase in the community, we provided first evidence of the capabilities of our method in this regime.
Our NEXAFS simulations for the water molecule in Section 4.2.4 have reproduced reference theoretical data perfectly with the same settings. We further showed that the native FHI-aims basis sets are very well-suited for such calculations. It should be noted that our calculations with the 'tight+aug2' basis set were significantly faster, as compared to the reference 'Sapporo-QZP-diffuse' set (however, it must be said that FHI-aims is not a native GTO-based code). In addition, we made clear in this context that we correctly implemented inclusion of hybrid exchange-correlation functionals, too.
Our benchmark study, presented in Section 4.2.5, has given some insight about the general reconstruction of linear-response absorption spectra from RT-TDDFT, the calculation of triplet excitations in this context, and the agreement between LR- and RT-TDDFT in this framework. Here, we found that both singlet and triplet excitation spectra agree as expected and that the doubly augmented 'tight+aug2' basis set can provide significant basis set convergence with comparably low additional computational effort also in the real-time TDDFT framework.
As the FHI-aims code scales formally with $\mathcal{O}(N_{at})$ for larger systems, we provide an attractive alternative to LR-TDDFT approaches for large systems and will show later that our implementation is efficient.

4.3 Response of Periodic Systems

In this chapter, we will present results for real-time TDDFT simulations with periodic boundary conditions. The first part is about the computation of the linear-response dielectric function of silicon – we compare our results with theoretical reference data and assess numerical settings. The second part covers the simulation of both valence and core-level absorption spectra of silicon carbide, and we compare our results with reference data and discuss specifics of the basis set. In the third part, we present and discuss simulation results for non-linear dynamics in silicon, namely for high-harmonic generation.

4.3.1 Introduction

While the basic motivation to characterize the linear optical absorption is the same for bulk matter, this state has its own implications for theoretical treatment. As in any experiment, the sample is finite and intrinsically includes surface or environment effects, the first formal approach is to consider a bulk system with periodic boundary conditions mimicking infinite extent. Many material properties can be derived from this perspective, and one is even able to describe surface effects by constructing systems that do *effectively* have a surface. Typical applications in this regime are given by simulations for solid-state semiconductors like in the prototypical case silicon. The tuning of optical absorption of elemental or compound semiconductors by various mechanisms is a huge and relevant research field with important applications, most importantly in solar energy acquisition. TDDFT has made many significant contributions to this topic [59] and in recent years, real-time TDDFT applications in solids became more frequent. This includes linear-response calculations of the dielectric function of bulk lithium and diamond [85], photoabsorption spectra of graphene nanoribbons [184], excitons [153] or core-level linear response [74], but also simulations of non-perturbative phenomena like non-linear conductivity [76], non-linear susceptibilities [77] and laser-induced demagnetization [185].
Another typical example for highly nonlinear electron dynamics is the process of high-harmonic generation (HHG) where an atomic, molecular or solid-state system is subject to strong laser pulses and which emits higher-order harmonics of the exciting laser field. This is a rather recently applied technique which can be used to generate ultrashort laserpulses in the attosecond regime, giving opportunity to analyze electron dynamics with very high temporal resolution [186]. High-harmonic generation is usually modeled by a 3-step-process [187] (in a single-electron picture): in the first step, the target is ionized by the strong infrared pulse, followed by the second step of the excited electron being accelerated in the field, while the third step is the recombination of the electron with its parent ion, as consequence of the sign change of the driving field. The recombination causes emission of coherent radiation in the near- or soft X-ray range with high time resolution in the attosecond range.
Real-time TDDFT was recently used for the simulation of HHG in atoms [188, 189,

190], molecules [191, 192, 193] and solids [194, 195, 196, 197]. However, in this highly non-perturbative regime, the strong fields acting on the electrons require that continuum and Rydberg states need to be correctly described by both the functional [192] (e.g., via long-range corrected functionals [198]) and the basis set [199]. The latter quickly becomes limiting for molecular systems when localized basis sets are used, as these naturally have limited spatial extent. While HHG simulations for finite systems are rather unproblematic with extended basis sets (but possibly computationally less efficient) or real-space grids, some effort has been put into methods that allow strong-field dynamics with local basis sets. Such approaches are, e.g., to place 'ghost' atoms in space, essentially extending the spatial integration grid [189], continuum-adapted sets [200], or complex absorbing potentials [168, 201, 202].

4.3.2 Theory

As described in Section 3.3.3, our implementation is also able to perform simulations for systems with periodic boundary conditions. Like noted in Section 2.2.5, the most straightforward way to include an external field in this case is provided by the velocity gauge, i.e., the Hamiltonian being coupled to a vector potential via a modified time-dependent kinetic term including the vector potential $\mathbf{A}(t)$. Analogously, the electronic dipole moment (i.e., the macroscopic polarization) can not be used in a trivial way to, e.g., compute absorption spectra, as the position operator is required to do so, which is ill-defined. The key observable in this case is the time-dependent macroscopic electronic current $\mathbf{I}(t)$ which is calculated from the electronic current density that incorporates the generalized momentum operator $\hat{\boldsymbol{\pi}}(t) = -i\nabla + \mathbf{A}(t)$ in the velocity gauge,

$$\begin{aligned}
\mathbf{j}(\mathbf{r},t) &= \frac{1}{2}\sum_{n\mathbf{k}} w_{\mathbf{k}} f_{n\mathbf{k}} \Big(\psi^*_{n\mathbf{k}}(\mathbf{r},t)\hat{\boldsymbol{\pi}}(t)\psi_{n\mathbf{k}}(\mathbf{r},t) + \text{c.c.} \Big) \\
&= \frac{1}{2}\sum_{n\mathbf{k}} w_{\mathbf{k}} f_{n\mathbf{k}} \Big(\psi^*_{n\mathbf{k}}(\mathbf{r},t)\big(-i\nabla + \mathbf{A}(t)\big)\psi_{n\mathbf{k}}(\mathbf{r},t) + \text{c.c.} \Big) \\
&= \rho(\mathbf{r},t)\mathbf{A}(t) + \frac{1}{2}\sum_{n\mathbf{k}} w_{\mathbf{k}} f_{n\mathbf{k}} \Big(\psi^*_{n\mathbf{k}}(\mathbf{r},t)\big(-i\nabla\big)\psi_{n\mathbf{k}}(\mathbf{r},t) + \text{c.c.} \Big) \\
&\equiv \mathbf{j}_{\text{d}}(\mathbf{r},t) + \mathbf{j}_{\text{p}}(\mathbf{r},t)
\end{aligned} \tag{4.25}$$

($f_{n\mathbf{k}}$ are occupation numbers and $w_{\mathbf{k}}$ are $\mathbf{k}$-point integration weights), where we introduced the contributions $\mathbf{j}_{\text{d}}(\mathbf{r},t)$ and $\mathbf{j}_{\text{p}}(\mathbf{r},t)$, commonly denoted as diamagnetic and paramagnetic current density, respectively [203]. The macroscopic current is then computed via

$$\begin{aligned}
\mathbf{I}(t) &= -\frac{1}{V_{\text{uc}}}\int_{V_{\text{uc}}} \mathrm{d}^3\mathbf{r}\; \mathbf{j}(\mathbf{r},t) \\
&= -\frac{N_{\text{el}}}{V_{\text{uc}}}\mathbf{A}(t) + \frac{1}{V_{\text{uc}}}\sum_{n\mathbf{k}} w_{\mathbf{k}} f_{n\mathbf{k}} \text{Re}\left\{ i\mathbf{c}^*_{n\mathbf{k}}\mathbf{G}_{\mathbf{k}}\mathbf{c}_{n\mathbf{k}} \right\}
\end{aligned} \tag{4.26}$$

with V_{uc} being the volume of the unit cell, $\mathrm{N_{el}}$ as the number of electrons therein, and the basis gradient matrix $G_{\mu,ij\mathbf{k}} = \langle \chi_{i\mathbf{k}} | \partial_\mu | \chi_{j\mathbf{k}} \rangle$, i.e., the matrix element of the gradient operator in the generalized Bloch basis.

Linear Response

We will here consider the linear response characterized by Ohm's law:

$$\mathcal{F}[\mathbf{I}(t)](\omega) = \sigma(\omega)\mathcal{F}[\mathbf{E}(t)](\omega). \tag{4.27}$$

Employing the gauge connection

$$\mathbf{E}(t) = -\partial_t \mathbf{A}(t), \tag{4.28}$$

one obtains the linear electronic conductivity tensor via

$$\sigma_{ij}(\omega) = \frac{\mathcal{F}[I_i(t)](\omega)}{\mathcal{F}[E_j(t)](\omega)} \tag{4.29}$$

by performing 3 individual calculations, each with a different field polarization. For a broadband excitation, the electric field is a delta-kick $\mathbf{E}(t) = \mathbf{E}_0\delta(t - t_0)$, and analogously, the vector potential is $\mathbf{A}(t) = -\mathbf{E}_0\Theta(t - t_0)$ with the Heaviside function $\Theta(t)$. Finally, the conductivity tensor can be used to calculate the complex dielectric function

$$\epsilon(\omega) = 1 + i\frac{4\pi}{3\omega}\mathrm{Tr}\Big[\sigma(\omega)\Big]. \tag{4.30}$$

As known from classical electrodynamics [204], the imaginary part of $\epsilon(\omega)$ is a measure of a material's absorption of electromagnetic radiation. It should be added that we do not consider the feedback of the electron system onto the external vector potential here. However, Yabana et al. have demonstrated a RT-TDDFT velocity gauge approach where the dynamical equation for the (microscopically uniform) macroscopic vector potential is solved on a macroscopic grid, allowing them to characterize the non-linear interplay between reflectivity and field strength in a silicon slab model [72].

For internal reference checks, we computed the linear dielectric tensor $\epsilon_{ij}(\omega)$ from Kohn-Sham orbitals based on Lindhard theory and employing the random phase approximation (RPA) [205, 206, 207]. The level of theory here essentially corresponds to linear-response TDDFT with $f_{\mathrm{xc}} = 0$ [208]. This functionality is a built-in feature of FHI-aims and is conducted as post-processing after a normal SCF cycle. The

corresponding formula reads

$$\epsilon_{ij}(\omega) = \delta_{ij} - \frac{4\pi}{V_{\text{uc}}\omega^2} \sum_{nn'\mathbf{k}} \left(-\frac{\partial f_0}{\partial \epsilon} \right)_{\epsilon_{n\mathbf{k}}} p_{i,nn'\mathbf{k}}\, p_{j,nn'\mathbf{k}} + \frac{4\pi}{V_{\text{uc}}} \sum_{\mu\nu\mathbf{k}} \frac{p_{i,\mu\nu\mathbf{k}}\, p_{j,\mu\nu\mathbf{k}}}{(\epsilon_{\mu\mathbf{k}} - \epsilon_{\nu\mathbf{k}} - \omega)(\epsilon_{\mu\mathbf{k}} - \epsilon_{\nu\mathbf{k}})^2} \tag{4.31}$$

where the second term describes intraband contributions and the third term describes interband contributions [208]. Here, $\epsilon_{n\mathbf{k}}$ is the self-consistent Kohn-Sham eigenvalue of the eigenstate n with wave vector $\mathbf{k}$, f_0 is the Fermi function and $p_{i,nn'\mathbf{k}} = \langle \psi_{n'\mathbf{k}} | \nabla_i | \psi_{n\mathbf{k}} \rangle$ are the momentum matrix elements. Gaussian broadening is used for finite lifetimes. For more details, we refer to the FHI-aims manual [114].

Nonlinear Response

Given the established framework, one can compute HHG spectra in solids straightforwardly by Larmor's formula [209]

$$\text{HHG}(\omega) = \omega^2 \left| \mathcal{F}[\mathbf{I}(t)](\omega) \cdot \mathbf{e}_F \right|^2, \tag{4.32}$$

where $\mathbf{e}_F$ is the unit vector of the external field polarization direction. As integer multiple responses of the incident field frequency define the HHG process, the Fourier spectrum of the macroscopic current is expected to show corresponding peaks when the HHG regime is reached. The intensity of the field needs to be high enough, often stronger than 10^{10} W/cm^2.

4.3.3 Dielectric Response of Bulk Silicon

A prototypical example in the literature for evaluation of real-time TDDFT for periodic systems is the calculation of the dielectric function of bulk silicon by its linear response [72, 74] and we will thus also employ this example here. The study by Pemmaraju et al. [74] used the SIESTA code [43] which is a real-space NAO pseudopotential code.

In complete analogy to the above mentioned study, we used the 8-atom cubic unit cell of silicon with a lattice constant of 5.402 Å. We also employed the PZ-LDA [20] exchange-correlation functional and chose the 'tight' basis set for our calculations (a double-ζ+p basis set used in the SIESTA study). We employed a time step of 0.08 a.u. = 0.002 fs together with the semi-implicit EM propagator. As in the reference, the electric field strength was set to 0.001 a.u. = $5.14 \cdot 10^8$ V/m, being polarized along the z-axis. The vector potential corresponding to a delta-like electric field, which we use here to probe the linear response, is a step function. Thus, from $t = 0$ a constant vector potential was switched on. For the Fourier transforms required for the computation of the dielectric function, we used the polynomial damping function and some artificial smoothing via zero-padding as last postprocessing step.

It is known that real-time velocity-gauge simulations cause artificial peaks near $\omega = 0$ [71, 72, 74, 159], which we solve by subtracting the dielectric function of the $t_{\max}$ component of the electronic current from the total dielectric function, illustratively shown in Fig. 4.14.

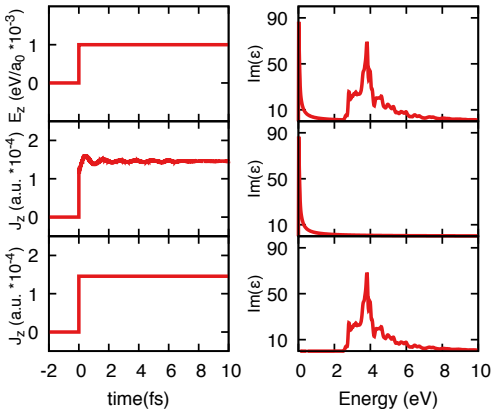

FIGURE 4.14: Method to remove the artificial peaks near $\omega = 0$. Left column (top-bottom for z-component only): vector potential, induced current, $t \to \infty$ current. Right column (top-bottom for Im(ϵ)): normal evaluation, only for $\mathbf{I}(t \to \infty)$, difference.

In order to check the convergence with respect to the number of **k**-points, we performed simulations for a $16 \times 16 \times 16$, a $48 \times 48 \times 48$ and a $16 \times 16 \times 16$ grid that was shifted by an offset $\Delta\mathbf{b} = 0.01\mathbf{b}_1 + 0.45\mathbf{b}_2 + 0.36\mathbf{b}_3$, with the reciprocal lattice vectors $\{\mathbf{b}_i\}$ (the other grids are Γ-centered). This is motivated by the fact that a shifted **k**-point mesh can help to reduce unwanted redundant contributions in the dielectric function by breaking the symmetry [71, 108]. For comparison, the Lindhard dielectric function was computed with a $48 \times 48 \times 48$ **k**-point mesh, using the same basis set and functional. It is known that the RPA dielectric function of silicon is in very close agreement to the LR-TDDFT result with the LDA-kernel [210]. The results of our calculations are shown in Figure 4.15. On the first view, the agreement between the different methods is reasonable. However, for the unshifted $16 \times 16 \times 16$ **k**-grid, we observe pronounced artificial peaks between 4 eV and 6 eV (for both the imaginary and real parts). For the real part, another peak not visible in the Lindhard dielectric function (LDF) is found at 2.9 eV. When comparing the results between the LDF and the $48 \times 48 \times 48$ dielectric function, an excellent agreement is found overall, but modulo the 2.9 eV peak. The RT-TDDFT calculation thus mostly converges to the Lindhard model calculation for the same numerical setup and also shows the desired qualitative increase by increasing the number of **k**-points. However, already the use of a shifted **k**-mesh reduces artifacts, as can be observed in the dielectric functions with shifted $16 \times 16 \times 16$ grids. We did not systematically converge these calculations in this manner but expect good results for shifted grids already below a relatively dense $48 \times 48 \times 48$ grid.

As a second example, we show our results together with those from the SIESTA study [74], as mentioned above. These calculations were done with a $16 \times 16 \times 16$ **k**-mesh but we present our $48 \times 48 \times 48$ and shifted $16 \times 16 \times 16$ results, as the reference appears slightly better converged. The results are shown in Figure 4.16. Overall, a very good agreement is found, as the most prominent spectral features are matching very well. Some differences remain especially between 4 eV and 6 eV.

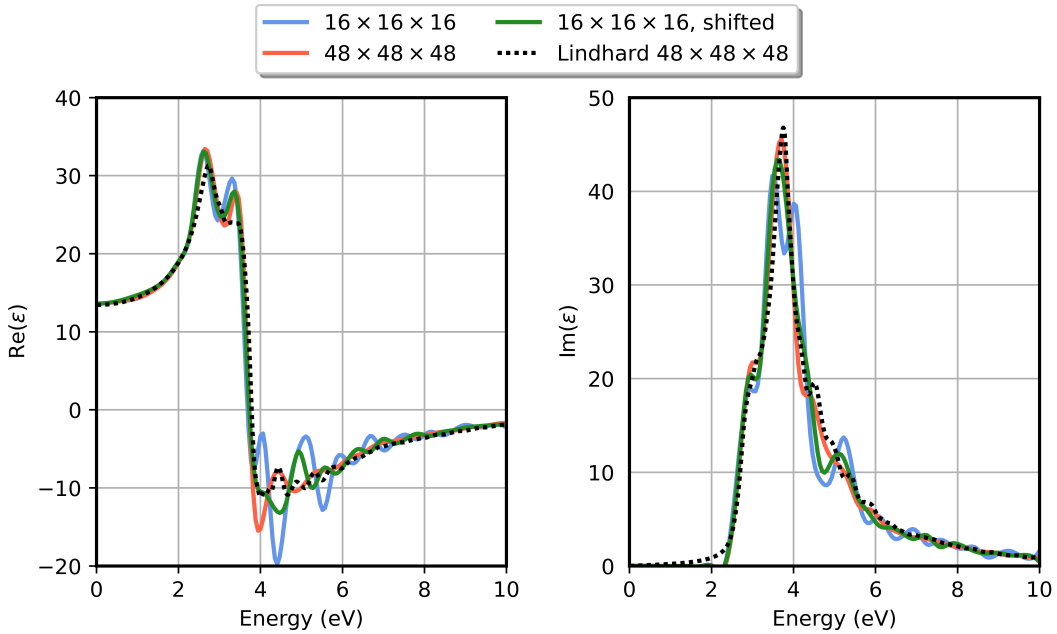

FIGURE 4.15: Real and imaginary part of the dielectric function for bulk silicon, obtained from RT-TDDFT simulations and the Lindhard model within FHI-aims. Results are shown for some different **k**-meshes, also including shifts away from the Γ-centered default. The artificial $\omega = 0$ peaks were explicitly removed from our dataset.

We further note that these calculations were not very sensitive to the basis set, as basically the same results were attained for the 'light', 'intermediate' and 'tight' basis sets. The 'intermediate' set contains one additional f basis function as the 'light' set, but has a denser integration grid, while the 'tight' set extends the 'intermediate' set by one additional d and g basis function. One can thus use a very small basis set for such standard calculations as this one, but needs to pay some more attention to the **k**-mesh. Since FHI-aims RT-TDDFT scales mostly with the basis- and grid-related operations, as compared to the number of **k**-points, a quite economic approach is found. Overall, these results confirm that our implementation works as desired for this important testcase.

4.3.4 Core-Level and Valence Absorption of 2H-SiC

We provide a second example in which we also explicitly cover X-ray absorption spectrum simulations (NEXAFS) for extended systems, namely silicon carbide in the 2H polytype (2H-SiC). This polytype has a hexagonal unit cell with 4 atoms in it. We employed the same crystal structure as in Ref. [74], which is given by experiment: the lattice parameters of the hexagonal unit cell are given by a $= 3.076$ Å and c $= 5.048$ Å. The procedure is the same as before, i.e., a weak step function z-polarized vector potential corresponding to an electric field with amplitude 0.001 a.u. $= 5.14 \cdot 10^8$ V/m was applied at $t = 0$ and the dielectric function $\epsilon_{zz}(\omega)$ was calculated from the conductivity which in turn was obtained by the Fourier transform

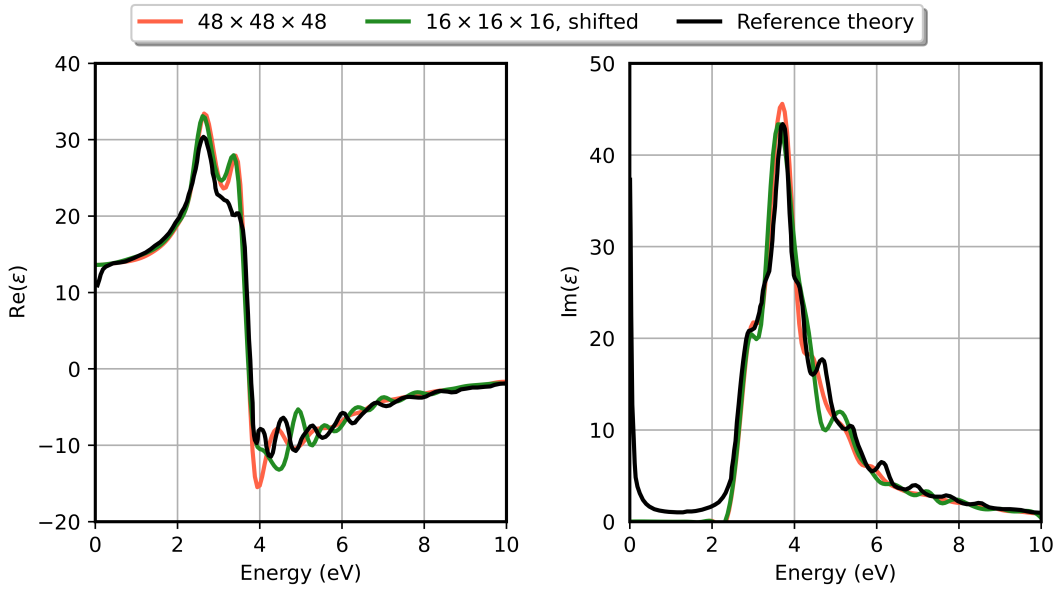

FIGURE 4.16: Real and imaginary part of the dielectric function for bulk silicon, obtained from RT-TDDFT simulations with our code (red/green) and the SIESTA reference [74]. The artificial $\omega = 0$ peaks were explicitly removed from our dataset.

of the dynamical macroscopic current. In order to resolve the core-level excitations, a very small time step of 0.01 a.u. $=$ 0.00024 fs was used to propagate the system over a simulation time of 400 a.u. $=$ 9.7 fs. We used a **k**-point grid of $20 \times 20 \times 12$ for the sampling of the Brillouin zone. If not stated otherwise, the presented results were obtained from the 'intermediate' basis set for both atom types. This set extends the 'light' set by one f basis function both for carbon and silicon (in combination with a denser integration grid).

In the study by Pemmaraju et al. [74], the results obtained from the SIESTA code were compared with those from the all-electron LAPW-based ELK code [211], showing good agreement. We restrict our evaluation on the results generated by the ELK code, as it also offers intrinsic all-electron description.
Similar to before, we removed the artificial $\omega \to 0$ peak in the spectra and computed the dielectric function via the Lindhard formula with FHI-aims. Figure 4.17 shows the results for $\epsilon_{zz}(\omega)$ for the valence (0-20 eV), silicon L-edge (87-107 eV) and carbon K-edge (258-278 eV) regions together with the results generated by the Lindhard formula. For the valence region, the results are nearly identical, while some smaller deviations are visible for the shown core-virtual transitions. However, the spectral structure is reproduced very well.
Comparison with the same data from the ELK code is shown in Figure 4.18. The valence region values overlap nearly perfectly, while some more differences are seen especially for the case of the silicon L-edge range. The plateau onset is however consistent between the methods and the bump-like feature below 90 eV in the FHI-aims

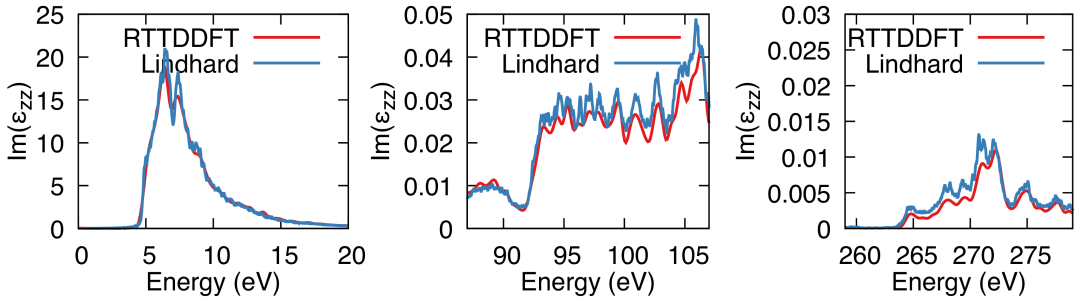

FIGURE 4.17: Imaginary part of the zz-component of the dielectric tensor for the valence region (left), the silicon L-edge region (center) and the carbon K-edge region (right). Results from RT-TDDFT are given in red and from the Lindhard formula in blue.

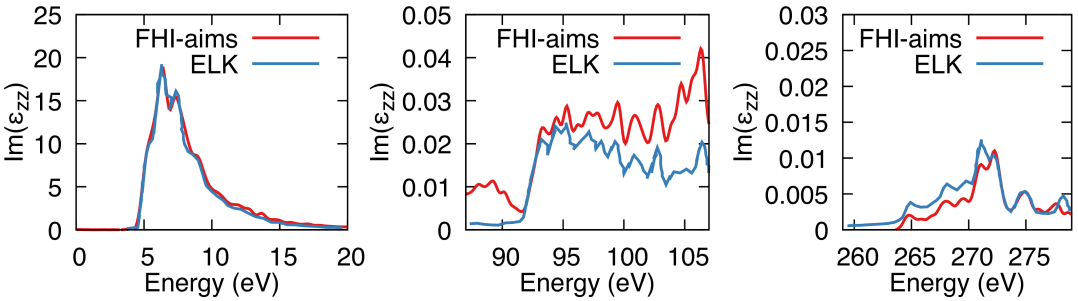

FIGURE 4.18: Imaginary part of the zz-component of the dielectric tensor for the valence region (left), the silicon L-edge region (center) and the carbon K-edge region (right). Results from FHI-aims RT-TDDFT are given in red and from ELK RT-TDDFT in blue.

case is also present in the dielectric function obtained from the Lindhard formula, indicating an origin from the basis set. Overall, the essential features are reproduced and show a good agreement between the approaches.

We next discuss the convergence with respect to the basis set size and present results for the 'light', 'intermediate' and 'tight' sets in Figure 4.19. A perfect overlap is seen in the valence region, while more differences appear for the core-level excitation ranges. Especially for the carbon K-edge region, we can observe quite sig-

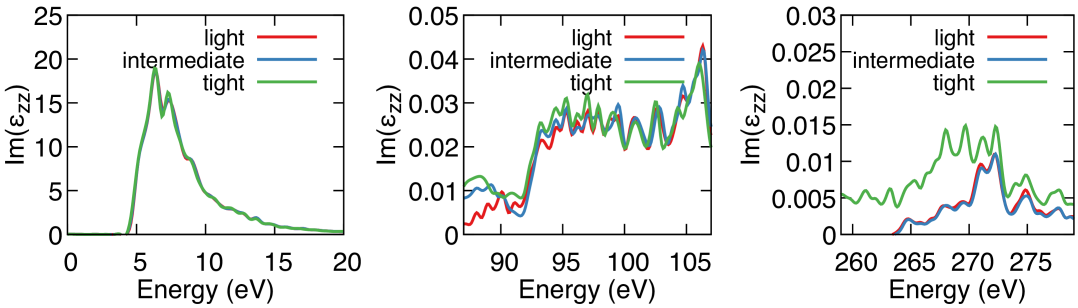

FIGURE 4.19: Imaginary part of the zz-component of the dielectric tensor for the valence region (left), the silicon L-edge region (center) and the carbon K-edge region (right) from our code but for different types of basis sets.

nificant differences between the 'tight' basis set and the smaller sets (which on the other hand yield basically equal results). While spectral features from 272 eV on are similar but higher, a different structure below this value is observed. Pemmaraju et al. [74] explained a similar observation in their analysis by the increased capability of the larger basis set to describe high-energy continuum excitations, resulting in corresponding peaks in the spectrum here.
In order to better understand this characteristic, we calculated ϵ_{zz} from the Lindhard function, but only summing up contributions from carbon K-edge excitations. Figure 4.20 shows a plot for the imaginary part of ϵ_{zz} from RT-TDDFT 'tight', Lindhard 'tight', Lindhard 'intermediate' and Lindhard 'tight' only for the C K-edge. We can clearly see here that the 'tight' Lindhard and RT-TDDFT values exhibit the same structure in the discussed region, shown in the inset. However, when only considering the Lindhard C K-edge contributions, the 'intermediate' results are reproduced. This observation thus underlines the previous assumption, making it necessary to have in mind that more and more complete basis sets may introduce unwanted excitations into the continuum in the high-energy regions of absorption spectra. However, when carefully checking the basis set convergence, this issue can be resolved. In our case, the smaller basis sets already offer a very good description here.

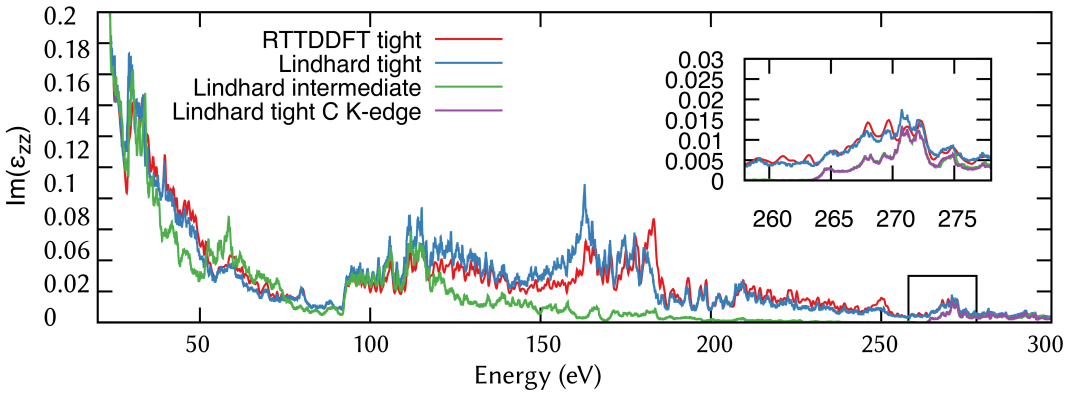

FIGURE 4.20: Imaginary part of the zz-component of the dielectric tensor for the region from 0 eV to 300 eV, for RT-TDDFT 'tight' (red), Lindhard 'tight' (blue), 'intermediate' (green) and 'tight' with carbon K-edge contributions only (purple). The inset shows the C K-edge region and one can clearly observe the continuum excitation contributions from the 'tight' sets adding to the core-level excitation contributions.

4.3.5 High-Harmonic Spectrum of Bulk Silicon

As an illustrative example for the computation of HHG simulations in solids, we again chose bulk silicon, according to the study by Pemmaraju et al. [74]. We took the same laser pulse, described by the vector potential

$$A_z(t) = \frac{E_0}{\omega_0} \sin^2\left(\frac{\pi(t-t_0)}{T}\right) \cos\left(\omega_0(t-t_0)\right) \tag{4.33}$$

where $\omega_0 = 1.6$ eV is the carrier frequency, $T = 10$ fs is the pulse length and $t_0 = 0$. This describes a pulse of Gaussian-like shape centered at 5 fs. The electric field amplitude E_0 generally corresponds to the pulse intensity via $I_0 = 3.50941 \cdot 10^{16} E_0^2$ W/cm^2, where the amplitude is given in atomic units. As indicated, the pulse is parallel to the z-axis in the unit cell. We used the same numerical settings as before for silicon, namely the 'tight' basis set together with the PW-LDA exchange-correlation functional [23], employing a $16 \times 16 \times 16$ **k**-point grid. Time-propagation was carried out with a time step of $\Delta t = 0.08$ a.u. $= 0.002$ fs, using the semi-implicit Crank-Nicolson propagator of 1st order. We restrict our discussion to the case of $I_0 = 10^{13}$ W/cm^2 which showed high-harmonic generation most clearly in the reference.

Our first analysis concerns the energetics in the dynamics and we show the total electronic energy per atom relative to $t = 0$ in Figure 4.21 (bottom panel). This figure also includes the shape of the vector potential pulse in the top panel. While the increase in energy due to the non-linear absorption between around 1 and 8 fs shows higher absolute oscillations in our case, as compared to the reference, the overall energy gain per atom, measured as $E_{\text{at}}(0) - E_{\text{at}}(t \to \infty) \approx 5.6$ eV, is matched very well between the methods. In fact, a relative difference of only 1.8% is seen, with our value being higher. As this is the core measure, we find excellent agreement here.

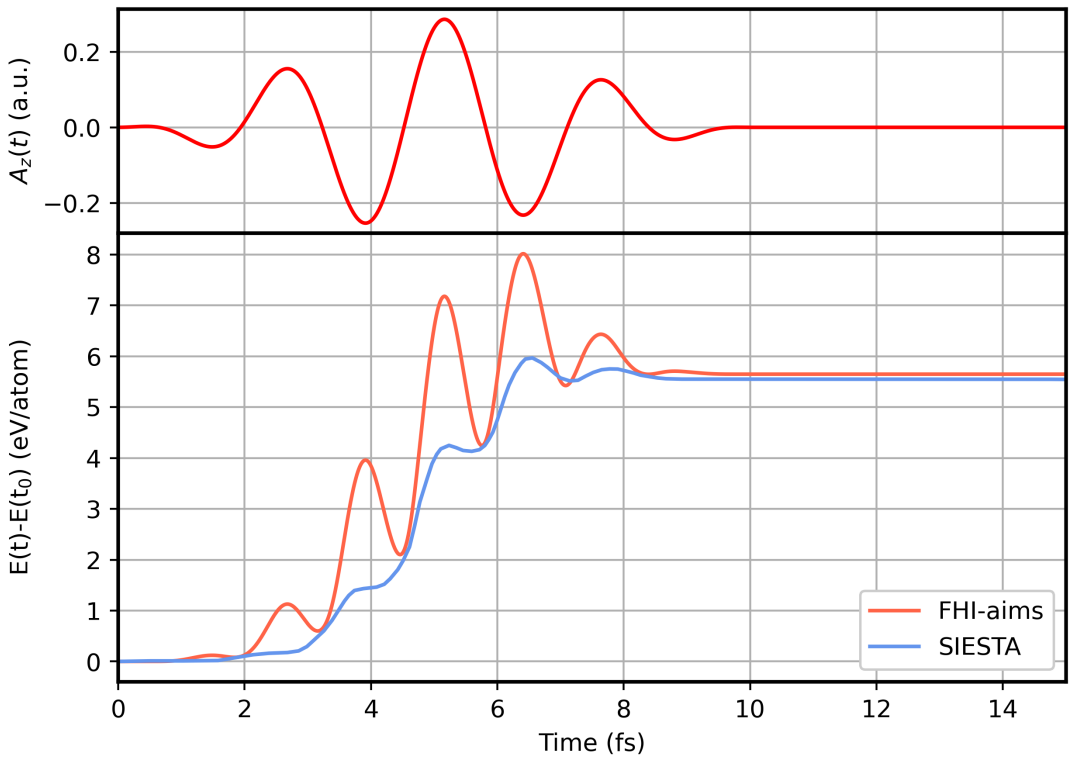

FIGURE 4.21: Top panel: z-component of the time-dependent vector potential that was applied to the system. Bottom panel: difference in electronic energy relative to $t = 0$ as function of time, for our simulation (red line) and from the references (blue line).

We next discuss the HHG spectra, as obtained by the squared absolute of the macroscopic current's Fourier transform for the z-axis, $|\mathcal{F}[I_z(t)](\omega)|^2$; we applied polynomial damping and zero-padding in order to smoothen the spectrum, as also most likely done in the reference. Figure 4.22 shows the spectra from our code and the reference in comparison. A specificity of this case is that even harmonics are forbidden due to the centrosymmetry of the Si unit cell [74, 212]. We therefore only observe

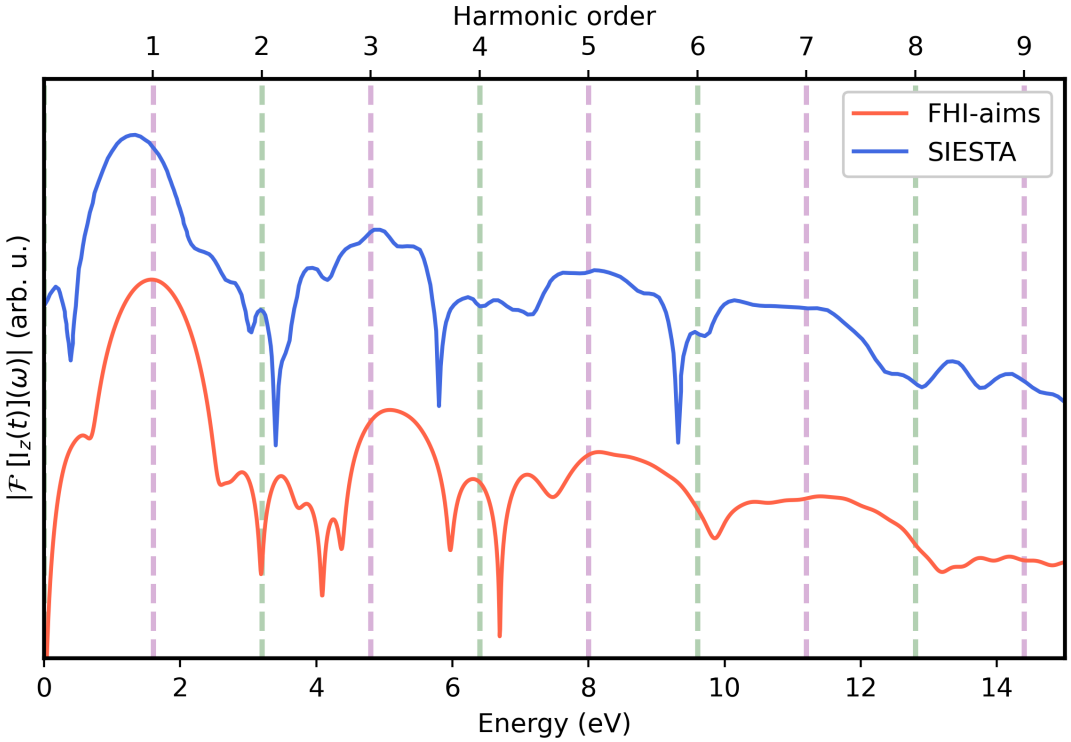

FIGURE 4.22: HHG response characterized by the squared absolute of the z-component of the time-dependent macroscopic current's Fourier transform on an arbitrary scale. The spectra from our code (red) and the reference (blue) were shifted along the y-axis to allow better comparison. The top x-axis shows the integer multiples of the pulse carrier frequency $\omega_0 = 1.6$ eV where uneven values are purple and even values are green. Due to the shape of the Si unit cell, even harmonic orders are symmetry-forbidden.

uneven harmonics; both spectra have dips at or around the locations where even harmonics were to be expected. Overall, the structure of the spectra is quite similar, most importantly showing peaks at uneven harmonic locations. While in the reference, the 1st peak shows a significant shift relative to the carrier frequency, this is not observed in our case. However, we observe a blueshift in the second harmonic. This peak has a clearer structure in our simulation, as compared to the reference, and it is thus hard to judge whether the reference peak also shows some shifting. In general, we observe relative shifts between similar features in the spectra, albeit the general shape is very similar. At this point, we note that we did not try to converge our results to the reference, although relatively similar basis sets were used.

The differences in the spectra may also originate in the fact that SIESTA does not

employ an all-electron description, but rather a pseudopotential approach. It has been found before that *all-electron* velocity-gauge RT-TDDFT HGG simulations have a slower convergence with respect to the spatial integration grid, as the dipole matrix elements $\langle\phi_i|\nabla|\phi_j\rangle$ occurring in the VG Hamiltonian and the current operator introduce significant contributions near the nucleus [190].
Another reason could originate in the fact, that when a pseudopotential approach is employed, additional non-local pseudopotential terms are introduced into the generalized momentum operator (cf. theory part of this section) [74]:

$$\hat{\boldsymbol{\pi}} = -i\nabla + \mathbf{A}(t) + i\left[\hat{V}_{\mathrm{pp}}, \hat{\mathbf{r}}\right], \tag{4.34}$$

where $\hat{V}_{\mathrm{pp}}$ is the non-local pseudopotential operator and $\hat{\mathbf{r}}$ is the position operator. While this expression yields formally a gauge-invariant current density, numerical approximations always effectively break the gauge invariance. We are not aware of any systematic study evaluating this specific case, but mention it as another possible explanation.
However, the general agreement is reasonable and most importantly, we have shown that our implementation can also be used for the simulation of highly non-perturbative dynamics, in this case for the HHG simulation in solids. A systematic study of the grid convergence of all-electron HHG simulations can be interesting as future work.

4.3.6 Discussion

We have here provided very solid proof that our implementation works equally well for systems under periodic boundary conditions and discussed several aspects of this. In the first part of this chapter, we evaluated a prototypical study, namely the calculation of the dielectric function of bulk silicon. Here, we could show that our code excellently reproduces both internal reference data from the Lindhard dielectric function (which was in this case expected) and external theoretical data generated by the SIESTA-based RT-TDDFT code. We found out here that already the smaller FHI-aims basis sets offer a very good description, while some more care has to be taken when converging the **k**-grid. Of course, this is heavily system-dependent.
Our NEXAFS simulations of 2H-SiC agree excellently with our internal reference based on the Lindhard dielectric function (this is of course not expected in general) and with the RT-TDDFT results from the all-electron ELK code. Further, we systematically provided interpretation of the basis set's influence onto core-level excitations and found that more complete FHI-aims basis sets may introduce significant continuum contributions which one has to be aware of. Overall, this makes FHI-aims one of the few all-electron DFT codes that can perform real-time simulations with periodic boundary conditions.
In the third part of this chapter, we have shown results for explicitly non-linear dynamics by simulation of high-harmonic spectra. Our results agree reasonably well

with the SIESTA reference, taking into account the different approaches. Overall, our results show the expected characteristics of this regime. This gives the opportunity to study also highly non-linear phenomena within our framework. A specific advantage here is that the all-electron treatment enables a formally correct gauge-invariant description of the velocity gauge, in contrast to pseudopotential methods. The systematic in-depth discussion of gauge-related characteristics could yield important insights for this regume.

4.4 Circular Dichroism

We cover the topic of circular dichroism spectroscopy in this chapter, starting with a short overview of the fundamentals. Thereafter, we present validation simulations for the prototypical molecule (R)-methyloxirane and provide comparison with both theoretical and experimental data. The second part includes a model study where we analyze chirality transfer in a non-covalently bonded chiral molecular complex composed of chiral and achiral components.

4.4.1 Introduction

The word dichroism, based on the greek expression *dikhroos* which essentially means two-colored, refers to the property of a given optically active material to absorb light in dependence of the polarization, i.e., the orientation of the electric field amplitude [143]. One can generally distinguish between *linear* and *circular* dichroism (CD), each referring to the polarization of the incident field. While linear dichroism refers to splitting of the incident linearly polarized radiation into rays of different wavelength, depending on the relative orientation of the amplitude to the material's distinguished optical axes, circular dichroism means the different absorption of left- and right-handed circularly polarized light (each corresponding to two different photon spin angular momentum states).
While there are several regimes in this context, e.g., magnetic circular dichroism (MCD), where the CD is induced by strong magnetic fields, or vibrational circular dichroism (VCD) referring to the infrared radiation range, we only cover here the case of CD in the visible/UV range. Circular dichroism is exhibited by *chiral* molecules, i.e., molecules that exist in two forms with the same chemical composition (enantiomers) that correspond to each other's mirror image (the typical analogue are hands) – the enantiomers absorb fixed circularly polarized radiation differently (or equivalently, an enantiomer absorbs left- and right-handed circularly polarized light differently).
Circular dichroism spectra belong to the class of linear-response quantities and calculations were often carried out by wave function-based methods and LR-TDDFT [213, 214]. Although LR-TDDFT is a comparably economic and often sufficiently accurate method, its formal $\mathcal{O}(N_{at}^6)$ scaling has recently motivated several RT-TDDFT studies in the subject, as this approach offers a better scaling [215, 216, 217, 218].

4.4.2 Theory

Experimentally, a key observable to characterize electronic CD is given by the difference in the molar extinction coefficients (with respect to incident field polarization), in SI units given by

$$\Delta\epsilon(\omega) = \frac{32\pi^2}{3\log(10)} \frac{N_A e^2 \hbar}{c\, m_e \alpha} 10^3 \omega R(\omega), \tag{4.35}$$

with the incident field frequency ω and the so-called rotatory strength function (RSF) $R(\omega)$. The latter is the quantity that is here accessible from the theoretical perspective, which we will show in the following. The magnetic dipole response $\mathbf{m}(t)$ due to an external electric field excitation $\mathbf{E}(t)$ can be expanded as

$$m_i(t) = \frac{1}{c}\sum_{j=1}^{3}\int_{-\infty}^{\infty} \mathrm{d}t'\, \tilde{\beta}_{ij}(t-t')\frac{\partial E_j(t')}{\partial t'} + \text{h.o.t.} \tag{4.36}$$

(with the speed of light c, also in the following), where the response is mediated by the so-called rotatory response tensor $\tilde{\beta}(t) \equiv \mathcal{F}^{-1}[\beta(\omega)](t)$ (indicating that the convention is to use the frequency-space representation of this quantity) [213, 217, 218]. The first step is now to restrict the discussion onto the linear response regime, i.e., dropping all higher-order terms in the expansion of the magnetic dipole moment, completely analogous to Section 4.2.2. The rotatory response tensor is reconstructed by the same procedure as for the polarizability or conductivity tensors, i.e., by applying three orthogonal pulses. One then has

$$\beta_{ij}(\omega) = i\frac{c}{\omega}\frac{\mathcal{F}[m_i(t)](\omega)}{\mathcal{F}[E_j(t)](\omega)}. \tag{4.37}$$

The relationship between the rotatory response tensor and the RSF, characterizing the CD response, is given by

$$R(\omega) = \frac{\omega}{\pi c}\mathrm{Im}\Big\{\mathrm{Tr}\big[\beta(\omega)\big]\Big\}. \tag{4.38}$$

One can also define the transition-RSF as

$$R_{0l} = \mathrm{Im}\Big\{\langle\Psi_0|\hat{\boldsymbol{\mu}}|\Psi_l\rangle\langle\Psi_0|\hat{\mathbf{m}}|\Psi_l\rangle\Big\}, \tag{4.39}$$

where $\hat{\boldsymbol{\mu}} = e\hat{\mathbf{r}}$ and $\hat{\mathbf{m}} = (-i/2c)(\hat{\mathbf{r}}\times\nabla)$ are the electric and magnetic dipole operators, respectively, and Ψ_0 is the ground state wave function, while Ψ_l is an excited state wave function [213]. This form directly illustrates the electro-magnetic coupling response and additionally that a determination of this quantity requires accurate description of both the dipole and magnetic transition moments in a simulation. The magnetic moment $\mathbf{m}(t)$, as the key observable in this context, is calculated from the time-dependent Kohn-Sham states via

$$\mathbf{m}(t) = \sum_{n=1}^{\mathrm{N_{occ}}} f_n\langle\psi_n(t)|-\frac{i}{2c}\hat{\mathbf{r}}\times\nabla|\psi_n(t)\rangle = -\frac{i}{2c}\sum_{n=1}^{\mathrm{N_{occ}}} f_n\mathbf{c}_n^{\dagger}(t)\mathbf{L}\mathbf{c}_n(t) \tag{4.40}$$

with $\mathbf{L}_{ij} = \langle\phi_i|\mathbf{r}\times\nabla|\phi_j\rangle$ being the angular momentum matrix. As before, weak δ-like external fields are used in three individual calculations to resolve above quantities. It must be noted that the theoretical description of circular dichroism suffers from two gauge-related problems: dependency on the origin of the chosen coordinate system and finite basis set expansion [219]. We do not cover these topics further but

point out that methods exist to tackle these problems, see, e.g., Refs. [218, 219, 220, 221, 222]. As it was pointed out by Goings et al. [215], the mentioned problems are reduced for large basis sets, which we used for our simulations.

4.4.3 Rotatory Strength of (R)-Methyloxirane

For the validation of the method, we chose to perform calculations for (R)-methyloxirane, a small chiral organic molecule with the sum formula C_3H_6O, which is a popular benchmark system for electronic circular dichroism studies [214, 215, 217, 219, 222]. For the comparison, we chose experimental data from Ref. [223] and theoretical data from Ref. [217]. Latter publication is a real-time TDDFT based study performed with the GPAW code [224], a projector-augmented wave based DFT software package. Here, Makkonnen et al. employed the PBE exchange-correlation functional [26] with double-zeta polarized basis sets additionally extended with diffuse Gaussian-type augmentation functions known to improve response calculations with atom-centered basis sets [99] (they actually also provide results for grid-based calculations, but we will here not refer to these).
We chose to perform our calculations with comparable settings, meaning that we also employed the PBE exchange-correlation functional [26]. As a comparable basis set, we employed the 'tight+aug2' set which is also equipped with diffuse Gaussian-type augmentation functions. Real-time propagation was performed for 1240 a.u. $=$ 30.0 fs (equal to the theory reference) with a time-step of 0.4 a.u. $=$ 0.0097 fs with the semi-implicit exponential midpoint propagator. We chose an initial delta-like external field kick of 0.01 a.u. $= 5.14 \cdot 10^9$ V/m amplitude as perturbation.

Figure 4.23 (bottom) shows the computed spectrum and the reference spectra. Note that we shifted both theoretical spectra such that the lowest peaks match the corresponding experimental peak: +1.38 eV for the reference and +1.45 eV for our spectrum. The reason for these discrepancies are expected to originate in the exchange-correlation functional which likely underestimates excitation energies in this case. A constant shift is thus valid to align the spectra [217]. It should additionally be noted that the reference used rather generous line broadening which we adapted here, too. The figure also shows the RT-TDDFT DSF together with excitations obtained via LR-TDDFT (for the same setup) in the top panel. This allows a clearer location of the individual electronic transitions that are responsible for the CD peaks. As to be expected, LR- and RT-TDDFT yield the same information in this regime. One can further see that an additional peak at around 7.7 eV is effectively hidden in the broadened CD spectrum and that the large feature at 7.6 eV is composed of two excitations. This could explain the structure of the corresponding experimental peak.
In general, both theoretical RT-TDDFT-PBE spectra agree quite well; the locations of the second-lowest peak differ by around 0.12 eV (ours being lower) and the overall structure is quite similar, although deviations in the higher energy range exist.
The 3 lowest peaks have comparable relative positions between these two spectra.

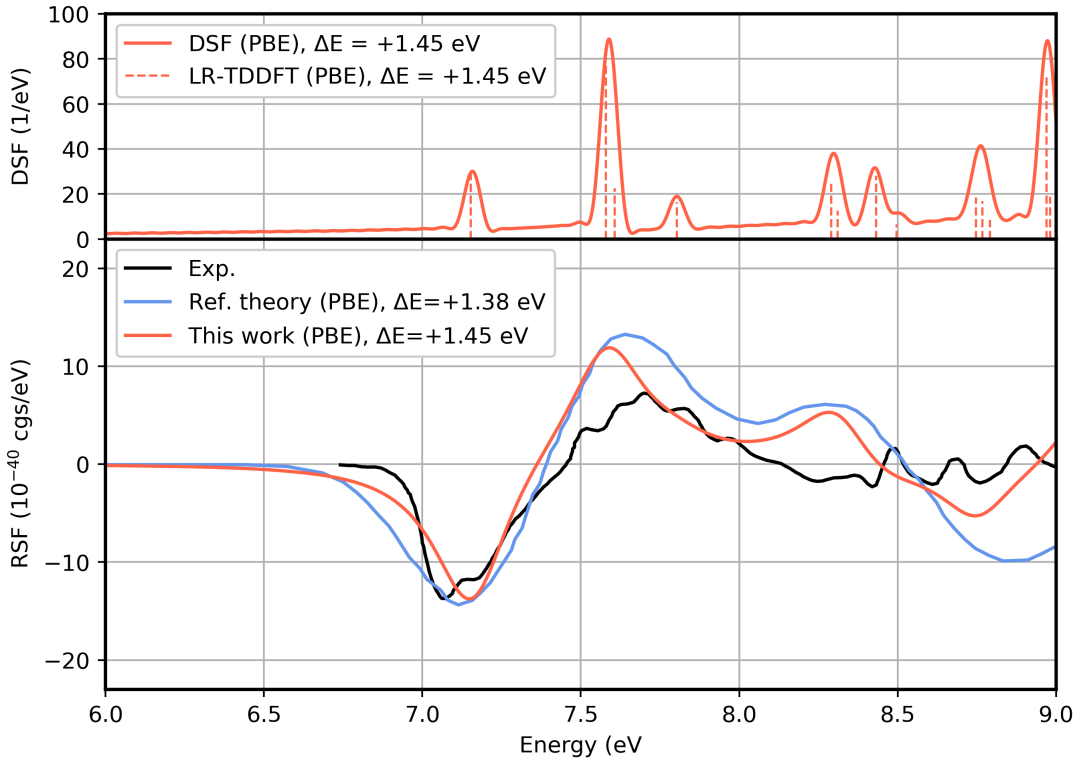

FIGURE 4.23: Comparison of rotatory strength function for (R)-methyloxirane. Experimental spectrum in black [223], RT-TDDFT reference spectrum [217] in blue and spectrum from our work in red. The theoretical spectra are x-shifted such that the lowest peak locations coincide with the corresponding experimental excitation.

Overall, the agreement between both RT-TDDFT results can be regarded as good and the differences are in this case expected to originate in the different basis set approaches, and since the calculation of CD response is very prone to numerical settings, as stated before. For the comparison with the experimental spectrum (given the constant shifts), the theory reference better seems to capture the second peak. However, the overall structure is reasonable. The DSF indicates that several excitations may be responsible for the the positive CD peak around 7.7 eV, where also the experimental spectrum shows some structure.

4.4.4 Modeling Chiral Transfer in Molecules

Introduction

An interesting question is about whether and how chiral response can be imprinted into a system. In this context, a system means a molecule that is intrinsically non-chiral. An obvious way to do so is to induce geometrical changes that alter the molecule's geometry such that its symmetry allows chiral response. Differently from this is the introduction of chirality by chemically modifying the system. For example, Tohgha et al. [225] showed that native achiral cadmium selenide quantum dots can attain chiral response by introducing chiral cysteine ligands. Yet another process

is chiral transfer mediated by field effects of adjacent electron populations. Such phenomena were observed in situations of chiral transfer via plasmon resonances. For example, Ostovar pour et al. [226] could show that chirality was transferred from a chiral analyte to an achiral dye molecule via a plasmon resonance of an achiral metallic nanostructure to which both molecules were bonded. Further, in a recent experiment by Vázquez-Nakagawa et al. [227], it could be shown that chirality of graphene quantum dots can be transferred to the native non-chiral molecule pyrene. Both molecules interact by π-π-stacking and the chiral response of pyrene could be located clearly by comparison of the energy-resolved molar exctinction coefficient with the absorption spectrum of pyrene, as no other compound absorbing in this range was prevalent.
We here aim to simulate chiral transfer between chiral and achiral molecules in a model system to show that this process can be simulated with RT-TDDFT. In this setup, we consider a closed-shell structure composed of two chiral molecules embedding an achiral center molecule. This complex is only formed by van der Waals interactions, invoking the chiral transfer by charge fluctuations of neighboring electron subsystems as near-field effect.

Simulation Setup

The intrinsically chiral molecule in this study was α-methylbenzylamin (MBA). For the non-chiral compound, we ultimately chose pyrene, a medium-sized polycyclic hydrocarbon. Both molecules are shown in Fig. 4.24. Initially, we probed several non-chiral molecules with respect to their absorption characteristics, as isolated excitations needed to be found that can show non-zero rotatory response (i.e., the spectra of MBA and the non-chiral compound must not have overlap in the range of lowest excitations). We will present some illustrations for these considerations in the results section. Another advantage of pyrene is its simple planar structure which thus also includes the molecule's inversion center. The conjugated π-system serves as suitable chirality acceptor for above and below aligned chirally active states of MBA. We relaxed the individual molecules at the same level of theory, utilizing the PBE

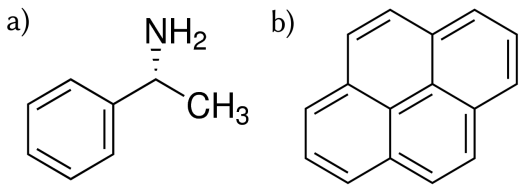

FIGURE 4.24: a) (R)-α-methylbenzylamin (R-MBA). b) Pyrene.

exchange-correlation functional [26]. A more sophisticated choice could have been a hybrid functional, e.g., B3LYP, but we note here that we only aimed to capture the physical process rather than obtaining accurate results, as we set up a model system. The MBA molecules were relaxed with the 'tight' basis set, while pyrene was

relaxed using a 'tight+aug2' basis set. The rationale in doing so was to attain a trade-off between computational efficiency and a good description of the chiral center in the resulting molecular complex. We expect the additional diffuse basis functions to better capture molecular orbital overlap between the MBAs and pyrene. Further, explicit description of van der Waals interaction was employed in the structure relaxation via the Tkatchenko-Scheffler method [92]. Two structures were prepared such that the pyrene molecule is in between the two MBA molecules: a chiral structure with R-MBA on both sides, and an achiral structure with one of MBAs enantiomers on each side (such that the structure has a mirror plane). All constituents were pre-relaxed with above-mentioned settings, and the whole structures were constructed thereafter such that the MBA molecules are symmetrically aligned along the z-axis, with the origin at middle of the central C-C bond within pyrene. See Figure 4.25 for a depiction of the relaxed structures. The relaxation was carried out with constraints

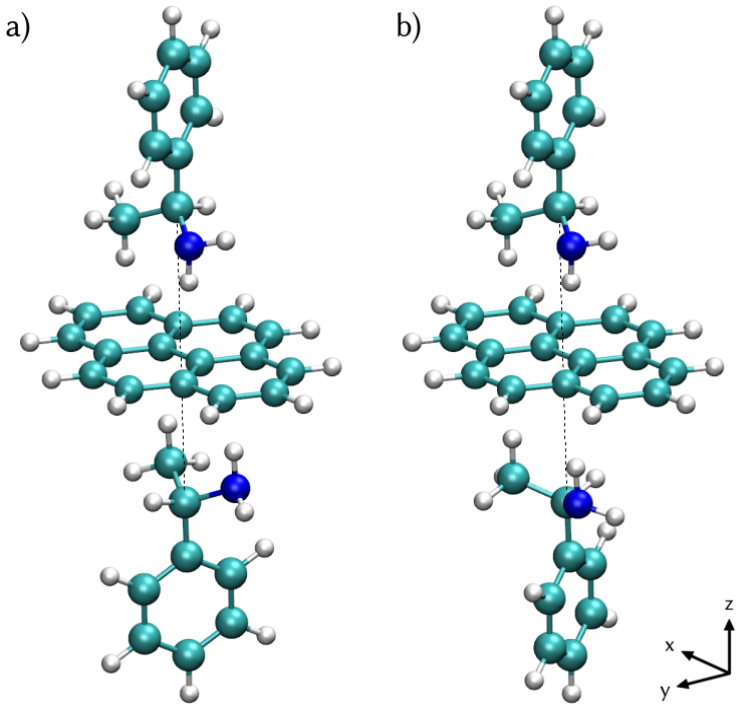

FIGURE 4.25: Composition structures of 2 MBA and pyrene in between. a) chiral setup, b) non-chiral setup. The MBA's are parallel to the z-axis with respect to their C(1)-C(4) axis and pyrene is coplanar to the x-y plane.

for the x- and y-coordinates for the MBAs and full constraints for pyrene, such that only the z-coordinates of the MBAs were optimized. In Figure 4.25, a dashed line is shown that connects two opposing carbon atoms of the MBAs: this distance is 8.37 Å in both relaxed structures.

For the real-time simulations, we employed the same settings for the XC functional and the basis set. The structure was composed of 66 atoms with 1870 basis functions overall, making it already a medium-sized system. We propagated the system for 5200 a.u. $\approx$ 125 fs with a time step of 0.4 a.u. $=$ 0.0096 fs, using the semi-implicit

exponential midpoint propagator. The linear response of the system was excited by an initial $t = 0$ kick of amplitude 0.01 a.u. $= 5.14 \cdot 10^9$ V/m.

Results

In Figure 4.26 we show the absorption spectra (via the DSF) and the rotatory response (via the RSF) for both isolated molecules. In the absorption spectra, one can clearly observe that two significant excitations of pyrene are located at 3.35 eV and 4.15 eV. As desired, no excitations of R-MBA are visible in the direct vicinity. The lowest peak of the MBA spectrum is located at 4.51 eV and it is thus well-separated. The rotatory response of pyrene is everywhere zero, as expected. The excitations seen in the R-MBA absorption spectrum all contribute to the RSF, as seen in the corresponding spectrum. So far, we provided the required consistency check for the upcoming calculations.

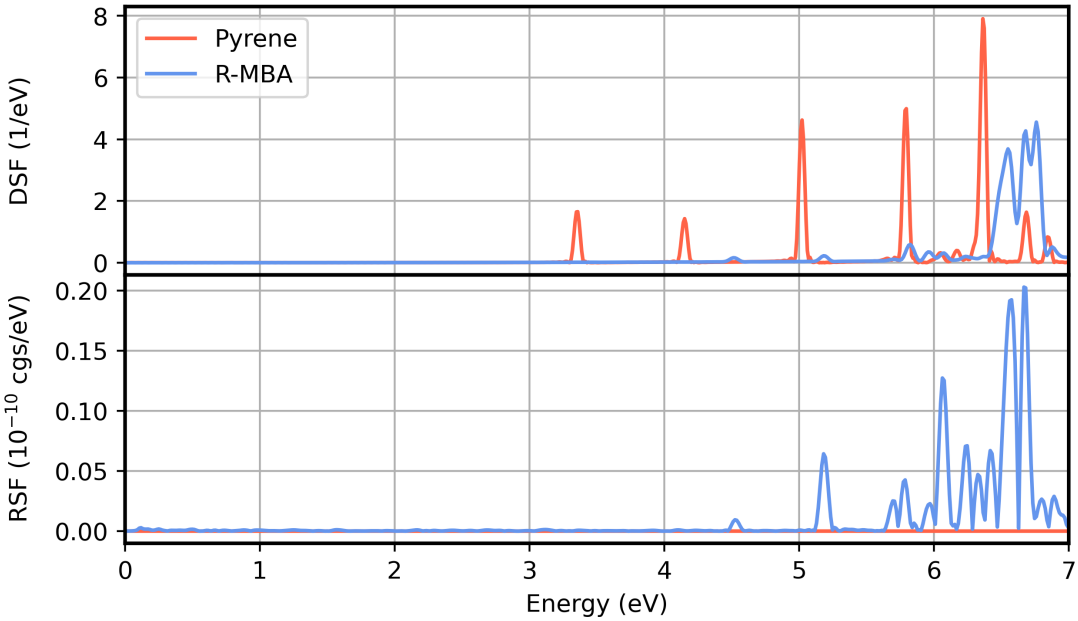

FIGURE 4.26: Dipole strength function (DSF, upper panel) and rotatory strength function (RSF, lower panel) for pyrene and MBA, computed via RT-TDDFT.

The results for the combined system are shown in Figure 4.27. The upper panel contains the DSF of the system together with the DSFs of the isolated systems. One can see here that the major absorption peaks of the isolated pyrene are visible in the combined system. The strong excitation at 3.35 eV is basically unaffected while the other major excitation at 4.15 eV is slightly shifted. Weaker excitations at 3.25 eV and 3.64 eV can be attributed to pyrene, too. The lower panel shows the RSF of the chiral and non-chiral complexes. As expected, the non-chiral version does not show any CD signal, underlining the correct setup. The chiral version on the other hand shows a significant CD response. In the given spectral range, actually only excitations from pyrene are prevalent, let aside the R-MBA peak at 4.5 eV. This means that

we observe actual chiral transfer here, as the native non-chiral pyrene contributes to the observed response. This is particularly seen for the excitation at 3.35 eV, as indicated in the figure by a dashed line, perfectly matching the corresponding peaks in the DSF and RSF. The excitation around 4.2 eV is the most distinct here and also belongs to pyrene. We have thus successfully simulated chiral transfer for our test system.

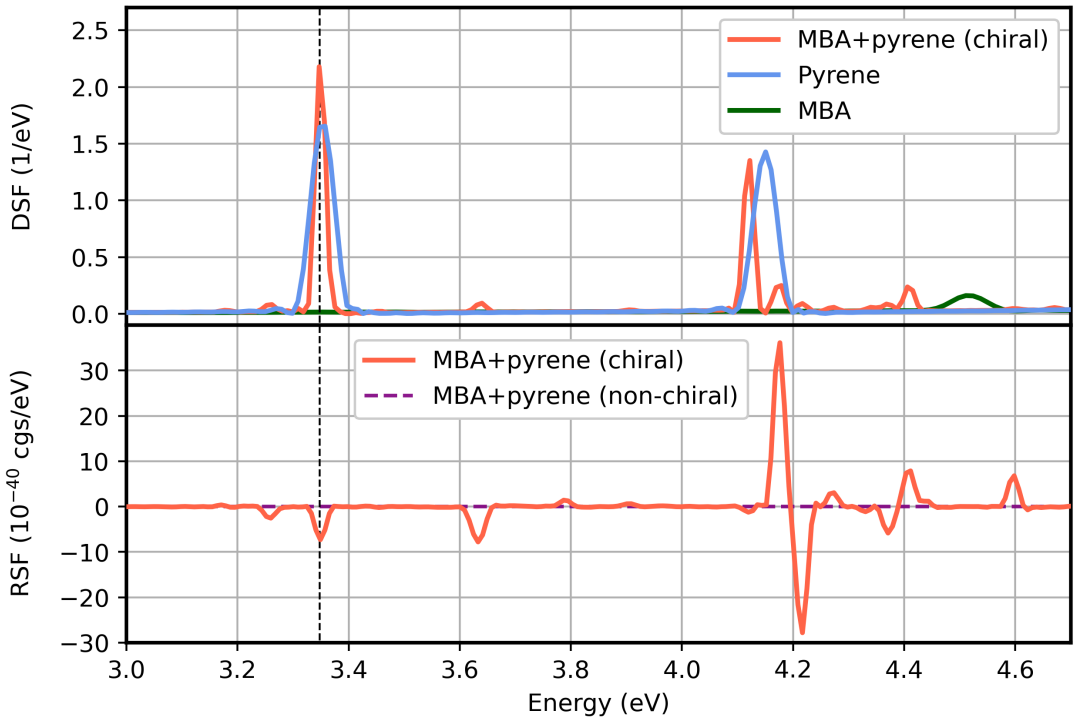

FIGURE 4.27: Dipole strength function (DSF, upper panel) for pyrene, MBA and the chiral combined system. Rotatory strength function (RSF, lower panel) for the chiral and non-chiral combined system.

4.4.5 Discussion

In this chapter, we first provided simulations for the common circular dichroism benchmark molecule (R)-methyloxirane. It was shown that our implementation produces reasonable data, as measured by experimental and theoretical references. Since the rotatory response is a quantity that is very sensitive for numerical approximations, it could be beneficial here that FHI-aims is a very accurate electronic structure code that is very flexible, too.

In the second part, we presented new data for a model study of chiral transfer. In contrast to wider known manifestations of this phenomenon, we analyzed the case of chiral transfer between adjacent chiral and achiral molecules that are not covalently bonded, but are only interacting via van der Waals forces. Here, the achiral molecule pyrene showed clear CD response when arranged between two equal

enantiomers of α-methylbenzylamine. Our setup directly illustrated the chiral transfer. It is an interesting question for further studies how this phenomenon's manifestation can be understood better or how it can be made of use.

4.5 Ehrenfest Dynamics

Within this chapter, we present simulations of non-adiabatic Ehrenfest molecular dynamics. The first part covers bond breaking by internal rotation in a small molecule, showing the strong non-adiabatic character of this process. In the second part, we employ the capability of our code to perform Ehrenfest dynamics simulations in systems with periodic boundary conditions in a setup where a graphene layer is bombarded with a single atom with high kinetic energy.

4.5.1 Introduction

The Ehrenfest approach belongs to a broader class of methods that can be denoted as *molecular dynamics* (MD) [57]. Most of these methods have in common that the dynamics of nuclei are described via the separation of nuclear and electronic wave functions, and that the nuclei are treated in the classical limit, i.e., as point particles. The dynamics of the atoms are described by some type of interaction potential that essentially specifies the individual approach. The most simple (but also very successful) approach is given by the so-called *classical* MD: here, the interaction potentials, often called *force fields* in this branch, are defined as rather simple functions that are parametrized by data from experiments or first-principles calculations [58]. While these approaches can be used for very large systems up to millions of atoms [228], the most important drawback is that electronic interactions are not described in a first-principles way, making the correct description of chemical reactions or electronic excitations difficult to impossible.
The ab-initio description of interaction potentials leads to the term of *ab-initio molecular dynamics* (AIMD). These methods use first-principles electronic structure methods to generate the corresponding potentials on which the nuclear dynamics take place. Note that this is already an approximation, incorporating the factorization of nuclear and electron wave functions – the exact solution is the single full wave function incorporating all electronic and nuclear degrees of freedom.
In practice, density functional theory is often the preferred method to provide the electronic potential, given its good cost-to-accuracy ratio. The most widely used AIMD methods describe the nuclear dynamics on ground state potential energy surfaces: so-called Born-Oppenheimer MD (BOMD) is defined by finding the electronic ground state for each nuclear configuration (cf. Section 2.1.7) via self-consistent electronic energy minimization, while Car-Parrinello MD (CPMD) relies on actual dynamics of a fictitious electron wave function that mimics the ground state evolution without the need of minimization [57, 229].
As BOMD and CPMD only describe temporal evolution on a single ground state potential energy surface, the dynamics are adiabatic, i.e., electronic excited states are completely neglected. Any process of interest where this becomes important, e.g., light-induced dissociation or collision experiments, is thus not correctly feasible with aforementioned methods. Extending the methodology to the non-adiabatic

regime thus requires the computation of electronic excited state potential energy surfaces (ES-PES). A very successful approach is given by the so-called trajectory surface hopping (TSH) technique [230, 231] where the evolution always takes place on *one* (out of multiple) specific ES-PES, with the possibility of switching, based on some defined algorithm. The ES-PESs may be obtained via multi- or single reference methods (like DFT), with the formers being more accurate but also much more costly [231]. In contrast to TSH, Ehrenfest dynamics (ED) based molecular dynamics always potentially formally involves a mixture of excited state contributions, as the forces are constructed from the average electronic energy involving multiple excited states. After a region of non-adiabatic coupling is encountered, the remaining dynamics are governed by one effective PES that corresponds to an average of the involved excited states.

Figure 4.28 shows an illustration that points out the differences between BOMD and ED for a model system that has a single reaction coordinate. However, when the physical situation allows this approximation (meaning that the different potential energy surfaces incorporated in the average potential do not correspond to very different trajectories), ED is a viable approach [88]. Such situations are given by, e.g., ion-matter collisions [232, 233, 234, 235] or light-induced charge transfer on rather short timescales [236]. As solids are characterized by high density of electronic states with similar character, the Ehrenfest method works particularly well for such systems.

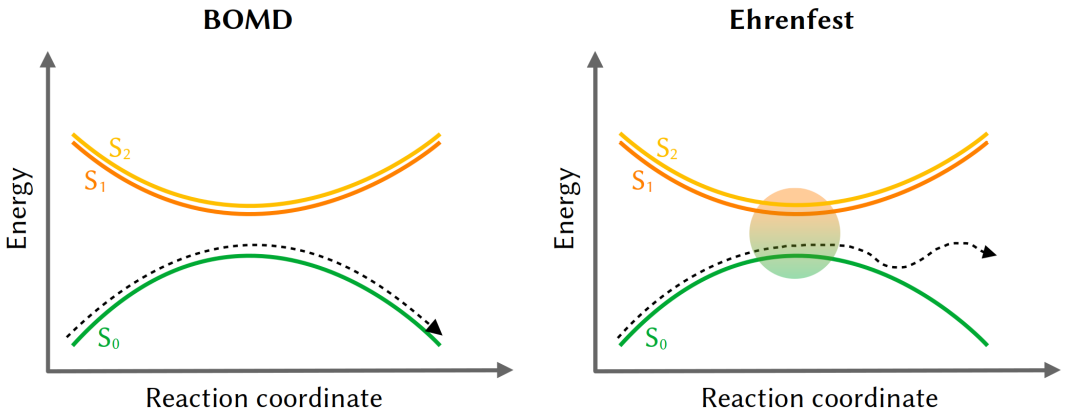

FIGURE 4.28: Potential energy surfaces for ground (S_0) and excited states (S_1, S_2) in dependence of a fictitious reaction coordinate. The dashed lines show the trajectories for BOMD (left) and ED (right). The non-adiabaticity in ED means that ground- and excited-state potential energy surfaces mix into the dynamics when the trajectory comes into a region of close vicinity. The exact solution here corresponds to a multiconfigurational wave function.

4.5.2 Forced Rotation of $H_2C{=}N^+H_2$

Our first example will cover the explicitly non-adiabatic dynamics via an established test case. This example has previously been covered within the context of Hartree-Fock based Ehrenfest dynamics [138], RT-TDDFT based Ehrenfest dynamics [136] and also with the trajectory surface hopping method [237]: the forced torsion of the $H_2C{=}N^+H_2$ molecule around its C=N axis, as illustrated in Figure 4.29 (a similar study with the ethene molecule was conducted by Wang et al. [140]). The initial ve-

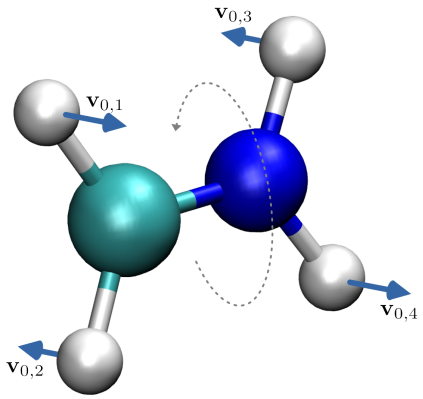

FIGURE 4.29: Rotation of the $H_2C{=}N^+H_2$ molecule around its C=N bonding axis, initialized by according initial velocities placed on the hydrogen atoms, corresponding to a kinetic energy of 10 eV. The carbon and nitrogen atoms reside in their initial locations.

locities on the hydrogen atoms are chosen as $|\mathbf{v}_{0,I}| = 219.0$ Å/ps which corresponds to a total kinetic energy of 10 eV. This energy is enough to initialize a rotation that will break the C=N double bond and one can expect significant non-adiabatic character from this point, as an excited state potential energy curve is approached at 90° [138].
We will also compare the results of the RT-TDDFT-Ehrenfest dynamics (RT-TDDFT-ED) simulations with DFT-based Born-Oppenheimer MD dynamics – which is only able to describe adiabatic dynamics. The PW-LDA functional [23] was chosen together with the 'tight' basis set if not stated otherwise, while the time propagation was carried out via the semi-implicit EM propagator in combination with the scaling and squaring method for the matrix exponential. The total simulation time was always 60 fs; we will discuss the time stepping later in our discussion.

As a first demonstration of the correctness of our method, we provide a comparison between BOMD and Ehrenfest dynamics for a low initial kinetic energy of 2.96 eV (using the same settings for both simulations). In this regime, the dynamics are adiabatic and both approaches are expected to yield the same results. In Figure 4.29 we show the dynamics of the dihedral angle defined by $\phi_D(H_1,C,N,H_4)$, i.e., the angle between the planes spanned by H_1-C-N and C-N-H_4 (upper panel), and the total electronic energy difference relative to $t_0 = 0$ (lower panel). One can clearly see that the dihedral angle stays below 90° for the whole time and that the electronic energy

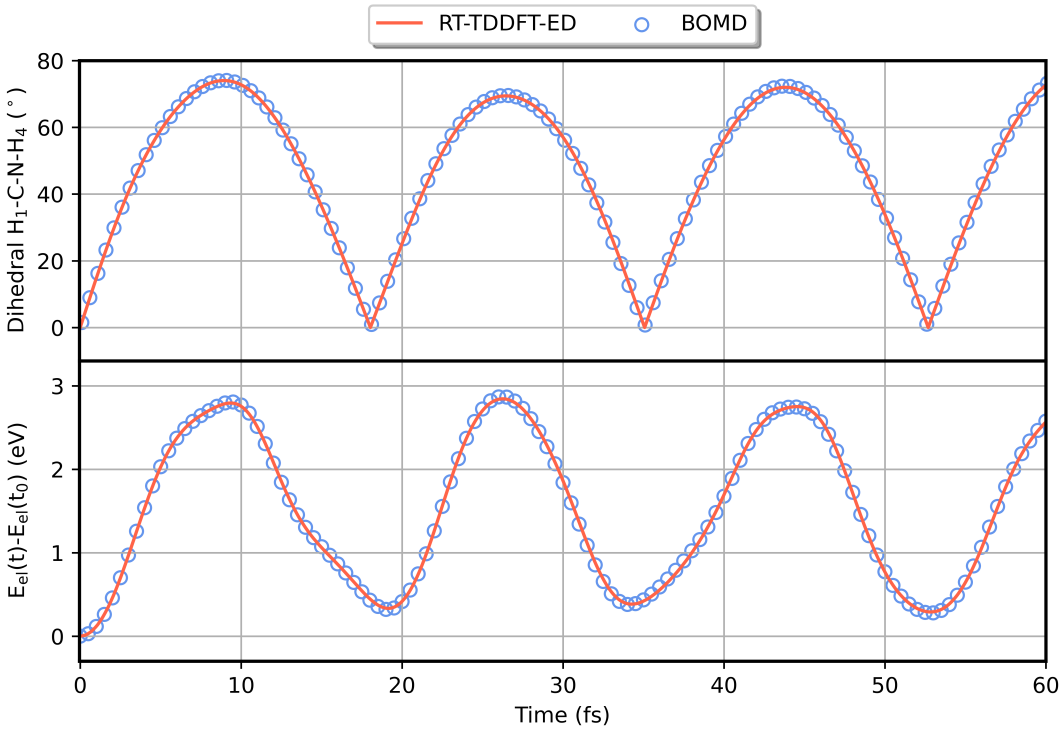

FIGURE 4.30: Dynamics of the H_1-C-N-H_4 dihedral angle (upper panel) and electronic energy change $E_{el}(t) - E_{el}(t_0 = 0)$ (lower panel) for BOMD (blue) and RT-TDDFT-ED (red), with an initial kinetic energy of 2.96 eV.

difference is bound by the initial kinetic nuclear energy of 2.96 eV, i.e., both methods yield the same trajectory. Overall, the agreement is excellent, underlining the correct implementation of the technique.

We now turn our discussion to the case with initial nuclear kinetic energy of 10 eV. In Figure 4.30 we illustrate the electronic excitation and the degree of energy conservation in dependence of simulation time: the upper panel shows the z-component (parallel to the C=N axis) of the electronic dipole moment's change relative to $t = 0$ (as the molecule has a permanent dipole moment) for RT-TDDFT-Ehrenfest dynamics and Born-Oppenheimer molecular dynamics, while the lower panel shows the difference in total energy relative to the value at $t_0 = 0$, for two different time steppings of the Ehrenfest dynamics. We can see here that the energy conservation is acceptable but declining for the time steps $\Delta t = 0.1$ a.u. $= 0.024$ fs, $\Delta T = 0.4$ a.u. $= 0.096$ fs, being within the 40 meV range, but gets considerably better for a tenth of the respective time step, as it is to be expected, with a maximum range below 10 meV. As discussed before [140], this regime requires relatively small time steps to be numerically stable. The significant onset of dipolar oscillations around 8 fs clearly indicates the electronic excitation. When looking closer, one can locate the onset of these oscillations at around 4.5 fs, as marked by the purple line. At this point, the internal torsion reaches 90°, causing the double bond to break and reorganize, corresponding to excited state contributions from then on.

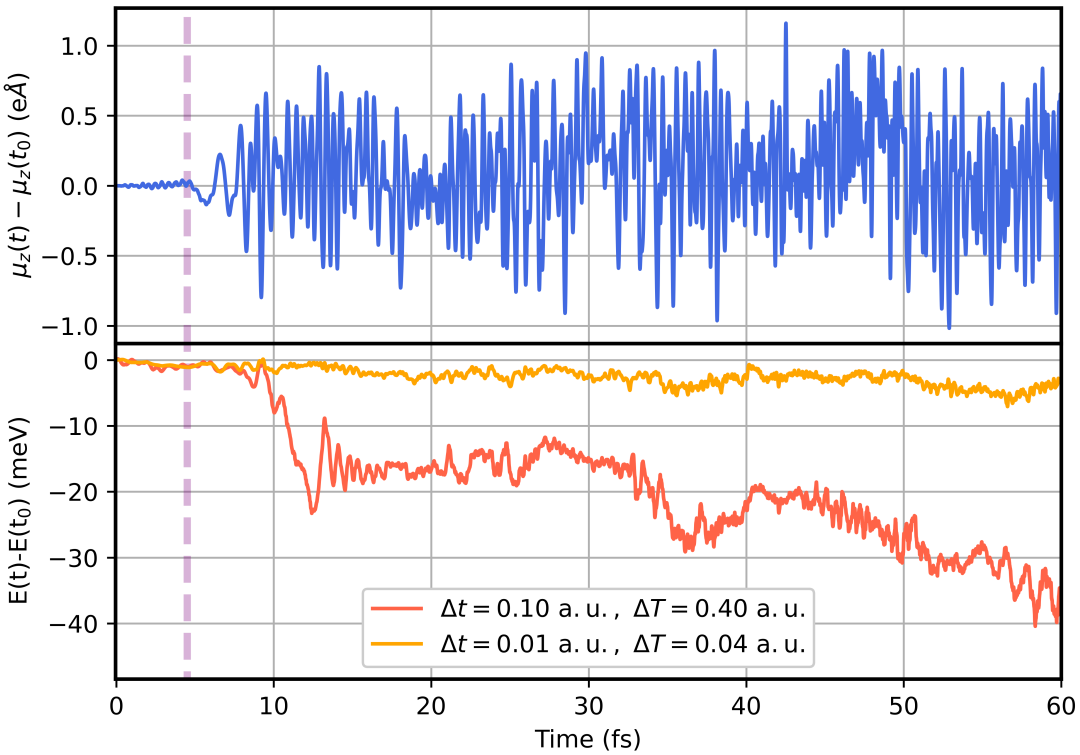

FIGURE 4.31: Dynamics of electronic dipole moment change $\mu_z(t) - \mu_z(t_0)$ (upper panel) and change of total energy $E(t) - E(t_0)$ as measure for energy conservation, the latter for two different time steps (lower panel). The time for which the internal rotation angle is at 90° is marked by the purple line.

Figure 4.32 shows the dihedral angle and the difference of the electronic energy relative to the values at $t_0 = 0$ in dependence of simulation time for RT-TDDFT-Ehrenfest dynamics and Born-Oppenheimer dynamics, now for the case of initial kinetic energy of 10 eV. We here conducted both the BOMD and the RT-TDDFT-ED simulations not only for the 'tight', but also for the 'tight+aug2' basis set in order to analyze the basis set influence in the non-adiabatic case where electronic excitations come into play. While the results coincide perfectly for both observables and basis sets until 4.5 fs, visible differences between BOMD and RT-TDDFT-ED occur from this time on. An average increase of the electronic energy over the whole simulation time is accompanied by a decrease of nuclear torsional frequency, as indicated by the dihedral angle. This clearly illustrates the excited-state contributions altering the trajectory. Regarding the impact of the basis set, we observe that noticeable differences occur in RT-TDDFT-ED, but not in BOMD (the total energy conservation deviation was always below 0.01 eV). We interpret this as a consequence of electronic excitation present in the case of Ehrenfest dynamics, as the excited-state wave functions are naturally more sensitive to the basis set. The 'tight+aug2' set likely provides a better description of the excited electronic states in general. Overall, our observations for this case are in agreement with former results for RT-TDDFT-ED [136, 138], allowing us to conclude on the correct implementation of the technique.

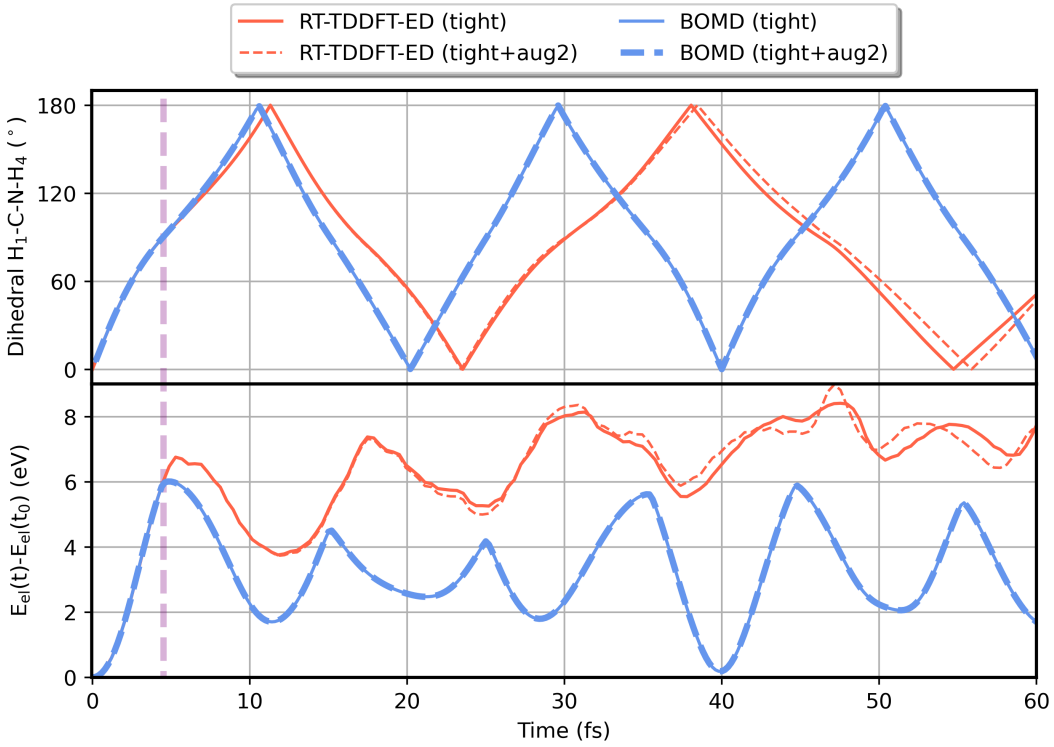

FIGURE 4.32: Dynamics of the H_1-C-N-H_4 dihedral angle (upper panel) and electronic energy change $E_{el}(t) - E_{el}(t_0 = 0)$ (lower panel) for BOMD (blue) and RT-TDDFT-ED (red), with an initial nuclear kinetic energy of 10 eV. The time for which the internal rotation angle is at 90° is marked by the purple line.

4.5.3 Collision of a Cl Atom with Graphene

As we stated in the introduction, simulations of ion collisions with surfaces or channeling of ions in crystals are very common applications for Ehrenfest dynamics. Therefore, our second example was motivated by a calculation that was done by Jia et al. [163], where the collision of a Cl^- ion with graphene was simulated. This may describe the experimental implantation of foreign dopants into a substrate. In fact, this study used a graphene nanoflake, i.e., a molecular system. Instead of doing so, we provide results for a calculation that was performed with periodic boundary conditions, as our implementation is capable of doing so and as this is more natural to the given problem. Also, the FHI-aims code is currently not able to place ions in a periodic supercell (but will probably be in the future), and we thus used a neutral Cl atom.

We prepared a (5×5) surface supercell consisting of 50 carbon atoms, lying in the x-y-plane, as illustrated in Figure 4.33. Here, the supercell had an extent of 200 Å in z-direction to avoid spurious interactions (note that this comes without significant additional cost, as the basis set is localized). The Cl atom was placed 3 Å above the surface along the z-axis, directly above the center of a carbon ring, and it was given an initial velocity of $v_z(t = 0) = -1058.4$ Å/ps which corresponds to a kinetic energy of 2057.9 eV. We employed an electronic time step of 0.04 a.u. $= 0.0009$ fs and

a nuclear time step of 0.16 a.u. $= 0.0039$ fs, using the CN(1) propagator. Analogous to the reference, we employed the PW-LDA [23] exchange-correlation functional. A $5 \times 5 \times 1$ **k**-point mesh was set for the Brillouin zone sampling. We conducted the same simulation with the built-in BOMD functionality of FHI-aims, using a time step of 0.1 fs.

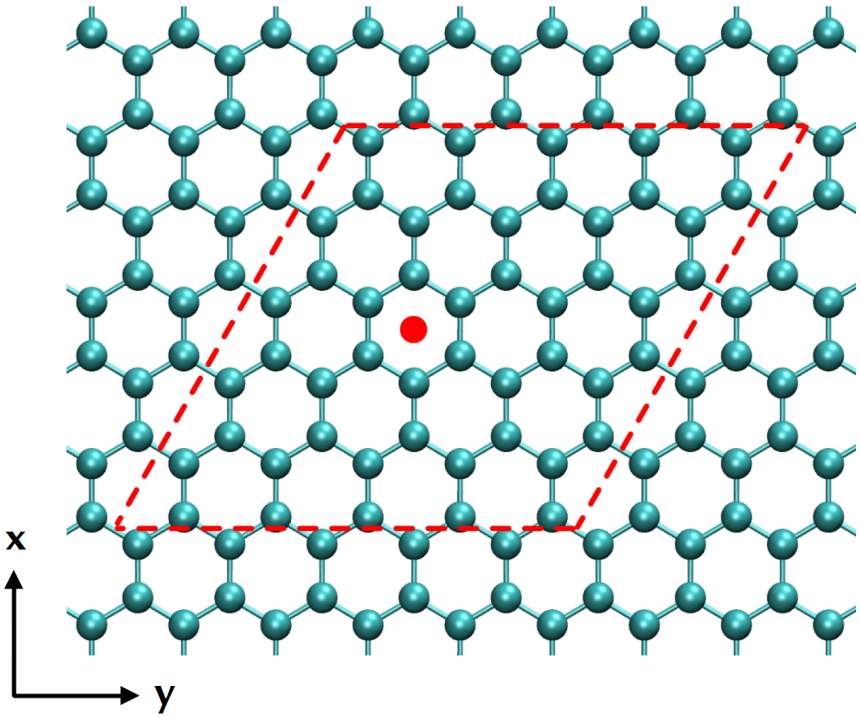

FIGURE 4.33: Supercell used for the simulation of Cl impact on graphene, containing 50 C atoms. The graphene layer initially resides at $z = 0$. The initial location of the Cl atom, as projected into the x-y-plane is marked by the red dot. The corresponding initial z-location is at 3 Å.

Figure 4.34 illustrates the non-adiabatic dynamics on the time axis in the upper panel. The lower panel shows the z-coordinate of the Cl atom; the graphene layer resides at $z = 0$. Thus, the Cl atom enters the lower half-space at approximately 2.8 fs. At this time, the kinetic energy of the Cl atom shows a minimum. This is directly accompanied by an increase of the overall electronic energy which is obviously dominated by the graphene contribution. One can further observe a slow increase in the kinetic energy of the graphene layer, as the traversing Cl atom pushes away carbon atoms on the central ring, causing a breathing oscillation within the x-y-plane, as observed in the trajectory. The key feature of the Ehrenfest description (in contrast to BOMD) is now that the electronic subsystem remains in an excited state, as can be seen in the fact that the potential energy remains on an elevated level long after the Cl atom has traversed the graphene layer. In contrast, the BOMD potential energy returns to its initial value. Finally, the Cl atom has lost 22.2 eV in kinetic energy and the overall energy gain by the electron system is 20.9 eV which is considerable; the final kinetic energy of the graphene layer is around 1.3 eV.

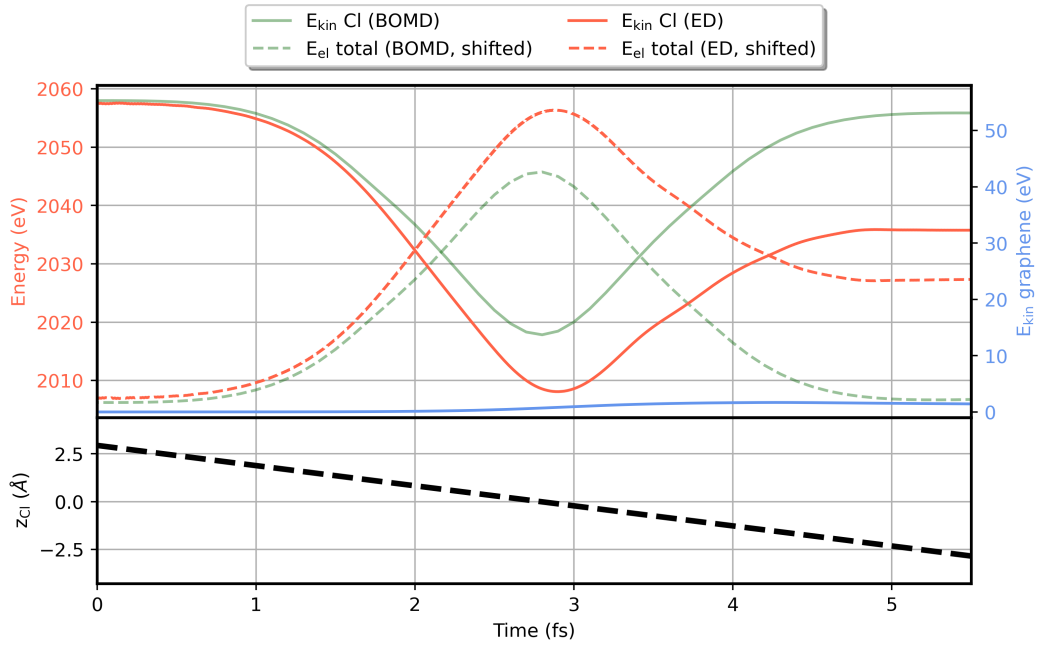

FIGURE 4.34: Top panel: kinetic energy of the Cl atom (solid red line: ED, solid green line: BOMD) and total electronic energy (dashed red line: ED, dashed green line: BOMD, both shifted), while the y-axis refers to the kinetic energy of Cl. The blue line denotes the total kinetic energy of the graphene layer and is associated to the right blue y-scale (from ED, but the BOMD result is very similar). Bottom panel: z-location of the Cl atom. The graphene layer resides at $z = 0$.

These observations are in good agreement with the reference, but we do not provide a direct comparison, as the setup is not equal (due to the PBC and negative singly charged Cl atom). However, we note that in the reference, 22.5 eV were transferred into the electron system and 0.84 eV into the graphene layer. In order to provide some more insight about the energy transfer on the surface, Figure 4.35 shows the kinetic energy of the carbon atoms within the graphene layer at the final simulation time of 5.5 fs. Here, the impact point is symbolized by a cross and the kinetic energy of the carbon atoms is visualized by a color mapping. As we noted before, the atoms in the central ring are mostly displaced within the x-y-plane (on average by 0.08 Å and by 0.017 on the z-axis, relative to $t = 0$), and such that the ring opens symmetrically. From the kinetic energy distribution, one can see that the ring atoms gain the major part of the energy, while for the upper and lower atoms, some energy is transferred to the above and below neighbor, respectively. This can only be explained as an effect of the symmetry and size of the supercell, as the distribution can be expected as isotropic in the infinitely extended layer case.
Overall, the results are as expected and the obtained key values already have agreement with the reference values.

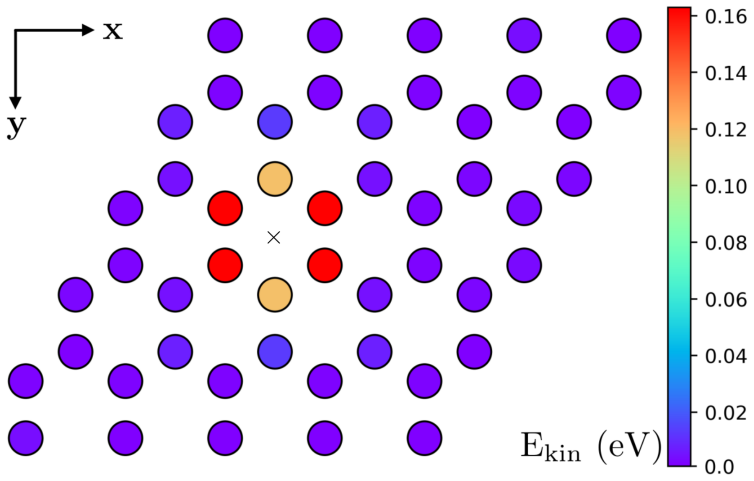

FIGURE 4.35: Kinetic energy on individual carbon atoms at $t = t_{max} = 5.5$ fs, which are illustrated by circles. The color is associated to the kinetic energy scale on the right side. The symbol $\times$ denotes the point where the Cl atom traverses through the graphene layer.

4.5.4 Discussion

Clear evidence was provided for the correct implementation of the RT-TDDFT-based Ehrenfest technique. For this, in the first part, we have shown results for a common test system in this context. Here, the perfect agreement between ED and BOMD for the low energy initial condition has shown that the approach is implemented correctly. In the non-adiabatic case, we clearly observed the expected behavior, i.e., the transfer of nuclear kinetic energy into the electron system. The observations here are as expected, showing that the RT-TDDFT-ED approach also works well with NAOs in the FHI-aims framework. The effect of the basis set was noticeable and further investigations will likely yield important insights.
In the second part, we have shown that our Ehrenfest dynamics approach also works well for systems with periodic boundary conditions, making it an interesting tool to simulate, e.g., collision or channeling experiments. The obtained data is in good agreement with reference values, even though a slightly different setup was used. In contrast to plane-wave approaches, the absence of significant additional computational cost in slab unit cells with large vacuum regions makes our framework especially useful for these systems. We think that this is a major advantage, making this implementation attractive for such studies. Another advantage could be the all-electron description: when describing high-energy ion impact, it is possible that not only valence, but also core-level states contribute to the excited-state dynamics. This makes our approach again more general.

4.6 Imaginary Time Propagation

In this chapter, we present our implementation of the imaginary-time propagation technique, providing an alternative way to obtain converged ground state solutions of the Kohn-Sham equation. We first introduce the theory and thereafter present several benchmarks both for finite and extended systems.

4.6.1 Introduction

Another interesting application based on the real-time TDDFT framework is the so-called *imaginary-time* TDDFT (IT-TDDFT) [238]. This subject is rather distinct from the typical application of RT-TDDFT, as it is not about simulation of actual electron dynamics, but rather about providing an alternative approach to the *ground state* self-consistent field procedure of standard DFT. We shortly introduced the standard diagonalization-based SCF approach in Sec. 2.1.6 - however, this is not the only way to solve the Kohn-Sham equations. For example, one can also try to directly determine the minimum of the total Kohn-Sham energy [239, 240]. IT-TDDFT is yet another approach to do so, being distinct from the others in several ways. Reasons to consider IT-TDDFT for this purpose are cases in which the SCF approach takes too long or fails entirely, i.e., when the iterative scheme does not find a fixed-point solution, even with sophisticated mixing procedures like DIIS [55]. Such problematic cases are often found in metallic systems, as the high density of states around the Fermi level leads to occupation oscillations within the SCF procedure [241]. Another advantage is the better usability compared to traditional SCF procedures, as only very minimal parameter input (essentially only the time step) has to be provided by the user. Standard SCF techniques on the other hand, e.g., require to set a specific mixing technique, several mixing parameters, or the amount of electronic smearing (which stabilizes SCF in metallic systems and highly degenerate systems, as it prevents occupation oscillations).

4.6.2 Theory

Considering a quantum system with a time-independent Hamiltonian $\mathcal{H}$ with some eigenstate Ψ_n, the time-evolution of this state is given by

$$\Psi_n(t) = e^{-it\mathcal{H}}\Psi_n(0) = e^{-it\epsilon_n}\Psi_n(0), \tag{4.41}$$

which just means that this stationary state will be rotated in time by a phase that corresponds to its eigenenergy ϵ_n. One can now introduce the concept of imaginary time by substituting $t := -i\tau$, $\tau \in \mathbb{R}$, resulting in the equation

$$\Psi_n(\tau) = e^{-i\tau\mathcal{H}}\Psi_n(0) = e^{-\tau\epsilon_n}\Psi_n(0). \tag{4.42}$$

In this representation, the imaginary time evolution simply describes an exponential decay of the state with a decay factor given by its eigenenergy. The first insight at this point is thus for an ensemble of several eigenstates of the Hamiltonian, that the ones with lowest energy will decay slowest, while the high energy states evolve to zero rapidly. The method is also valid for explicitly time-dependent Hamiltonians for sufficiently small imaginary time steps [238]. We now consider an arbitrary superposition state given by a linear combination

$$\Psi(\tau) = \sum_{n=0}^{\infty} C_n(0) e^{-\tau\epsilon_n} \Psi_n \tag{4.43}$$

with the corresponding zero-time expansion coefficients $\{C_n(0)\}$. Normalizing the superposition state via its time-dependent norm

$$N(\tau) = \sqrt{\langle \Psi(\tau) | \Psi(\tau) \rangle} = \left(\sum_{n=0}^{\infty} |C_n(0)|^2 e^{-2\tau\epsilon_n} \right)^{\frac{1}{2}} \tag{4.44}$$

yields the result

$$\Psi(\tau) = \frac{1}{N(\tau)} \sum_{n=0}^{\infty} C_n(0) e^{-\tau\epsilon_n} \Psi_n. \tag{4.45}$$

Evaluating the infinite imaginary time limit yields $\lim_{\tau\to\infty} \Psi(\tau) = \Psi_m$ where Ψ_m is the state with the lowest eigenenergy ϵ_m. This means that among all states in this superposition, only the one with the lowest energy will ultimately dominate in the imaginary-time propagation. Flamant et al. [238] showed that this also applies to Kohn-Sham systems by extending the van Leeuwen existence theorem to this case. The ultimately converged states are invariant under further imaginary time evolution and correspond to self-consistent solutions of the Kohn-Sham equations [238].
In practice, one employs the simple transformation $t := -i\tau$ in the time-evolution propagator of choice and makes use of the RT-TDDFT framework for time propagation. For example, the EM propagator is then given by

$$\mathcal{U}(\tau_k + \Delta\tau, \tau_k) = \exp\left(-\Delta\tau \mathcal{H}_{\mathrm{KS}} \left(\tau_k + \frac{\Delta\tau}{2} \right) \right) \tag{4.46}$$

with $\mathcal{H}_{\mathrm{KS}}(\tau_k) = \mathcal{H}_{\mathrm{KS}}[\rho(\tau_k)]$ which can be solved in a similar way to the standard case. It should be noted that any imaginary-time propagator lacks the property of being unitary due to its mathematical form, imposing the need for reorthonormalization of the propagated states after each step.
The practical advantage over conventional SCF methods is not only the guaranteed convergence to a final and physical state (given a reasonably small time step which can actually be higher than in the standard case since the system does not oscillate rapidly), but also that it is very easy to apply. In contrast, problematic SCF cases need to be adjusted manually with iterative mixing solvers, possibly requiring advanced knowledge of the topic.

We integrated imaginary time propagation in our method and use conventional modified Gram-Schmidt orthonormalization [242].

4.6.3 Benchmarks for IT-TDDFT

In order to show the fundamental correctness of our implementation, we first provide results for two systems that are non-pathological SCF cases: bulk silicon and benzene. In all our IT-TDDFT calculations, the 'light' basis set was used together with the PW-LDA exchange-correlation functional. For imaginary-time propagation, the semi-implicit EM scheme was used. The periodic calculations were performed with a $8 \times 8 \times 8$ **k**-point grid. Results can be found in Figure 4.36, where the imaginary time-dependent total energies are shown relative to the final values, and in addition the values of the SCF solution. Note that sharp dips on the logarithmic y-scale correspond to negative values. For both systems, the energies converge to below 10^{-10} eV. While the silicon system was essentially converged within around 3 fs imaginary time, benzene was even faster with about 1 fs imaginary time. One can thus see that the method works well for these simple cases in our implementation both for finite and periodic systems.

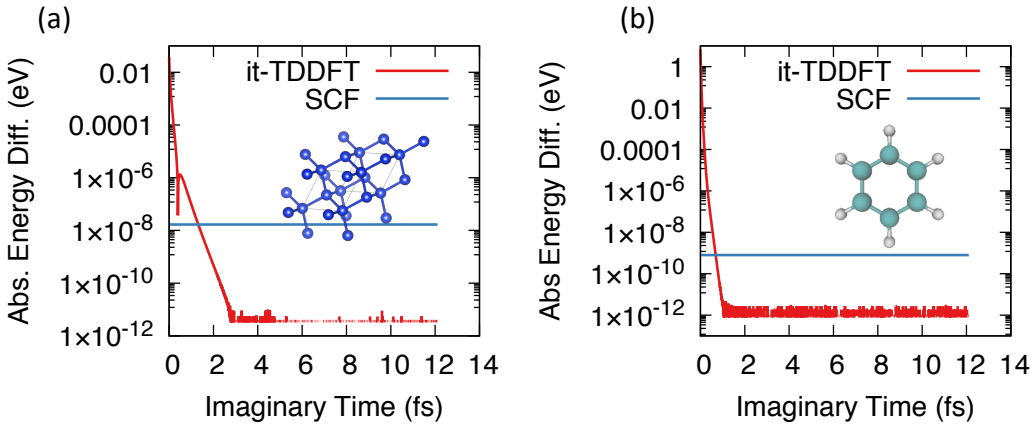

FIGURE 4.36: Illustration of total energy convergence $E(\tau) - E_{\text{conv}}$ via IT-TDDFT (red) and SCF (blue) for bulk silicon (a) and benzene (b). The references are the IT-TDDFT converged energies which are given by -15748.061263551753655 eV for silicon and -6263.340286733794528 eV for benzene.

The next examples correspond to bond-breaking situations of simple molecules. Such processes are often hard to converge, but of high interest when modeling chemical reactions. The first example is the fluoromethane molecule with the C-F bond length elongated to 4 Å (from 1.38 Å in the corresponding relaxed ground state geometry) and the second example is the NaCl molecule with an elongated bond length of 6 Å (from 2.33 Å in the corresponding relaxed ground state geometry). Both systems could not be converged to the ground state by us via the standard

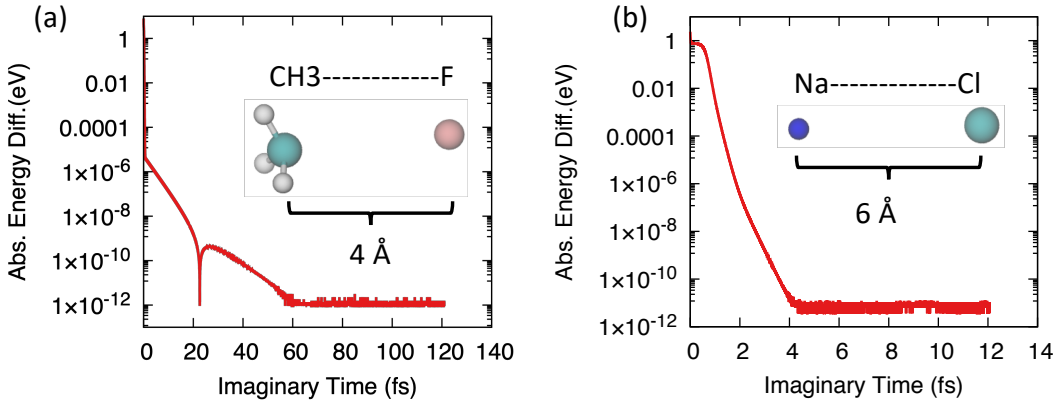

FIGURE 4.37: Illustration of total energy convergence $E(\tau) - E_{\text{conv}}$ via IT-TDDFT (red) and SCF (blue) for fluoromethane with elongated C-F bond length (a) and NaCl with elongated Na-Cl bond length (b). The references are the IT-TDDFT converged energies which are given by -3798.948559291503443 eV for fluoromethane and -17001.015232680390909 eV for NaCl.

SCF approach, using the conventional Pulay/DIIS mixing method [55]. The imaginary time evolutions converged after about 4 fs for NaCl and about 60 fs for fluoromethane, see Fig. 4.37. The latter is a comparably long simulation time, underlining the pathological character of this testcase. This may point towards a relationship between the SCF convergence difficulty level and the imaginary time it takes to converge the solution.

As a final example, now for periodic systems, we chose a single layer of hexagonal boron nitride, a wide-gap semiconductor. With a boron vacancy, the system could not be converged via standard SCF, while it could be with a nitrogen vacancy (employing zero-valued occupation broadening). It was shown that a boron vacancy shifts down the Fermi energy to the valence band maximum (VBM) [243], probably causing the problematic SCF convergence due to charge sloshing, as described above. Figure 4.38 shows the results of the calculations and the corresponding systems' unit cells. While the system with nitrogen vacancy converged around 6 fs imaginary time, the version with boron vacancy needed significantly more time with around 50 fs.
We provide some technical details for the imaginary time evolution technique in Chapter 6.2.3.

4.6.4 Discussion

We have implemented the imaginary-time propagation technique into our RT-TDDFT framework and could show that it works as intended. For the trivial testcases, convergence was reached in short imaginary times well below under 10 fs. The pathological cases needed noticeably more time, but always converged in the end. Our

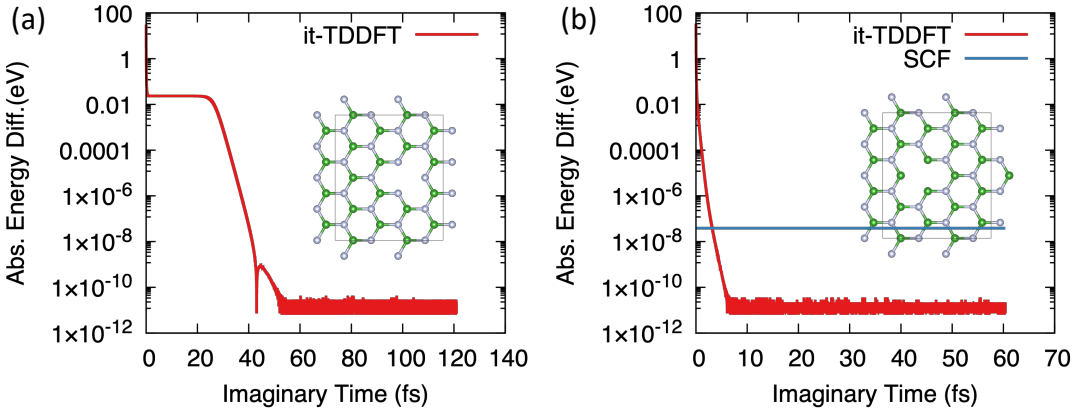

FIGURE 4.38: Illustration of total energy convergence $E(\tau) - E_{\text{conv}}$ via IT-TDDFT (red) and SCF (blue) for hex-BN single layer with boron vacancy (a) and hex-BN with nitrogen vacancy (b). The references are the IT-TDDFT converged energies which are given by -34022.176308515248820 eV for the boron vacancy and -33210.584275109766168 eV for the nitrogen vacancy.

implementation was shown to work both for finite and periodic systems. IT-TDDFT is thus an alternative to the standard iterative SCF methods, being of real importance for pathological cases. In addition, it is an extremely convenient method to converge a ground state solution, as it requires minimal input that does not demand expert knowledge.

Chapter 5

Time-Independent Methods for Vibrational Spectroscopy

5.1 Overview and Motivation

We present results here that were obtained by time-independent techniques for vibrational spectroscopy, also employing perturbative treatment of electric fields acting on electrons. This yields another ingredient towards a more general picture of spectroscopic simulations in this context.

5.2 Theory

In principle, we use the already elaborated framework of DFT in this study. However, some techniques that were not already elucidated were also applied. We will give short introductions to all relevant methods that we used in this frame and will refer to them later in the results section whenever it is needed.

5.2.1 Vibrational Spectra and Harmonic Approximation

Vibrational analysis refers to nuclear vibrational motion and thus, these additional degrees of freedom need to be described. In this context, the perturbative *harmonic approximation* is used which assumes the nuclear wave function being subject to a harmonic, i.e., quadratic potential with respect to nuclear coordinates [244]. The Born-Oppenheimer approximation is incorporated here, decoupling electronic and nuclear motion. We follow the discussions by Neugebauer et al. [245] and Bahar et al. [246] for further details. For this we first consider the stationary nuclear Schrödinger equation

$$\left(-\sum_{I=1}^{N_{at}} \frac{1}{2M_I} \nabla_{\mathbf{R}}^2 + \mathcal{V}(\{\mathbf{R}\}) \right) \Phi(\{\mathbf{R}\}) = E_{tot} \Phi(\{\mathbf{R}\}) \tag{5.1}$$

with the nuclear masses M_I, the nuclear wave function Φ and the potential $\mathcal{V}(\{\mathbf{R}\}) = \langle \Psi | \mathcal{H}_{KS} | \Psi \rangle$ given by the electronic energy, where $\{\mathbf{R}\}$ denotes all atomic coordinates. The starting point for the harmonic approximation is to expand the potential by a

Taylor series around the equilibrium configuration $\{\mathbf{R}_0\}$ as

$$\mathcal{V}(\{\mathbf{R}\}) = \mathcal{V}(\{\mathbf{R}_0\}) + \sum_{i=1}^{3N_{at}} \left(\frac{\partial \mathcal{V}}{\partial R_i}\right)\Bigg|_{\mathbf{R}_0} \Delta R_i + \frac{1}{2}\sum_{ij=1}^{3N_{at}} \left(\frac{\partial^2 \mathcal{V}}{\partial R_i \partial R_j}\right)\Bigg|_{\mathbf{R}_0} \Delta R_i \Delta R_j + \text{h.o.t.} \tag{5.2}$$

with the displacement vectors $\Delta R_i = R_i - R_{i,0}$ and where we used indices that run over all $3N_{at}$ coordinates. The expansion is now truncated after the quadratic term which includes the Hessian

$$\bar{H}_{ij} := \frac{\partial^2 \mathcal{V}(\{\mathbf{R}\})}{\partial R_i \partial R_j}\Bigg|_{\mathbf{R}_0}. \tag{5.3}$$

The second term vanishes, as the potential derivative is zero at the equilibrium geometry. This means that the effective potential $\mathcal{V}_h$ is quadratic, resembling the form of the potential of a harmonic oscillator, setting $\mathcal{V}(\{\mathbf{R}_0\}) = 0$ for convenience,

$$\mathcal{V}_h(\{\mathbf{R}\}) = \Delta\mathbf{R}^T \, \bar{\mathbf{H}} \, \Delta\mathbf{R}, \tag{5.4}$$

where we introduced a general matrix notation for the displacement vectors and the Hessian. We introduce the atomic mass matrix

$$\mathbf{M} = \text{diag}\Big(M_1, M_1, M_1, M_2, M_2, M_2, ..., M_{3N_{at}}, M_{3N_{at}}, M_{3N_{at}}\Big) \tag{5.5}$$

for further discussions. At this point, one considers the atoms as classical point particles at the coordinates $\{\mathbf{R}\}$. Given the harmonic potential, the equation of motion (EOM) for the atom displacements is provided as

$$\mathbf{M}\frac{\mathrm{d}^2}{\mathrm{d}t^2}\Delta\mathbf{R} + \bar{\mathbf{H}}\,\Delta\mathbf{R} = 0, \tag{5.6}$$

which corresponds to the EOM of a harmonic oscillator. By using the ansatz

$$\Delta\mathbf{R}_L(t) = \mathbf{u}_L \exp(-i\omega_L t), \tag{5.7}$$

the equation is transformed into a generalized eigenvalue problem of the form

$$\bar{\mathbf{H}}\mathbf{U} = \mathbf{\Omega}\mathbf{M}\mathbf{U} \tag{5.8}$$

with $\mathbf{U} = (\mathbf{u}_1, ..., \mathbf{u}_L)$ and $\mathbf{\Omega} = \text{diag}(\omega_1^2, ..., \omega_L^2)$ for $\forall L = 1, ..., 3N_{at}$. This eigenvalue problem is reduced to an ordinary eigenvalue problem via the transformations $\mathbf{X} = \mathbf{M}^{1/2}\mathbf{U}$ and $\bar{\mathbf{H}}' = \mathbf{M}^{-1/2}\bar{\mathbf{H}}\mathbf{M}^{-1/2}$ (which is commonly denoted as the *mass-weighted* Hessian), i.e.,

$$\bar{\mathbf{H}}'\mathbf{X} = \mathbf{\Omega}\mathbf{X}. \tag{5.9}$$

This is the key equation in the approach: the orthonormal eigenvectors $\mathbf{x}_L$ are the so-called *normal modes* of the system, describing the collective atomic displacements of a certain mode L with the frequency ω_L.
In practice, the electronic Hessian can be obtained by different methods, and in this study, a finite-difference approach was employed to calculate the (Cartesian) Hessian from the atomic forces,

$$\bar{H}_{ij} = \left.\frac{\partial^2 \bar{E}_{\mathrm{el}}}{\partial R_i \partial R_j}\right|_{\mathbf{R}_0} \approx \frac{F_i(R_j + \Delta_j) - F_i(R_j - \Delta_j)}{2\Delta_j}, \tag{5.10}$$

where $i, j = 1, ..., 3\mathrm{N_{at}}$. This means here that the Hessian is constructed from 2 finite-difference displacements Δ_j per atom and per Cartesian direction, for all atoms in the system not being subject to constraints. The forces are obtained from the corresponding ground state DFT calculation of a displaced geometry. Thus, $6\mathrm{N}_{\mathrm{at}}^{u}$ calculations have to be performed with $\mathrm{N}_{\mathrm{at}}^{u}$ being the number of unconstrained atoms.

5.2.2 Density Functional Perturbation Theory

Considering a system that is subject to a weak external electric field of the form $\mathbf{E} = \left(E_x, E_y, E_z\right)^T$ and the KS Hamiltonian being coupled via the length gauge, i.e.,

$$\mathcal{H}'_{\mathrm{KS}}[\rho] = \mathcal{H}_{\mathrm{KS}}[\rho] - \mathbf{r} \cdot \mathbf{E}, \tag{5.11}$$

the total energy of the Kohn-Sham system incorporates an additional term

$$E_{\mathbf{E}}[\rho] = -\int \mathrm{d}^3\mathbf{r}\, \rho(\mathbf{r})\, \mathbf{r} \cdot \mathbf{E}. \tag{5.12}$$

The first step is now to conduct a perturbative Taylor expansion of the total energy in the sense that the external field is viewed as the perturbation [247]. This yields

$$E_{\mathrm{tot}}(\mathbf{E}) \approx E^0_{\mathrm{tot}} + \boldsymbol{\mu} \cdot \mathbf{E} + \frac{1}{2}\sum_{ij}^{3} \alpha_{ij} \mathrm{E}_i \mathrm{E}_j + \mathrm{h.o.t.} \tag{5.13}$$

where the electronic dipole moment $\boldsymbol{\mu}$ and the polarizability tensor α appear as 1st and 2nd order response functions. They are in this limit given as

$$\mu_i = \left.\frac{\partial E_{\mathbf{E}}[\rho_0]}{\partial \mathrm{E}_i}\right|_{\mathbf{E}=\mathbf{0}} = -\int \mathrm{d}^3\mathbf{r}\, \rho_0(\mathbf{r})\, r_i \tag{5.14}$$

with the ground state density $\rho_0(\mathbf{r})$. As one can directly see, this quantity is trivial to compute, given a converged ground state solution of the KS equations. The polarizability tensor is given by

$$\alpha_{ij} = \left.\frac{\partial^2 E_{\mathbf{E}}[\rho_0]}{\partial \mathrm{E}_i \partial \mathrm{E}_j}\right|_{\mathbf{E}=\mathbf{0}} = \left.\frac{\partial \mu_i}{\partial \mathrm{E}_j}\right|_{\mathbf{E}=\mathbf{0}} = -\int \mathrm{d}^3\mathbf{r}\, r_i \left.\frac{\partial \rho_0(\mathbf{r})}{\partial \mathrm{E}_j}\right|_{\mathbf{E}=\mathbf{0}} \tag{5.15}$$

and it becomes directly clear that the density-response of the ground state to the external field cannot be obtained in a simple way from a ground state calculation solely. At this point, the density functional perturbation theory (DFPT) ansatz is employed to compute the 2nd-order response. Perturbation theory is employed to solve the equation

$$(\epsilon_n^0 - \epsilon_m^0)\langle\psi_n^0|\psi_m^1\rangle = -\left(\langle\psi_n^0|\mathcal{H}_{\mathrm{KS}}^1|\psi_m^0\rangle - \epsilon_m^1\delta_{nm}\right) \tag{5.16}$$

for the perturbed single-particle orbitals ψ_m^1. Here, the perturbed Hamiltonian is given by $\mathcal{H}_{\mathrm{KS}}^1 = \mathcal{H}_{\mathrm{KS}}[\rho^1]$, i.e., as a functional of the 1st order density of the perturbation expansion. Above equation must thus be solved self-consistently. We do not cover more details on this – see, e.g., Shang et al. [100] for a sophisticated description. In the end, one obtains solutions ψ_m^1 which are then used to calculate the density response in order to obtain the polarizability tensor via Eq. 5.15:

$$\left.\frac{\partial\rho_0(\mathbf{r})}{\partial \mathrm{E}_j}\right|_{\mathbf{E}=\mathbf{0}} = \sum_{n=1}^{\mathrm{N_{occ}}} f_n\left(\psi_n^1(\mathbf{r})\psi_n^0(\mathbf{r}) + \psi_n^0(\mathbf{r})\psi_m^1(\mathbf{r})\right). \tag{5.17}$$

We note that above derivation is only valid for finite systems, as extended systems require some effort in order to handle the ill-defined position operator appearing in the length gauge coupling operator as well as in the electronic dipole moment. For this, the Berry phase approach can be used, similar to our comment in the theory section 2.2.5. Further details can be found in the literature, e.g., Refs. [100, 248].
In summary, DFPT can be used to compute the static polarizability α_{ij}. In combination with the finite-difference technique presented in Section 5.2.1, one can compute derivatives of the polarizability with respect to the normal mode vectors $\mathbf{x}_L$, i.e.,

$$\frac{\alpha_{ij}}{\partial \mathbf{x}_L} = \sum_{k=1}^{3\mathrm{N_{at}}} \frac{1}{\sqrt{M_k}} \frac{\alpha_{ij}(R_k + \Delta_k) - \alpha_{ij}(R_k - \Delta_k)}{2\Delta_k} x_{L,k} = \sum_{k=1}^{3\mathrm{N_{at}}} \frac{1}{\sqrt{M_k}} \frac{\partial \alpha_{ij}}{\partial R_k} x_{L,k}. \tag{5.18}$$

In above expression, the directional derivative of the polarizability with respect to the non-mass-weighted Cartesian normal coordinates is defined [249]. This quantity can be used for the computation of Raman intensities: this is intuitive, since Raman activity is connected to a change of the electronic polarizability with respect to vibrational modes.

5.3 Vibrational Analysis of Nitrothiophenyls on Au(111) Surfaces

In this section, we present a detailed study of a subject that is still in discussion: the adsorption characteristics of nitrothiophenols on Au(111) surfaces. We here apply ground state and the perturbative techniques presented before in order to provide

further clarification to this topic. This study was a collaborative theoretical and experimental work within the CRC 1242 (cf. Chapter 1 and Ref. [250]).

5.3.1 Introduction

The adsorption of long-chain alkylthiols and (oligo-)phenylthiols on gold surfaces is a topic that has sparked some research in the past, as these molecules can form ordered layers here. It could be shown via scanning tunneling microscopy [251, 252] that the spatial ordering of the molecules is maximal for dense layers of molecules that have multiple phenyl rings. As the molecules are covalently bonded to the surface by the sulfur anchor atom, one could suspect that this bond dictates the orientation. However, the nature of it can not be determined ad hoc and one could hypothesize about a directional bonding situation depending on orbital hybridization, or a rather flexible orientation due the sulfur getting immersed into the surface's electron liquid. Further, intermolecular interactions as well as electrostatic or van der Waals (vdW) interactions between molecule and surface can be thought of as playing a role.
In order to answer these questions, several experiments were conducted in the past, but still, a clear picture is missing, as some studies found evidence for upright standing molecules while others found evidence for rather tilted molecules. A study where near-edge X-ray absorption fine structure spectroscopy (NEXAFS) was employed found evidence for thiophenol (TP) SAMs on Au that are tilted by approximately 50° relative to the gold surface normal [253]. On the other hand, a study via electron spectroscopy suggested that the TP SAMs lie flat on the gold surface [254]. Further, an investigation that employed reflection absorption infrared spectroscopy found that the SAMs tend to be inclined towards the Au surface – however, it was noted that this technique is not accurate for this objective [255]. Experiments that used the same technique together with ellipsometry contrastingly found nearly upright standing molecules [256]. Another experiment using surface-enhanced infrared absorption spectroscopy stated that a tilt angle of around 30° could be determined [257]. Finally, we note that a surface-enhanced Raman scattering experiment found a tilt angle of about 14° [258]. In summary, it is thus quite difficult to draw conclusions from the heterogeneous experimental data.
This motivated us to conduct a combined experimental-theoretical study in order to further clarify the subject of 4-nitrothiophenol (4-NTP) and its bi- and terphenyl variants' adsorption on the Au(111) surface. Our study thus provides a multi-perspective view on the problem. We conducted ab-initio DFT simulations explicitly including periodic boundary conditions in order to model slab geometries, allowing us to quantify the influence of coverage and intermolecular interaction on the adsorption geometry. Raman spectroscopy was applied to 4-NTP on Au(111) for different surface coverages, yielding vibrational imprints of these situations. As in-plane modes yield strong signals for standing molecules while out-of-plane modes are amplified for flat lying molecules, we observe evidence for rather tilted molecules

due to the presence of out-of-plane modes in our spectra. In addition, vibrational sum frequency spectroscopy (vSFS) experiments were conducted: here, the information about the molecular orientation is accurately obtained by the polarization-dependency of the symmetric stretch mode of the NO_2 group of 4-NTP. The vSFS method was used before to characterize the adsorption of 4-NTP on Au(111) surfaces [259, 260] and evidence for a tilt angle of 60° was found [259]. However, the question of the surface coverage of the adsorbents was not conclusively studied and different values were given in the experimental literature, e.g., 0.23 and 0.31 [257] or 0.45 [261], while previous theoretical studies were only conducted for cluster geometries that do not take into account this degree of freedom explicitly [262].

5.3.2 Simulation Setup

For all simulations, we employed the 'tight' basis set in combination with the PBE exchange-correlation functional [26]. Explicit description of van der Waals interactions was included via the method by Tkatchenko and Scheffler (TS) [92] that computes density-dependent C_6 coefficients and vdW interaction radii via Hirshfeld partitioning of the electron density. These corrections were applied to the energy and the forces if necessary, after a converged SCF solution was obtained. Any geometric and vibrational data discussed in this part was obtained by using this method. Former studies could show that this approach is well-suited to describe vdW interaction between organic molecules and coinage metal surfaces [263, 264, 265]. We additionally used two many-body dispersion (MBD) methods [93, 94] which offer an even more general description of vdW interactions for testing purposes. The MBD approach models the dipolar interactions via coupled quantum harmonic oscillators. In detail, we used the range-separated self-consistently screened version (rsSCS-MBD) [95] and the recently introduced non-local version (MBD-NL) [96], which are both included in the code via the Libmbd library [266].
Any used structure was pre-relaxed and we provide the lattice constants for bulk Au by $a_0 = 4.151$ Å for PBE only and $a_0 = 4.108$ Å for PBE+vdW. The latter value is only about 0.7% larger than the experimental value of 4.080 Å [267]. The Au(111) slab geometries were prepared such that the gold layer of 4 atoms thickness resides in the x-y-plane, while vacuum is imposed along the z-axis. The corresponding supercells had an extent of minimum 100 Å in z-direction in order to circumvent undesired interactions between periodic slab images. Additionally, we employed the dipole-correction [268], disabling any long-range effects due to the polar slab (since the adsorbate resides on only one side). The corresponding **k**-point grid was chosen as $12 \times 12 \times 1$. As gold is a heavy element, relativistic treatment was included via the atomic ZORA approach [107]. Force calculations always had a rather tight convergence criterion of 10^{-4} eV/Å.
The vibrational calculations were carried out with a python script that is included in the FHI-aims software package. This script was modified by us to also yield the

required polarizability derivatives via the DFPT functionality as already included in FHI-aims [100] from the finite-difference calculations for the vibrational spectra.

5.3.3 Equilibrium Geometries and Energetics

To simulate different adsorbate coverages, we set up surface supercells with different lattice parameters, to be specific ($\sqrt{3} \times \sqrt{3}$), (2×2) and (3×3). The corresponding coverages are thus 0.33, 0.25 and 0.11 in the same order. As we also targeted to evaluate the impact of 4-NTP chain length with respect to adsorption characteristics, we conducted all simulations also for the 2-ring variant 4-nitro-biphenyl-4'-thiol (4-NBPT) and the 3-ring variant 4-nitro-terphenyl-4''-thiol (4-NTPT), as shown in Figure 5.1 a). In any of these calculations, the initial orientation of the corresponding

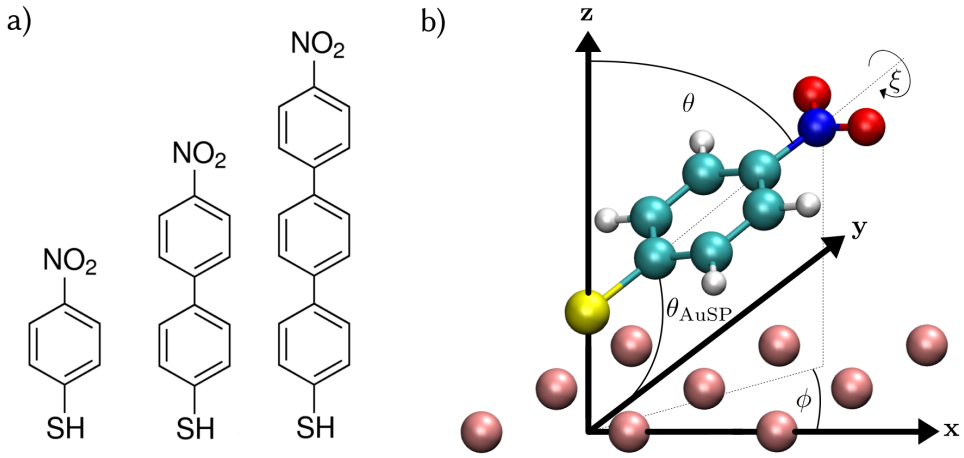

FIGURE 5.1: a) Chemical structures of 4-NTP, 4-NBPT and 4-NTPT (for free molecules, i.e., with hydrogen bonded to sulfur). b) Illustration for geometric data: bond angle θ_{AuSP}, tilt angle θ between molecule axis (S–N) and surface normal, in-plane angle ϕ relative to the x-axis/$[1\bar{1}0]$ crystallographic direction, twist angle ζ describing rotation around the molecule axis, which is defined as $\zeta = 0°$ when the normal of the phenyl ring is parallel to the z-axis/surface normal.

molecule was chosen such that the S atom resides on the hollow position, i.e., in the middle of the triangle spanned by gold atoms. Also, the molecules were tilted in the sense that $\phi = 30°$, as indicated in Fig. 5.1 b). The latter figure also includes definitions of other angles which we will refer to: θ describes the tilting between the molecular axis defined by the vector $\mathbf{X}_{\mathrm{S-N}}$ and the z-axis/normal of the Au(111) surface. As we also consider deformations (i.e., non-planar molecules), we additionally introduce the sulfur bond tilt angle θ_{AuSP} which measures the angle between the surface normal and the vector $\mathbf{X}_{\mathrm{S-C_1}}$. This quantity in combination with the distance between S and the Au surface, $d_{\mathrm{S-Au}}$, yields information about the covalent bonding situation. Other parameters are the in-plane angle ϕ, defined via the angles between the projection of the vector $\mathbf{X}_{\mathrm{S-N}}$ into the surface plane and the $[1\bar{1}0]$ crystallographic direction (the x-axis here), and the twist angle ζ which measures the rotation around the axis $\mathbf{X}_{\mathrm{S-N}}$.

TABLE 5.1: Calculated values of the bond angle θ_{AuSP}, tilt angle θ, in-plane angle ϕ, twist angle ξ, distance between Au(111) surface and sulfur and adsorption position of sulfur. Angles as defined in Fig. 5.1. All values are from simulations including Tkatkchenko-Scheffler vdW interactions.

Geometry	Rings	θ_{AuSP}	θ (°)	ϕ (°)	ξ (°)	d_{S-Au} (Å)	Position
$(\sqrt{3} \times \sqrt{3})$	1	136	32.4	29.9	1.5	2.01	near bridge
	2	149	24.8	307.5	103.7	1.99	near bridge
	3	151	22.2	113.9	105.0	1.98	near bridge
(2×2)	1	123	52.8	14.2	4.6	2.05	bridge
	2	122	50.1	13.5	7.8	2.05	near bridge
	3	122	48.3	21.0	8.1	2.05	bridge
(3×3)	1	111	75.7	30.0	2.3	2.14	bridge
	2	110	77.2	19.8	8.1	2.13	bridge
	3	108	70.7	23.6	1.2	2.12	bridge

Coming to the obtained results, we note that we will here only discuss simulations including explicit Tkatchenko-Scheffler vdW interaction (the geometries from the rsSCS-MBD and MBD-NL methods were essentially equal to the ones obtained by the TS vdW method, only differing by $1-2\%$ by the defined measures). The data obtained from the relaxations are listed in Table 5.1, sorted by surface unit cells and number of rings in the molecules. Additionally, we show the relaxed geometries for 4-NTP on the $(\sqrt{3} \times \sqrt{3})$ and (2×2) surfaces in Figure 5.2. On the first glance, the smaller unit cell yields nearly standing molecules with sulfur mainly located at the hollow position, while the (2×2) unit cell leads to the moleculs bonding closer to the bridge position and tilting more towards each other, also by rotating towards each other. The relaxed structures for both 4-NBPT and 4-NTPT on the (3×3) surface can be found in Figure 5.3. One can observe that both cases exhibit quite similar orien-

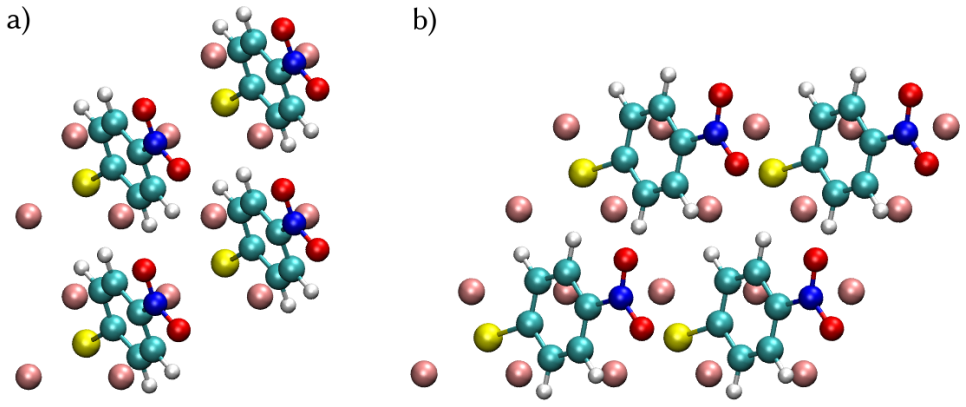

FIGURE 5.2: Top view of relaxed geometries for 4-NTP on Au(111). a) $(\sqrt{3} \times \sqrt{3})$ surface unit cells, b) (2×2) surface unit cells. All pictures contain 4 unit cells and show only the topmost gold layer for better visibility.

tation, with the difference that 4-NBPT shows relatively increased internal phenyl

ring rotation. We will now discuss the findings by the values shown in Table 5.1. Taking a look the sulfur bond angle θ_{AuSP}, we see a notable dependence on the coverage for all considered molecules, with values ranging between 108° and 151°, decreasing with smaller coverage. The characteristics for all molecules are quite similar, i.e., the quantity is not too sensitive to the short- or long-chain versions. However, small deviations are visible with the exception of 4-NTP on the $(\sqrt{3} \times \sqrt{3})$ surface, were θ_{AuSP} is off by $13° - 15°$. Overall, this behavior indicates that the sulfur bond tilt angle is noticeably affected by the steric repulsion of neighboring

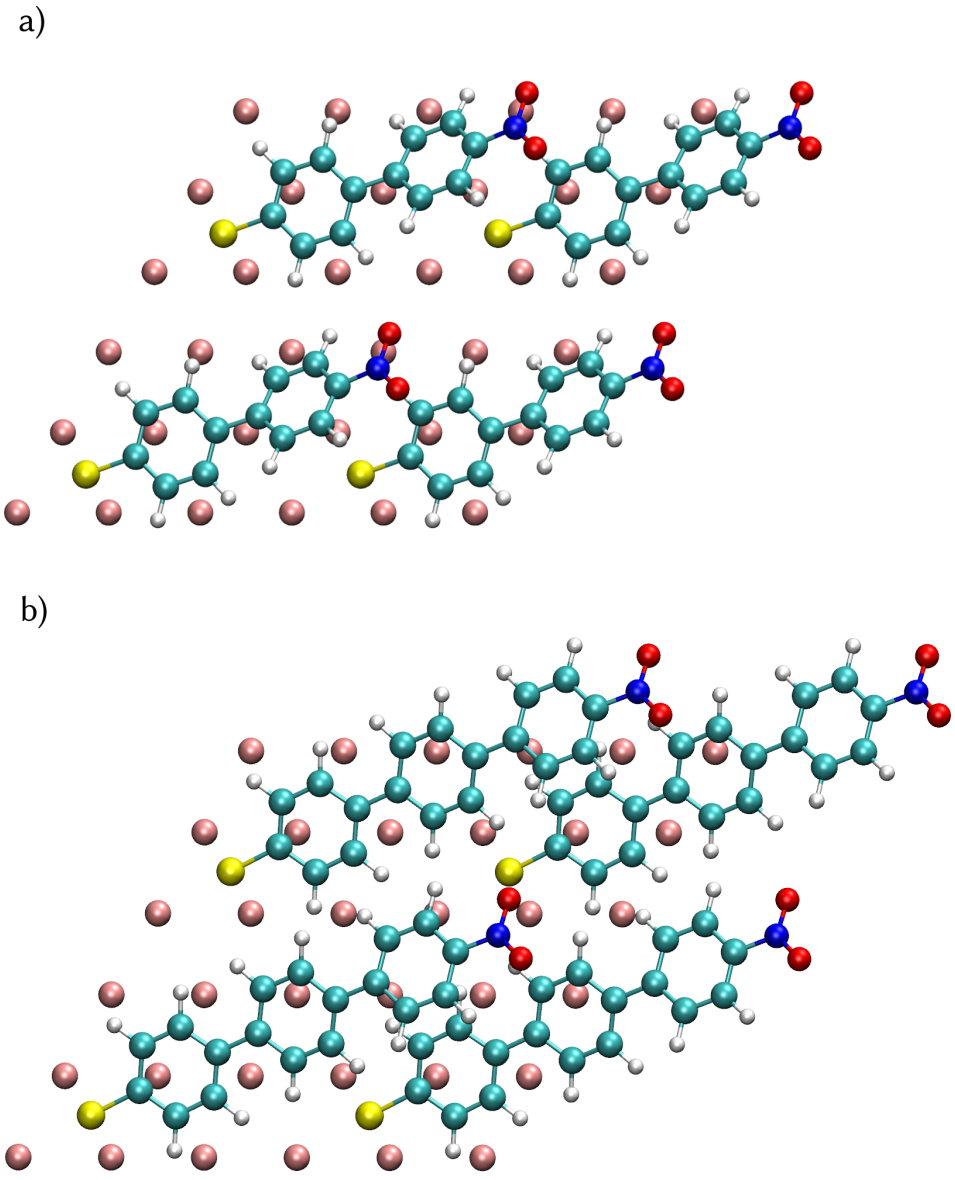

FIGURE 5.3: Top view of relaxed geometries for polyphenyl variants on Au(111) for the (3×3) unit cell. a) NBPT, b) NTPT. All pictures contain 4 unit cells and show only the topmost gold layer for better visibility.

molecules, especially forcing the longer 4-NBPT and 4-NTPT to stand upright. A similar trend is observed for the molecule tilt angle θ, however, this quantity is

more sensitive to the number of phenyl rings. This characteristic was also observed in an angle-resolved NEXAFS based experiment [253]. The overall range for this value is observed from values of 22.2° up to 77.2°, depending on the setup. As before, lower coverage corresponds to stronger tilting and vice versa for higher coverage. It should be noted at this point that significantly smaller tilt angles were obtained from simulations without vdW treatment.
For the in-plane angle ϕ, we observe different regimes, indicating the following characteristics: for the (3×3) surface unit cell, i.e., the one with lowest coverage and relatively isolated molecules, the range of ϕ between 20° and 30° suggests a primary contribution of the Au(111) lattice, as the difference to the initial condition $\phi = 30°$ is rather low. For the coverage of 0.25, ϕ has noticeable smaller values as in the former case, which corresponds to neighboring NO_2 groups being able to come closer to each other. In the structure with highest coverage of $1/3$, ϕ takes very different values for all molecules, indicating that the very close-aligned molecules now primarily interact with each other, degrading the influence of the lattice bond.
Evaluating the sulfur-surface distance d_{S-Au} reveals mainly three regimes primarily depending on the surface coverage. The bond distance is smallest for the layers with highest coverage $1/9$, having values of 2.00 ± 0.02 Å. For the $1/4$ coverage, values around 2.05 Å are observed, while the lowest density structure with $1/3$ coverage exhibits distances of 2.13 ± 0.01 Å . For the individual coverages, the bond distances seem to correlate with the tilting angles θ_{AuSP} and θ. Our interpretation for these combined observations is that the molecules tend to lie flat on the surface when allowed to do so by the imposed coverage, and that for all phenyl rings, an optimal distance to the surface is established, maximizing the vdW attraction. This competes with the bonding distance, which is elongated as the overall vdW interaction with lower coverage is able to reduce the total energy ultimately.

To assess the energetics, we calculated the adsorption energies for the different geometries via the formula

$$\Delta E_{ads} = E^{UC}_{Au+4NTP} + \frac{1}{2}E_{H_2} - \left(E_{4NTP+H} + E^{UC}_{Au}\right). \tag{5.19}$$

Here, $E^{UC}_{Au+4NTP}$ is the total energy of the gold unit cell with molecules adsorbed, E_{H_2} is the energy of the H_2 molecule, E_{4NTP+H} is the energy of the 4-NTP (or 4-NBTP/4-NPTP) molecule with hydrogen bonded to the sulfur atom, and E^{UC}_{Au} is the total energy in the gold slab unit cell without any other compounds. This formula thus describes the energy difference between the total structure and its fragments. Any positive value indicates energetically non-favorable situations. Note that all individual calculations had equal settings for basis set, XC functional and vdW method.
Results are shown in Figure 5.4 for 4-NTP, 4-NBPT and 4-NPTP, with and without TS/rsSCS-MBD/MBD-NL vdW treatment. One can directly observe an overall trend of the adsorption energy ΔE_{ads} to decrease with the number of phenyl

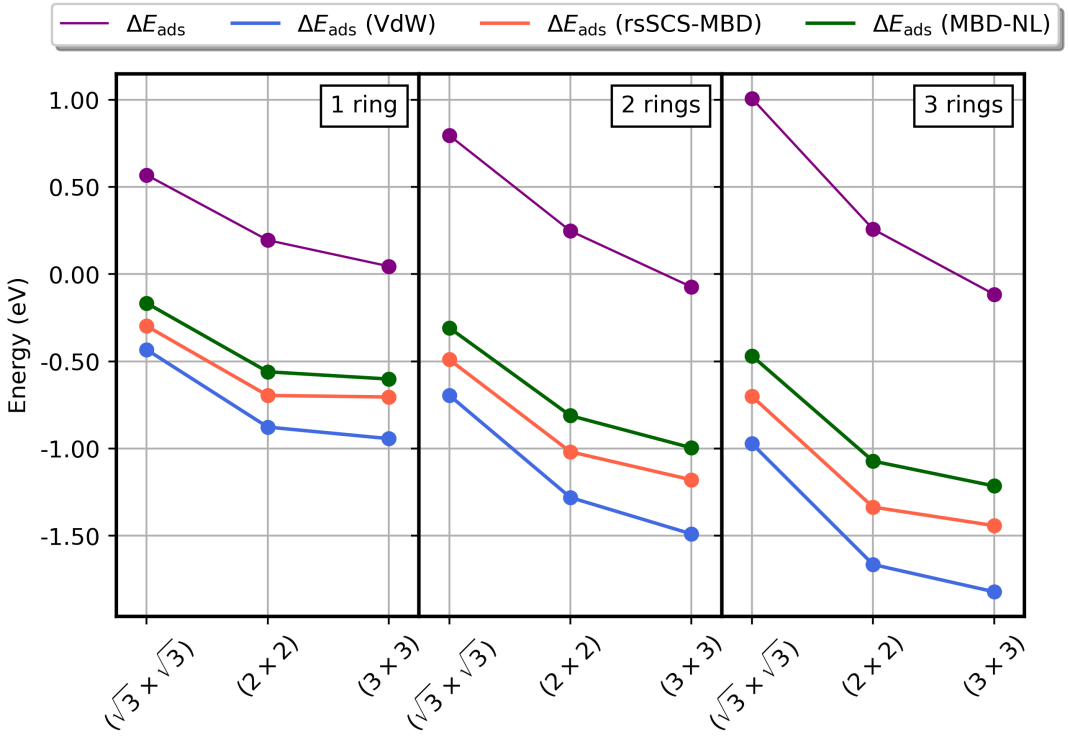

FIGURE 5.4: Adsorption energies calculated from the results of our calculations, as defined by Eq. 5.19. All results for PBE and for different vdW treatments. Generally, lower adsorption energies indicate energetically more favorable structures.

rings, with significantly lower values for calculations with vdW description. Actually, when disregarding the vdW interaction, all molecules have positive or nearly positive adsorption energy and would thus not bond to the surface.

Another clear observation is the reduction of adsorption energy with respect to lower coverage. All molecules are most strongly bonded in the (3×3) system. With regard to the vdW method, only essentially constant shifts are visible. The TS method yields the most negative adsorption energies and thus the strongest adsorption, while the MBD-NL method yields the comparably weakest (although always negative and thus bonding). The TS vdW and MBD-NL adsorption energies differ by approx. 0.3 eV for one phenyl ring, by approx. 0.5 eV for two rings, and by approx. 0.6 eV for three rings, whereas the rsSCS-MBD method's values lie in between. Generally, the reason for the observations is likely the repulsion between molecules in the dense structures.

Overall, one can suspect a linear dependence between the adsorption energy decrease and the number of rings in the molecules. For the case of lowest coverage, it is clear that the energy drops are large, as the molecules tilt down onto the surface, ultimately benefiting from the interaction between phenyl rings and the Au surface. We conducted a Mulliken analysis [269] of the relaxed structures and consider in the following only the situations with explicit TS vdW interaction. Using the geometrical data and the localized Mulliken charges, we computed the dipole moments in

TABLE 5.2: Absolute dipole moments generated from Mulliken charges for 4-NTP, 4-NBPT, 4-NTPT where $\boldsymbol{\mu}_{\text{tot}}^{\text{Mulliken}}$ incorporates the whole respective molecule and $\boldsymbol{\mu}_{\text{NO}_2}^{\text{Mulliken}}$ only incorporates the NO_2 group located at the C(4) atom of the outmost phenyl ring. $q_{\text{tot}}^{\text{Mulliken}}$ and $q_{\text{NO}_2}^{\text{Mulliken}}$ denote the total Mulliken charge of the whole 4-NTP/4-NBPT/4-NTPT molecule and only the NO_2 group, respectively. Results for simulations including TS vdW interactions.

Geometry	Rings	$\lvert\boldsymbol{\mu}_{\text{tot}}^{\text{Mulliken}}\rvert$ (eÅ)	$\lvert\boldsymbol{\mu}_{\text{NO}_2}^{\text{Mulliken}}\rvert$ (eÅ)	$q_{\text{tot}}^{\text{Mulliken}}$ (e)	$q_{\text{NO}_2}^{\text{Mulliken}}$ (e)
$(\sqrt{3}\times\sqrt{3})$	1	0.421	0.964	-0.133	-0.100
	2	0.354	1.599	-0.1325	-0.111
	3	0.364	1.993	-0.138	-0.106
(2×2)	1	0.417	1.707	-0.082	-0.159
	2	0.370	2.383	-0.073	-0.158
	3	0.355	3.054	-0.071	-0.157
(3×3)	1	0.372	2.028	-0.026	-0.193
	2	0.269	3.093	0.059	-0.209
	3	0.189	3.906	0.034	-0.202

a point charge model. The results, i.e., the Mulliken charges for the total structure and the NO_2 group together with the respective dipole moments, are shown in Table 5.2. In most cases, the total Mulliken charge on the molecules is negative, indicating charge transfer from the surface onto them. One can clearly see a connection between transferred charge and surface coverage, being nearly independent on the number of phenyl rings in the $(\sqrt{3}\times\sqrt{3})$ geometry. An explanation for this is that the densely ordered standing molecules in this case form a static dipole layer which drags charge out of the surface. The strength of the dipole layer field declines with lower coverage, as fewer molecules per unit surface area exist. We note that most negative charge is located on the S atom, followed by the O atoms in the NO_2 group, which is not surprising due to the electronegativity of oxygen. The phenyl rings as well as the nitrogen atoms are positively charged. When analyzing the Mulliken charges of the NO_2 group, one finds a clear dependency of the surface coverage in the sense that more negative charge gets accumulated with increased unit cell size. Also, the NO_2 dipole moment increases by approximately a factor of 2 from coverage 1/3 to coverage 1/9. Altogether, this points towards a vivid interaction of the NO_2 group with the metallic gold surface, resulting in a build-up of dipolar polarization which scales with the tilting of the molecules towards the surface.

Overall, different effects are important for the respective adsorption energy and geometry: we found that dispersive interactions not only play a role between neighboring molecules, but also between molecules and the metallic surface, strongly increasing with chain length; also, the electrostatic interaction between the molecules is significant and increases with less dense coverage, as electrostatic dipoles are built up when the tilt angle increases. The general tendency of the molecules to lie flat on the surface is thus governed by vdW interaction, electrostatic interaction and also by

the geometry of the single Au-S bond, but is effectively limited by steric repulsion in the cases where higher packing is prevalent.

5.3.4 Vibrational Characteristics

We conducted vibrational analysis for the slab geometries and additionally for two cluster models, one with 7 Au atoms, and one with 19 Au atoms, as shown in Figure 5.5 (A) (1,2). The cluster geometries were additionally employed to further quan-

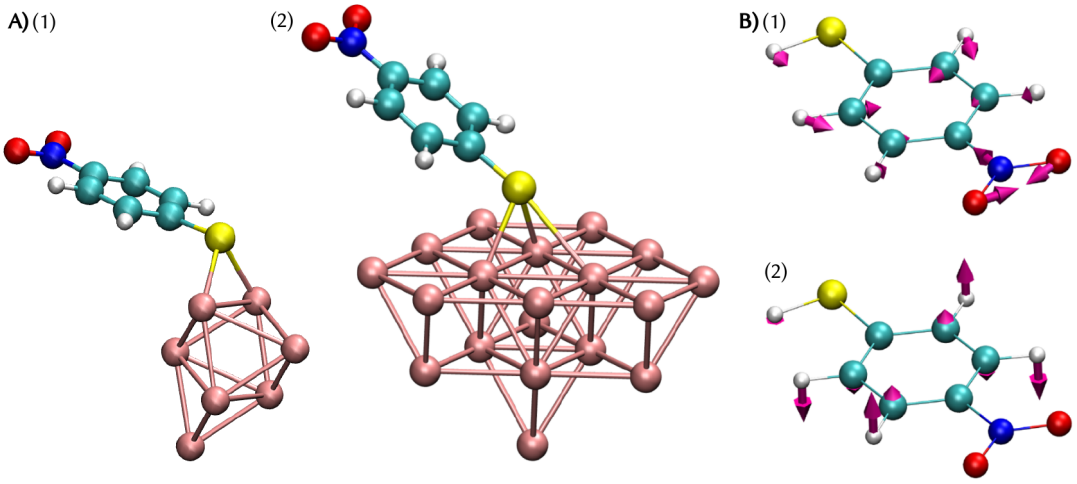

FIGURE 5.5: Left (A): 4-NTP on Au_7 cluster (1) and on Au_{19} cluster (2). Right (B): displacement vectors for the in-plane NO_2 scissoring mode at 840 cm^{-1} (exp. 853 cm^{-1}) (1) and for the out-of-plane C–H wagging mode at 403 cm^{-1} (exp. 407 cm^{-1}) (2).

tify the vibrational characteristics with respect to the adsorption site, going from a small cluster to a cluster more resembling a surface, and ultimately to the slab. The vibrational frequencies for the free molecule, the two clusters and the different surface unit cells are presented in Table 5.3. We first note that the eigenmodes are quite similar between the cluster geometries. Small differences to the free molecule are seen for the ring deformation and for the C=C modes, located at 739 cm^{-1} and 1579 cm^{-1}, respectively (values for the free molecule).

Comparing the different slab geometries, one observes significant differences with respect to coverage. The out-of-plane C–H wagging mode is especially sensitive and experiences a considerable shift when going to higher coverage; between the $(\sqrt{3} \times \sqrt{3})$ and the (2×2) cells for example, a difference of around 50 cm^{-1} is observed, i.e., above 10%. Other significant differences are found for the in-plane NO_2 stretching mode, which is downshifted for lower coverage. For example, the downshift is about 46 cm^{-1} from $(\sqrt{3} \times \sqrt{3})$ to (3×3). The C–H wagging and the NO_2 scissoring (which we discuss later) mode's displacement vectors are exemplary depicted in Fig. 5.5 (B) (1,2). While one can expect that the out-of-plane C–H wagging mode is mainly affected by intermolecular interactions, our former analysis (see Table 5.2) indicates that the in-plane NO_2 mode is sensitive to surface-molecule charge transfer, as the NO_2 group tends to accumulate negative charge with decreased cov-

TABLE 5.3: Selected vibrational modes from DFT calculations within the harmonic approximation for different 4-NTP setups, all relaxed at same level of theory (PBE+vdW).

Vibrational frequencies of various modes in different adsorption models (cm^{-1})						
mode	free	Au_7	Au_{19}	$\sqrt{3} \times \sqrt{3}$	2×2	3×3
C–H wagging	403.5	400.1	401.1	462.8	411.3	403.4
NO_2 rocking	516.5	516.0	516.4	517.8	527.2	516.2
ring deformation	719.9	712.8	711.1	714.8	716.2	704.4
out-of-plane bending	738.4	740.0	735.4	742.1	735.1	734.0
NO_2 scissoring	840.0	838.9	838.1	843.3	842.4	832.0
C–S	–	1058.1	1052.0	1063.6	1060.0	1039.0
C–C	1084.8	1081.8	1082.6	1084.7	1095.5	1076.9
NO_2 stretch	1302.3	1301.2	1296.1	1313.3	1305.6	1267.2
C=C	1579.2	1568.1	1564.5	1573.5	1571.1	1551.0

erage. This in turn affects the vibrational frequencies, as the associated dipolar field build-up is incorporated in the self-consistent electronic potential that goes into the nuclear harmonic potential. The downshift of the NO_2 stretching mode thus seems like a valuable indicator of low coverage.

These observations helped us to interpret the experimental measurements: Figure 5.6 shows Raman spectra for 4-NTP solution in chloroform (top), adsorbed on a Au(111) single crystal in a 5 mM solution, i.e., with high concentration (middle), and in a 1 mM solution, i.e., low concentration (bottom). The three most prominent peaks at 1101, 1341 and 1579 cm^{-1} correspond to the phenyl ring C–C stretching mode, the NO_2 stretching mode, and the pheyl ring C=C stretching modes, respectively. These modes' theoretical values are found in this order in Table 5.3 and agreement within a few percent is established in general.

The C–S stretching mode at around 1080 cm^{-1}, as marked in the plot, is significantly amplified for the molecules adsorbed on the Au(111) surface, which can be explained by the increased polarizability of the C–S bond, as electrons are transferred from the gold surface onto the sulfur atom [270], indicating the bonding of 4-NTP to the gold surface. The most interesting features are visible in the range from 400 to 900 cm^{-1}: the modes at 528, 721 and 855 cm^{-1} are in-plane vibrations; the last one is also depicted in Figure 5.5 (B,2), as computed by DFT. In the case of 5 mM solution, a peak is found at 465 cm^{-1}, which is absent in the case with lower coverage. Both cases exhibit a mode at 407 cm^{-1}. Comparing to our theoretical results, this can be interpreted as follows: since the C–H wagging mode is upshifted from around 407 cm^{-1} in the (3×3) case to 465 cm^{-1} in the $(\sqrt{3} \times \sqrt{3})$ case, the observation of both these peaks in the experimental spectrum for 5 mM hints to the presence of both standing and tilted molecules, while the missing 465 cm^{-1} peak in the 1 mM spectrum indicates that no standing molecules are present in this situation. Additionally, we do not observe a significant downshifting of the NO_2 stretch mode in the experimental spectra, which was associated with the lowest coverage

in the simulations. This leads us to the conclusion that the very low coverage (3×3) situation is not present in the experiment, but rather that an intermediate or mixed coverage between $(\sqrt{3} \times \sqrt{3})$ and (2×2) is present, depending on the concentration. In former STM experiments [271], the presence of two domains of 4-NTP on Au(111) (one ordered, and one disordered) was also observed, underlining our observations.

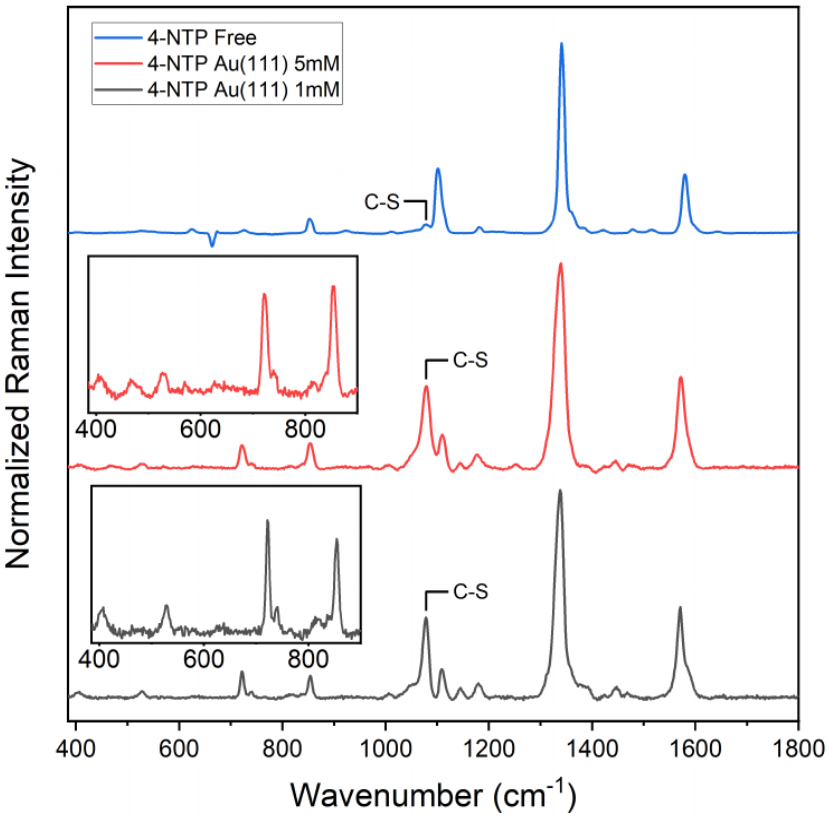

FIGURE 5.6: Normalized experimental Raman spectra. Top: saturated 4-NTP solution in chloroform. Middle: 4-NTP in 5 mM solution on Au(111). Bottom: 4-NTP in 1 mM solution on Au(111).

In our study, polarization-dependent vibrational sum - frequency spectroscopy (p-vSFS) experiments were conducted in order to obtain additional data to characterize the orientation of 4-NTP on the Au(111) substrate. We provided additional data from DFT calculations in order to support the experimental data, as we will elucidate now. In the p-vSFS experiment, the NO_2 stretch mode at 1339 cm^{-1} is specifically probed with two differently polarized laser pulses (ssp and ppp). By a fitting procedure described in the publication (cf. Page 203), the p-vSFS line strengths $A_{ssp/ppp}$ and line widths $\Gamma_{ssp/ppp}$ are determined, from which the ratio of the second-order nonlinear susceptibilities can be reconstructed:

$$\left(\frac{\chi^{(2)}_{ssp}}{\chi^{(2)}_{ppp}}\right)^2 = \left(\frac{|A_{ssp}/i\Gamma_{ssp}|}{|A_{ppp}/i\Gamma_{ppp}|}\right)^2, \tag{5.20}$$

which is specific for a certain molecular tilt angle [272]. To determine this specific angle, a theoretical model for the given ratio was given by Wang et al. [272] as

$$\left(\frac{\chi^{(2)}_{ssp}}{\chi^{(2)}_{ppp}}\right)^2 = \left(\frac{|\mathcal{L}_{yyz}\sin\left(\Omega^{\mathrm{IR}}\right)\chi^{(2)}_{yyz}|}{|\sum_{ijk}\mathcal{L}_{ijk}O_{ijk}\chi^{(2)}_{ijk}|}\right)^2, \tag{5.21}$$

where $\mathcal{L}_{ijk} = L^{\mathrm{SF}}_{ii}L^{\mathrm{VIS}}_{jj}L^{\mathrm{IR}}_{kk}$ is determined by the Fresnel factors L_{ii} (with i denoting a direction in the laboratory coordinate system), Ω being the angle of the incident laser field (SF/VIS/IR), $O_{ijk} = M_i(\Omega^{\mathrm{SF}})M_j(\Omega^{\mathrm{VIS}})M_k(\Omega^{\mathrm{IR}})$ with $M_i(\Omega) = \cos(\Omega)\delta_{ix} + \sin(\Omega)\delta_{iz}$. Here, the susceptibilities $\chi^{(2)}_{ijk}$ are functions of the tilt angle θ (where the C_{2v} symmetry group of the NO_2 group is used):

$$\begin{aligned}\chi^{(2)}_{xxz} = \chi^{(2)}_{yyz} &= \frac{1}{4}N_s\left(\beta_{aac}+\beta_{bb}+2\beta_{ccc}\right)\langle\cos\theta\rangle \\ &\quad+\frac{1}{4}N_s\left(\beta_{aac}+\beta_{bbc}-2\beta_{ccc}\right)\langle\cos^3\theta\rangle, \end{aligned}\tag{5.22}$$

$$\chi^{(2)}_{xzx} = \chi^{(2)}_{zxx} = -\frac{1}{4}N_s\left(\beta_{aac}+\beta_{bbc}-2\beta_{ccc}\right)\left(\langle\cos\theta\rangle-\langle\cos^3\theta\rangle\right), \tag{5.23}$$

$$\begin{aligned}\chi^{(2)}_{zzz} &= \frac{1}{2}N_s\left(\beta_{aac}+\beta_{bbc}\right)\langle\cos\theta\rangle \\ &\quad-\frac{1}{2}N_s\left(\beta_{aac}+\beta_{bbc}-2\beta_{ccc}\right)\langle\cos^3\theta\rangle, \end{aligned}\tag{5.24}$$

with the hyperpolarizabilities β_{ijk}. In this notation a, b, c correspond to the x', y', z' axes of the molecular coordinate system, where z' is parallel to the axis of the C-N bond in the molecule. At this point, the theoretical results come into play, providing the first derivatives of the polarizability tensor with respect to this mode's normal coordinate, $\bar{\alpha}_{i'j'} := \partial\alpha_{i'j'}/\partial\mathbf{x}_L$ (these quantities were obtained via DFPT in combination with the finite-difference procedure, cf. Eq. 5.18), which let us compute the hyperpolarizabilities needed to compute the second-order susceptibilities via

$$\beta_{i'j'k'} = -\frac{1}{2\epsilon_0\omega_L}\frac{\partial\alpha_{i'j'}}{\partial\mathbf{x}_L}\frac{\partial\mu_{k'}}{\partial\mathbf{x}_L}, \tag{5.25}$$

where ω_L is this mode's frequency and where the derivatives of the dipole moment, $\partial\mu_{k'}/\partial\mathbf{x}_L$, and the number density of the interface's moiety N_s don't need to be determined, as they cancel out in the ratio in Eq. 5.21. The remaining parameters like the Fresnel factors, incident angles or indices of refraction were determined from experiment or external sources.

We computed the Raman tensor derivatives for the free molecule and for the molecule on the Au_{19} cluster; they are given in Table 5.4. With these values, a continuous calibration curve of the intensity ratio was computed, as defined in Eq. 5.21. In Figure 5.7, the curve is shown together with the experimentally determined ratio, which is given by 0.157. The theoretical and experimental data coincide at angles of 53° and 51° for the Raman tensor derivatives of the free molecule and cluster, respectively.

TABLE 5.4: Calculated molecular Raman tensor components of the free molecule and the molecule adsorbed on a Au_{19} cluster for the NO_2 symmetric stretching mode.

	$\bar{\alpha}_{aa}$ ($Å^2u^{-0.5}$)	$\bar{\alpha}_{bb}$ ($Å^2u^{-0.5}$)	$\bar{\alpha}_{cc}$ ($Å^2u^{-0.5}$)
free molecule	0.56	-0.04	7.59
on Au_{19} cluster	1.70	1.10	8.59

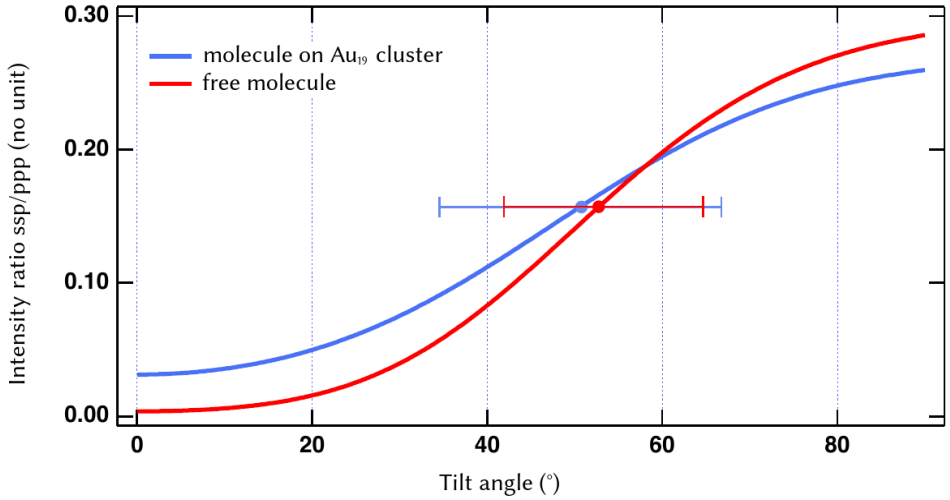

FIGURE 5.7: The continuous curves show the theoretical models for the ssp/ppp line strength ratios for the two different Raman tensor components. The dots denote the experimentally determined values with error bars that symbolize the 95% confidence interval based on the standard deviation of the fitting parameters.

5.3.5 Discussion

Sophisticated theoretical methods together with modern experimental approaches were employed to gain additional understanding of the adsorption of thiophenols on Au(111) surfaces. It became clear that the adsorption geometry of 4-NTP and its polyphenyl versions is steered by covalent contributions, dispersive and electrostatic interactions. The molecules are tilted towards the surface, when allowed to: steric repulsion between adjacent molecules limits the tilting and yields standing geometries when high coverage is imposed. The theory-supported vSFS analysis predicts a tilt angle of around 50°. This angle is very close to 53° which is found in the (2×2) theory structure, i.e., for a coverage of 1/4, in our simulations with different coverages. These simulations together with the Raman spectroscopy analysis let us draw the conclusion that at higher coverages, several tilting regimes can be prevalent and that the dependence of the NO_2 stretching mode's vibrational frequency on the coverage may have predictive power in this sense. As we also did not observe a vibrational shift that was theoretically observed for the low coverage (3×3) structure, it can be assumed that higher coverages existed in the experiments. These findings make it rather unlikely that 4-NTP adsorbs in the $(\sqrt{3} \times \sqrt{3})$ structure on Au(111), as often assumed.

Chapter 6

Analysis of Real-Time TDDFT Implementation and Methods

6.1 Overview and Motivation

Since our real-time TDDFT implementation embodies a substantial amount of functionality, we are able to compare different methods which are presented or suggested in the literature (and thus often incorporated in different software packages and numerical methods) implemented in the same software framework – the FHI-aims code package – with its specific technical implications. We thus aim to give an overview of the core functionalities of the time-propagation in this chapter for future applications or extensions, and in order to point out possible characteristics. In addition, we present an analysis of the numerical efficiency of our implementation.

6.2 Evaluation of Propagation Schemes

In the following section, we will define and analyze the stability of numerical time-propagation in this context. For this, we discuss the self-consistency order in the semi-implicit predictor-corrector scheme as well as the extrapolation order for the extrapolated time-dependent Hamiltonian. Thereafter, we analyze specific time-propagation schemes and derive recommendations for specific tasks.

6.2.1 Measures of Numerical Stability

As we cover the aspect of numerical stability in this section, useful measures have to be defined. Like mentioned before, any suitable propagator is formally unitary (i.e., it conserves charge), but this must also hold for its numerical representation. For example, a formally unitary exponential-type propagator using a truncated Taylor series can loose its unitarity, depending on the number of terms included in the expansion [130]. However, computing a measure for unitarity deviation, e.g., via

$$\delta_U(t) = ||\mathbf{U}^\dagger(t)\mathbf{S}\mathbf{U}(t) - \mathbf{S}|| \tag{6.1}$$

(where $\mathbf{S}$ is the overlap matrix and $\mathbf{U}(t)$ the propagator matrix for this step) with some given norm introduces a numerical overhead that one wants to avoid in practice. In addition, it is not clear a priori whether unitarity is a strong indicator of numerical stability in general, as it mostly measures how accurate the matrix exponential is computed by some algorithm for a given time step. Since any RT-TDDFT calculation should always be checked for numerical/physical consistency along the time-propagation, a natural choice for a stability measure is a physical observable which is computed anyway. As any closed system must retain its energy conservation, we chose this as a core measure for any application. We compute time-dependent energy differences relative to some initial point t_0 as

$$\Delta E_{\text{tot}}(t) := |E_{\text{tot}}(t) - E_{\text{tot}}(t_0)|. \tag{6.2}$$

However, it should be noted that other observables like, e.g., the dipole moment can be sensitive to numerical approximations in their own way [134]. For example, a simulation with a high degree of energy conservation can still yield flawed electronic dipolar response, resulting in spectra that are not converged yet, as measured by the time step. One thus has to keep in mind that energy conservation is a sensible, but not complete measure of a correct simulation.

6.2.2 Extrapolation and Predictor-Corrector Order

For the first step and before discussing some of the (semi-implicit) propagation schemes, we want to shed some light onto the specific characteristics of the predictor-corrector (PC) scheme and the extrapolation technique presented before. Since the PC scheme requires at least one update of density, potentials and the Hamiltonian, each being a potentially expensive operation, it is of great importance to achieve high efficiency in this context.

For our example calculations, we applied a field kick with Gaussian shape (FWHM = 0.8 a.u = 0.02 fs) and two different electric field amplitudes, one weak ($\mathrm{E}_0 = 5.14 \cdot 10^8$ V/m, $I = 3.51 \cdot 10^{10}$ W/cm^2) and one strong ($\mathrm{E}_0 = 5.14 \cdot 10^{10}$ V/m, $I = 3.51 \cdot 10^{14}$ W/cm^2), to benzene and recorded the deviation of the total energy from the value shortly after the pulse was applied (resulting in an increased electronic energy). The pulse shape is sufficiently small to excite the whole spectrum which we purposely do in order to probe the schemes also with highly oscillatory core states. We used the PBE XC functional [26] together with the 'tight' basis set for these calculations. The propagator used here was the exponential midpoint (EM) scheme, matrix exponentials were calculated by diagonalization. The total simulation time was set to 3000 a.u. = 72.6 fs.

Figure 6.1 shows the results and we will first discuss characteristics for the weak excitation. Regarding the extrapolation order, the energy is conserved up to 10^{-4} eV for 0th (no extrapolation) and 2nd order for all time steps, but strongly diverges with 4th order extrapolation for time steps above 0.6 a.u. = 0.014 fs. Comparing 0th

and 2nd order extrapolation, one can see that the latter yields 3-fold to 10-fold (highest/lowest time step) accuracy increase in the energy conservation by virtually no additional cost. However, 4th order extrapolation results in unstable dynamics for larger steps. Regarding the number of corrector steps, going from 1 to 3 steps consistently yields around 30-fold reduction of the error, while 2 corrector steps show somehow inconsistent behavior. The small differences to 3 steps below a time step of 1.0 a.u. = 0.0242 fs may be explained by numerical precision or small fluctuations. Larger time steps offer a clearer picture in this sense. While it is clear here that additional corrector steps yield significantly higher accuracy, one must think carefully about this approach, as one relatively expensive real-space operation set (density, Hamiltonian, etc.) is added in each propagation step with each additional corrector iteration.

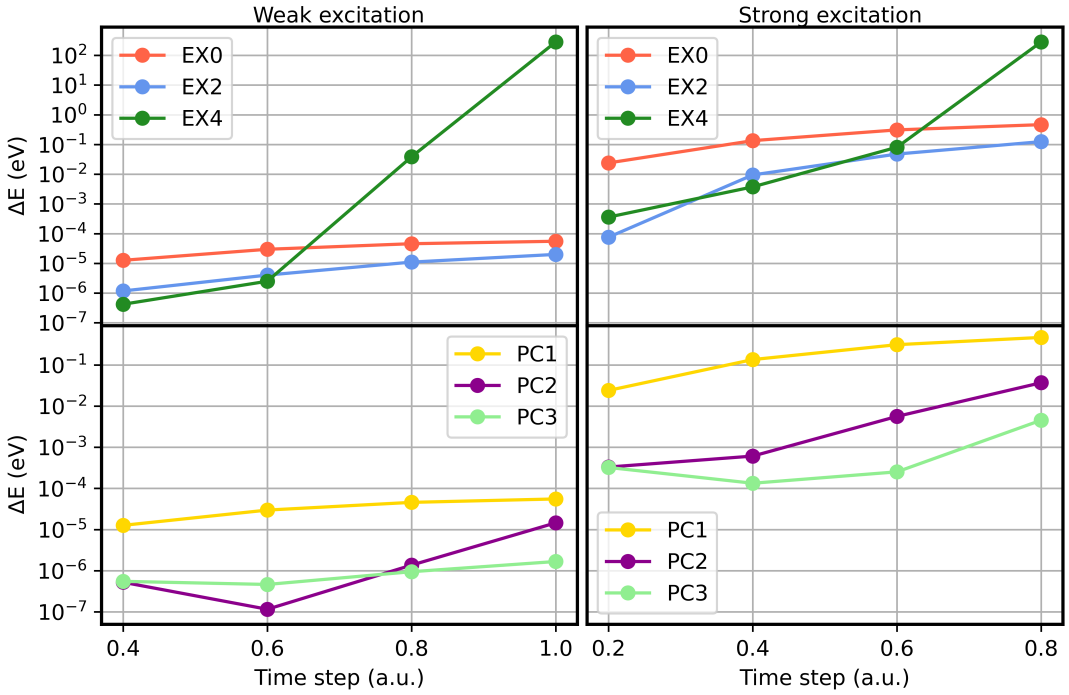

FIGURE 6.1: Characteristics of energy conservation $\Delta E = |E_{\text{tot}}(t_{\text{max}}) - E_{\text{tot}}(t_0)|$ in dependence of time step, extrapolation order (EX) and predictor-corrector order (PC) for weak field excitation (left column, $I = 3.51 \cdot 10^{10}$ W/cm^2) and strong field excitation (right column, $I = 3.51 \cdot 10^{14}$ W/cm^2) for benzene. Simulations were carried out with the EM propagator using exact diagonalization for the matrix exponential. The first row was conducted with 1 predictor-corrector step, the 2nd row with 2nd order extrapolation.

For the strong excitation, the overall characteristic is very similar to the weak field case, although the absolute errors are unsurprisingly significantly higher, as the density fluctuations are much larger. Note here that the relevant x-axis covers smaller values for the time steps. While 4-fold extrapolation is again resulting in instabilities, 2-fold extrapolation can reduce the error from a factor of 3.7 up to a factor of 317.5 (highest/lowest time step).

As noted in the introduction, the quality of resulting spectral observables (like the DSF) depends explicitly on the time step due to the nature of the involved Fourier transforms. The most obvious connection is between the time step and the maximum resolvable frequency of the system with $\Delta t \sim 1/f_{\max}$, being of special importance when attempting to resolve deep core states.
Figure 6.2 shows DSF results obtained from simulations with the weak excitation and for different time steps (0.6 a.u. = 0.0140 fs, 0.8 a.u. = 0.0190 fs, 1.0 a.u. = 0.0242 fs), with a reference spectrum that was generated from a Δt = 0.4 a.u. = 0.0096 fs simulation and that can be regarded as converged. Furthermore, these simulations were conducted with order 2 extrapolation and 1 PC step with energy being conserved below deviations of 0.0001 eV. The upmost row plot for Δt = 0.6 a.u. =

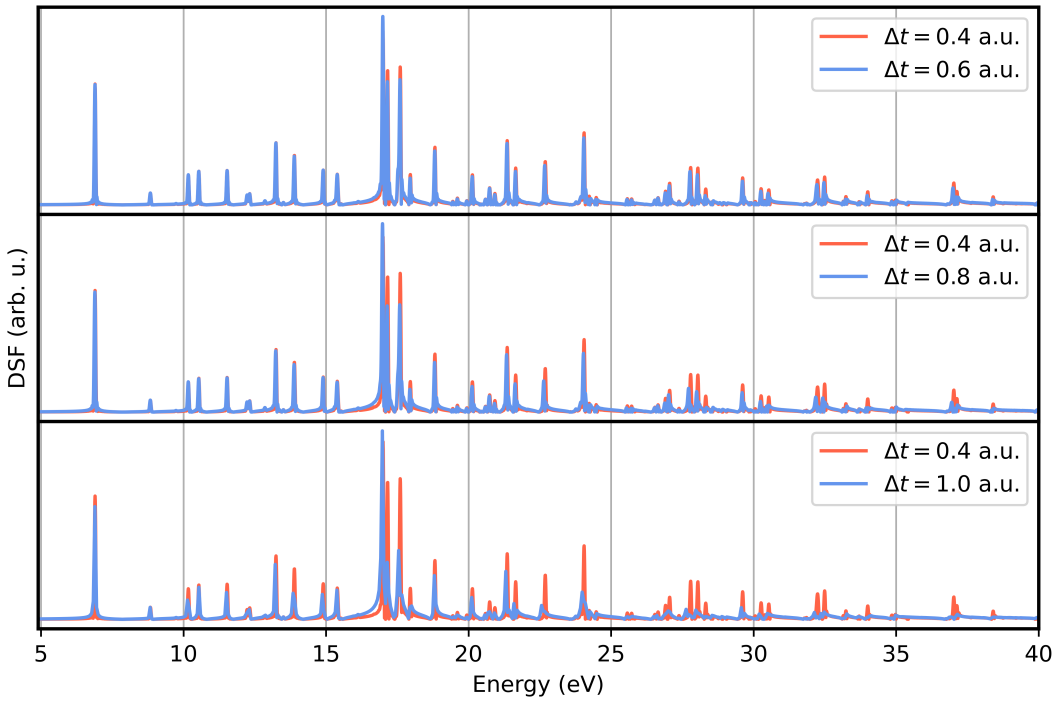

FIGURE 6.2: DSF spectra of benzene for the weak excitation of I= $3.51 \cdot 10^{10}$ W/cm^2 for different time steps. The reference spectrum is generated via a Δt =0.4 a.u. = 0.0096 fs simulation and can be regarded as converged for the given spectral range.

0.0014 fs shows very little deviation, and if so, only for the peak heights/oscillator strengths of peaks above 16 eV. Further increasing the step size by 0.2 a.u. = 0.0048 fs (mid row plot) yields more deviations and also peak shifts in the upper spectral range, while another increase by 0.4 a.u. = 0.0096 fs results in largely deviating spectra. In this case, while excitations below 15 eV are still correctly located, the oscillator strengths are already affected, while the rest of the spectrum shows strong differences with excitations above 25 eV being hardly resolved anymore. Although the energy is conserved very good in these simulations, one must pay attention to the spectra - on the other hand, if one is only interested in locations of low valence excitations, rather large time steps may be safely applied.

6.2.3 Evaluation of Propagation Schemes

Having assessed the characteristics of the predictor-corrector scheme, we now turn to the specific propagators. While we already employ a set of good and established propagators, we think that among these, it is still worth to look for an optimal choice, as also small relative advantages can be important for economic considerations, especially when doing large-scale simulations.
Despite having implemented several more schemes than presented here, we will only cover those which we found to be of most practical relevance and prototypical character, namely the EM, CN and CFM4 schemes (cf. Section 3.5). It should be noted that all of these schemes are very competitive, offering excellent cost to accuracy ratios [120, 121, 123]. We first analyze the respective stability regions for the EM, CN(n) and CFM4 propagators with respect to the time step and for two different systems. The first system is again benzene, while we chose Au_2 as the second system in order to probe dynamics for a Hamiltonian with very deep eigenvalues (due to the gold core states). This is an important case, possibly affecting the numerical stability and/or accuracy. Both systems were probed with a weak ($E_0 = 5.14 \cdot 10^8$ V/m, $I = 3.51 \cdot 10^{10}$ W/cm^2) and a strong ($E_0 = 5.14 \cdot 10^{10}$ V/m, $I = 5.14 \cdot 10^{14}$ W/cm^2) broadband excitation for a total simulation time of 3000 a.u. $= 72.6$ fs, similarly to the former chapter. We used diagonalization for the matrix exponentials, one corrector step and 2nd order Lagrangian extrapolation, as for the solver settings.
The combined results are shown in Figure 6.3. Overall, very small differences between the individual propagators are seen within their respective regimes. Also the lowest order Crank-Nicolson scheme shows good results with the gold system and performs equally to the other methods. The lower columns nevertheless do not show any results for the CFM4 propagator which has to be proven as unstable in this case (which we checked with different exponential methods). Shortly after the onset in both regimes, the dynamics became unstable with very large error blow-ups. We suspect two reasons for this: first, the CFM4 scheme formally requires the evaluation of the Hamiltonian at two different time steps; we did not self-consistently obtain these Hamiltonians but rather used simple linear interpolation within the predictor-corrector scheme, which in turn may introduce instabilities due to the rapidly oscillating dynamics. Second, the CFM4 propagator (similarly to, e.g., the ETRS scheme [87] which showed the same problem) is built as a product of two matrix exponentials – this may amplify errors if the numerical approximation of the matrix exponentials become sensitive to errors introduced by the dynamics, as argued before.
It should further be noted that the specific dynamics are determined by many different factors like the physical system, the type of the external perturbation and even the type of the exchange-correlation functional, as shown by Zhu et al. [134].
In order to evaluate the numerical cost of the presented schemes, we set up linear chains of carbon atoms for variable length N_c and performed simulations for a short time on a single core (AMD Ryzen 9 5900X, max. 4.8 GHz). While this does not take

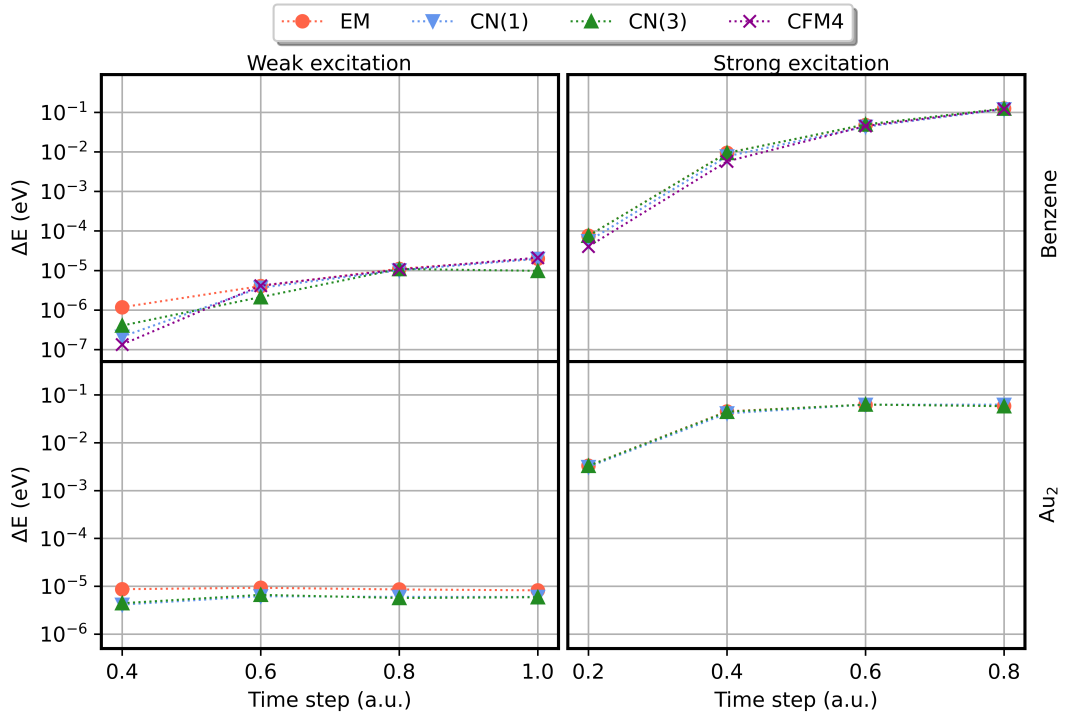

FIGURE 6.3: Characteristics of energy conservation $\Delta E = |E_{\text{tot}}(t_{\text{max}}) - E_{\text{tot}}(t_0)|$ in dependence of time step and propagator for weak field excitation (left column, $I = 3.51 \cdot 10^{10}$ W/cm^2) and strong field excitation (right column, $I = 3.51 \cdot 10^{14}$ W/cm^2). Exponential integrators (EM/CFM4) used exact diagonalization for the matrix exponential. All simulations were carried out with 1 corrector step and 2nd order extrapolation. The first row shows results for the benzene molecule and the second row shows results for the Au dimer.

into account any parallel functionality, it still provides a first fundamental characterization of the numerical demand of the methods. The basis set was chosen arbitrarily to the 'tight' set and we thus probed systems with 39 ($N_c = 1$) up to 390 ($N_c = 10$) basis functions in total. As the numerical effort scales formally with $\mathcal{O}(N_c^3)$ via matrix operations like multiplication, diagonalization, inversion, etc., we employed a cubic fit for the computation time T_p in dependence of the involved number of basis functions N_b,

$$T_p(N_b) = \alpha_p {N_b}^3 + c_p, \tag{6.3}$$

in order to determine the prefactors specific to a propagation scheme, α_p. Only the total computation time for *all* numerical operations of a time-propagation step (but without any real-space operations within the corrector update) was taken into account here. For the exponential propagators, the calculation of the matrix exponential is the critical operation, which again can be conducted in different ways, as noted before: diagonalization, truncated Taylor expansion and via the scaling and squaring method. We thus only probed the EM scheme for different exponential methods and the Crank-Nicolson scheme for different orders, as presented in Chapter 3.6. Figure 6.4 shows the obtained scaling characteristics in an illustrative way (i.e., without any

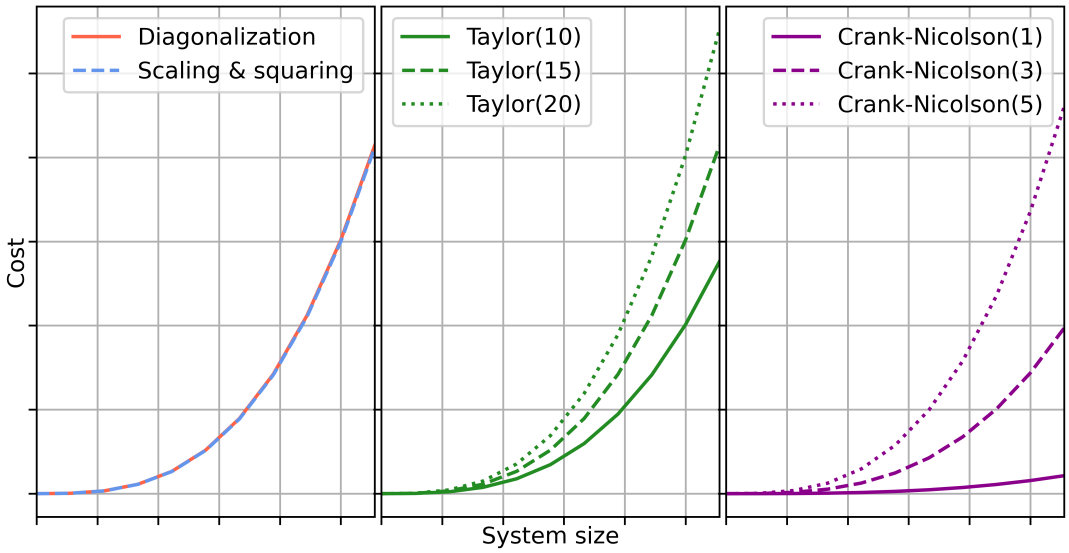

FIGURE 6.4: Cubic fit functions for the computation time corresponding to 'Cost' on the y-axis with respect to the number of basis functions, here denoted by 'System size' on the x-axis, for the different propagation techniques: the first two columns correspond to the different matrix exponential approaches and the notation Taylor(m) specifies the m-th order truncated Taylor series; the third column corresponds to the Crank-Nicolson(n) propagator of n-th order.

explicit, but fixed numerical scales). It should be noted that we observed a minimum order of 10-12 for the truncated Taylor expansion to actually work well in several systems (given a reasonable time step), which is why we present results for order 10, 15 and 20. This is likely a result of the all-electron nature in our case, as studies with localized basis functions in a pseudopotential framework reported orders of 4-6 to work well [119, 130]. Further, the scaling and squaring method (ScSq) does not have an easily predictable scaling, as the method always choses a computation that depends on the input (but is bound). In this case, the computation converged within the first few steps, only using the Padé approximant, as described in Section 3.5.5. For more demanding systems and dynamics, the effort can be expected to increase, up to approximately 1.5-fold at maximum. However, we observe a nearly equal scaling for the diagonalization and the ScSq methods. The order-15 truncated Taylor expansion also has comparable scaling. The 1st order Crank-Nicolson method has a significantly lower scaling compared to the other methods, and even the 3rd order version is very good. Table 6.1 shows the derived prefactors with the prefactor of diagonalization as reference, and the associated additional workspace requirements by each scheme, as measured by the memory required for one $N_b \times N_b$ matrix (however, this value is reduced if distributed memory is in use).

Finally, we conclude that the Crank-Nicolson scheme is probably the most efficient propagation scheme, as it always showed the smallest prefactor in our simulations and also applies in Ehrenfest dynamics. The possibility to simply include further terms in the expansion by very little additional cost is a very attractive option if the

TABLE 6.1: Prefactors from cubic fit of the numerical effort, as measured by the number of basis functions, for each method. The prefactor of the diagonalization serves as reference. The factor $\bar{\beta}$ in the ScSq method depends on the dynamics and may approximately be $\bar{\beta} \in [0.2, 1.5]$. The case † depends on whether only the Padé method or the full procedure is called and can not be predicted. The memory demand is measured in units of storage requirements of a full $N_b \times N_b$ matrix.

	Diagonalization	Scaling+Squaring	Taylor(m)	CN(n)
Prefactor	α_D	$\alpha_D \bar{\beta}$	$\alpha_D \frac{m}{15}$	$\alpha_D \left(\frac{1}{20} + \frac{n-1}{5}\right)$
Memory	0	5 (6)†	1	1

1st order expression does not suffice. The Taylor expansion may be used for simulations with small time steps and not too heavy elements involved. Outside this regime, the ScSq method may be used when non-Hermitian matrices are involved and if the Crank-Nicolson scheme cannot be used. However, the basic machinery for efficient matrix exponential computations allows for possible extensions of related schemes that could be of even higher quality.

Several tests for the *imaginary time evolution* functionality (Chapter 4.6) have indicated that the discussed propagators show a significantly different characteristic compared to the normal time-propagation case, as measured by the possible time step (i.e., the highest stepsize that will converge an imaginary time propagation correctly). We found that exponential propagators with the diagonalization method have significant problems, as the negative Kohn-Sham eigenvalues ϵ_i in the expression (cf. Section 3.5.5)

$$\exp\left(-\Delta\tau \mathbf{H}\right) = \Sigma_{\mathbf{H}} \mathrm{diag}\left(e^{-\Delta\tau\epsilon_1}, ..., e^{-\Delta\tau\epsilon_{N_b}}\right) \Sigma_{\mathbf{H}}^{\dagger} \tag{6.4}$$

quickly yield floating point overflow in the evaluated exponential functions. This applies slightly weaker for the scaling and squaring method. The truncated Taylor expansion seems to work much better for a rather low order (e.g., around 10-15, depending on the system), as higher-order terms lead to divergence faster. The Crank-Nicolson propagator appeared much more stable and interestingly worked better with higher orders. For the NaCl example in Sec. 3.5.5, the EM propagator with diagonalization could not converge above $\Delta\tau = 0.2$ a.u. $= 0.0048$ fs and equally for the scaling and squaring method. The order-20 Taylor-based computation was able to converge with $\Delta\tau = 0.4$ a.u. $= 0.0096$ fs and with order-10 to $\Delta\tau = 0.8$ a.u. $= 0.0194$ fs. The Crank-Nicolson propagator was able to converge in 1st order up to $\Delta\tau = 0.4$ a.u. $= 0.0096$ fs, in 3rd order up to $\Delta\tau = 0.6$ a.u. $= 0.0145$ fs, in 5th order up to $\Delta\tau = 0.8$ a.u. $= 0.0194$ fs and in 9th order up to $\Delta\tau = 1.0$ a.u. $= 0.0242$ fs. We therefore expect the Crank-Nicolson propagator to perform best in IT-TDDFT applications, especially since its numerical stability can be significantly improved by

considering higher orders.
We also found that in the case of IT-TDDFT, it is less important to use the semi-implicit predictor-corrector scheme, which was also noted in the literature [238]. While simple (non-self-consistent) forward propagation was rather unstable for larger stepsizes, results were significantly improved when used in combination with 2-fold linear or Lagrange extrapolation. In this sense, the results suggest that it would generally make sense to try a higher-order Crank-Nicolson propagator together with extrapolation-supported forward propagation for economic IT-TDDFT simulations.

6.3 General Scaling Characteristic

As we aimed to implement a method that is efficient and that can thus be used for large-scale simulations, we want to provide some information about the scaling with respect to system size. Practical applications for large-scale RT-TDDFT simulations are for example calculations to obtain absorption spectra, as traditional LR-TDDFT approaches have a formal $\mathcal{O}(N^6)$ scaling [146], making the method impossible to use for big systems (although some approximate methods exist that lead to better scaling, see, e.g., Refs. [147, 148, 149]). Another disadvantage is the potentially huge memory demand, as LR-TDDFT requires the evaluation of occupied-unoccupied transition pairs, making the corresponding matrices large. The $\mathcal{O}(N^3)$ scaling and the scalable memory demand of real-time TDDFT is thus attractive under above considerations.
For small systems, e.g., molecules like benzene, the RT-TDDFT computational demand is clearly dominated by the real-space operations like the electron density update or integration of matrix elements. In this regime, all RT-TDDFT related matrix algebra (MA) computations have very low performance impact relative to real-space (RS) operations. For example, in benzene with the 'tight' basis set (324 basis functions) and the CN(1) propagator, over 99.7% of the computation time per time step is consumed by RS operations, and over 99.9% when using the 'tight+aug2' basis set (372 basis functions) which has by default a much denser and more extended integration grid. However, these two numerical complexes have different scaling behavior, as MA operations usually scale as $\mathcal{O}(N^3)$ and RS operations asymptotically scale as $\mathcal{O}(N)$ due to the sparse density-matrix based functionality [42].

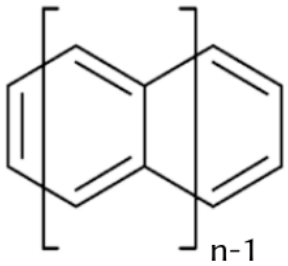

FIGURE 6.5: Oligoacene

For this reason, we constructed an artificial example that let us systematically increase its size in order to characterize the scaling: oligoacenes for a variable number of benzene rings, namely 5, 10, 20, 40 and 80. The corresponding numbers of atoms and basis functions are given in Table 6.2. This table also shows the size of full non-distributed square basis matrices with 8 Byte real data types. Such matrices are, e.g.,

TABLE 6.2: Oligoacenes in our benchmark test set. The number of benzene rings is indicated by n. The size of corresponding full-dimension real-type (non-distributed) square matrices (e.g., the overlap matrix) is also provided.

n	atoms	basis functions	square 8 Byte real matrix size (GB)
5	36	1068	0.009
10	66	1998	0.032
20	126	3858	0.119
40	246	7578	0.459
80	486	15018	1.804

the Hamiltonian matrix or the overlap matrix. In principle, each process needs to keep a copy of these matrices for the time propagation, causing very high memory demand for large structures. However, since our code uses block-cyclically distributed matrix storage, the required memory is massively reduced (approximately by a factor of $1/N_P$ with N_P being the number of parallel processes).
In Figure 6.6 we provide the computation times (for real-space operations, matrix inversions, other propagator operations and in total) in seconds per individual RT-TDDFT time step for 32, 64 and 128 parallel tasks. We used the standard predictor-

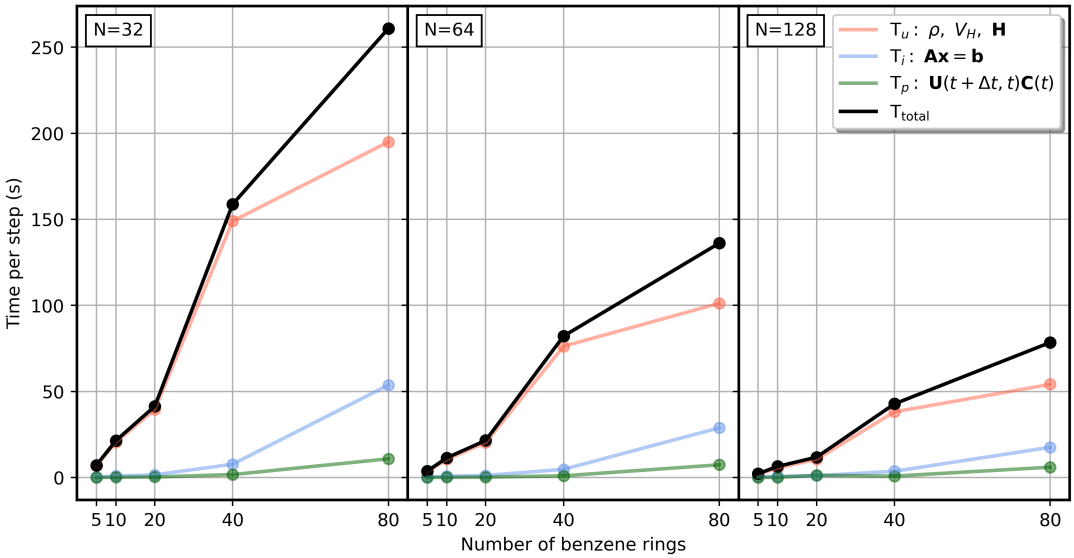

FIGURE 6.6: Absolute computation times per real-time integration step for oligoacenes with n = 5, 10, 20, 40 and 80 benzene rings and for N = 32, 64 and 128 parallel tasks (Intel Xeon E5-2670, 2.6 GHz CPU's). T_u is the time for all real-space operations, T_i is the time for the linear system solve, T_p is the time for remaining propagator operations, and T_{total} is the total computation time.

corrector scheme, resulting in 2 real-space updates per step. The propagator used here is the CN(1) scheme which is particularly well-suited for large systems due to its very low memory and computational demand, as it only requires one linear system solve and a few matrix multiplications. Different regimes are visible in the presented data: RS operations are always dominant relative to the MA operations,

ranging from a factor from over 10- to 2-fold from smaller to larger molecules, but show a significant kink from n = 40 to n = 80. The reason for this is that the code switches from the orbital-based to the density matrix-based update method of the electron density, resulting in a better scaling of these operations [42]. Based on this data, we performed a linear fit of the real-space computation time (for n $\geq$ 40) and a cubic fit for the total propagator computation time and found a crossover at approximately n = 136 which would be an oligoacene with about 800 atoms (around 25300 basis functions) - a very large system. The crossover point can likely be shifted further by employing a more efficient solver.
In Figure 6.7, the relative composition of computational effort is shown for n = 40, 80 (with 128 parallel tasks), and one can see that the propagator-related operations ($T_p + T_i$) consume less than 10% and less than 30% of the computation time, respectively, which is a good result for the size of these systems. One can also see that out-

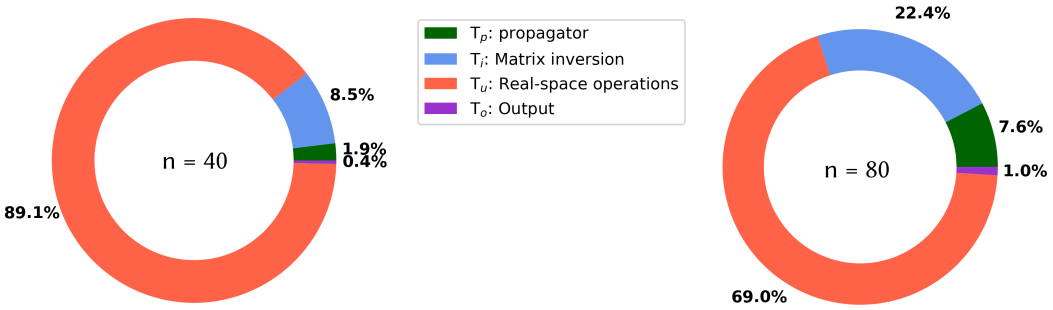

FIGURE 6.7: Relative computation timings for n = 40 and n = 80 oligoacenes for calculations with N=128 parallel processes.

put (expectation values for total energy and dipole moment in this case) produces very little cost, i.e., below 1%. Based on this data, one could compute an absorption spectrum for the n = 80 oligoacene with nearly 500 atoms in few days or less, provided a sufficient number of parallel tasks, N $\geq$ 128, is used. For this estimate, we assume a propagation time of 40 fs = 1666 a.u. and a time step of 0.3 a.u. = 0.072 fs, likely being sufficient to resolve at least the whole valence spectrum. This would correspond to a total amount of approximately 5550 real-time propagation steps. Overall, our implementation shows a solid efficiency and scalability, making it also applicable for large systems.

6.4 Discussion

We have here provided numerical results suggesting that our methods to solve the time-dependent Kohn-Sham equation are correctly implemented and show the expected and desired numerical behavior. This means that not only the methods have very robust numerical properties, but also that convergence with respect to energy conservation and spectral information, and numerical stability can be systematically reached. Moreover, we provided sufficient data such that any future user can follow

the proposed strategies to find an optimal setup for simulations to be conducted.
The corrector extrapolation technique has proven as valuable, since already two-fold extrapolation significantly increases the numerical stability. As said, this does not require any additional numerical effort, and for many applications, the additional memory demand is insignificant, especially for distributed setups.
All of the standard propagation schemes evaluated here yielded quite comparable results for the employed testcases. The largest limitation can probably be seen in the solver. The numerical demand probed via single-core calculations is in some sense likely transferable to parallel computations. However, one should keep in mind that operations like diagonalization or linear equation system solvers may scale quite differently in this sense. The results let us strongly recommend the Crank-Nicolson scheme for *all* applications, as it is numerically cheap and performs really well in general. Additional, possibly significant improvements could be achieved by implementation of customized linear solvers. However, larger systems with heavy elements may impose a challenge; considering a higher order can be helpful to tackle these situations.
Furthermore, we could show that we not only implemented a correct, but also efficient framework for RT-TDDFT applications. This means especially that our code can easily be scaled up to tackle larger and/or specific problems requiring certain considerations, e.g., large and diffuse basis sets or heavy elements. For small systems, the effort for propagation-related operations is insignificant, but naturally scales noticeably when considering larger setups. The density-matrix based electron density update functionality in FHI-aims is obviously of great value also in this context.

Chapter 7

Conclusion and Outlook

We discussed our implementation of real-time TDDFT functionality into the all-electron NAO-based FHI-aims software package and provided not only substantial proof of its correctness, but also presented applications and results for very different physical situations. We further analyzed situations where certain phenomena can be treated in a time-independent perturbative manner, establishing a broader perspective.

One of the main contributions of this thesis was the code development and we gave a very transparent methodology in Chapter 3. For this, we introduced the most important features of the FHI-aims code package and then generally outlined our strategy and methods for the code implementation. Subsequently, we discussed the various mathematical techniques that the time-propagation of the Kohn-Sham orbitals demands. Here, various strategies for different numerical and physical situations were presented.

Based on the presented framework, we studied a wide range of applications, as shown in Chapter 4:

- The first part covered the simulation of molecular absorption spectra. We showed here that our implementation is able to accurately reproduce experimental and theoretical reference data both for core and valence absorption spectra, as given by the benzene and water examples. Subsequently, we presented a detailed benchmark study for a set of 28 molecules where we successfully validated our real-time TDDFT approach by linear-response TDDFT, additionally showing that the different approaches have a very comparable basis set sensitivity. These results are important, as RT-TDDFT is attractive for large-scale absorption spectrum calculations where LR-TDDFT cannot be employed.
- In the second part, we investigated the capability of our approach for real-time simulations with periodic boundary conditions. Here, theoretical reference simulations for the dielectric function of silicon were matched very well. We also showed by the silicon carbide example that the functionality can be used for core-level excitations and discussed the impact of the NAO basis set onto

the spectra. As a first demonstration for the successful simulation of highly non-linear phenomena, we provided high-harmonic spectra for bulk silicon. This is an important application that can be simulated in the given frame with higher generality, as compared to pseudopotential approaches which may be more prone to gauge-related problems.

- The third part includes linear-response circular dichroism calculations. Simulations for the prototypical example R-methyloxirane let us conclude the correct implementation of the technique. We then presented new results for a model setup where we could show that chiral transfer in a non-covalently bonded molecular complex can be simulated with RT-TDDFT. It was shown that the achiral molecule pyrene exhibits a chiral response due to neighboring chiral R-methylbenzylamin molecules when the complex structure allows chirality. Our method was applied to a rather large system incorporating nearly 70 atoms with nearly 2000 basis functions, underlining again that it is an alternative to LR-TDDFT for larger systems.

- Within the fourth part, results from RT-TDDFT-based Ehrenfest molecular dynamics were shown for two scenarios. The first case for the $H_2C{=}N^+H_2$ molecule illustrated the correct implementation of the technique. We here confirmed the need of a rather small time step and found strong evidence that a more complete basis set is important. In the second case, we applied our method successfully in a system with periodic boundary conditions, namely the impact of a Cl atom on a graphene layer. This is an important application, as RT-TDDFT-ED is one of the few ab-initio approaches feasible to simulate ion-matter collisions. The NAO framework could offer a very economic approach here, too.

- In the fifth part we presented our implementation of the imaginary-time propagation technique. Several results both for finite and periodic systems were shown that illustrated how useful the method can be when conventional self-consistent field procedures are problematic.

This part of the thesis thus offered a multi-perspective view: we included solid evidence of the correctness of our method, provided insight into the specifics of the all-electron NAO DFT foundation, showed a multitude of the method's capabilities – including new findings –, and highlighted strategies on how specific tasks can be conducted.

In Chapter 5, we took a different perspective and presented our theory contributions within a collaborative theoretical-experimental study that incorporated a sophisticated theoretical apparatus based on perturbative treatment. We not only provided insightful physical data and interpretation, but also showed up, how time-independent approaches can yield accurate spectroscopic analysis. We contributed

knowledge to the topic of surface adsorption of nitrothiophenols by applying several methods in combination. The most important findings here are that the adsorption geometries are dictated by a complex interplay of electrostatic, van der Waals, and covalent contributions, and that the often assumed $(\sqrt{3} \times \sqrt{3})$ surface unit cell is actually not preferred, as concluded from the theoretical and experimental spectroscopic data.

In order to shed some light onto the technical properties of the RT-TDDT implementation, we analyzed the numerical methods with respect to their stability and computational cost in Chapter 6. Based on the data, we were able to identify optimal choices for typical tasks and pointed out characteristics that are important in practice. To be specific, the general Crank-Nicolson scheme together with extrapolation used within a semi-implicit predictor-corrector scheme appears as the most solid choice for any application. Further, it could be shown that our implementation is efficient and can be used for large-scale calculations. This was evaluated via artificial benchmark systems with up to 500 atoms and around 15000 basis functions.

Last, we note that a detailed manual and description of the implementation is included in this work (in the appendix), as we sincerely hope that our effort will motivate use and possibly extensions of the presented functionality.

While the presented framework already includes a sophisticated amount of functionality that can be used for linear and non-linear response simulations of both finite and periodic systems, including Ehrenfest-based molecular dynamics, there are even more applications or developments possible within the scope of the approach. As noted in the theory part in Chapter 2, several approximations are commonly used for TDDFT applications. A more general version of RT-TDDFT is offered by real-time time-dependent current DFT, which can also be used to include memory effects, going beyond the adiabatic approximation. Given a formulation for a generalized current-density exchange-correlation functional, the extension of RT-TDDFT to RT-TDCDFT is manageable. The Vignale-Kohn current-XC functional [68] has recently motivated developments in this direction [67].
In order to describe highly excited states in molecular systems, localized basis sets usually need special treatment, as discussed in Section 4.3.1. With regard to continuum - adapted basis sets, we think that one could learn from the GTO-based TDDFT community, where recent studies indicated the usefulness of this approach [200]. This also applies for complex absorbing potentials [168, 202].
A recent interesting development within the context of non-adiabatic ab-initio molecular dynamics is the so-called exact factorization technique by Gross et al. [273], which was lately implemented within a TDDFT framework [274] in a mixed quantum - classical fashion. This theory offers a more general approach as, e.g., Ehrenfest

MD or trajectory surface hopping MD, and one could think about an implementation within the given context.
Some possible and interesting further extensions of our real-time TDDFT implementation are also connected to current developments in the FHI-aims parent codebase: a relativistic quasi-four-component Dirac-equation implementation was recently introduced [101], which can in principle be extended to RT-TDDFT. Also, non-collinear spin treatment is to our knowledge at least a planned project that could have very interesting applications also in the time-dependent case.
From a technical perspective, possible developments for time-propagation schemes could lead to a more efficient framework, e.g., allowing to choose larger time steps for the propagation. Further refinement of existing numerical methods for, e.g., diagonalization or linear system solvers, could also lead to even more efficient time-propagation in general.

Appendix A

Manual

We here provide a manual that incorporates all keywords that a user may possibly employ (note that we also incorporated this content in the official FHI-aims manual [114]). There are other keywords which were introduced for debugging purposes. We do not list these here but note that they can be found in the parent package's file `runtime_choices.f90` within the `FHI-aims/src` directory.
Since there are many keywords that may or may not be employed for production calculations, we emphasize that there are testcases within the `regression_tests` folder that give an overview of the included functionality. We also provide some prototypical commented examples in Section B.

In the manual, note that some parameters have default values, while others don't. The latter are only associated to options that are not used unless a value is provided.

Further, some RT-TDDFT related settings must be accompanied by settings that are native to the FHI-aims core package. We will give a comment at the appropriate place. Since we do not provide the full FHI-aims manual [114] here, we refer the reader to it for the corresponding keywords, which are here appearing in the style `aims_keyword`.

A.1 Core Settings

Tag: `RT_TDDFT_input_units` (control.in)

Usage: `RT_TDDFT_input_units  units`

`units`: String that specifies in which unit system the input is given. If `atomic`, the remaining parameters are read in atomic units, if `spec`, the remaining parameters are read in as what we call spectroscopic (see table below).

This setting affects every physical input quantity given such that one has to pay attention to the consistent use of units. The following table depicts possible unit sets. Quite 'typical' values for time steppings are 0.1 a.u. $=$ 0.0024 fs or for electric field amplitudes 0.01 a.u. $=$ 51.42 eV/Å (in the perturbative regime).

Quantity	`atomic`	`spec`	Example
Time	$\hbar/E_h$	fs	Sim. time, steppings, pulse center/width
Frequency	$E_h/\hbar$	fs^{-1}	Ext. field frequency
Electric field	$E_h/a_0 e$	eV/Å	–

This keyword must be set by the user or the code will not run which is intended to prevent unit confusions.

Tag: `RT_TDDFT_propagation` (control.in)

Usage: `RT_TDDFT_propagation t_tot dt_prop dt_output`

Purpose: Performing a real-time TDDFT simulation.

`t_tot`: Total simulation time for which the time-propagation will be performed.

`dt_prop`: Time step which will be used.

`dt_output`: Time step for which output like energy, dipole, etc. is sent to standard output and is written to file/s.

The choice of the time step heavily affects the accuracy and stability of the time-propagation and is restricted by internal or external degrees of freedom, e.g., the spectral range of the Hamiltonian or the frequency of an external field oscillation. Generally, a small time step yields better results but significantly increases the computation time. The possible time step also depends on the propagation scheme which is explained later. A conservative choice is `dt_prop` $\leq$ 0.1 a.u. ($=$ 0.0024 fs) but 0.2 a.u. to 0.5 a.u. might also be possible. Remember using consistent units set by the `RT_TDDFT_input_units` keyword. Note that the time step is also a convergence parameter for spectral information.

Tag: `RT_TDDFT_td_field_gauge` (control.in)

Usage: `RT_TDDFT_td_field_gauge gauge`

Purpose: Setting the gauge for a possible external field (in the dipole approximation).

`gauge`: String. The field can be applied either in `length` gauge (electric field) or `velocity` gauge (vector potential). Default: `length` for cluster systems, `velocity` for periodic systems.

While this makes no difference formally, it has some technical implications. When doing periodic simulations, only the velocity gauge can be used. In the cluster case, the length gauge should be used because it is computationally cheaper. However, the formal gauge invariance is broken in any numerical approximation and it is likely possible that basis set and/or real-space grid settings converge differently for

length and velocity gauge.
Note that the gauge is a universal setting for each individual RT-TDDFT simulation and applies to all fields specified.

Tag: `RT_TDDFT_td_field` (control.in)

Usage: `RT_TDDFT_td_field t_start t_end type freq cycle center width Ex Ey Ez`

Purpose: Setting the type and shape of a possible external field (in the dipole approximation).

`t_start`: Start time after which the field is evaluated.

`t_end`: End time before which the field is evaluated (0 = infinite).

`type`: Integer that defines the field type as in rt_tddft_external_field.f90. Possible choices are defined below.

`freq`: Frequency if applicable (see type).

`cycle`: Cycle if applicable (see type).

`center`: Center if applicable (see type).

`width`: Width if applicable (see type).

`Ex`, `Ey`, `Ez`: Electric field amplitudes.

The choice of the external field depends on the type of calculation that one wants to perform. To obtain an absorption spectrum via the dynamical electronic dipole response, a delta-kick field can be applied by, e.g., setting `type` = 2, `center`, `width` and `Ez` to some values which will apply a Gaussian pulse of given amplitude at center time/width and along the z-axis. `width` should then be chosen quite small, e.g., to 0.05 fs. Alternatively, one can provide a constant field for the first time step, which saves computation time and provides a sharp pulse naturally. This would be `type` = 1 and `t_end` = `dt`.
To apply a field pulse with a defined wavelength, one can, e.g., set `type` = 3, `freq`, `cycle`, `Ez` which will result in a modulated Gaussian pulse of given wavelength around center time.
Multiple instances of this keyword with different settings can be given, e.g., to apply multiple different pulses over time. Internally, all defined fields are simply added up, so pay attention to temporal localization (if intended).
Note that the field amplitudes are always given as the amplitudes of the electric field, even in the case when the velocity gauge is used (see `RT_TDDFT_td_field_gauge`).
Currently, the following field types are implemented:

- 0: No field at all. This is the default when `RT_TDDFT_td_field` is not specified.
- 1: Constant field.

- 2: Delta kick pulse via Gaussian:

$$\mathbf{E}(t) = \mathbf{E}_0 \exp\left(\frac{t-t_0}{t_w}\right)\left(1+\exp\left(\frac{t-t_0}{t_w}\right)\right)^{-2}$$
$$\mathbf{A}(t) = -\mathbf{E}_0 t_w \left(1-\left(\exp\left(\frac{t-t_0}{t_w}\right)\right)^{-1}\right)$$

- 3: Localized field oscillation via sine-modulated Gaussian:

$$\mathbf{E}(t) = \mathbf{E}_0 \exp\left(-\frac{(t-t_0)^2}{2w^2}\right)\sin\left(\omega(t-t_0)\right)$$
$$\mathbf{A}(t) := \mathbf{E}(t)$$

  with $w = t_w/(2\sqrt{2\log(2)})$, $t_w = \text{FWHM}$.

- 4: Sinusoidal field with reference frequency:

$$\mathbf{E}(t) = \mathbf{E}_0 \sin\left(\frac{\omega}{c}(t-t_0)\right)$$
$$\mathbf{A}(t) = \mathbf{E}_0 \frac{c}{\omega}\cos\left(\frac{\omega}{c}(t-t_0)\right)$$

- 5: Sin^2 envelope pulse:

$$\mathbf{E}(t) = \mathbf{E}_0\Bigg(\sin^2\left(\frac{\pi}{c}(t-t_0)\right)\sin(\omega(t-t_0)) - \left(\frac{\pi}{c\omega}\sin\left(\frac{2\pi}{c}(t-t_0)\right)\cos(\omega(t-t_0))\right)\Bigg)$$
$$\mathbf{A}(t) := \frac{\mathbf{E}_0}{\omega}\sin^2\left(\frac{\pi}{c}(t-t_0)\right)\cos(\omega(t-t_0))$$

- 6: Ramp field:

$$\mathbf{E}(t) = (t-t_0)\mathbf{E}_0$$
$$\mathbf{A}(t) := \mathbf{E}(t)$$

where $t_0 =$ `t_start`, $\omega = 2\pi f$ and $f =$ `freq`, $c =$ `cycle`, $t_c =$ `center`, $t_w =$ `width`, $\mathbf{E}_0 = (E_x, E_y, E_z)^T$. Parameters not occurring in a function definition are not referenced and can be set to any value.

Note that user-defined fields can easily be included in the corresponding subroutine `src/rt-tddft/src/rt_tddft_ext_field.f90`.
Remember using consistent units set by the `RT_TDDFT_input_units` keyword.

Tag: `RT_td_field_spin_set` (control.in)

Usage: `RT_td_field_spin_set spin`

Purpose: Setting this will result in the external field only being applied to `spin` = 1 or 2 eigenvectors.

`spin`: Integer that specifies the spin component.

If this setting is specified for a collinear calculation (see keyword `spin` in the FHI-aims manual), only the spin = `spin` time-dependent eigenvectors will be excited by the specific external field. This may, e.g., be used to model triplet excitations, see Sec. 4.2.5.

Tag: `RT_TDDFT_propagator` (control.in)

Usage: `RT_TDDFT_propagator propagator`

Purpose: Setting the propagation scheme used in RT-TDDFT.

`propagator`: String that defines the numerical integration scheme. See below for possible options. Default: `crank_nicolson`.

The possible integration schemes are:

- `exponential_midpoint` (EM): Section 3.5.3

$$\mathbf{U}(t_k + \Delta t, t_k) = \exp\left(-i\Delta t \mathbf{S}^{-1}\mathbf{H}(t_k + \Delta t/2)\right)$$

- `crank_nicolson` (CN): Section 3.6; the order $\mathrm{N_{CN}}$ can be set via the keyword `RT_TDDFT_crank_nicolson_order order`.

$$\mathbf{U}(t_k + \Delta t, t_k) = \frac{\sum_{m=0}^{\mathrm{N_{CN}}} \frac{1}{m!}\left(-i\Delta t \mathbf{S}^{-1}\mathbf{H}(t_k + \Delta t/2)\right)^m}{\sum_{m=0}^{\mathrm{N_{CN}}} \frac{1}{m!}\left(i\Delta t \mathbf{S}^{-1}\mathbf{H}(t_k + \Delta t/2)\right)^m}$$

- `etrs` (Enforced Time-Reversal Symmetry): see Ref. [87]

$$\mathbf{U}(t_k + \Delta t, t_k) = \exp\left(-i\frac{\Delta t}{2}\mathbf{S}^{-1}\mathbf{H}(t_k + \Delta t)\right)\exp\left(-i\frac{\Delta t}{2}\mathbf{S}^{-1}\mathbf{H}(t_k)\right)$$

- `cfm4` (Commutator-Free Magnus Expansion 4): Section 3.5.4.

$$\mathbf{U}(t_k + \Delta t, t_k) = \exp\left(-i\Delta t \mathbf{S}^{-1}\left(\alpha_1\mathbf{H}_1 + \alpha_2\mathbf{H}_2\right)\right)\exp\left(-i\Delta t \mathbf{S}^{-1}\left(\alpha_1\mathbf{H}_2 + \alpha_1\mathbf{H}_2\right)\right)$$

$$\alpha_{1/2} = \frac{1}{4} \mp \frac{\sqrt{3}}{6}\ , \quad \mathbf{H}_{1/2} = \mathbf{H}\left(t_k + \left(\frac{1}{2} \mp \frac{\sqrt{3}}{6}\right)\Delta t\right)$$

- `m4` (Magnus Expansion 4): see Ref. [123]

$$\mathbf{U}(t_k + \Delta t, t_k) = \left(\frac{\Delta t}{2} \mathbf{S}^{-1} (\mathbf{H}_1 + \mathbf{H}_2) + \Delta t^2 \frac{\sqrt{3}}{12} [\mathbf{S}^{-1}\mathbf{H}_2, \mathbf{S}^{-1}\mathbf{H}_1] \right)$$
$$\mathbf{H}_{1/2} = \mathbf{H} \left(t_k + \left(\frac{1}{2} \mp \frac{\sqrt{3}}{6} \right) \Delta t \right)$$

- `runge_kutta_4`: Standard explicit Runge-Kutta 4 scheme. Works only for very small time steps but is a good choice for doing accurate reference simulations because its properties are well-known.

- `parallel_transport_cn`: Crank-Nicolson integration scheme within the parallel transport approach [163]. This requires the accelerated Anderson solver, see `RT_TDDFT_propagator_solver`. [EXPERIMENTAL]

$$\begin{aligned}\mathbf{C}(t_k + \Delta t) = \mathbf{C}(t_k) &- i\frac{\Delta t}{2}\Big(\mathbf{S}^{-1}\mathbf{H}(t_k)\mathbf{C}(t_k) - \mathbf{C}(t_k)\big(\mathbf{C}^\dagger(t_k)\mathbf{H}(t_k)\mathbf{C}(t_k)\big)\Big) \\ &- i\frac{\Delta t}{2}\Big(\mathbf{S}^{-1}\mathbf{H}(t_k + \Delta t)\mathbf{C}(t_k + \Delta t) \\ &\qquad - \mathbf{C}(t_k + \Delta t)\big(\mathbf{C}^\dagger(t_k + \Delta t)\mathbf{H}(t_k + \Delta t)\mathbf{C}(t_k + \Delta t)\big)\Big)\end{aligned}$$

Note that all above mentioned implicit schemes are defined as implicit, as they require evaluation of the Hamiltonian matrix at some future time. Currently, there are two ways implemented on how to solve this type of equation which can be set by the `RT_TDDFT_propagator_solver` keyword.
It should also be noted here that, when using a predictor-corrector scheme (which is the default solver for all implicit propagators), accuracy can be enhanced by using extrapolation, see the keyword `RT_TDDFT_extrapolate_predictor`.

Some additional schemes are implemented for testing purposes, namely the M6 (`m6`), CFM4:3 (`cfm4_3`) and CFM6:5 (`cfm6_5`) schemes [123].

For general purpose, we recommend to use the `crank_nicolson` propagation scheme.

Tag: `RT_TDDFT_propagator_solver` (control.in)

Usage: RT_TDDFT_propagator_solver solver

Purpose: Lets one choose the solver technique used for time propagation and for the selected propagator.

solver: String that can be

- predictor_corrector: Standard semi-implicit predictor-corrector scheme, see Sec. 3.7.
- forward_extra: Uses extrapolation to approximate future Hamiltonian in implicit schemes, see Sec. 3.7. This is not an implicit scheme, as no corrector step is performed.
- anderson: Anderson acceleration to solve implicit schemes, see [275]. Currently only works with the crank_nicolson and parallel_transport_cn propagators. [EXPERIMENTAL]

This keyword must usually not be set explicitly since every RT_TDDFT_propagator has its own default setting for the solver. Anyway, one can set the solver manually, e.g., to use one of the implicit exponential propagators with extrapolation, which is much cheaper since the corrector integration of the Hamiltonian matrix is not applied (however, this may be much less stable, not justifying the setting). Some combinations are not possible and a warning will be given that default settings will be used. Please use this option with caution.

Tag: RT_TDDFT_use_precor_tol (control.in)

Usage: RT_TDDFT_use_precor_tol tol

Purpose: Sets a tolerance of density change after which no more corrector steps are applied when multiple corrector steps may be performed.

tol: Float that sets convergence criterion to exit the corrector-loop. Not used by default.

Performing additional corrector steps until a convergence criterion is reached will formally increase accuracy. It should nevertheless be noted that the biggest error is probably introduced already by the predictor step and that significant improvements by doing additional corrector steps are not to be expected. Every corrector update involves another integration of the Hamiltonian matrix which is the most expensive part in RT-TDDFT usually. Before doing more corrector steps, it probably makes more sense to choose a smaller time step – if accuracy is a problem. If one wants to use this functionality anyway, values of 10^{-5}-10^{-9} would make sense usually. Note that a maximum number of 10 corrector steps is hardcoded to avoid unnecessarily many corrector updates (one should check settings when this happens).

Tag: `RT_TDDFT_precor_steps` (control.in)

Usage: `RT_TDDFT_precor_steps steps`

Purpose: Lets the user choose the (fixed) number of corrector steps to be done in the predictor-corrector solver.

`steps`: Integer setting a fixed number of corrector steps. Default: 1

Please see `RT_TDDFT_use_precor_tol` and Sec. 3.7 for further remarks. The default value is usually a good choice.

Tag: `RT_TDDFT_extrapolate_predictor` (control.in)

Usage: `RT_TDDFT_extrapolate_predictor extrapol`

Purpose: Extrapolation is used for the predictor step in case a predictor-corrector scheme is used.

`extrapol`: Bool that defines whether the Hamiltonian in a predictor propagator is extrapolated. Default: `.false.`

The Hamiltonian (matrix) used in the predictor step will be extrapolated by a given method which can be set via the `RT_TDDFT_ham_extrapolation` keyword. This also means that additional storage is needed. The extrapolated Hamiltonian (matrix) is applied in the predictor step. Tests indicate that extrapolation can noticeably improve accuracy. However, one should check this setting when unexpected instabilities occur.

Tag: `RT_TDDFT_ham_extrapolation` (control.in)

Usage: `RT_TDDFT_ham_extrapolation method order`

Purpose: Controls order and method of extrapolation for the Hamiltonian matrix if applicable.

`method`: String that can be either `linear` or `lagrange`. Default: `linear`.

`order`: Integer that defines the order of the extrapolation, i.e., how many past Hamiltonian matrices are used (and saved) for extrapolation. Default: 1.

The default setting indicating linear extrapolation works well in tests, whereas, in contrast, the Lagrange extrapolation approach sometimes produces odd results and should be used only with caution. Some of our tests indicate that higher-order extrapolation (≥ 4) can yield instabilities, thus one should check this.

Tag: `RT_TDDFT_propagator_predictor` (control.in)

Usage: RT_TDDFT_propagator_predictor prop

Purpose: A specific predictor propagator can be set in case a predictor-corrector scheme is used.

prop: String that defines the propagator to be used in the predictor step.

This only makes sense if an explicit scheme like runge_kutta_4 is used as a predictor, or, and this is the usual setting here, if any applicable implicit scheme is used in combination with extrapolation. A well-functioning scheme consists of an extrapolated exponential_midpoint predictor in combination with the cfm4 propagator for the corrector. This keyword is ignored if no predictor-corrector scheme is in use.

Tag: RT_TDDFT_exponential_method (control.in)

Usage: RT_TDDFT_exponential_method method

Purpose: Lets one choose the method for the calculation of matrix exponentials as required by some propagators.

method: String that can be either eigenvectors, scaling_squaring or taylor, see Sec. 3.5.5. Default: eigenvectors.

Currently, three different approaches to compute matrix exponentials needed for the exponential-type propagators can be used. The diagonalization-based approach is usually working perfectly but in the current implementation, it cannot be used for non-Hermitian matrices – this can be the case for effective Hamiltonian matrices occurring in Ehrenfest dynamics. In this case, the scaling and squaring - method [129] will be applied. Anyway, this setting will then be adjusted automatically. One can modify this setting mainly for benchmarking or testing. Note that using the taylor method requires to choose an order of the expansion, see RT_TDDFT_exponential_taylor_order.

Tag: RT_TDDFT_exponential_taylor_order (control.in)

Usage: RT_TDDFT_exponential_taylor_order order

Purpose: Sets the order of the truncated Taylor expansion method for the matrix exponential.

order: Integer that sets the order. Default: 10.

The Taylor method applies to general matrices and can be an economic choice. However, the order must be set with caution, as we found that the here employed all-electron approach likely requires higher orders. It may not even work when heavy elements are involved. This setting also highly depends on the time step. We found values of 10-20 to work well in certain cases.

Tag: `RT_TDDFT_crank_nicolson_order` (control.in)

Usage: `RT_TDDFT_crank_nicolson_order order`

Purpose: Sets the order of the expansion used in the Crank-Nicolson propagator, cf. Section 3.6.

`order`: Integer that sets the order. Default: 1.

Usually, 1st order seems to suffice for most applications. However, it can be beneficial to use higher order, e.g., 2/3, when instabilities are observed, especially possibly for heavier elements.

Tag: `RT_TDDFT_crank_nicolson_solve_inv` (control.in)

Usage: `RT_TDDFT_crank_nicolson_solve_inv solve`

Purpose: Sets the inversion method in the Crank-Nicolson scheme, cf. Section C.2.

`solve`: Boolean that sets the direct inversion method. Default: `.false.`

This only makes sense when the software bug explained in Section C.2 occurs. Setting the flag to `.true.` should resolve the issue. It is possible that the performance is impacted by this setting.

Tag: `RT_TDDFT_check_total_energy` (control.in)

Usage: `RT_TDDFT_check_total_energy start_time thresh`

Purpose: Compares the total energy to a fixed value at t = `start_time` and checks whether it is conserved below `thresh`.

`start_time`: Float that sets the time for which the reference energy is saved.

`thresh`: Float that sets the maximum energy deviation (in eV).

This can be used to prevent a simulation of 'blowing up', i.e., becoming unstable, as measured by the degree of energy conservation. The start time should be chosen such that the reference value makes sense: for example, when applying a finite resonant excitation, the total energy will increase, but should stay constant thereafter; thus, the reference value should be set a while after the excitation ends.

Tag: `RT_TDDFT_imaginary_time` (control.in)

Usage: RT_TDDFT_imaginary_time flag

Purpose: Peforms the simulation with imaginary time.

flag: Boolean that sets imaginary time. Default: .false.

Imaginary time propagation can be used as an alternative approach to the standard SCF procedure to converge a ground-state solution [238]. See also Chapter 4.6. This does only require a time step as control parameter and may be used to converge situations where SCF fails. Note that we recommend the Crank-Nicolson propagator for this functionality (higher orders may also be beneficial in order to enable higher time steps).
After convergence is reached, the eigenvectors are written back into the native data structures so that postprocessing methods should be usable.

Tag: RT_TDDFT_anderson_order_iter (control.in)

Usage: RT_TDDFT_anderson_order_iter order iter tol

Purpose: Sets specific parameters that are important in the anderson solver.

order: Order of the scheme, i.e., the number of eigenvectors used for the Anderson acceleration. Default: 4.

iter: Maximum number of steps in the fixed-point iteration. Default: 30.

tol: Convergence criterion for the fixed-point iteration. Default: 1e-14.

These parameters are explained in detail by Walker et al. [275]. We refer to algorithm 'AA' in this reference. The parameter m = order, $k_{\max}$ = iter as in the reference. The tolerance parameter depends on the setting RT_TDDFT_anderson_cond_type and should generally be chosen as a very small number. The most important parameter here is iter, which can be crucial to obtain a converged fixed-point iteration, but may also increase the possible numerical demand.

Tag: RT_TDDFT_anderson_cond_type (control.in)

Usage: RT_TDDFT_anderson_cond_type type

Purpose: Sets the type of the convergence check in the accelerated Anderson fixed-point iteration.

type: String that can be either ev_maximum, ev_individual or delta_rho. Default: delta_rho.

This defines which quantity is used as convergence measure in the fixed-point iteration. ev_maximum defines that $\max\{|\psi_n^{(i)} - \psi_n^{(i+1)}| \; \forall n \in \mathrm{N_{occ}}\}$ must be below tol as defined via RT_TDDFT_anderson_order_iter. ev_individual means that all solutions must be below the threshold tol. delta_rho only requires that the average change in charge density $\Delta\rho^i$ must be below the tolerance.

A.2 Ehrenfest Dynamics Settings

Tag: `RT_TDDFT_ehrenfest` (control.in)

Usage: `RT_TDDFT_ehrenfest type dt_geo`

Purpose: Performing a RT-TDDFT+Ehrenfest simulation, i.e., coupled electron-ion dynamics.

`type`: String that defines the Ehrenfest scheme. Must currently only be chosen as `default`.

`dt_geo`: Time step for geometry update and force computation.

The time step for Ehrenfest dynamics must obviously be at least the same value as for electron propagation. Usually, it can be chosen around 5- to 20-fold while maintaining stable propagation. Since updating the geometry and calculating forces is expensive, the Ehrenfest time step should be as large as possible. Additionally, the specific interplay of time propagation, force update and geometry update works very good when `dt_geo` $= N\times$ `dt` with $N = 2^n$. A reasonable choice for doing Ehrenfest dynamics should be `dt` $= 0.1$ a.u. in combination with `dt_geo` $= 0.4 - 0.64$ a.u. Monitoring energy conservation and norm conservation of the eigenvectors is advised when trying out settings.
Remember using consistent units set by the `RT_TDDFT_input_units` keyword.

Tag: `RT_TDDFT_ehrenfest_start_time` (control.in)

Usage: `RT_TDDFT_ehrenfest_start_time t_start`

Purpose: Setting the start time for Ehrenfest dynamics.

`t_start`: Time after which non-adiabatic forces are calculated and geometry is updated in case an Ehrenfest simulation is requested. Default: 0.

Usually, Ehrenfest dynamics start with the begin of a RT-TDDFT simulation when requested, but employing this key can modify the start time in case specific tasks require this.
Remember using consistent units set by the `RT_TDDFT_input_units` keyword.

Tag: `RT_TDDFT_ehrenfest_full_nc_forces` (control.in)

Usage: RT_TDDFT_ehrenfest_full_nc_forces key

Purpose: When requested, the full non-adiabatic Ehrenfest forces are evaluated.

key: Boolean that controls whether the full force contributions are calculated at each force computation step. Default: .false.

Usually, it seems that using the 'normal' non-adiabatic Ehrenfest forces conserving the energy (but not necessarily the momentum) is sufficient, but by using this keyword, the complete expression is evaluated – this might be important in specific situations and is of course more general. Anyway it is more expensive.

Tag: RT_TDDFT_ehrenfest_remove_com (control.in)

Usage: RT_TDDFT_ehrenfest_remove_com key

Purpose: Controls whether the center of mass is set to origin in Ehrenfest dynamics.

key: Boolean. Default: .false.

A.3 Output Settings

Tag: RT_TDDFT_write_file_prefix (control.in)

Usage: RT_TDDFT_write_file_prefix prefix

Purpose: Controls naming of all output files produced by the RT-TDDFT module.

prefix: String that is used to specify output files. Default: output.

All output files have the format PREFIX.rt-tddft.OBSERVABLE.SUFFIX or PREFIX.rt-tddft-ehrenfest.OBSERVABLE.SUFFIX where PREFIX can be set by the user to specify simulation settings. For example, energies are by default written to a file named output.rt-tddft.energies.dat. The corresponding quantities are always specified (format, units, etc.) in comment headers inside the files. Note that for any file output, existing files will not be overwritten. Instead, new files named PREFIX.N.rt-tddft.OBSERVABLE.SUFFIX with N $= 1, 2, ..$ will be created.

Tag: RT_TDDFT_write_ext_field (control.in)

Usage: `RT_TDDFT_write_ext_field key`

Purpose: Controls whether the time-dependent external field is written to a file.

`key`: Boolean. Default: `.true.`

The external field and all corresponding parameters are written to a file before a real-time simulation in this case. This information can, e.g., be used for postprocessing or visualization. Note that our postprocessing tool `eval_tddft.py` (Section D) requires this file.

Tag: `RT_TDDFT_write_cube` (control.in)

Usage: `RT_TDDFT_write_cube dt_cube`

Purpose: Controls whether time-dependent cube files are written.

`dt_cube`: Real value determining the time step for which output will be generated. If possible, this value should be much higher than the real-time time stepping since computing cubes is costly.

Default cube output is deactivated until this flag is given and the output frequency is specified. All options that can be used for cube output via the `output cube` keyword can be applied here and must be set in addition to this keyword.
Remember using consistent units set by the `RT_TDDFT_input_units` keyword.

Tag: `RT_TDDFT_output_level` (control.in)

Usage: `RT_TDDFT_output_level level`

Purpose: Controls the amount of console output written by the RT-TDDFT subroutine.

`level`: Integer with valid values of:

- 0: Min output - nearly nothing except basic information is written (NOTE: no information about physical observables is written in this case, too – use file output then)
- 1: Low output - some additional information is written, e.g., energies, dipole moment
- 2: Mid output - more is written out, e.g., convergence or accuracy parameters, timings
- 3: Max output - this prints info on anything that is being performed

Default: 1.

Since RT-TDDFT simulations are usually performed for a significant number of time-integration/density update/force calculation/etc. operations, the associated output will result in very large amounts of mostly unnecessary data which can be avoided by setting this keyword. The default should yield sufficient information on what is happening, but setting it to 2 will give some more information about numerical properties which can be important to follow.
Please note that important observables, e.g., energies, dipole moment, geometry, etc. are written to separate files which can be controlled further and which eases post-processing (see `RT_TDDFT_write_file_prefix`).

Tag: `RT_TDDFT_output_priority_override` (control.in)

Usage: `RT_TDDFT_output_priority_override priority`

Purpose: Lets one override the FHI-aims native output level for functionality used within RT-TDDFT.

`priority`: Integer that sets the output level. Default: 3 (minimal).

In the RT-TDDFT module, several routines from the parent code are called which may produce their own output. By default, the output level for these calls is set to minimal, i.e., not output will be sent to the console. However, this can be overridden by this keyword. We refer to the keywork `output_level` in the FHI-aims manual for specific choices.

Tag: `RT_TDDFT_output_energies` (control.in)

Usage: `RT_TDDFT_output_energies key_std key_file`

Purpose: Controls whether time-dependent energies are calculated, sent to output and written to a file.

`key_std`: Boolean controlling whether energies are written to standard output. Default: `.true.`

`key_file`: Boolean controlling whether energies are written to a file. Default: `.false.`

Energy should always be observed in order to validate a properly running simulation, i.e., total energy conservation. Note that when values are written to a file too, the corresponding file is named `PREFIX.rt-tddft.energies.dat` where PREFIX can be changed via the `RT_TDDFT_write_file_prefix` keyword.

Tag: `RT_TDDFT_output_dipole` (control.in)

Usage: `RT_TDDFT_output_dipole key_std key_file`

Purpose: Controls whether the time-dependent dipole moment is calculated, sent to output and written to a file.

`key_std`: Boolean controlling whether the dipole moment is written to standard output. Default: `.true.` for cluster systems, else `.false.`

`key_file`: Boolean controlling whether dipole moment is written to a file. Default: `.false.`

The electronic dipole is usually an observable of major interest in many RT-TDDFT applications. Note that when values are written to a file too, the corresponding file is named `PREFIX.rt-tddft.dipole.dat` where PREFIX can be changed via the `RT_TDDFT_write_file_prefix` keyword.

Tag: `RT_TDDFT_output_dipole_xyz` (control.in)

Usage: `RT_TDDFT_output_dipole_xyz out_x out_y out_z`

Purpose: Controls whether the x, y, z components of the electronic dipole moment are actually computed.

`out_x`: Boolean controlling whether the x-component is computed. Default: `.true.`

`out_y`: Boolean controlling whether the y-component is computed. Default: `.true.`

`out_z`: Boolean controlling whether the z-component is computed. Default: `.true.`

This keyword can be used to save unnecessary computation time for components that are not of interest. However, the computational effort for observables is generally low, as compared to the remaining functionality.

Tag: `RT_TDDFT_output_transition_dipole` (control.in)

Usage: `RT_TDDFT_output_transition_dipole key_std key_file state_min state_max`

Purpose: Controls whether and which transition dipole moments are computed.

`key_std`: Boolean controlling whether transition dipole moments are written to standard output. Default: `.false.`

`key_file`: Boolean controlling whether transition dipole moments are written to files. Note that a file for each transition is created. Default: `.false.`

`state_min`: Index of the lowest occupied state that will be considered.

`state_max`: Index of the highest unoccupied state that will be considered.

The computation of transition dipole moments is explained in Section 4.2.2. The lower and upper index define the set of occupied/unoccupied Kohn-Sham states for which time-dependent transition dipole moments will be computed. It is necessary that the native keyword `empty_states` is set accordingly high (e.g., to the number of basis functions or, e.g., 10000), else it is possible that not enough unoccupied states are available in the corresponding arrays. This is one of the rather computationally expensive observables.

Tag: `RT_TDDFT_output_transition_dipole_xyz` (control.in)

Usage: `RT_TDDFT_output_transition_dipole_xyz out_x out_y out_z`

Purpose: Controls whether the x, y, z components of the transition dipole moments are actually computed.

`out_x`: Boolean controlling whether the x-component is computed. Default: `.true.`

`out_y`: Boolean controlling whether the y-component is computed. Default: `.true.`

`out_z`: Boolean controlling whether the z-component is computed. Default: `.true.`

This keyword can be used to save unnecessary computation time for components that are not of interest.

Tag: `RT_TDDFT_output_state_dipoles` (control.in)

Usage: RT_TDDFT_output_state_dipoles key_std

Purpose: Controls whether time-dependent dipole moments of individual occupied states are calculated and sent to standard output.

key_std: Boolean. Default: .false.

If given, the dipole expectation values for all occupied (and thus, time-propagated) states are computed and sent to output. Note that this computation requires the explicit evaluation of the dipole matrix $\langle\phi_i|\mathbf{r}|\phi_j\rangle$ and could cause additional computational cost.

Tag: RT_TDDFT_output_magnetic_moment (control.in)

Usage: RT_TDDFT_output_magnetic_moment key_std key_file

Purpose: Controls whether the time-dependent magnetic moment is calculated, sent to output and written to a file.

key_std: Boolean controlling whether the magnetic moment is written to standard output. Default: .false.

key_file: Boolean controlling whether the magnetic moment is written to a file. Default: .false.

The magnetic moment is usually an observable of major interest in RT-TDDFT applications for circular dichroism. See Section 4.4 for more details. Note that when values are written to a file too, the corresponding file is named PREFIX.rt-tddft.magmom.dat where PREFIX can be changed via the RT_TDDFT_write_file_prefix keyword.

Tag: RT_TDDFT_output_magnetic_moment_xyz (control.in)

Usage: RT_TDDFT_output_dipole_xyz out_x out_y out_z

Purpose: Controls whether the x, y, z components of the magnetic moment are actually computed.

out_x: Boolean controlling whether the x-component is computed. Default: .true.

out_y: Boolean controlling whether the y-component is computed. Default: .true.

out_z: Boolean controlling whether the z-component is computed. Default: .true.

This keyword can be used to save unnecessary computation time for components that are not of interest. However, the computational effort for observables is generally low, as compared to the remaining functionality.

Tag: `RT_TDDFT_output_current` (control.in)

Usage: `RT_TDDFT_output_current key_std key_file`

Purpose: Controls whether the time-dependent electronic current is calculated, sent to output and written to a file.

`key_std`: Boolean controlling whether the current is written to standard output. Default: `.false.` for cluster systems, else `.true.`

`key_file`: Boolean controlling whether the current is written to a file. Default: `.false.`

The electronic current is often the main observable of interest in periodic RT-TDDFT simulations (analog to the dipole in finite systems). Note that when values are written to a file too, the corresponding file is named `PREFIX.rt-tddft.current.dat` where PREFIX can be changed via the `RT_TDDFT_write_file_prefix` keyword.

Tag: `RT_TDDFT_ehrenfest_output_trajectory` (control.in)

Usage: `RT_TDDFT_ehrenfest_output_trajectory key_std key_file`

Purpose: Controls whether time-dependent coordinates, velocities and forces are sent to output and written to a file in Ehrenfest dynamics.

`key_std`: Boolean controlling whether trajectory information is written to standard output. Default: `.true.` for Ehrenfest dynamics, else `.false.`

`key_file`: Boolean controlling whether trajectory information is written to a file. Default: `.false.`

Note that when values written are to a file too, the corresponding file is named PREFIX.rt-tddft-ehrenfest.trajectory.xyz where PREFIX can be changed via the `RT_TDDFT_write_file_prefix` keyword.

Tag: `RT_TDDFT_output_n_excited` (control.in)

Usage: `RT_TDDFT_output_n_excited key_std`

Purpose: Controls whether the time-dependent number of excited electrons based on ground-state projection is computed and sent to standard output.

`key_std`: Boolean controlling whether this quantity is computed and written to standard output. Default: `.false.`

This quantity is computed as

$$N_e^{\mathrm{ex}}(t) = \sum_{n=1}^{\mathrm{N_{occ}}} f_n (N_{electrons} - |\langle \psi_n(0) | \psi_n(t) \rangle|^2), \tag{A.1}$$

i.e., via projection of time-dependent orbitals on ground-state orbitals [276]. This refers to the number of electrons that are possibly excited within the introduced dynamics.

A.4 Restart Settings

Tag: `RT_TDDFT_restart_write` (control.in)

Usage: `RT_TDDFT_restart_write t_write_restart`

Purpose: Writes a RT-TDDFT restart file for a specified time.

`t_write_restart`: Real value corresponding to specific time for which a restart file should be written.

All necessary information to perform a RT-TDDFT restart is written to file/s in this case. In detail, all the eigencoefficients, coordinates, settings, etc. Multiple entries of this keyword for different times can be given. Note that this can potentially produce huge files, especially when periodic boundary conditions are in use (as for every **k**-point, eigenvectors are written).

Tag: `RT_TDDFT_restart_write_period` (control.in)

Usage: `RT_TDDFT_restart_write_period t_write_restart_period`

Purpose: Writes a RT-TDDFT restart file repeatedly after each specified time period.

`t_write_restart`: Real value corresponding to specific time period after which a restart file should be written.

See `RT_TDDFT_restart_write` for details. When doing very demanding simulations and/or very long simulations, one should set a sensible value here to avoid needing to restart from the beginning after a job was canceled. Writing a restart file automatically when a kill signal is received is on the to-do list.

Tag: `RT_TDDFT_restart_read` (control.in)

Usage: `RT_TDDFT_restart_read restart_file`

Purpose: Reads a RT-TDDFT restart file and starts the simulation based on it.

`restart_file`: String describing the corresponding restart file.

Besides the physical quantities, the restart file contains all relevant real-time simulation parameters which are compared to what is given in control.in. The settings must be the same or the simulation will abort. This also works for Ehrenfest dynamics. Note that when performing a restart, FHI-aims will run a SCF cycle, but the

resulting eigenvectors, etc. will be overwritten from what is read in the restart file - based on this, the real-time simulation will be re-initialized.

A.5 Geometry Settings

Tag: `RT_TDDFT_initial_velocity` (geometry.in)

Usage: `RT_TDDFT_initial_velocity v_x v_y v_z`

Purpose: Initial velocity of corresponding (i.e., last specified) `atom` when peforming RT-TDDFT-Ehrenfest dynamics.

`v_x, v_y, v_z`: Initial velocities in units of Å/ps.

Putting initial kinetic energy into the ionic subsystem is a common initial condition used in Ehrenfest dynamics, e.g., when simulating ion bombardment or to evaluate molecular potential energy surfaces. Note that it can make sense to employ the native `constrain_relaxation` parameter here in order to reduce the amount of forces computed, which is expensive (if the problem/symmetry allows it).

A.6 Important Remark

Some functionality in our implementation may not be applied in certain situations or is not compatible with some specific methods in the FHI-aims software. We could not test any possible interoperability, so that caution has to be paid when non-standard functionality is combined. In general, the code will raise a warning when non-compatible options are requested that we are aware of. The checks are performed in the modules `check_consistency_of_keywords.f90` and `RT_TDDFT_initialization.f90`.

Appendix B

Examples

We provide here some examples that were also used in our work and which we presented results for. This serves both the purpose of reproducibility, but also that a user can more easily learn about different settings and their importance in practice. In order to not provide unnecessary content, we here only provide the settings that are related to real-time propagation. Other settings, e.g., XC functional, basis set, grid settings, etc. are assumed as given in the control.in and geometry.in in files. Illustrative examples can also be found in the regression test suite incorporated in the software package. Comments are given in blue color.

B.1 Benzene: Absorption Spectrum

These settings mostly correspond to the results presented in Section 4.2.3. The total calculation consists of 3 individual calculations. Each of these incorporates a weak initial delta-like kick along one of the Cartesian axes. The following input corresponds to the x-polarized field.

control.in

```
# specifies input units to atomic units
RT_TDDFT_input_units atomic

# total simulation time, time step, output time step (in a.u.)
RT_TDDFT_propagation    3000    0.1    0.1

# 2-fold Lagrangian extrapolation of the Hamiltonian is used
RT_TDDFT_ham_extrapolation    lagrange    2
RT_TDDFT_extrapolate_predictor    T

# check that energy is conserved below 5e-3 eV from t = 10 a.u. on
RT_TDDFT_check_total_energy    10    5e-3
```

```
# specification for the external field: start at 0 a.u., end at 0.05 a.u.
# type 1 - constant field, the 4 following parameters are not in use;
# amplitudes: 0.005 a.u., 0, 0 corresponding to x,y,z
RT_TDDFT_td_field  0  0.05  1  0  0  0  0  0.005  0.0  0.0

# all output files have the prefix 'kick-x'
RT_TDDFT_write_file_prefix    kick-x

# write energy to console and file every 2.0 a.u.
RT_TDDFT_output_energies   T   T   2

# write dipole to file and console; in this case, only compute x-component
RT_TDDFT_output_dipole   T   T
RT_TDDFT_output_dipole_xyz   T   F   F

# compute transition dipole moments between min. occupied state
# 15 and max. unoccupied state 23; only the x-components are
# computed; we set the empty_states keyword to its maximum implicitly
RT_TDDFT_output_transition_dipole   T   T   15   23
RT_TDDFT_output_transition_dipole_xyz   T   F   F
empty_states   10000
```

B.2 Silicon: High-Harmonic Spectrum

The provided parameters correspond to the calculations discussed in Section 4.3.5. This is only a single calculation. The excitation is a $\sin^2$-like pulse with a defined carrier frequency of 1.6 eV. The observable of interest is here the time-dependent macroscopic current.
If non-zero x- and y-components of the macroscopic current are observed, we recommend to use a higher grid density. This will eliminate the spurious components and is an indicator of grid convergence.

control.in

```
# specifies the k-point grid; we cannot exploit symmetry as of now
k_grid    16 × 16 × 16
k_offset    0.01    0.45    0.37
symmetry_reduced_k_grid    .false.

RT_TDDFT_input_units atomic
```

```
RT_TDDFT_propagation    2000    0.08    0.08

RT_TDDFT_propagator    crank_nicolson

# specifies the field: start at 0 a.u., (pulse) end at 413.4 a.u.
# type 5 - sin^2 envelope oscillation, frequency 0.009361275 a.u.,
# half wavelength 413.4 a.u., next 2 parameters not in use,
# zero x- and y-component, z-amplitude is 0.016880322 a.u.
RT_TDDFT_td_field  0  413.4  5  0.009361275  413.4  0  0  0  0  0.016880322

# only the velocity gauge can be used, i.e., a vector potential is applied
RT_TDDFT_td_field_gauge    velocity

RT_TDDFT_output_energies   T   T   2

RT_TDDFT_output_current   T   T

RT_TDDFT_write_file_prefix    si_hhg_161616
```

B.3 CH_2=NH_2^+: Ehrenfest Dynamics

The proposed settings correspond to the results presented in Section 4.5.2. This is also a single calculation. Both the control.in and geometry.in files must be modified. We here give the full geometry.in file to illustrate the initial velocities set on the hydrogen atoms. The observables of interest are here the energies and the trajectory, which is written to a .xyz file.

control.in

```
RT_TDDFT_input_units atomic

RT_TDDFT_propagation    3000    0.01    0.04

RT_TDDFT_propagator    crank_nicolson

# only the so-called default scheme can be used right now; the 2
# provided time steps are equal; actually, they can be chosen much
# higher, e.g., to 0.96; this should not alter the results, as the
# electronic time step is crucial for the stability
RT_TDDFT_ehrenfest    default    0.04    0.04
```

```
# write trajectory to file
RT_TDDFT_ehrenfest_output_trajectory    T    T

RT_TDDFT_output_energies    T    T

RT_TDDFT_output_dipole    T    T

RT_TDDFT_write_file_prefix    cnh4+_ef_10ev
```

geometry.in

```
atom    -0.00000000    0.95258597    -1.17726214    H
RT_TDDFT_initial_velocity    -219    0    0

atom    -0.00000000    -0.95258597    -1.17726214    H
RT_TDDFT_initial_velocity    219    0    0

atom    0.00000000    -0.00000000    -0.63397950    C
atom    0.00000000    -0.00000000    0.63399133    N

atom    -0.00000000    0.87480220    1.17725622    H
RT_TDDFT_initial_velocity    219    0    0

atom    -0.00000000    -0.87480220    1.17725622    H
RT_TDDFT_initial_velocity    -219    0    0
```

Appendix C

Code Structure and Installation

C.1 Installation

We provide here a more detailed overview and description of our computer code in order to ease access for any developer intending to modify it. When compiling FHI-aims, the RT-TDDFT functionality is already included and does not have to be installed additionally in any way, as our implementation is part of the development version. We denote the parent directory as `FHIaims`. The RT-TDDFT module is included in the regression test suite and the corresponding testcases in the `regression_tests/testcases/rt-tddft` folder may also serve as examples for the user.

C.2 Compatibility Remarks

We tested our software for Intel-based parallelization together with the MKL numerical linear algebra library, and for GNU OpenMPI-based parallelization together with the numerical linear algebra libraries ScaLAPACK/OpenBLAS (versions 2019 / 2020). It seems like there exists a bug in the recent MKL versions (Intel Parallel Studio XE 2019 / 2020) that affects the linear equation solver subroutines `pzgetrs` and `pzgesv`, causing memory leakage at every call, resulting in excessive memory usage by the code. This was not observed with the non-Intel framework. These operations are conducted when the Crank-Nicolson propagator is used or when the scaling and squaring method for matrix exponentials is employed. We implemented a fix that will result in the code using explicit inversion instead of solving a linear system, i.e.:

$$\textbf{Linear solver}: \quad \text{solve} \quad \mathbf{AX} = \mathbf{B} \quad \text{for} \quad \mathbf{X} \tag{C.1}$$

$$\textbf{Inversion}: \quad \text{compute } \mathbf{A}^{-1} \quad \text{for} \quad \mathbf{X} = \mathbf{A}^{-1}\mathbf{B} \tag{C.2}$$

For this, the user has to provide the flag

```
RT_TDDFT_crank_nicolson_solve_inv .true.
```

in the `control.in` file.

C.3 Code Structure

The RT-TDDFT implementation is located in the directory `src/rt-tddft` which itself contains a `README` file and the directory `src` which contains the source code. Note that this is only the on-top code, as there are several modifications or additions in the parent code, too. All related global flags, I/O variables and arrays have the prefix `RT_TDDFT_` which identifies them as belonging to this functionality.
The `rt-tddft/src` directory contains 18 modules which serve different purposes which we will explain here. It should be noted that several subroutines of the RT-TDDFT module communicate with base-code subroutines via global flags. For example, this could mean that the RT-TDDFT code requests the real-space integration subroutine for the Hamiltonian matrix to also compute other matrix elements, e.g., of the dipole or gradient operator. A few global arrays are used for such computations that are allocated within the RT-TDDFT module and which are within the scope of some base-code modules. The reason for this strategy is that this keeps modifications to the parent code minimal. Also, our module may use global data structures that are related to the ScaLAPACK module and which are implicitly used therein. For example, many subroutines in the ScaLAPACK module operate on global work arrays that cannot be passed explicitly. We therefore also make use of these quantities when it cannot be avoided.
Note that the mode of operation (parallel/non-parallel, periodic/non-periodic) affects much functionality on a very fundamental level. For example, the code will try to use the `real*8` datatype for all arrays, if possible, and uses `complex*16` in all other cases. Also, any numerical array-related functionality uses either a full local storage and computation of distributed storage and parallel computation, or a full local storage and computation without distributed storage, meaning that many array-related functions are specified two times, i.e., corresponding to the two modes of operation. We also were required to modify the parent code at many different places which we will not elaborate in detail here. Anyway, we consistently commented these modifications in the code via

```
!JH-MOD:rt-tddft:  COMMENT; BEGIN ------>

...

!JH-MOD:rt-tddft:  END <----------------
```

Where `COMMENT` is replaced by a short description about the modification.

In the following list, all the files that build our implementation are given and we provide a short description.

- **Function** `rt_tddft.f90`: this function is called from the FHI-aims `main` routine and executes any RT-TDDFT functionality by calling `rt_tddft_initialization`, `rt_tddft_main` and `rt_tddft_finalize` in this order.

- **Module** `rt_tddft_initialization.f90`: general initialization in order to prepare a real-time simulation.
  - Consistency checks for input flags
  - Setting of computation flags
  - Array allocations
  - Initialization of global variables
  - Initialization and specification of output units for file output
- **Module** `rt_tddft_main.f90`: the core functionality of the RT-TDDFT module.
  - Possibly read-in of restart file content
  - Preprocessing and output of initial observables
  - Real-time simulation loop
- **Module** `rt_tddft_global_variables.f90`: all module-global variables, flags and arrays.
  - Computation flags for core quantities
  - Counters and variables for real-time iteration and output
  - Work and storage arrays, where Fortran `type` structures are used to encapsulate related quantities
  - Constants
- **Module** `rt_tddft_time_propagation.f90`: all real-time propagation functionalities (modulo Ehrenfest dynamics).
  - Main propagation subroutine that calls specific solvers and propagation schemes
  - Predictor-corrector, extrapolation and Anderson solvers
  - All time-propagation schemes
  - Specification of flags that are passed to different subroutines, depending on the type of simulation, e.g., for coupled dynamics where two different time steps for the electrons and nuclei are in use
- **Module** `rt_tddft_matrix_operations.f90`: numerical and parallelization - related matrix functionalities.
  - ScaLAPACK local/global array transformations
  - Matrix exponential methods: diagonalization, Taylor-expansion, scaling and squaring
  - Matrix operations like multiplication, inversion, diagonalization, etc.

- **Module** `rt_tddft_hamiltonian_operations.f90`: any operations that are related to the construction of the time-dependent Hamiltonian.
  - Computation of density, potentials and Hamiltonian, where specific flags may be set to only perform a subset of these operations
  - Global flags may be set such that specific matrices are integrated in the real-space integration loop, e.g., the basis gradient matrix
  - Transformation of sparse or upper diagonal formats into other formats, depending on parallelization
  - Computation of exchange matrix and addition of the corresponding matrix elements to the Hamiltonian
  - Computation of velocity-gauge matrix elements that are added to the Hamiltonian
  - Storage of Hamiltonians for extrapolation and interpolation functionality
  - Computation of transition dipole matrix and density matrix
- **Module** `rt_tddft_overlap_operations.f90`: any functionality that is related to the overlap matrix.
  - Re-integration of overlap matrix
  - Checks for conditioning and treatment of singular overlap matrices
  - Computation of inverse or square root overlap matrix
  - Data format conversions
- **Function** `rt_tddft_external_field.f90`: explicit computation of time-dependent external field/vector potential for a given input time step; the field is written into a global variable `ext_field`; this also allows easy definition of additional fields.
- **Module** `rt_tddft_ehrenfest.f90`: all functionality that is related to Ehrenfest dynamics.
  - Propagation of nuclei via modified velocity Verlet scheme
  - Geometry reinitialization
  - Calculation of forces
- **Module** `rt_tddft_observables_and_output.f90`: calculation of observables, console and file output.
  - Calculation of specific expectation values, e.g., dipole moment
  - Computation of total energy expression
  - Specification of individual output flags
  - Write to output files

  - Print and manage computation timings
  - Cube output

- **Module** `rt_tddft_base_code_additions.f90`: this module stores subroutines from the parent software package that were modified to be used in this context or that were added to be used explicitly within the parent code. This mostly affects functionality that had to be adapted to the case of complex-type eigenvectors and that had to be added for the integration of specific real-space matrix elements.

  - Array transformations, e.g., sparse to square format
  - Real-space integration subroutines, e.g., for basis function gradients
  - Computation of exchange matrix for explicitly complex density matrix

- **Module** `rt_tddft_messaging.f90`: incorporates a function that is used for level-specified console output. The RT-TDDFT module uses its own output levels, as it is important to avoid unnecessary output when a large number of similar operations is conducted.

- **Module** `rt_tddft_stepping.f90`: incorporates a function that is responsible for printing and setting the current time step. This exists for possible future extensions that introduce variable time steps.

- **Module** `rt_tddft_restart.f90`: manages the restart functionality which uses fixed-format files for geometry and eigenvectors that may be used to restart calculations.

  - Write restart files
  - Read restart files

- **Module** `rt_tddft_finalization.f90`: functionality to finalize a RT-TDDFT calculation.

  - Closes output files
  - De-allocates all module-global workspace

- **Module** `rt_tddft_testing.f90`: test-suite that was used for development and that can be extended to test core functionalities. The tests can be called as an alternative to the actual real-time simulation which will not be performed in this case.

- **Module** `rt_tddft_debug.f90`: incorporates some functionalities that were used by the author for debugging.

  - Output of specific matrix properties
  - Structured console output of arrays

Appendix D

Postprocessing Tools

D.1 Evaluation of Spectral Quantities: eval_tddft.py

This is a postprocessing tool written in python that can be used to generate results for any of the electronic frequency-space observables (the corresponding output files of the RT-TDDFT module are indicated by their suffixes), i.e.,

- Electronic dipole moment $\boldsymbol{\mu}(t)$ (`*.rt-tddft.dipole.dat`) $\rightarrow$ polarizability $\alpha(\omega)$, dipole strength function $S(\omega)$, high-harmonic spectra HHG(ω)
- Electronic current $\mathbf{I}(t)$ (`*.rt-tddft.current.dat`) $\rightarrow$ conductivity $\sigma(\omega)$, dielectric function $\epsilon(\omega)$, high-harmonic spectra HHG(ω)
- Magnetic dipole moment $\mathbf{m}(t)$ (`*.rt-tddft.magmom.dat`) $\rightarrow$ rotatory response tensor $\beta(\omega)$, rotatory strength $R(\omega)$

The script can be found in the `utilities/rt-tddft` subfolder and needs python 3.x for optimal functionality. Any units are handled internally and the output can directly be visualized (see Fig. D.1, where results of an absorption spectrum calculation are depicted by the script) or written to files, including the respective units in headers. The script needs only the corresponding observables and the file for the external field (`*.rt-tddft.ext-field.dat`) which is used as raw input, or to provide parameters from its header for analytical field expressions. The script essentially computes Fourier transforms and may perform various operations on in- or output data. Calling the script via `eval_tddft -h` prints out a help message which explains all available options in detail.
A typical call for the calculation of an absorption spectrum would be

```
eval_tddft -pol x.rt-tddft.dipole.dat y.rt-tddft.dipole.dat
z.rt-tddft.dipole.dat -field x.rt-tddft.ext-field.dat -fa -p -d 0
poly -w output
```

which reads the x,y,z files for electronic dipole moments from 3 individual calculations, each with a weak delta-kick field applied, and the external field file x.rt-tddft.ext-field.dat which suffices, as the field parameters are equal in the 3 calculations (but with different polarizations). The option `-fa` makes the script use the

analytical expression for the external field (in this case, e.g., a Gaussian pulse), `-p` requests a plot window, `-d 0 poly` applies a polynomial damping function from $t = 0$ to the dipole moments and `-w output` requests output files with the prefix `output` (in this case for the Fourier transforms of the electronic dipole moments, the polarizability tensor and the DSF).

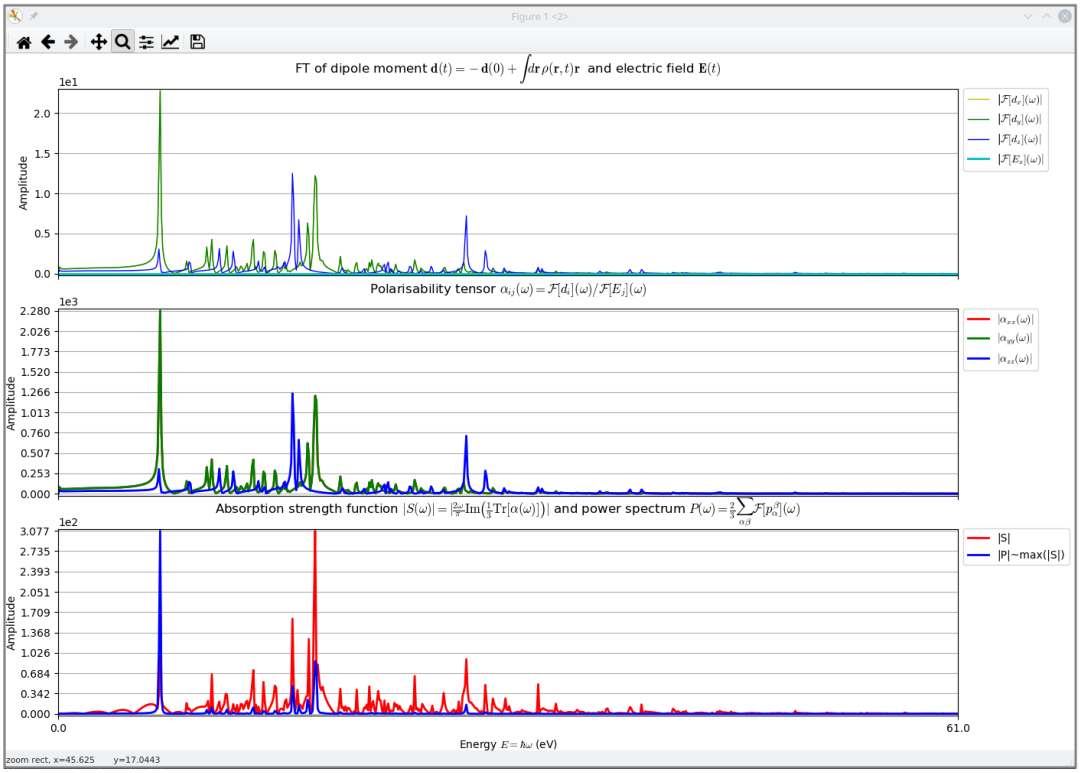

FIGURE D.1: Graphical output produced by the `eval_tddft.py` script. This corresponds to a polarizability calculation based on the electronic dipole moment. The top row shows the bare Fourier transforms, the middle row shows the absolute polarizability tensor diagonal components and the bottom row shows the absolute DSF and the power spectrum.

Remark: in order to obtain *clean* spectra, it may be important to prepare the input. This especially applies to the case when an initial step-like kick was applied (e.g., only for the first time step). In the output files containing the time series, it can in this case be that the first $t = 0$ value of the corresponding observable is zero, followed by non-zero values. This will introduce unwanted artifacts in the Fourier spectra. We advise to remove these $t = 0$ values from the data set and shift up the remaining entries such that the $t = 0$ value is also the first non-zero entry (due to the excitation).

D.2 DSF Fitting for Spectra Acceleration: ifit_abs.py

This postprocessing python script can be used to apply the fitting technique described in Section 4.2.5 based on output generated with the `eval_tddft` script, i.e., the DSF. This requires zero-padded DSF's and the script may also use spectra obtained with the Padé method in order to ease operation by visually identifying peaks. A window will open (such an output is given in Figure D.2) where one can manually select excitations by clicking on the peaks in the plot; closing the window will result in a subsequent fit which can be repeated if insufficient (Figure D.3 shows a fit that is reasonably, but not perfectly converged). There is also the option to automatically select input parameters for the fit, however it is safer to do it manually, as this requires some intuition.
One can easily evaluate the success of the fit visually, as by the overlap of the fitted function with the data. It can help to select a smaller spectral range to fit specific peaks. On the other hand, if a fit does not converge as desired, it is possible that contributions of usually significant peaks outside the visible range are required for convergence. Providing too many fitting parameters for peaks that incorporate multiple excitations, as indicated by the Padé-FT spectrum, may result in the procedure failing.
Calling the script with the `-h` argument will result in it printing a help message, where all control arguments are explained in more detail.

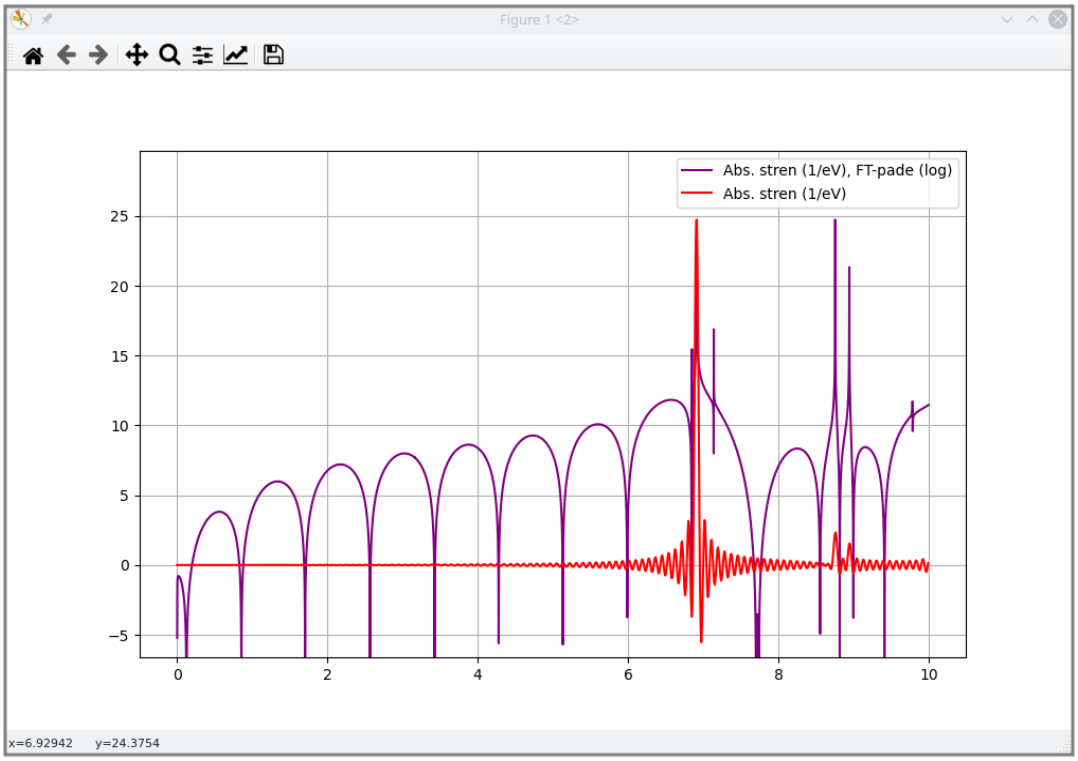

FIGURE D.2: 1st step in the fitting procedure: manual selection of peaks.

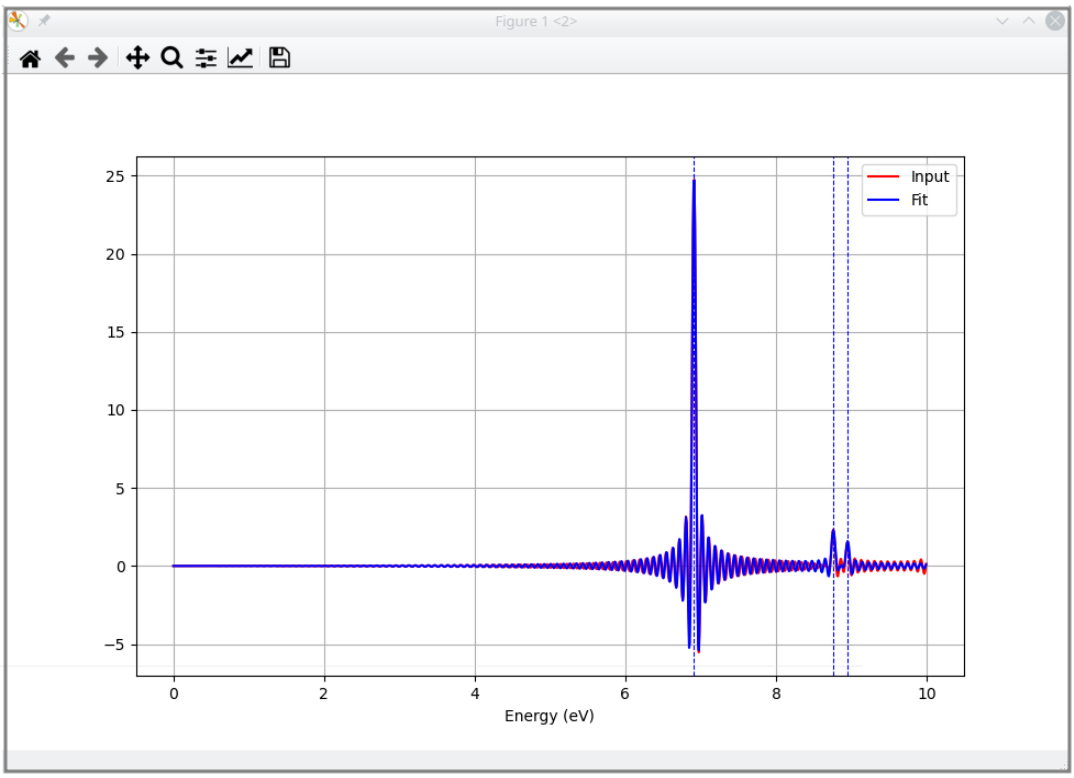

FIGURE D.3: 2nd step in the fitting procedure: the resulting fitted spectrum is plotted.

Publications

Publication 1

Some content presented in Chapter 4 is incorporated in the publication

> J. Hekele, Y. Yao, V. Blum, Y. Kanai and P. Kratzer, *Real-Time and Imaginary-Time Time-Dependent Density Functional Theory within a Numeric Atom-Centered Basis Function Framework*, in preparation.

In general, the author developed the whole RT-TDDFT code and assisted in the implementation of the IT-TDDFT functionality. He further developed the postprocessing tools and carried out many of the simulations and evaluations. Also, he contributed significantly to the manuscript text and took care of the publication process.

Publication 2

All content presented in Chapter 5 is incorporated in the publication

> J. Hekele, M. Linke, T. Keller, J. Jose, M. Hille, E. Hasselbrink, S. Schlücker and P. Kratzer, *A fresh look at the structure of aromatic thiols on Au surfaces from theory and experiment*, submitted.

The author was responsible for all DFT calculations and evaluations presented here, contributed to the manuscript text and took care of the publication process. This study was also embedded in the CRC 1242 [250] and was conducted as collaborative work between the physics department and the physical chemistry department of the University of Duisburg-Essen.

Bibliography

[1] W. Heisenberg. "Über quantentheoretische Umdeutung kinematischer und mechanischer Beziehungen." In: *Zeitschrift für Physik* 33.1 (1925).

[2] M. Born and P. Jordan. "Zur Quantenmechanik". In: *Zeitschrift für Physik* 34.1 (1925).

[3] M. Born, W. Heisenberg, and P. Jordan. "Zur Quantenmechanik. II." In: *Zeitschrift für Physik* 35.8 (1926).

[4] E. Schrödinger. "An undulatory theory of the mechanics of atoms and molecules". In: *Physical Review* 28 (1926).

[5] E. Schrödinger. "Quantisierung als Eigenwertproblem". In: *Annalen der Physik* 385.13 (1926).

[6] M. Born and R. Oppenheimer. "Zur Quantentheorie der Molekeln". In: *Annalen der Physik* 389.20 (1927).

[7] W. Kohn. "Nobel lecture: Electronic structure of matter – wave functions and density functionals". In: *Reviews of Modern Physics* 71 (1999).

[8] D. R. Hartree. "The wave mechanics of an atom with a non-Coulomb central field. Part I. Theory and methods". In: *Mathematical Proceedings of the Cambridge Philosophical Society* 24.1 (1928).

[9] V. Fock. "Näherungsmethode zur Lösung des quantenmechanischen Mehrkörperproblems". In: *Zeitschrift für Physik A* 61.1 (1930).

[10] L. H. Thomas. "The calculation of atomic fields". In: *Mathematical Proceedings of the Cambridge Philosophical Society* 23.5 (1927).

[11] E. Fermi. "Eine statistische Methode zur Bestimmung einiger Eigenschaften des Atoms und ihre Anwendung auf die Theorie des periodischen Systems der Elemente". In: *Zeitschrift für Physik* 48.1 (1928).

[12] P. Hohenberg and W. Kohn. "Inhomogeneous electron gas". In: *Physical Review* 136 (1964).

[13] W. Ritz. "Über eine neue Methode zur Lösung gewisser Variationsprobleme der mathematischen Physik." In: *Journal für die reine und angewandte Mathematik* 1909.135 (1909).

[14] M. Levy. "Universal variational functionals of electron densities, first-order density matrices, and natural spin-orbitals and solution of the v-representability problem". In: *Proceedings of the National Academy of Sciences* 76.12 (1979).

[15] O. Gunnarsson and B. I. Lundqvist. "Exchange and correlation in atoms, molecules, and solids by the spin-density-functional formalism". In: *Physical Review B* 13 (1976).

[16] G. Vignale and M. Rasolt. "Density-functional theory in strong magnetic fields". In: *Physical Review Letters* 59 (1987).

[17] W. Kohn and L. J. Sham. "Self-consistent equations including exchange and correlation effects". In: *Physical Review* 140 (1965).

[18] K. Capelle. "A bird's-eye view of density-functional theory". In: *Brazilian Journal of Physics* 36 (2006).

[19] J. P. Perdew, R. G. Parr, M. Levy, and J. L. Balduz. "Density-functional theory for fractional particle number: Derivative discontinuities of the energy". In: *Physical Review Letters* 49 (1982).

[20] J. P. Perdew and A. Zunger. "Self-interaction correction to density-functional approximations for many-electron systems". In: *Physical Review B* 23 (1981).

[21] J. P. Perdew and S. Kurth. "Density functionals for non-relativistic Coulomb systems in the new century". In: *A Primer in Density Functional Theory*. Ed. by C. Fiolhais, F. Nogueira, and M. A. L. Marques. Berlin, Heidelberg: Springer Berlin Heidelberg, 2003.

[22] N. Mardirossian and M. Head-Gordon. "Thirty years of density functional theory in computational chemistry: An overview and extensive assessment of 200 density functionals". In: *Molecular Physics* 115.19 (2017).

[23] J. P. Perdew and Y. Wang. "Accurate and simple analytic representation of the electron-gas correlation energy". In: *Physical Review B* 45 (1992).

[24] R. O. Jones and O. Gunnarsson. "The density functional formalism, its applications and prospects". In: *Reviews of Modern Physics* 61 (1989).

[25] J. Kohanoff. *Electronic Structure Calculations for Solids and Molecules: Theory and Computational Methods*. Cambridge University Press, 2006.

[26] J. P. Perdew, K. Burke, and M. Ernzerhof. "Generalized gradient approximation made simple". In: *Physical Review Letters* 77 (1996).

[27] J. P. Perdew, J. A. Chevary, S. H. Vosko, K. A. Jackson, M. R. Pederson, D. J. Singh, and C. Fiolhais. "Atoms, molecules, solids, and surfaces: Applications of the generalized gradient approximation for exchange and correlation". In: *Physical Review B* 46 (1992).

[28] C. Lee, W. Yang, and R. G. Parr. "Development of the Colle-Salvetti correlation-energy formula into a functional of the electron density". In: *Physical Review B* 37 (1988).

[29] J. Tao, J. P. Perdew, V. N. Staroverov, and G. E. Scuseria. "Climbing the density functional ladder: Nonempirical meta–generalized gradient approximation designed for molecules and solids". In: *Physical Review Letters* 91 (2003).

[30] S. Kümmel and L. Kronik. "Orbital-dependent density functionals: Theory and applications". In: *Reviews of Modern Physics* 80 (2008).

[31] B. Moore, H. Sun, N. Govind, K. Kowalski, and J. Autschbach. "Charge-transfer versus charge-transfer-like excitations revisited". In: *Journal of Chemical Theory and Computation* 11.7 (2015).

[32] R. Martin. *Electronic Structure: Basic Theory and Practical Methods*. Cambridge University Press, 2004.

[33] A. D. Becke. "Density-functional thermochemistry. III. The role of exact exchange". In: *Journal of Chemical Physics* 98.7 (1993).

[34] C. Adamo and V. Barone. "Toward reliable density functional methods without adjustable parameters: The PBE0 model". In: *Journal of Chemical Physics* 110.13 (1999).

[35] T. L. Beck. "Real-space mesh techniques in density-functional theory". In: *Reviews of Modern Physics* 72.4 (2000).

[36] T. Torsti, T. Eirola, J. Enkovaara, T. Hakala, P. Havu, V. Havu, T. Höynälänmaa, J. Ignatius, M. Lyly, I. Makkonen, T. T. Rantala, J. Ruokolainen, K. Ruotsalainen, E. Räsänen, H. Saarikoski, and M. J. Puska. "Three real-space discretization techniques in electronic structure calculations". In: *Physica Status Solidi (b)* 243.5 (2006).

[37] A. Castro, H. Appel, M. Oliveira, C. A. Rozzi, X. Andrade, F. Lorenzen, M. A. L. Marques, E. K. U. Gross, and A. Rubio. "Octopus: A tool for the application of time-dependent density functional theory". In: *Physica Status Solidi (b)* 243.11 (2006).

[38] J. C. Slater. "Atomic shielding constants". In: *Physical Review* 36 (1930).

[39] J. VandeVondele and J. Hutter. "Gaussian basis sets for accurate calculations on molecular systems in gas and condensed phases". In: *Journal of Chemical Physics* 127.11 (2007).

[40] T. H. Dunning. "Gaussian basis sets for use in correlated molecular calculations. I. The atoms boron through neon and hydrogen". In: *Journal of Chemical Physics* 90.2 (1989).

[41] Y. Inada and H. Orita. "Efficiency of numerical basis sets for predicting the binding energies of hydrogen bonded complexes: Evidence of small basis set superposition error compared to Gaussian basis sets". In: *Journal of Computational Chemistry* 29.2 (2008).

[42] V. Blum, R. Gehrke, F. Hanke, P. Havu, V. Havu, X. Ren, K. Reuter, and M. Scheffler. "Ab initio molecular simulations with numeric atom-centered orbitals". In: *Computer Physics Communications* 180.11 (2009).

[43] J. M. Soler, E. Artacho, J. D. Gale, A. García, J. Junquera, P. Ordejón, and D. Sánchez-Portal. "The SIESTA method for ab initio order-N materials simulations". In: *Journal of Physics: Condensed Matter* 14.11 (2002).

[44] J. Junquera, O. Paz, D. Sánchez-Portal, and E. Artacho. "Numerical atomic orbitals for linear-scaling calculations". In: *Physical Review B* 64 (2001).

[45] F. B. van Duijneveldt, J. G. C. M. van Duijneveldt-van de Rijdt, and J. H. van Lenthe. "State of the art in counterpoise theory". In: *Chemical Reviews* 94.7 (1994).

[46] F. Knuth, C. Carbogno, V. Atalla, V. Blum, and M. Scheffler. "All-electron formalism for total energy strain derivatives and stress tensor components for numeric atom-centered orbitals". In: *Computer Physics Communications* 190 (2015).

[47] P. Pulay. "Ab initio calculation of force constants and equilibrium geometries in polyatomic molecules". In: *Molecular Physics* 17.2 (1969).

[48] M. C. Payne, M. P. Teter, D. C. Allan, T. A. Arias, and J. D. Joannopoulos. "Iterative minimization techniques for ab initio total-energy calculations: Molecular dynamics and conjugate gradients". In: *Reviews of Modern Physics* 64 (1992).

[49] P. Broqvist, A. Alkauskas, and A. Pasquarello. "Hybrid-functional calculations with plane-wave basis sets: Effect of singularity correction on total energies, energy eigenvalues, and defect energy levels". In: *Physical Review B* 80 (2009).

[50] J. C. Slater. "Wave functions in a periodic potential". In: *Physical Review* 51 (1937).

[51] D. J. Sing and L. Nordström. *Planewaves, Pseudopotentials and the LAPW Method*. 2nd ed. Springer, 2006.

[52] P. E. Blöchl, C. J. Först, and J. Schimpl. "Projector augmented wave method: Ab initio molecular dynamics with full wave functions". In: *Bulletin of Materials Science* 26.1 (2003).

[53] P. E. Blöchl. "Projector augmented-wave method". In: *Physical Review B* 50 (1994).

[54] K. Lejaeghere, G. Bihlmayer, T. Björkman, P. Blaha, S. Blügel, V. Blum, D. Caliste, I. E. Castelli, S. J. Clark, A. Dal Corso, S. de Gironcoli, T. Deutsch, J. K. Dewhurst, I. Di Marco, C. Draxl, M. Dułak, O. Eriksson, J. A. Flores-Livas, K. F. Garrity, L. Genovese, P. Giannozzi, M. Giantomassi, S. Goedecker, X. Gonze, O. Grånäs, E. K. U. Gross, A. Gulans, F. Gygi, D. R. Hamann, P. J. Hasnip, N. A. W. Holzwarth, D. Iuşan, D. B. Jochym, F. Jollet, D. Jones, G. Kresse, K. Koepernik, E. Küçükbenli, Y. O. Kvashnin, I. L. M. Locht, S. Lubeck, M. Marsman, N. Marzari, U. Nitzsche, L. Nordström, T. Ozaki, L. Paulatto, C. J.

Pickard, W. Poelmans, M. I. J. Probert, K. Refson, M. Richter, G.-M. Rignanese, S. Saha, M. Scheffler, M. Schlipf, K. Schwarz, S. Sharma, F. Tavazza, P. Thunström, A. Tkatchenko, M. Torrent, D. Vanderbilt, M. J. van Setten, V. Van Speybroeck, J. M. Wills, J. R. Yates, G.-X. Zhang, and S. Cottenier. "Reproducibility in density functional theory calculations of solids". In: *Science* 351.6280 (2016).

[55] P. Pulay. "Convergence acceleration of iterative sequences. The case of SCF iteration". In: *Chemical Physics Letters* 73.2 (1980).

[56] W. Press, S. Teukolsky, W. Vetterling, and B. Flannery. *Numerical Recipes 3rd Edition: The Art of Scientific Computing*. Cambridge University Press, 2007.

[57] D. Marx and J. Hutter. *Ab Initio Molecular Dynamics: Basic Theory and Advanced Methods*. Cambridge University Press, 2009.

[58] D. Frenkel and B. Smit. *Understanding molecular simulation: from algorithms to applications*. Vol. 1. Elsevier, 2001.

[59] C. A. Ullrich and Z.-h. Yang. "A brief compendium of time-dependent density functional theory". In: *Brazilian Journal of Physics* 44.1 (2014).

[60] E. Runge and E. K. U. Gross. "Density-functional theory for time-dependent systems". In: *Physical Review Letters* 52 (1984).

[61] N. T. Maitra, K. Burke, and C. Woodward. "Memory in time-dependent density functional theory". In: *Physical Review Letters* 89 (2002).

[62] C. A. Ullrich. *Time-Dependent Density-Functional Theory: Concepts and Applications*. Oxford Graduate Texts. Oxford University Press, 2011.

[63] R. van Leeuwen. "Mapping from densities to potentials in time-dependent density-functional theory". In: *Physical Review Letters* 82 (1999).

[64] M. Marques, N. Maitra, F. Nogueira, E. Gross, and A. Rubio. *Fundamentals of Time-Dependent Density Functional Theory*. Springer Berlin Heidelberg, 2012.

[65] S. K. Ghosh and A. K. Dhara. "Density-functional theory of many-electron systems subjected to time-dependent electric and magnetic fields". In: *Physical Review A* 38 (1988).

[66] F. Ding, W. Liang, C. T. Chapman, C. M. Isborn, and X. Li. "On the gauge invariance of nonperturbative electronic dynamics using the time-dependent Hartree-Fock and time-dependent Kohn-Sham". In: *Journal of Chemical Physics* 135.16 (2011).

[67] J. M. Escartin, M. Vincendon, P. Romaniello, P. M. Dinh, P.-G. Reinhard, and E. Suraud. "Towards time-dependent current-density-functional theory in the non-linear regime". In: *Journal of Chemical Physics* 142.8 (2015).

[68] G. Vignale and W. Kohn. "Current-dependent exchange-correlation potential for dynamical linear response theory". In: *Physical Review Letters* 77 (1996).

[69] N. T. Maitra, I. Souza, and K. Burke. "Current-density functional theory of the response of solids". In: *Physical Review B* 68 (2003).

[70] G. Vignale. "Mapping from current densities to vector potentials in time-dependent current density functional theory". In: *Physical Review B* 70 (2004).

[71] R. R. Pela and C. Draxl. *All-electron full-potential implementation of real-time TDDFT in exciting*. arXiv: 2102.02630. 2021.

[72] K. Yabana, T. Sugiyama, Y. Shinohara, T. Otobe, and G. F. Bertsch. "Time-dependent density functional theory for strong electromagnetic fields in crystalline solids". In: *Physical Review B* 85 (2012).

[73] K. Yabana, T. Nakatsukasa, J.-I. Iwata, and G. F. Bertsch. "Real-time, real-space implementation of the linear response time-dependent density-functional theory". In: *Physica Status Solidi (b)* 243.5 (2006).

[74] C. Pemmaraju, F. Vila, J. Kas, S. Sato, J. Rehr, K. Yabana, and D. Prendergast. "Velocity-gauge real-time TDDFT within a numerical atomic orbital basis set". In: *Computer Physics Communications* 226 (2018).

[75] S. A. Sato, K. Yabana, Y. Shinohara, T. Otobe, and G. F. Bertsch. "Numerical pump-probe experiments of laser-excited silicon in nonequilibrium phase". In: *Physical Review B* 89 (2014).

[76] X. Andrade, S. Hamel, and A. A. Correa. "Negative differential conductivity in liquid aluminum from real-time quantum simulations". In: *European Physical Journal B* 91.10 (2018).

[77] V. A. Goncharov. "Nonlinear optical response in solids from time-dependent density-functional theory simulations". In: *Journal of Chemical Physics* 139.8 (2013).

[78] A. D. Bandrauk, F. Fillion-Gourdeau, and E. Lorin. "Atoms and molecules in intense laser fields: Gauge invariance of theory and models". In: *Journal of Physics B: Atomic, Molecular and Optical Physics* 46.15 (2013).

[79] Y.-C. Han and L. B. Madsen. "Comparison between length and velocity gauges in quantum simulations of high-order harmonic generation". In: *Physical Review A* 81 (2010).

[80] V. S. Yakovlev and M. S. Wismer. "Adiabatic corrections for velocity-gauge simulations of electron dynamics in periodic potentials". In: *Computer Physics Communications* 217 (2017).

[81] C. Attaccalite and M. Grüning. "Nonlinear optics from an ab initio approach by means of the dynamical Berry phase: Application to second- and third-harmonic generation in semiconductors". In: *Physical Review B* 88 (2013).

[82] R. Resta. "Quantum-mechanical position operator in extended systems". In: *Physical Review Letters* 80 (1998).

[83] R. D. King-Smith and D. Vanderbilt. "Theory of polarization of crystalline solids". In: *Physical Review B* 47 (1993).

[84] I. Souza, J. Íñiguez, and D. Vanderbilt. "Dynamics of Berry-phase polarization in time-dependent electric fields". In: *Physical Review B* 69 (2004).

[85] G. F. Bertsch, J.-I. Iwata, A. Rubio, and K. Yabana. "Real-space, real-time method for the dielectric function". In: *Physical Review B* 62 (2000).

[86] C. Attaccalite. "Non-linear response in extended systems: A real-time approach". PhD thesis. Aix-Marseille Universite, 2017.

[87] A. Castro, M. A. L. Marques, and A. Rubio. "Propagators for the time-dependent Kohn-Sham equations". In: *Journal of Chemical Physics* 121.8 (2004).

[88] B. F. E. Curchod, U. Rothlisberger, and I. Tavernelli. "Trajectory-based nonadiabatic dynamics with time-dependent density functional theory". In: *ChemPhysChem* 14.7 (2013).

[89] L. X. Benedict, E. L. Shirley, and R. B. Bohn. "Optical absorption of insulators and the electron-hole interaction: An ab initio calculation". In: *Physical Review Letters* 80 (1998).

[90] M. E. Casida. "Time-dependent density functional response theory for molecules". In: *Recent Advances in Density Functional Methods*. Ed. by D. P. Chong. Vol. 1. World Scientific, 1995.

[91] V. Havu, V. Blum, P. Havu, and M. Scheffler. "Efficient O(N) integration for all-electron electronic structure calculation using numeric basis functions". In: *Journal of Computational Physics* 228.22 (2009).

[92] A. Tkatchenko and M. Scheffler. "Accurate molecular van der Waals interactions from ground-state electron density and free-atom reference data". In: *Physical Review Letters* 102 (2009).

[93] A. Tkatchenko, A. Ambrosetti, and R. A. DiStasio. "Interatomic methods for the dispersion energy derived from the adiabatic connection fluctuation-dissipation theorem". In: *Journal of Chemical Physics* 138.7 (2013).

[94] A. Tkatchenko, R. A. DiStasio, R. Car, and M. Scheffler. "Accurate and efficient method for many-body van der Waals interactions". In: *Physical Review Letters* 108 (2012).

[95] A. Ambrosetti, A. M. Reilly, R. A. DiStasio, and A. Tkatchenko. "Long-range correlation energy calculated from coupled atomic response functions". In: *Journal of Chemical Physics* 140.18 (2014).

[96] J. Hermann and A. Tkatchenko. "Density functional model for van der Waals interactions: Unifying many-body atomic approaches with nonlocal functionals". In: *Physical Review Letters* 124 (2020).

[97] X. Ren, P. Rinke, V. Blum, J. Wieferink, A. Tkatchenko, A. Sanfilippo, K. Reuter, and M. Scheffler. "Resolution-of-identity approach to Hartree–Fock, hybrid density functionals, RPA, MP2 and GW with numeric atom-centered orbital basis functions". In: *New Journal of Physics* 14.5 (2012).

[98] F. Caruso, P. Rinke, X. Ren, A. Rubio, and M. Scheffler. "Self-consistent *GW*: All-electron implementation with localized basis functions". In: *Physical Reviews B* 88 (2013).

[99] C. Liu, J. Kloppenburg, Y. Yao, X. Ren, H. Appel, Y. Kanai, and V. Blum. "All-electron ab initio Bethe-Salpeter equation approach to neutral excitations in molecules with numeric atom-centered orbitals". In: *Journal of Chemical Physics* 152.4 (2020).

[100] H. Shang, N. Raimbault, P. Rinke, M. Scheffler, M. Rossi, and C. Carbogno. "All-electron, real-space perturbation theory for homogeneous electric fields: Theory, implementation, and application within DFT". In: *New Journal of Physics* 20.7 (2018).

[101] R. Zhao, V. W.-z. Yu, K. Zhang, Y. Xiao, Y. Zhang, and V. Blum. "Quasi-four-component method with numeric atom-centered orbitals for relativistic density functional simulations of molecules and solids". In: *Physical Review B* 103 (2021).

[102] B. Delley. "Analytic energy derivatives in the numerical local density-functional approach". In: *Journal of Chemical Physics* 94.11 (1991).

[103] R. Stratmann, G. E. Scuseria, and M. J. Frisch. "Achieving linear scaling in exchange-correlation density functional quadratures". In: *Chemical Physics Letters* 257.3 (1996).

[104] A. D. Becke. "A multicenter numerical integration scheme for polyatomic molecules". In: *Journal of Chemical Physics* 88.4 (1988).

[105] B. Delley. "High order integration schemes on the unit sphere". In: *Journal of Computational Chemistry* 17.9 (1996).

[106] J. Baker, J. Andzelm, A. Scheiner, and B. Delley. "The effect of grid quality and weight derivatives in density functional calculations". In: *Journal of Chemical Physics* 101.10 (1994).

[107] E. van Lenthe, E. J. Baerends, and J. G. Snijders. "Relativistic total energy using regular approximations". In: *Journal of Chemical Physics* 101.11 (1994).

[108] P. Kratzer and J. Neugebauer. "The basics of electronic structure theory for periodic systems". In: *Frontiers in Chemistry* 7 (2019).

[109] V. W.-z. Yu, F. Corsetti, A. García, W. P. Huhn, M. Jacquelin, W. Jia, B. Lange, L. Lin, J. Lu, W. Mi, and et al. "ELSI: A unified software interface for Kohn–Sham electronic structure solvers". In: *Computer Physics Communications* 222 (2018).

[110] E. Anderson, Z. Bai, C. Bischof, S. Blackford, J. Demmel, J. Dongarra, J. Du Croz, A. Greenbaum, S. Hammarling, A. McKenney, and D. Sorensen. *LAPACK Users' Guide*. Third. Philadelphia, PA: Society for Industrial and Applied Mathematics, 1999.

[111] *ScaLAPACK—Scalable Linear Algebra PACKage*. http://www.netlib.org/scalapack/.

[112] *Open MPI Documentation*. ttps://www.open-mpi.org/doc/.

[113] I.-M. Hoyvik. "The spectrum of the atomic orbital overlap matrix and the locality of the virtual electronic density matrix". In: *Molecular Physics* 118.21-22 (2020).

[114] *All-Electron Electronic Structure Theory with Numeric Atom-Centered Basis Functions: A User's Guide*. https://aimsclub.fhi-berlin.mpg.de/.

[115] K. Lopata and N. Govind. "Modeling fast electron dynamics with real-time time-dependent density functional theory: Application to small molecules and chromophores". In: *Journal of Chemical Theory and Computation* 7.5 (2011).

[116] M. Hochbruck and A. Ostermann. "Exponential integrators". In: *Acta Numerica* 19 (2010).

[117] A. L. Frapiccini, A. Hamido, S. Schröter, D. Pyke, F. Mota-Furtado, P. F. O'Mahony, J. Madroñero, J. Eiglsperger, and B. Piraux. "Explicit schemes for time propagating many-body wave functions". In: *Physical Review A* 89 (2014).

[118] F. Casas and A. Iserles. "Explicit Magnus expansions for nonlinear equations". In: *Journal of Physics A* 39.19 (2006).

[119] A. Russakoff, Y. Li, S. He, and K. Varga. "Accuracy and computational efficiency of real-time subspace propagation schemes for the time-dependent density functional theory". In: *Journal of Chemical Physics* 144.20 (2016).

[120] D. Kidd, C. Covington, and K. Varga. "Exponential integrators in time-dependent density-functional calculations". In: *Physical Review E* 96 (2017).

[121] A. Gómez Pueyo, M. A. L. Marques, A. Rubio, and A. Castro. "Propagators for the time-dependent Kohn–Sham equations: Multistep, Runge–Kutta, exponential Runge–Kutta, and commutator free Magnus methods". In: *Journal of Chemical Theory and Computation* 14.6 (2018).

[122] W. Magnus. "On the exponential solution of differential equations for a linear operator". In: *Communications on Pure and Applied Mathematics* 7.4 (1954).

[123] N. Auer, L. Einkemmer, P. Kandolf, and A. Ostermann. "Magnus integrators on multicore CPUs and GPUs". In: *Computer Physics Communications* 228 (2018).

[124] A. Alvermann and H. Fehske. "High-order commutator-free exponential time-propagation of driven quantum systems". In: *Journal of Computational Physics* 230.15 (2011).

[125] S. Blanes, F. Casas, J. Oteo, and J. Ros. "The Magnus expansion and some of its applications". In: *Physics Reports* 470.5 (2009).

[126] S. Blanes and P. C. Moan. "Fourth-and sixth-order commutator-free Magnus integrators for linear and non-linear dynamical systems". In: *Applied Numerical Mathematics* 56.12 (2006).

[127] C. Moler and C. Van Loan. "Nineteen dubious ways to compute the exponential of a matrix, twenty-five years later". In: *SIAM Review* 45.1 (2003).

[128] B. Ghojogh, F. Karray, and M. Crowley. *Eigenvalue and generalized eigenvalue problems: Tutorial*. arXiv: 1903.11240. 2019.

[129] N. J. Higham. "The scaling and squaring method for the matrix exponential revisited". In: *SIAM Journal of Matrix Analysis and Applications* 26.4 (2005).

[130] C. O'Rourke and D. R. Bowler. "Linear scaling density matrix real time TDDFT: Propagator unitarity and matrix truncation". In: *Journal of Chemical Physics* 143.10 (2015).

[131] A. Tsolakidis, D. Sánchez-Portal, and R. M. Martin. "Calculation of the optical response of atomic clusters using time-dependent density functional theory and local orbitals". In: *Physical Review B* 66 (2002).

[132] J. Crank and P. Nicolson. "A practical method for numerical evaluation of solutions of partial differential equations of the heat-conduction type". In: *Mathematical Proceedings of the Cambridge Philosophical Society* 43.1 (1947).

[133] Y. Saad and M. H. Schultz. "GMRES: A generalized minimal residual algorithm for solving nonsymmetric linear systems". In: *SIAM Journal on Scientific and Statistical Computing* 7.3 (1986).

[134] Y. Zhu and J. M. Herbert. "Self-consistent predictor/corrector algorithms for stable and efficient integration of the time-dependent Kohn-Sham equation". In: *Journal of Chemical Physics* 148.4 (2018).

[135] O. Sugino and Y. Miyamoto. "Density-functional approach to electron dynamics: Stable simulation under a self-consistent field". In: *Physical Review B* 59 (1999).

[136] A. Ojanperä, V. Havu, L. Lehtovaara, and M. Puska. "Nonadiabatic Ehrenfest molecular dynamics within the projector augmented-wave method". In: *Journal of Chemical Physics* 136.14 (2012).

[137] T. Kunert and R. Schmidt. "Non-adiabatic quantum molecular dynamics: General formalism and case study H_2^+ in strong laser fields". In: *European Physical Journal D* 25 (2003).

[138] X. Li, J. C. Tully, H. B. Schlegel, and M. J. Frisch. "Ab initio Ehrenfest dynamics". In: *Journal of Chemical Physics* 123.8 (2005).

[139] S. Meng and E. Kaxiras. "Real-time, local basis-set implementation of time-dependent density functional theory for excited state dynamics simulations". In: *Journal of Chemical Physics* 129.5 (2008).

[140] F. Wang, C. Y. Yam, L. Hu, and G. Chen. "Time-dependent density functional theory based Ehrenfest dynamics". In: *Journal of Chemical Physics* 135.4 (2011).

[141] G. Kolesov, O. Grånäs, R. Hoyt, D. Vinichenko, and E. Kaxiras. "Real-time TDDFT with classical ion dynamics: Methodology and applications". In: *Journal of Chemical Theory and Computation* 12.2 (2016).

[142] W. C. Swope, H. C. Andersen, P. H. Berens, and K. R. Wilson. "A computer simulation method for the calculation of equilibrium constants for the formation of physical clusters of molecules: Application to small water clusters". In: *Journal of Chemical Physics* 76.1 (1982).

[143] L. D. Barron. *Molecular Light Scattering and Optical Activity*. 2nd ed. Cambridge University Press, 2004.

[144] P. Elliott, F. Furche, and K. Burke. "Excited states from time-dependent density functional theory". In: *Reviews in Computational Chemistry*. John Wiley and Sons, Ltd, 2008.

[145] N. T. Maitra. "Perspective: Fundamental aspects of time-dependent density functional theory". In: *Journal of Chemical Physics* 144.22 (2016).

[146] S. Tretiak, C. M. Isborn, A. M. N. Niklasson, and M. Challacombe. "Representation independent algorithms for molecular response calculations in time-dependent self-consistent field theories". In: *Journal of Chemical Physics* 130.5 (2009).

[147] F. Trani, G. Scalmani, G. Zheng, I. Carnimeo, M. J. Frisch, and V. Barone. "Time-dependent density functional tight binding: New formulation and benchmark of excited states". In: *Journal of Chemical Theory and Computation* 7.10 (2011).

[148] S. Grimme. "A simplified Tamm-Dancoff density functional approach for the electronic excitation spectra of very large molecules". In: *Journal of Chemical Physics* 138.24 (2013).

[149] L. A. Bartell, M. R. Wall, and D. Neuhauser. "A time-dependent semiempirical approach to determining excited states". In: *Journal of Chemical Physics* 132.23 (2010).

[150] S. Tussupbayev, N. Govind, K. Lopata, and C. J. Cramer. "Comparison of real-time and linear-response time-dependent density functional theories for molecular chromophores ranging from sparse to high densities of states". In: *Journal of Chemical Theory and Computation* 11.3 (2015).

[151] C. Müller, M. Sharma, and M. Sierka. "Real-time time-dependent density functional theory using density fitting and the continuous fast multipole method". In: *Journal of Computational Chemistry* 41.30 (2020).

[152] A. Bende and V. Toşa. "Modeling laser induced molecule excitation using real-time time-dependent density functional theory: application to 5- and 6-benzyluracil". In: *Physical Chemistry Chemical Physics* 17 (2015).

[153] C. Pemmaraju. "Valence and core excitons in solids from velocity-gauge real-time TDDFT with range-separated hybrid functionals: An LCAO approach". In: *Computational Condensed Matter* 18 (2019).

[154] X. Li, N. Govind, C. Isborn, A. E. DePrince, and K. Lopata. "Real-time time-dependent electronic structure theory". In: *Chemical Reviews* 120.18 (2020).

[155] A. Bruner, D. LaMaster, and K. Lopata. "Accelerated broadband spectra using transition dipole decomposition and Padé approximants". In: *Journal of Chemical Theory and Computation* 12.8 (2016).

[156] K. Lopata, B. E. Van Kuiken, M. Khalil, and N. Govind. "Linear-response and real-time time-dependent density functional theory studies of core-level near-edge X-ray absorption". In: *Journal of Chemical Theory and Computation* 8.9 (2012).

[157] M. R. Provorse and C. M. Isborn. "Electron dynamics with real-time time-dependent density functional theory". In: *International Journal of Quantum Chemistry* 116.10 (2016).

[158] I. Schelter and S. Kümmel. "Accurate evaluation of real-time density functional theory providing access to challenging electron dynamics". In: *Journal of Chemical Theory and Computation* 14.4 (2018).

[159] Y. Takimoto, F. D. Vila, and J. J. Rehr. "Real-time time-dependent density functional theory approach for frequency-dependent nonlinear optical response in photonic molecules". In: *Journal of Chemical Physics* 127.15 (2007).

[160] E. Koch and A. Otto. "Optical absorption of benzene vapour for photon energies from 6 eV to 35 eV". In: *Chemical Physics Letters* 12.3 (1972).

[161] E. Pantos, J. Philis, and A. Bolovinos. "The extinction coefficient of benzene vapor in the region 4.6 to 36 eV". In: *Journal of Molecular Spectroscopy* 72.1 (1978).

[162] M. A. Marques, A. Castro, G. F. Bertsch, and A. Rubio. "Octopus: A first-principles tool for excited electron–ion dynamics". In: *Computer Physics Communications* 151.1 (2003).

[163] W. Jia, D. An, L.-W. Wang, and L. Lin. "Fast real-time time-dependent density functional theory calculations with the parallel transport gauge". In: *Journal of Chemical Theory and Computation* 14.11 (2018).

[164] R. Baer, D. Neuhauser, P. R. Zdánská, and N. Moiseyev. "Ionization and high-order harmonic generation in aligned benzene by a short intense circularly polarized laser pulse". In: *Physical Review A* 68 (2003).

[165] M. Schreiber, M. R. Silva-Junior, S. P. A. Sauer, and W. Thiel. "Benchmarks for electronically excited states: CASPT2, CC2, CCSD, and CC3". In: *Journal of Chemical Physics* 128.13 (2008).

[166] M. Miura, Y. Aoki, and B. Champagne. "Assessment of time-dependent density functional schemes for computing the oscillator strengths of benzene, phenol, aniline, and fluorobenzene". In: *Journal of Chemical Physics* 127.8 (2007).

[167] B. P. Klein, S. J. Hall, and R. J. Maurer. "The nuts and bolts of core-hole constrained ab initio simulation for K-shell X-ray photoemission and absorption spectra". In: *Journal of Physics: Condensed Matter* 33.15 (2021).

[168] R. G. Fernando, M. C. Balhoff, and K. Lopata. "X-ray absorption in insulators with non-Hermitian real-time time-dependent density functional theory". In: *Journal of Chemical Theory and Computation* 11.2 (2015).

[169] A. P. Hitchcock, P. Fischer, A. Gedanken, and M. B. Robin. "Antibonding σ* valence MOs in the inner-shell and outer-shell spectra of the fluorobenzenes". In: *Journal of Physical Chemistry* 91.3 (1987).

[170] K. R. Wilson, B. S. Rude, T. Catalano, R. D. Schaller, J. G. Tobin, D. T. Co, and R. J. Saykally. "X-ray spectroscopy of liquid water microjets". In: *Journal of Physical Chemistry B* 105.17 (2001).

[171] M. Valiev, E. J. Bylaska, N. Govind, K. Kowalski, T. P. Straatsma, H. J. J. Van Dam, D. Wang, J. Nieplocha, E. Apra, T. L. Windus, and W. A. de Jong. "NWChem: A comprehensive and scalable open-source solution for large scale molecular simulations". In: *Computer Physics Communications* 181.9 (2010).

[172] T. Noro, M. Sekiya, and T. Koga. "Segmented contracted basis sets for atoms H through Xe: Sapporo-(DK)-nZP sets (n = D, T, Q)". In: *Theoretical Chemistry Accounts* 131.2 (2012).

[173] B. P. Pritchard, D. Altarawy, B. Didier, T. D. Gibson, and T. L. Windus. "New basis set exchange: An open, up-to-date resource for the molecular sciences community". In: *Journal of Chemical Information and Modeling* 59.11 (2019).

[174] A. D. Laurent and D. Jacquemin. "TD-DFT benchmarks: A review". In: *International Journal of Quantum Chemistry* 113.17 (2013).

[175] C. M. Isborn and X. Li. "Singlet-triplet transitions in real-time time-dependent Hartree-Fock/density functional theory". In: *Journal of Chemical Theory and Computation* 5.9 (2009).

[176] G. A. Baker and P. Graves-Morris. *Padé Approximants*. 2nd ed. Encyclopedia of Mathematics and its Applications. Cambridge University Press, 1996.

[177] C. R. Harris, K. J. Millman, S. J. van der Walt, R. Gommers, P. Virtanen, D. Cournapeau, E. Wieser, J. Taylor, S. Berg, N. J. Smith, R. Kern, M. Picus, S. Hoyer, M. H. van Kerkwijk, M. Brett, A. Haldane, J. F. del Rio, M. Wiebe, P. Peterson, P. Gerard-Marchant, K. Sheppard, T. Reddy, W. Weckesser, H. Abbasi, C. Gohlke, and T. E. Oliphant. "Array programming with NumPy". In: *Nature* 585.7825 (2020).

[178] P. Virtanen, R. Gommers, T. E. Oliphant, M. Haberland, T. Reddy, D. Cournapeau, E. Burovski, P. Peterson, W. Weckesser, J. Bright, S. J. van der Walt, M. Brett, J. Wilson, K. J. Millman, N. Mayorov, A. R. J. Nelson, E. Jones, R. Kern, E. Larson, C. J. Carey, I. Polat, Y. Feng, E. W. Moore, J. VanderPlas, D. Laxalde, J. Perktold, R. Cimrman, I. Henriksen, E. A. Quintero, C. R. Harris, A. M. Archibald, A. H. Ribeiro, F. Pedregosa, P. van Mulbregt, and SciPy 1.0 Contributors. "SciPy 1.0: Fundamental algorithms for scientific computing in Python". In: *Nature Methods* 17 (2020).

[179] M. A. Marques, M. J. Oliveira, and T. Burnus. "Libxc: A library of exchange and correlation functionals for density functional theory". In: *Computer Physics Communications* 183.10 (2012).

[180] R. A. Kendall, T. H. Dunning, and R. J. Harrison. "Electron affinities of the first-row atoms revisited. Systematic basis sets and wave functions". In: *Journal of Chemical Physics* 96.9 (1992).

[181] T. Tsuneda, J.-W. Song, S. Suzuki, and K. Hirao. "On Koopmans' theorem in density functional theory". In: *Journal of Chemical Physics* 133.17 (2010).

[182] A. M. Teale, F. De Proft, and D. J. Tozer. "Orbital energies and negative electron affinities from density functional theory: Insight from the integer discontinuity". In: *Journal of Chemical Physics* 129.4 (2008).

[183] W. W. Parson. *Modern Optical Spectroscopy*. Springer, 2007.

[184] C. Lian, M. Guan, S. Hu, J. Zhang, and S. Meng. "Photoexcitation in solids: First-principles quantum simulations by real-time TDDFT". In: *Advanced Theory and Simulations* 1.8 (2018).

[185] K. Krieger, J. K. Dewhurst, P. Elliott, S. Sharma, and E. K. U. Gross. *Laser induced ultrafast demagnetization: an ab-initio perspective*. arXiv: 1406.6607v1. 2014.

[186] P. M. Paul, E. S. Toma, P. Breger, G. Mullot, F. Augé, P. Balcou, H. G. Muller, and P. Agostini. "Observation of a train of attosecond pulses from high harmonic generation". In: *Science* 292.5522 (2001).

[187] P. B. Corkum. "Plasma perspective on strong field multiphoton ionization". In: *Physical Review Letters* 71 (1993).

[188] A. Castro, A. Rubio, and E. K. U. Gross. "Enhancing and controlling single-atom high-harmonic generation spectra: a time-dependent density-functional scheme". In: *European Physical Journal B* 88.8 (2015).

[189] A. F. White, C. J. Heide, P. Saalfrank, M. Head-Gordon, and E. Luppi. "Computation of high-harmonic generation spectra of the hydrogen molecule using time-dependent configuration-interaction". In: *Molecular Physics* 114.7-8 (2016).

[190] X.-M. Tong, G. Wachter, S. A. Sato, C. Lemell, K. Yabana, and J. Burgdörfer. "Application of norm-conserving pseudopotentials to intense laser-matter interactions". In: *Physical Review A* 92 (2015).

[191] F. Mauger, P. M. Abanador, T. D. Scarborough, T. T. Gorman, P. Agostini, L. F. DiMauro, K. Lopata, K. J. Schafer, and M. B. Gaarde. "High-harmonic spectroscopy of transient two-center interference calculated with time-dependent density-functional theory". In: *Structural Dynamics* 6.4 (2019).

[192] C. F. Pauletti, E. Coccia, and E. Luppi. "Role of exchange and correlation in high-harmonic generation spectra of H2, N2, and CO2: Real-time time-dependent electronic-structure approaches". In: *Journal of Chemical Physics* 154.1 (2021).

[193] A. M. Koushki, R. Sadighi-Bonabi, M. Mohsen-Nia, and E. Irani. "The control of electron quantum trajectories on the high-order harmonic generation of CO and N2 molecules in the presence of a low frequency field". In: *Journal of Chemical Physics* 148.14 (2018).

[194] A. Towfiq, J. Yoo, R. Prasankumar, and J.-X. Zhu. *A real-time TDDFT study of femtosecond laser driven monolayer NbSe2*. arXiv: 2008.07131. 2020.

[195] Z. Nourbakhsh, N. Tancogne-Dejean, H. Merdji, and A. Rubio. "High harmonics and isolated attosecond pulses from MgO". In: *Physical Review Applied* 15 (2021).

[196] G. Le Breton, A. Rubio, and N. Tancogne-Dejean. "High-harmonic generation from few-layer hexagonal boron nitride: Evolution from monolayer to bulk response". In: *Physical Review B* 98 (2018).

[197] N. Tancogne-Dejean, O. D. Mücke, F. X. Kärtner, and A. Rubio. "Impact of the electronic band structure in high-harmonic generation spectra of solids". In: *Physical Review Letters* 118 (2017).

[198] M. A. Rohrdanz, K. M. Martins, and J. M. Herbert. "A long-range-corrected density functional that performs well for both ground-state properties and time-dependent density functional theory excitation energies, including charge-transfer excited states". In: *Journal of Chemical Physics* 130.5 (2009).

[199] E. Luppi and M. Head-Gordon. "Computation of high-harmonic generation spectra of H2 and N2 in intense laser pulses using quantum chemistry methods and time-dependent density functional theory". In: *Molecular Physics* 110.10 (2012).

[200] E. Coccia and E. Luppi. "Optimal-continuum and multicentered Gaussian basis sets for high-harmonic generation spectroscopy". In: *Theoretical Chemistry Accounts* 135.2 (2016).

[201] P. Krause, J. A. Sonk, and H. B. Schlegel. "Strong field ionization rates simulated with time-dependent configuration interaction and an absorbing potential". In: *Journal of Chemical Physics* 140.17 (2014).

[202] M. Monfared, E. Irani, and R. Sadighi-Bonabi. "Controlling the multi-electron dynamics in the high harmonic spectrum from N2O molecule using TDDFT". In: *Journal of Chemical Physics* 148.23 (2018).

[203] P. de Boeij. "Solids from time-dependent current DFT". In: *Time-Dependent Density Functional Theory*. Ed. by M. A. Marques, C. A. Ullrich, F. Nogueira, A. Rubio, K. Burke, and E. K. U. Gross. Springer Berlin Heidelberg, 2006.

[204] D. J. Griffiths. *Introduction to Electrodynamics*. 4th ed. Cambridge University Press, 2017.

[205] J. Lindhard. "On the properties of a gas of charged particles". In: *Danske Matmatisk-fysiske Meddeleiser* 28.8 (1954).

[206] G. Giuliani and G. Vignale. *Quantum theory of the electron liquid*. Cambridge University Press, 2005.

[207] N. W. Ashcroft and N. D. Mermin. *Solid State Physics*. Holt-Saunders, 1976.

[208] C. Ambrosch-Draxl and J. O. Sofo. "Linear optical properties of solids within the full-potential linearized augmented planewave method". In: *Computer Physics Communications* 175 (2006).

[209] J. D. Jackson. *Classical Electrodynamics*. John Wiley & Sons, Inc., 1999.

[210] C. A. Ullrich and Z.-h. Yang. "Excitons in Time-Dependent Density-Functional Theory". In: *Density-Functional Methods for Excited States*. Ed. by N. Ferré, M. Filatov, and M. Huix-Rotllant. Cham: Springer International Publishing, 2016.

[211] *The ELK Code*. http://elk.sourceforge.net/.

[212] R. Boyd. *Nonlinear Optics*. 3rd ed. Academic Press.

[213] C. Diedrich and S. Grimme. "Systematic investigation of modern quantum chemical methods to predict electronic circular dichroism spectra". In: *Journal of Physical Chemistry A* 107.14 (2003).

[214] J. Autschbach, T. Ziegler, S. J. A. van Gisbergen, and E. J. Baerends. "Chiroptical properties from time-dependent density functional theory. I. Circular dichroism spectra of organic molecules". In: *Journal of Chemical Physics* 116.16 (2002).

[215] J. J. Goings and X. Li. "An atomic orbital based real-time time-dependent density functional theory for computing electronic circular dichroism band spectra". In: *Journal of Chemical Physics* 144.23 (2016).

[216] K.-M. Lee, K. Yabana, and G. F. Bertsch. "Magnetic circular dichroism in real-time time-dependent density functional theory". In: *Journal of Chemical Physics* 134.14 (2011).

[217] E. Makkonen, T. P. Rossi, A. H. Larsen, O. Lopez-Acevedo, P. Rinke, M. Kuisma, and X. Chen. "Real-time time-dependent density functional theory implementation of electronic circular dichroism applied to nanoscale metal–organic clusters". In: *Journal of Chemical Physics* 154.11 (2021).

[218] D. Varsano, L. A. Espinosa-Leal, X. Andrade, M. A. L. Marques, R. di Felice, and A. Rubio. "Towards a gauge invariant method for molecular chiroptical properties in TDDFT". In: *Physical Chemistry Chemical Physics* 11 (2009).

[219] N. Raimbault, P. L. de Boeij, P. Romaniello, and J. A. Berger. "Gauge-invariant formulation of circular dichroism". In: *Journal of Chemical Theory and Computation* 12.7 (2016).

[220] K. L. Bak, A. E. Hansen, K. Ruud, T. Helgaker, J. Olsen, and P. Jørgensen. "Ab initio calculation of electronic circular dichroism for trans-cyclooctene using London atomic orbitals". In: *Theoretica chimica acta* 90.5 (1995).

[221] J. Mattiat and S. Luber. "Electronic circular dichroism with real time time dependent density functional theory: Propagator formalism and gauge dependence". In: *Chemical Physics* 527 (2019).

[222] J. Autschbach. "Time-dependent density functional theory for calculating origin-independent optical rotation and rotatory strength tensors". In: *ChemPhysChem* 12.17 (2011).

[223] M. Carnell, S. Peyerimhoff, A. Breest, K. Gödderz, P. Ochmann, and J. Hormes. "Experimental and quantum-theoretical investigation of the circular dichroism spectrum of R-methyloxirane". In: *Chemical Physics Letters* 180.5 (1991).

[224] J. Enkovaara, C. Rostgaard, J. J. Mortensen, J. Chen, M. Dułak, L. Ferrighi, J. Gavnholt, C. Glinsvad, V. Haikola, H. A. Hansen, H. H. Kristoffersen, M. Kuisma, A. H. Larsen, L. Lehtovaara, M. Ljungberg, O. Lopez-Acevedo, P. G. Moses, J. Ojanen, T. Olsen, V. Petzold, N. A. Romero, J. Stausholm-Møller, M. Strange, G. A. Tritsaris, M. Vanin, M. Walter, B. Hammer, H. Häkkinen, G. K. H. Madsen, R. M. Nieminen, J. K. Nørskov, M. Puska, T. T. Rantala, J. Schiøtz, K. S. Thygesen, and K. W. Jacobsen. "Electronic structure calculations with GPAW: a real-space implementation of the projector augmented-wave method". In: *Journal of Physics: Condensed Matter* 22.25 (2010).

[225] U. Tohgha, K. K. Deol, A. G. Porter, S. G. Bartko, J. K. Choi, B. M. Leonard, K. Varga, J. Kubelka, G. Muller, and M. Balaz. "Ligand induced circular dichroism and circularly polarized luminescence in CdSe quantum dots". In: *ACS Nano* 7.12 (2013).

[226] S. Ostovar pour, L. Rocks, K. Faulds, D. Graham, V. Parchaňský, P. Bouř, and E. W. Blanch. "Through-space transfer of chiral information mediated by a plasmonic nanomaterial". In: *Nature Chemistry* 7.7 (2015).

[227] M. Vázquez-Nakagawa, L. Rodríguez-Pérez, M. A. Herranz, and N. Martín. "Chirality transfer from graphene quantum dots". In: *Chemical Communications* 52 (2016).

[228] P. L. Freddolino, A. S. Arkhipov, S. B. Larson, A. McPherson, and K. Schulten. "Molecular dynamics simulations of the complete satellite tobacco mosaic virus". In: *Structure* 14.3 (2006).

[229] R. Car and M. Parrinello. "Unified approach for molecular dynamics and density-functional theory". In: *Physical Review Letters* 55 (1985).

[230] J. C. Tully and R. K. Preston. "Trajectory surface hopping approach to nonadiabatic molecular collisions: The reaction of H+ with D2". In: *Journal of Chemical Physics* 55.2 (1971).

[231] M. Barbatti. "Nonadiabatic dynamics with trajectory surface hopping method". In: *Wiley Interdisciplinary Reviews: Computational Molecular Sciences* 1 (2011).

[232] A. V. Krasheninnikov, Y. Miyamoto, and D. Tománek. "Role of electronic excitations in ion collisions with carbon nanostructures". In: *Physical Review Letters* 99 (2007).

[233] M. A. Zeb, J. Kohanoff, D. Sánchez-Portal, A. Arnau, J. I. Juaristi, and E. Artacho. "Electronic stopping power in gold: The role of *d* electrons and the H/He anomaly". In: *Physical Review Letters* 108 (2012).

[234] A. A. Correa, J. Kohanoff, E. Artacho, D. Sánchez-Portal, and A. Caro. "Nonadiabatic forces in ion-solid interactions: The initial stages of radiation damage". In: *Physical Review Letters* 108 (2012).

[235] A. Ojanperä, A. V. Krasheninnikov, and M. Puska. "Electronic stopping power from first-principles calculations with account for core electron excitations and projectile ionization". In: *Physical Review B* 89 (2014).

[236] C. A. Rozzi, S. M. Falke, N. Spallanzani, A. Rubio, E. Molinari, D. Brida, M. Maiuri, G. Cerullo, H. Schramm, J. Christoffers, and C. Lienau. "Quantum coherence controls the charge separation in a prototypical artificial light-harvesting system". In: *Nature Communications* 4.1 (2013).

[237] E. Tapavicza, I. Tavernelli, and U. Rothlisberger. "Trajectory surface hopping within linear response time-dependent density-functional theory". In: *Physical Review Letters* 98 (2007).

[238] C. Flamant, G. Kolesov, E. Manousakis, and E. Kaxiras. "Imaginary-time time-dependent density functional theory and its application for robust convergence of electronic states". In: *Journal of Chemical Theory and Computation* 15.11 (2019).

[239] I. Stich, R. Car, M. Parrinello, and S. Baroni. "Conjugate gradient minimization of the energy functional: A new method for electronic structure calculation". In: *Physical Review B* 39 (1989).

[240] T. van Voorhis and M. Head-Gordon. "A geometric approach to direct minimization". In: *Molecular Physics* 100.11 (2002).

[241] G. Kresse and J. Furthmüller. "Efficient iterative schemes for ab initio total-energy calculations using a plane-wave basis set". In: *Physical Review B* 54 (1996).

[242] G. B. Arfken and H. J. Weber. *Mathematical Methods for Physicists*. 6th. Oxford: Elsevier, 2005.

[243] S. Azevedo, J. R. Kaschny, C. M. C. de Castilho, and F. de Brito Mota. "Electronic structure of defects in a boron nitride monolayer". In: *European Physical Journal B* 67.4 (2009).

[244] N. Manini. *Introduction to the Physics of Matter*. Springer, 2020.

[245] J. Neugebauer, M. Reiher, C. Kind, and B. A. Hess. "Quantum chemical calculation of vibrational spectra of large molecules – Raman and IR spectra for Buckminsterfullerene". In: *Journal of Computational Chemistry* 23.9 (2002).

[246] I. Bahar, T. R. Lezon, A. Bakan, and I. H. Shrivastava. "Normal mode analysis of biomolecular structures: Functional mechanisms of membrane proteins". In: *Chemical Reviews* 110.3 (2010).

[247] X. Gonze. "First-principles responses of solids to atomic displacements and homogeneous electric fields: Implementation of a conjugate-gradient algorithm". In: *Physical Review B* 55 (1997).

[248] N. A. Spaldin. "A beginner's guide to the modern theory of polarization". In: *Journal of Solid State Chemistry* 195 (2012).

[249] C. R. Jacob and M. Reiher. "Localizing normal modes in large molecules". In: *Journal of Chemical Physics* 130.8 (2009).

[250] *CRC 1242 – Non-Equilibrium Dynamics in the Time Domain*. https://www.uni-due.de/sfb1242.

[251] A. Dhirani, R. W. Zehner, R. P. Hsung, P. Guyot-Sionnest, and L. R. Sita. "Self-assembly of conjugated molecular rods: A high-resolution STM Study". In: *Journal of the American Chemical Society* 118 (1996).

[252] W. Azzam, A. Al-Rashdi, A. Subaihi, M. Rohwerder, M. Zharnikov, and A. Bashir. "Annealing effect for self-assembled monolayers formed from terphenylethanethiol on Au(111)". In: *Physical Chemistry Chemical Physics* (2020).

[253] S. Frey, V. Stadler, K. Heister, W. Eck, M. Zharnikov, M. Grunze, B. Zeysing, and A. Terfort. "Structure of thioaromatic self-assembled monolayers on gold and silver". In: *Langmuir* 17.8 (2001).

[254] C. M. Whelan, C. J. Barnes, C. G. H. Walker, and N. M. D. Brown. "Benzenethiol adsorption on Au(111) studied by synchrotron ARUPS, HREELS and XPS". In: *Surface Science* 425 (1999).

[255] Y.-T. Tao, C.-C. Wu, J.-Y. Eu, W.-L. Lin, K.-C. Wu, and C.-H. Chen. "Structure evolution of aromatic-derivatized thiol monolayers on evaporated gold". In: *Langmuir* 13.15 (1997).

[256] H. McNally, D. Janes, B. Kasibhatla, and C. Kubiak. "Electrostatic investigation into the bonding of poly (phenylene) thiols to gold". In: *Superlattices and Microstructures* 31.5 (2002).

[257] L.-J. Wan, M. Terashima, H. Noda, and M. Osawa. "Molecular orientation and ordered structure of benzenethiol adsorbed on gold(111)". In: *Journal of Physical Chemistry B* 104.15 (2000).

[258] K. Carron and L. Hurley. "Axial and azimuthal angle determination with surface-enhanced Raman spectroscopy: Thiophenol on copper, silver, and gold metal surfaces". In: *Journal of Physical Chemistry* 95.24 (1991).

[259] F. Cecchet, D. Lis, J. Guthmuller, B. Champagne, Y. Caudano, C. Silien, A. Addin Mani, P. A. Thiry, and A. Peremans. "Orientational analysis of dodecanethiol and p-nitrothiophenol SAMs on metals with polarisation-dependent SFG spectroscopy". In: *ChemPhysChem* 11.3 (2010).

[260] M. Linke, M. Hille, M. Lackner, L. Schumacher, S. Schlücker, and E. Hasselbrink. "Plasmonic effects of Au nanoparticles on the vibrational sum frequency spectrum of 4-nitrothiophenol". In: *Journal of Physical Chemistry C* 123 (2019).

[261] C. M. Whelan, M. R. Smyth, and C. J. Barnes. "HREELS, XPS, and electrochemical study of benzenethiol adsorption on Au(111)". In: *Langmuir* 15.1 (1999).

[262] F. Cecchet, D. Lis, J. Guthmuller, B. Champagne, G. Fonder, Z. Mekhalif, Y. Caudano, A. Addin Mani, P. A. Thiry, and A. Peremans. "Theoretical calculations and experimental measurements of the vibrational response of *p*-NTP SAMs: An orientational analysis". In: *Journal of Physical Chemistry C* 114 (2010).

[263] J. M. Morbec and P. Kratzer. "The role of van der Waals interactions in the adsorption of anthracene and pentacene on the Ag(111) surface". In: *Journal of Chemical Physics* 146 (2017).

[264] B. P. Klein, J. M. Morbec, M. Franke, K. K. Greulich, M. Sachs, S. Parhizkar, F. C. Bocquet, M. Schmid, S. J. Hall, R. Maurer, B. Meyer, R. Tonner, C. Kumpf, P. Kratzer, and J. M. Gottfried. "Molecule-metal bond of alternant versus nonalternant aromatic systems on coinage metal surfaces: Naphthalene versus azulene on Ag(111) and Cu(111)". In: *Journal of Physical Chemistry C* 123.48 (2019).

[265] S. R. Kachel, B. P. Klein, J. M. Morbec, M. Schöniger, M. Hutter, M. Schmid, P. Kratzer, B. Meyer, R. Tonner, and J. M. Gottfried. "Chemisorption and physisorption at the metal/organic interface: Bond energies of naphthalene and azulene on coinage metal surfaces". In: *Journal of Physical Chemistry C* 124 (2020).

[266] J. Hermann. *Libmbd*. 10.5281/zenodo.594879. Code as git repository.

[267] A. Maeland and T. B. Flanagan. "Lattice spacings of gold-palladium alloys". In: *Canadian Journal of Physics* 42.11 (1964).

[268] L. Bengtsson. "Dipole correction for surface supercell calculations". In: *Physical Review B* 59 (1999).

[269] R. S. Mulliken. "Electronic population analysis on LCAO–MO molecular wave functions. I". In: *Journal of Chemical Physics* 23.10 (1955).

[270] S. Schlücker. "Surface-enhanced Raman spectroscopy: Concepts and chemical applications". In: *Angewandte Chemie International Edition* 53.19 (2014).

[271] J. U. Nielsen, M. J. Esplandiu, and D. M. Kolb. "4-nitrothiophenol SAM on Au(111) investigated by in situ STM, electrochemistry, and XPS". In: *Langmuir* 17.11 (2001).

[272] H.-F. Wang, W. Gan, R. Lu, Y. Rao, and B.-H. Wu. "Quantitative spectral and orientational analysis in surface sum frequency generation vibrational spectroscopy (SFG-VS)". In: *International Reviews in Physical Chemistry* 24 (2005).

[273] A. Abedi, N. T. Maitra, and E. K. U. Gross. "Exact factorization of the time-dependent electron-nuclear wave function". In: *Physical Review Letters* 105 (2010).

[274] S. K. Min, F. Agostini, I. Tavernelli, and E. K. U. Gross. "Ab initio nonadiabatic dynamics with coupled trajectories: A rigorous approach to quantum (de)coherence". In: *Journal of Physical Chemistry Letters* 8.13 (2017).

[275] H. F. Walker and P. Ni. "Anderson acceleration for fixed-point iterations". In: *SIAM Journal on Numerical Analysis* 49.4 (2011).

[276] T. Otobe, M. Yamagiwa, J.-I. Iwata, K. Yabana, T. Nakatsukasa, and G. F. Bertsch. "First-principles electron dynamics simulation for optical breakdown of dielectrics under an intense laser field". In: *Physical Review B* 77 (2008).

Acknowledgements

In general, I want to thank everybody who accompanied and helped me on my way from the beginning to the end of these studies. I cannot imagine going this path alone.

First of all, I want to thank Prof. Peter Kratzer for the supervision of this project. You let me choose many points on my own, but also always pointed towards the goals and supported my way there. I know how important correct scientific conduct, appropriate description of physical phenomena, and the reflected use of models is to you. Thank you that you always took the time to discuss these and other topics.

I want to thank Prof. Volker Blum, Dr. Yi Yao, Prof. Yosuke Kanai, Dr. Ville Havu, Matthias Linke, Thomas Keller, Jesil Jose, Marvin Hille, Prof. Eckart Hasselbrink and Prof. Sebastian Schlücker for the professional and friendly collaborative work.

Special thanks to Michael and Jonathan for the thorough proofreading of this thesis and for the great time in our mutual studies. Thanks to Martin for offering to proofread the document, although it didn't happen eventually.

For the friendly and professional atmosphere in the workgroup Kratzer, I want to thank all former and current members, especially Sebastian. This also applies for the members of the workgroup Pentcheva, especially Vijaya.

Thanks to Dr. Dörmann and all other organizational staff of the CRC 1242 for the dedicated work in this context. I further want to thank all responsible persons within the CRC 1242, the DFG and the University of Duisburg-Essen for making this thesis possible.

Dank gilt weiterhin Frau Lukas und Frau Tappert für den freundlichen Umgang und ihre organisatorischen Mühen.

Ianine, für Deine gigantische Geduld und Unterstützung insbesondere gegen Ende dieser Arbeit kann ich Dir gar nicht genug danken. Es macht mich sehr glücklich, dass wir zueinander gefunden haben.

Iris und Wolfgang, Euch möchte ich hier noch einmal besonders für Eure stetige Unterstützung während meiner gesamten Wegfindung danken.

Declaration

Die hier vorliegende Dissertation wurde selbstständig von mir verfasst. Beim Verfassen dieser Arbeit wurden nur die angegebenen Hilfsmittel benutzt. Jegliche Ausführungen, die anderen Arbeiten schriftlich oder inhaltlich entnommen wurden, sind als solche gekennzeichnet. Diese Dissertation wurde nur in diesem Promotionsvorhaben eingereicht und ich habe bisher keinen erfolglosen Promotionsversuch unternommen. Ich strebe mit diesem Vorhaben den Doktorgrad Dr. rer. nat. an.

Unterschrift:

Datum:

DOI: 10.17185/duepublico/74983
URN: urn:nbn:de:hbz:464-20211125-100913-5